The Neonatal Locus Coeruleus is a Differentiated and Complex Neuromodulatory System as Revealed by Local Field Potential Analysis

by

Bijal Rawal

A thesis submitted in partial fulfillment of the requirements for the degree of

Doctor of Philosophy

Department of Physiology

University of Alberta

Abstract

The locus coeruleus (LC) in the pons of the brainstem provides the sole source of noradrenergic afferent input to most brain structures including the cerebral cortex, hippocampus, cerebellum and spinal cord. The resulting modulation of activity is important for controlling behaviors like sleep-wake cycle, pain sensitization, memory formation or opioid (withdrawal) reactions. It is still unclear how this small nucleus modulates activity in these brain areas in a diverse fashion. The aim of this thesis was to study, in brain slices from neonatal rats, properties of spontaneous electrical LC activity with emphasis on the involvement of subtypes of ionotropic glutamatergic receptors (iGluR) in modulation of both network discharge and cellular firing patterns.

It was firstly found with single unit recording that LC neurons discharge with a jitter of 30-100 ms at a rate of ~1 Hz single spikes that summate to a ~ 0.2 s-lasting local field potential (LFP) burst and that each neuron preferentially discharges in a particular phase of this network response. Elevating superfusate K^+ from 3 to 7 mM either increased LFP rate or transformed its pattern from a bell-shaped signal into multi-peak bursts lasting several seconds. The latter LFP pattern was also seen during recovery from inhibition of rhythm by μ-opioid receptor activation with DAMGO.

It was next investigated with simultaneous LFP and whole-cell membrane potential (V_m) recording whether the spontaneous jittered, yet phase-locked LC neuronal spiking and LFP pattern are altered by bath-applied glutamate or the iGluR agonists AMPA, KA, QUI and NMDA and whether a complex of the AMPA receptor (AMPAR) with TARP (auxiliary transmembrane AMPAR regulatory proteins) is functional. TARP-AMPAR complex activation via bath-application of the

partial agonist CNQX increased LFP rate via neuronal depolarization that accelerated spiking to increase the free cytosolic Ca^{2+} concentration (Ca_i). The Ca_i rise was blocked by the L-type Ca^{2+} channel blocker nifedipine and the electrophysiological CNQX effects were abolished by the non-competitive AMPAR blocker GYKI. AMPA and KA accelerated LFP rate and transformed the pattern to faster sinusoidally-shaped oscillatory events of shorter event duration with fluctuations of signal amplitude. Both agents also increased the regularity of LFP bursting and decreased cellular spike jitter, but did not increase network synchronization. Glutamate made the network rhythm more irregular and increased burst duration with decreased network synchronization whereas NMDA caused faster oscillatory events of shorter duration with rhythmic pauses and enhanced network synchronicity. Pattern transformation by QUI was similar to that evoked by glutamate, but without decreasing synchronicity, and this effect was mediated by iGluR activation as judged by the countering effect of the nonselective iGluR antagonist kynurenic acid.

This study is the first demonstration that spiking in the neonatal LC is not synchronous, but rather jittered, yet phase-locked to the population burst and that the pattern of this bursting is transformed by changes in network excitability evoked by K^+, opioids and iGluR agonists. These findings provide the basis for future studies aiming at understanding the causal link between LC firing patterns and resulting modulation of activities in the targeted brain areas and thus in their functions.

Preface

This thesis is the original work by Bijal Rawal. Some of the experiments were performed in collaboration with Dr. Vladimir Rancic, a postdoctoral fellow in the laboratory of my supervisor Dr. Klaus Ballanyi. All research projects described in thesis were approved by the University of Alberta Research Ethics Board: Protocol number - AUP00000221.

The thesis contains two published papers as mentioned below.

Chapter 3 of this thesis is published in Neuroscience Letters:

Rancic V, Rawal B, Panaitescu B, Ruangkittisakul A, Ballanyi K (2018) Suction electrode recording in locus coeruleus of newborn rat brain slices reveals network bursting comprising summated non-synchronous spiking. Neurosci Lett 671:103-107.

Chapter 4 of this thesis is published in Neuropharmacology:

Rawal B, Rancic V, Ballanyi K (2019) TARP mediation of accelerated and more regular locus coeruleus network bursting in neonatal rat brain slices. Neuropharmacology 148: 169-177.

Acknowledgments

This doctoral program is an important milestone in my education and my most cherished pursuits so far. I am fortunate to have several special people in my life who contributed in this journey.

First and foremost, I would like to thank my supervisor Dr. Klaus Ballanyi. The advice and direction he provided helped me craft this dissertation. I am grateful to Dr. Arun Raturi, who motivated and guided me in joining the doctoral program and building a research career. I am also thankful to all the members of my lab, Dr. Vladimir Rancic, Dr. Araya Ruangkittisakul, Dr. Jyoti Singh, and the current MSc student Marcela Louie for providing me both technical and emotional support. I am especially thankful to Vladimir for the many insightful discussions and a great friendship.

I am grateful to my committee members, Drs. Peter Smith, Yves Sauve and Robert Campbell for the time and feedback they have provided at various stages of my doctoral program. I will be forever thankful to my graduate program coordinator Dr. Gregory Funk for providing helpful advice many times during the program. I would also like to express my sincere gratitude to the arm-length and external members of my defense examination committee, Dr. Jesse Jackson and Dr. Jan-Marino Ramirez, respectively for their valuable time and suggestions.

This doctoral journey would also not have been possible without the love and support of friends and family. I thank my friends in Edmonton (too many to list here, but you know who you all are!) who became my family.

I have no words to thank my superman, my husband Saurabh, for being my only source of strength during my setbacks and challenges that I faced during the program. Thank you for keeping me sane rather, insane and I would not have enjoyed this journey without you. I will be forever indebted to my mom and dad for making my life easier in every way possible and I would not have made it this far without their sacrifices and love. Also, I can never be thankful enough to my parents-in-law for all that they have done for me. Thank you for the support and letting me be me and helping me achieve this. Last but not the least; I owe a deep sense of gratitude to my grandfather-in-law, dada, for believing in my pursuit. He would have been the proudest of all today seeing me accomplish this.

Table of Contents

List of Figures

Chapter 1

Chapter 3

Chapter 4

Chapter 5

Chapter 6

Chapter 7

List of Tables

Chapter 4

List of abbreviations

2-APV	2-Amino-5-phosphonopentanoic acid
AHP	After-hyperpolarization
AMPA	α-amino-3-hydroxy-5-methyl-4-isoxazolepropionic acid
AMPAR	AMPA receptor
AP	Action potential
ATP	Adenosine triphosphate
BAPTA	1,2-bis(o-aminophenoxy)ethane-N,N,N',N'-tetraacetic acid
cAMP	Cyclic-adenosine monophosphate
Ca_i	Cytosolic Ca^{2+}
CFE	Cross-correlation function estimate
CNQX	6-cyano-7-nitroquinoxaline-2,3-dione
DAMGO	[D-Ala_2, N-Me-Phe_4, Gly_5-ol] Enkephalin
DMSO	Dimethyl sulfoxide
DNQX	6,7-dinitroquinoxaline-2,3(1H,4H)-dione
FI	Fluorescence intensity
GABA	γ-aminobutyric acid
Glu	Glutamate
GIRK	G protein-coupled inward-rectifying K^+ channels
iGluR	ionotropic glutamate receptor
KA	Kainate
LC	Locus coeruleus

LFP	Local field potential
MUA	Multi-unit activity
NA	Noradrenaline
NMDA	N-methyl-D-aspartic acid
PAD	Post-agonist depression
QUI	Quisqualate
TARP	Transmembrane AMPAR regulatory protein
rFP	rhythmic field potential
ROI	Region of interest
SK	Small conductance Ca^{2+} activated K^{+}
TTX	Tetrodotoxin
V_m	Membrane potential

CHAPTER 1

General Introduction

1.1. Overview

The locus coeruleus (LC) in the brainstem is the major source for noradrenergic innervation of most brain structures. It thus controls multiple behaviors like arousal, sleep-wake cycle or memory. These behaviors are affected when the LC neuron activity pattern changes from normal spontaneous 'tonic' action potential (AP) firing to phasic discharge. Altered LC signaling can also contribute to neuropathological conditions such as Alzheimer's disease, anxiety or drug addiction. In the latter regard, the α_2 noradrenaline (NA) receptor agonist Lofexidine is used for treatment of opioid withdrawal symptoms. Despite the important role of the LC in brain control, the cellular mechanisms are still unclear by which this small nucleus of only several thousand neurons exerts its multiple functions. As one precondition for such 'multitasking', evidence is currently emerging that the LC has a modular organization. This means that neuron clusters in specific LC aspects are influenced by chemical neurotransmitters released from afferent axons which originate from remote brain circuits. Conversely, NA is released from the LC into specific areas within the neuroaxis by efferent axons from distinct neuron classes. These neurons show differences in their synaptic (i.e. neurotransmitter-modulated) and non-synaptic (i.e. intrinsic) ion channels and, thus, their capability to respond to afferent stimuli and generate activity patterns. For example, activation of ionotropic glutamate receptors (iGluR) in LC neurons is necessary to convert their tonic spiking into bursting under the influence of morphine. Similarly, cocaine changes their spiking into bursting by blocking NA uptake to raise its tonic background concentration in the extracellular space where it then acts on α_2 receptors to promote a burst-generating intracellular 'second-messenger' signaling cascade. Astrocytes are capable of modulating the activity of neighboring LC neurons as evident from the finding that release of lactate by these glial cells activates a yet unknown receptor on LC neurons to accelerate their spiking. In neonatal rodents, spontaneous LC neuron spiking is presumably synchronous and generates a rhythmic local field potential (LFP).

Note that the term 'rhythmic field potential' (rFP) was used in the publication resulting from project-1 (Rancic et al., 2018). In this thesis, properties of this LFP were firstly analyzed in neonatal rat brain slices in control superfusate with an ion composition similar to that in the extracellular space of the brain. Subsequently, LFP assessment was combined with membrane potential (V_m) recording or multiphoton imaging of the free cytosolic Ca^{2+} concentration (Ca_i) to analyze distinct LFP pattern transformations evoked by glutamate and iGluR (ant)agonists. The results show that the LC is a complex modular neuron-glia ('neural') neural network that is capable of adapting its output activity pattern, likely for the purpose of fine-tuning diverse brain functions.

1.2. Locus Coeruleus - A major guardian of brain functions

The mammalian brain can perform complex cognitive functions such as learning, memory, attention or rewards because of its ability of processing complex electrical and chemical synaptic activities, particularly in forebrain structures (Kandel et al., 2012). Such processing mechanisms require a dynamic range of neuronal AP firing patterns (Abeles, 1991). These adaptive AP discharge patterns are controlled by diverse brain nuclei which send out axons that release specific chemical neurotransmitters and (non-synaptic) neuromodulators such as noradrenaline (NA), dopamine, serotonin, acetylcholine or neuropeptides like substance-P or endorphines. The LC is an example for such neuromodulatory nuclei and neuroanatomical studies have established it since long as the most widely projecting one (Aston-Jones, 1995). Specifically, the LC supplies NA via its efferent axons to most forebrain structures, including the neocortex, hippocampus, amygdala, cerebellum, hypothalamus, thalamic relay nuclei, brainstem and the spinal cord. Because of this (partly 'diffuse') innervation of most of the neuraxis, it controls important behaviors, and other brain functions, like attention, arousal, sleep and wakefulness, perception, memory formation,

anxiety, pain sensation or breathing through modulating the discharge patterns in diverse brain areas exerting these processes (Foote et al., 1983; Berridge and Waterhouse, 2003).

In the following, examples are given for excitatory or inhibitory innervation of different efferent LC axon target areas and resulting (behavioral) effects. Considering all these effects, it is intriguing how a small cluster of only several thousand neurons (Swanson, 1976; Loughlin et al., 1986) can mediate all these modulatory actions.

1.2.1. Efferent LC output

LC axons provide the sole source of noradrenergic innervation to a variety of forebrain structures **(Fig. 1-1A)** (Clark and Proudfir, 1991; Sluka and Westlund, 1992; Schuerger and Balaban, 1993; Uematsu et al., 2015). For example, LC input to the (neo)cortex can be either excitatory or inhibitory (Pieribone et al., 1994; Domyancic and Morilak, 1997; Papay et al., 2006) and this can be seen also in forebrain EEG activity (Berridge and Foote, 1991). The differential NA effects on the cortex and neocortex and the fact that LC neurons exhibit increased AP firing during wakefulness and decreased activity during sleep makes this nucleus one of the crucial regulators of sleep-wake cycle (Foote et al., 1980). Moreover, a recent study revealed that phasic LC firing is responsible for increasing cortical excitability and inducing gamma oscillations that are essential for stimulating nociceptive signaling pathways (Neves et al., 2018). The LC also provides the sole source of NA for the hippocampus (Loughlin et al., 1986; Fu et al., 1999) and bilateral LC lesions disrupt associative olfactory memory in newborn rats by impairing β-type NA receptor-mediated memory formation in hippocampus (Sullivan et al., 1994).

The LC also provides excitatory input to the dorsal raphe, pedunculopontine tegmental nucleus and the laterodorsal tegmental nucleus and inhibitory input to the ventrolateral preoptic area (Samuels and Szabadi, 2008). Moreover, electrical or pharmacological LC activation shifts neural networks in the amygdala to a more excitable state resulting in increased anxiety in subjects (Redmond et al., 1976; Goddard et al., 1995, McDaggal et al., 1995). Related with that, the LC is involved in formation and retrieval of emotion-associated memory, possibly through modulation of neuronal activity in the amygdala (Kiernan, 2005; Sterpenich et al., 2006).

In addition to affecting central nervous system (CNS) structures, the LC innervates sympathetic and parasympathetic preganglionic neurons (Swanson and Sawchenko, 1983; Westlund et al., 1983; Hermann et al., 1997). In sympathetic autonomic pathways, LC axons innervate the kidney and urinary bladder (Williams and McGauff, 1993; Sly et al., 1999). A role in pain sensation is indicated by the findings that noxious stimuli increase the electrical activity of LC neurons and, consequently, NA release (Kimura and Nakamura, 1985; Rasmussen et al., 1986; Hirata and Aston-Jones, 1994). Furthermore, the LC innervates pain-sensitive neurons of the trigeminal sensory nuclei and the dorsal horn of the spinal cord (Senba et al., 1981; Fritschy and Grzanna, 1990). As a last example, electrical LC stimulation depresses inspiratory inhibition in the Bötzinger complex of the lower brainstem (Wang et al., 2004) suggesting that the LC modulates the activity of neural networks controlling breathing. This view is substantiated by many more findings like that the LC contains chemosensitive neurons involved in regulation of breathing in response to inspired CO_2 (Biancardi et al., 2008).

Most CNS neurotransmitters are released at an axon terminal forming a chemical synapse (Kandel et al., 2012). In contrast, LC axons release along their axon NA at multiple varicosities which comprise bulbous enlargements of their diameter serving as presynaptic 'boutons' (Geffen and Livett, 1971; Livett, 1973; Descarries et al., 1977). LC axonal varicosities facilitate 'volume transmission' of NA, therefore allowing its diffusion to areas relatively remote to the release site which are thus not directly synaptically connected (Ungerstedt et al., 1969; Fuxe and Ungerstedt, 1970; Descarries et al., 1977; Fuxe et al., 2007; Fuxe et al., 2010).

1.2.2. Afferent LC input

In summary, section **1.2.1.** exemplified that LC activity has diverse effects on multiple structures along the neuraxis. Next, it needs to be considered which afferent brain structures can change the activity of LC neurons, which then propagate their APs to the above described target areas. Contrary to the widespread efferent LC projections, findings from early studies indicated that LC afferents are restricted to two brainstem nuclei, specifically the paragigantocellularis and the prepositus hypoglossi (Aston-Jones et al., 1986; Aston-Jones et al., 1991b). However, subsequent work demonstrated the presence of further inputs to the LC including the cortex, amygdala, hypothalamus, nucleus of the solitary tract and the spinal cord **(Fig. 1-1B)** (Luppi et al., 1995; Zhu and Aston-Jones, 1996; Van Bockstaele et al., 1999; Aston-Jones et al., 2001).

In addition to several subtypes of NA autoreceptors (i.e. α_1, α_2, β_1, β_2, β_3), LC neurons express various other receptors, e.g. for opioids, y-aminobutyric acid (GABA), orexin, corticotropic releasing factor, dopamine or acetylcholine **(Fig. 1-2)** (Atweh and Kuhar, 1977; Rotter et al., 1979;

Young and Kuhar, 1980; Aston-Jones et al., 1995; Van Bockstaele et al., 1996; Delaville et al., 2011; Schwarz and Luo, 2015). This indicates that LC neuron activity is under ongoing control by neurotransmitters released from the afferent axons originating from the above structures.

Among the afferent neurotransmitters, glutamate has a particularly important effect on LC activity (Singlewald and Philippu, 1998). Retrograde tracer and immunostaining studies have demonstrated that the LC receives predominantly glutamatergic afferents from the paragigantocellularis nucleus (Aston-Jones et al., 1986; Guyenet and Young, 1987; Pieribone et al., 1988; Aston-Jones et al., 1991). Paragigantocellularis stimulation evokes an excitatory response in LC neurons which is abolished by kynurenic acid and γ-d-glutamylglycine (Ennis and Aston-Jones, 1988; Shiekhattar and Aston-Jones, 1991). These agents are both competitive antagonists for the iGluR subtype that is activated by the commonly used agonists α-amino-3-hydroxy-5-methyl-4-isoxazole propionic acid (AMPA), kainate (KA) and quisqualate (QUI), i.e. the AMPA receptor (AMPAR) (Traynelis et al., 2010). Contrary, 2-amino-7-phosphono-heptanoic acid (AP-7), an antagonist of the other iGluR subtype that is activated by N-methyl-D-aspartate (NMDA), i.e. the NMDA receptor, was not effective in the latter paragigantocellularis stimulation studies.

In addition to afferent signals, the activity of LC neurons is modulated by neurotransmitters that are released from collaterals of their own axons which terminate within the LC. For example, it was shown that endogenously released NA causes 'auto-inhibition' of LC neurons, thereby attenuating their AP 'spiking' and subsequent NA release (Aghajanian et al., 1977). While the main neurotransmitter of LC neurons is NA, they can also release other neurotransmitters like the neuropeptides galanin, neuropeptide-Y, somatostatin or enkephalin that all may serve to fine-tune

the primary NA action on remote target structures or within the LC itself (Olpe and Steinmann, 1991; Sutin and Jacobowitz, 1991; Berridge and Waterhouse, 2003; Schwarz and Luo, 2015).

1.2.3. Modular LC organization

In summary, section **1.2.2.** showed that the activity LC neurons is modulated by several afferent structures via diverse neurotransmitters and also by their own neurotransmitters acting on autoreceptors. While this indicates that LC output activity is under complex control, the neurons themselves also differ in various regards to form 'modules' within different aspects of the nucleus.

On the one hand, it was shown with anterograde and retrograde tracing methods and antibodies against the NA-synthesizing enzymes dopamine-beta-hydroxylase (DBH) and tyrosine hydroxylase (TH) that all LC neurons are catecholaminergic **(Fig. 1-3A)** (Dahlstrum and Fuxe, 1964; Hartman, 1973; Pickel et al., 1975; Sawchenko and Swanson, 1982). On the other hand, similar approaches revealed that LC neuron subclasses can be identified by their expression pattern for other endogenous neurotransmitters, e.g. glutamate, GABA, opioids, orexin, corticotropic releasing factor, dopamine or acetylcholine.

In addition, LC neurons express different sets of neurotransmitter receptors (Schwarz and Luo, 2015). The latter comprehensive review states that different approaches like viral-genetic axon tracing unraveled that an individual LC neuron receives inputs from at least 15 brain regions including the neocortex, amygdala, thalamus, hypothalamus or cerebellar cortex. In contrast to that convergence of afferent inputs, particularly retrograde tracer labeling studies showed that neurons in LC subregions innervate specific distinct targets **(Fig. 1-1A)** (Room et al., 1981; Fallon and

Loughlin, 1982; Loughlin et al.,1986a,b; Steindler and Tosko, 1989; Schwartz and Luo, 2015). For example, LC neurons innervating the hippocampus are prominent in the dorsal part of the LC whereas a cerebellum- and spinal cord-projecting neuronal module is located in its ventral region (Waterhouse et al., 1983; Loughlin et al., 1986). Moreover, cortex-innervating LC neurons are found in the caudal LC aspect whereas amygdala-innervating neurons are distributed throughout the nucleus (Mason and Fibiger, 1979; Loughlin et al., 1986; Schwarz and Luo, 2015). Conversely, studies using dual tracer injection revealed that the same LC neuron subclass can project to different brain areas (Nagai et al., 1981; Room et al., 1981; Steindler et al., 1981; Simpson et al., 1997). With 3D reconstruction of retrogradely labeled LC neurons, it was found that morphologically distinct neurons project to different target areas, thus suggesting for the first time a topo-morphological distribution of their efferent projections (Loughlin et al., 1986a,b).

Neurons in distinct LC regions can also differ in their biophysical properties **(Fig. 1-3C1, C2)**. For example, LC neurons projecting to different cortical regions show differences in their firing frequency as well as the amplitude of their AP after-hyperpolarization (AHP) (Chandler et al., 2014). Moreover, ventrally-located adult rat LC neurons with a shorter spike and smaller AHP than LC core neurons act as a 'pontospinal-projecting module' (Li et al., 2016) whereas dorsomedially-located small and densely packed GABAergic neurons in juvenile mice show faster spiking with enhanced adaptation (Jin et al., 2016).

1.2.4. Maturational state of the neonatal rodent LC

The above noted differences between LC neurons in different LC subregions regarding their AP properties were studied in brain slices (Jin et al., 2016; Li et al., 2016). This is because, e.g.,

experimental conditions are more stable and detailed pharmacology can be performed in vitro (Ballanyi, 1999). In fact, most pharmacological findings on LC neuron excitability and its modulation by neurotransmitters and (recreational) drugs were obtained by electrophysiological recordings in brain slices, initially from newborn, juvenile or adult rats and since several years also from mice. This has, on the one hand, the disadvantage that findings using slices from animals of different ages may differ as it is established that neuronal and network properties change during postnatal maturation (Dreyfus, 1983; Nakamura et al., 1987; Marshall et al., 1991; Kaila, 1994; Ballanyi, 1999; Ben-Ari et al., 2007). On the other hand, this led to the discovery that LC network connectivity changes during the first two postnatal weeks. Specifically, spontaneous single AP discharge of neonatal LC neurons seems to be synchronized via gap junctions whereas the extent and or type of coupling via these 'electrical synapses', formed by different types of connexins, appears to change during this time period (Christie et al., 1989; Christie, 1997; Ishimatsu and Williams, 1996; Alvarez et al., 2002; Van Bockstaele et al., 2004).

Despite this difference, and possibly other postnatal changes of LC network excitability, the neonatal LC is already functional. Specifically, in rats LC synaptogenesis begins at 19 days of gestation (Lauder and Bloom, 1975). While this is two days before the birth of rats, LC neurons and their processes containing catecholamines become visible with fluorescence staining already at 12 to 14 days of gestation indicating that already at this early stage the LC starts to synthesize NA and project to target areas (Olson and Seiger, 1972; Lauder and Bloom, 1974). This fact prompted the postulation that the LC is important for brain development (Marshall et al., 1991). For example, development in infant rats of odor-based maternal recognition and attachment involves a large release of NA into the olfactory bulb (Moriceau et al., 2004). This olfactory

learning ends at postnatal day 10 and at this stage the LC appears to have matured to an almost adult-like neural circuit (Moriceau et al., 2010).

1.2.5. In vitro analyses of biophysical and second-messenger LC signaling

To study LC network properties in vivo is important, but technically very challenging. Therefore, intrinsic and neurotransmitter-activated ion channels and also metabotropic, e.g. G protein-modulated, signaling pathways are mainly analyzed in LC neurons of brain slices. For example, it is established by work on LC neurons in slices that both α_2 NA and μ-opioid receptors exert a K^+ channel-mediated hyperpolarization and associated spike depression by activating the same $G_{i/o}$ protein-adenosine 3',5' cyclic monophosphate-protein kinase A-dependent signaling pathway (Williams and North, 1984; North and Williams et al., 1985; Alreja and Aghajanian, 1993; Nestler, 1996).

The next sections **(1.3. - 1.7.)** are organized as follows. Firstly, a brief background is provided about the use of brain slices. Then, an outline of techniques used to study neural network activity is given with emphasis on field potential recording and Ca_i imaging as commonly used tools to monitor neural circuit activities. Finally, the current knowledge on basic electrophysiological and neuropharmacological properties of LC neurons is reviewed.

1.3. Brain slices as models to study neuronal activity

Despite several advantages associated with studying brain activity in vivo, like the correlation between neuronal activities and behavior, use of isolated brain tissue is still a most effective and commonly used approach. Since the pioneering, initially biochemical, work of McIlwain and colleagues (McIlwain et al., 1951; Li and McIlwain, 1957), brain slices are abundantly used to study intrinsic cellular and neural network properties, neurotransmitter-mediated modulation of ionic conductance and the role of different types of the underlying ion channels and receptors in brain activity. In addition, brain slices offer the advantage of long-term stable recording and direct visualization of cells which facilitates the anatomical identification and functional characterization of specific neural circuits (Gibb and Edwards, 1994). For example, the use of slices was instrumental in developing a detailed understanding of how the interplay between voltage-gated fast non-inactivating Na^+ channels and voltage-gated low threshold ('T-type') Ca^{2+} channels causes spontaneous electrical activity in thalamic, Purkinje and inferior olive neurons (Llinas and Sugimori, 1980a,b; Llinas and Yarom, 1981a,b). These findings were substantiated by in vivo studies describing the involvement of T-type Ca^{2+} channels in regulating neural network discharges and behaviors during vigilance (Deschenes et al., 1984; Steriade and Deschenes, 1984).

In addition, in brainstem slices spontaneous in vivo-like tonic activity was revealed in neural circuits including the dorsal vagal nucleus, substantia nigra and LC (Jahnsen, 1986). With regards to the LC, findings from in vivo studies about distinct neuronal firing patterns in regulation of sleep and wake states (Aston-Jones, 1980) were further investigated in great detail using brain slices. For example, William and colleagues (1984) recorded spontaneous spiking from LC neurons in horizontal brainstem slices. Subsequent slice studies on LC neurons gave insight into the

mechanisms underlying their activity. Detailed electrophysiological properties of LC neurons are described in section **1.2.2.**

Although the above mentioned LC neuronal structures and properties were mostly studied in brain slices from juvenile or adult rodents (Andrade and Aghajanian, 1984; Jahnsen, 1986; Olpe et al., 1989; Alvarez et al., 2002), a major thrust in using slices from young or juvenile animals came after the development of advanced live-cell imaging techniques. This proved to be a technological breakthrough because it allowed the study of intracellular activities, such as Ca_i signaling in populations of cells, in combination with extra- plus intracellular electrophysiological recording (Ballanyi, 1999). Moreover, in slices from newborn or juvenile animals, particularly rats and mice, neurons and glial cells can be easier visualized due to yet incomplete myelination.

1.4. Electrophysiological recording of neural network activity

Neurons encode and transmit information as a pattern of propagated APs. Such electrical activity can be assessed in various ways ranging from recording of single ion channel currents in membrane patches from individual neurons to electroencephalogram monitoring in the intact brain (Kandel et al., 2012). In a neural network, (synchronized) electrical activity of many neurons gives often rise to an electrical potential in the surrounding extracellular space that can be detected with microelectrodes (Buzski et al., 2012; Einevoll et al., 2013). Monitoring the extracellular activity of a single neuron is commonly referred to as 'single-unit' recording whereas the corresponding approach for multiple neurons is termed either multi-unit activity (MUA) or local field potential (LFP) recording (Buzsáki et al., 2012; Einevoll et al., 2013). MUA reflects the summation of transmembrane currents generated by synaptic activity of neurons in the vicinity of the recording

electrode whereas the term LFP is mostly used when the activity rather comprises synchronous AP firing (Suter et al., 1999; Logothetis, 2003; Buzsáki et al., 2012). A further difference between LFP and MUA recording is regarding the use of electrode types and signal filtering. Specifically, MUA is measured with high impedance (1- 5 MΩ) electrodes using 'high pass' filtering >500 Hz whereas a LFP is recorded at 'low pass' filtering <300 Hz using low impedance (<1 MΩ) electrodes (Einevoll et al., 2013). In summary, LFP recording is particularly attractive for recording synchronized network activity because it can typically assess a wide range of neuronal oscillations from under 1 Hz to over 100 Hz (Buzsáki et al., 2012; Destexhe and Bedard, 2013).

Traditional electrophysiological methods to measure brain activity in vivo involve the use of electroencephalography and electrocorticography (Buzsáki et al., 2012; Obien et al., 2014). However, over the past several years the technological advancement has enabled extracellular neuronal recording from multiple sites using multi-electrode arrays (MEA) which contain tens to thousands of electrodes. MEA recording has been used to assess neuronal activity in behaving animals (Nicolelis, 2008; Viventi et al., 2011) as well as in brain slices and cultures (Taketani and Baudry, 2006; Baker, 2010; Field et al., 2010). With regards to LFP or MUA recording from brain slices, mostly single or multiple glass or metal electrodes are used (Llinas, 1988; Henze et al., 2000; Buzsáki et al., 2012).

In extension of exclusive extracellular electrophysiological recording, the association between intracellular neuronal activity and MUA or LFP signals provides information regarding the (synaptic) connectivity, i.e. coupling strength, within a neural circuit. In vivo and in vitro studies using a combination of (intra)cellular spike and MUA/LFP recordings on thalamus and cerebral

cortex have provided pivotal information about the extent of synchrony in these neural networks and thus their function (Kim et al., 1995; Steriade et al., 1996a).

As outlined above (**1.3.1.**), synchronous neural network activity can typically be recorded as MUA or a LFP. However, despite the presumably synchronous single AP spiking in the neonatal LC no study has recorded an LFP in the LC of rodent slices kept in solution with close-to-physiological ion and glucose content except our preliminary reports using suction electrodes **(Fig. 1-4)** (Kantor, 2012; Kantor et al., 2012; Panaitescu, 2012).

1.5. Ca_i imaging in neural networks

Intracellular Ca^{2+} is a pivotal second-messenger in living cells. In the brain, this divalent cation plays a crucial role in a variety of processes such as neural network communication, neuronal differentiation and synaptogenesis, neurotransmission or cell death (Yuste et al., 2006; Grienberger and Konnerth, 2012). Active neurons and glial cells show Ca_i oscillations and population imaging of these signals can accordingly be used to analyze their interactions and connectivity (Takahashi et al., 1999; Stosiek et al., 2003; Yuste et al., 2006; Yang and Yuste, 2017). As reviewed in the latter articles, activity-related neuronal Ca_i rises are mostly due to opening of Ca^{2+}-permeable neurotransmitter-gated cation channels and/or the resulting depolarization-related activation of voltage-gated Ca^{2+} channels, both causing an influx of Ca^{2+} into the cytosol. In contrast, the primary mode of communication of glial cells is via Ca_i rises mediated by a neurotransmitter-evoked 'metabotropic' Ca^{2+} release from the endoplasmic reticulum (ER) (Perea and Araque, 2005; Halassa and Haydon, 2010). Such release-related Ca_i increases can propagate, sometimes in wave-like fashion, within a network of glial cells that

are coupled via gap junctions forming electrical synapses (Newman, 2001; Scemes and Giaume, 2006). Schwann cells in the peripheral nervous system and oligodendrocytes in the CNS not only enwrap axons for electrical insulation, but also communicate mutually with these neuronal processes. Contrary, astrocytes in the grey matter of the CNS enwrap the area where a presynaptic bouton of one neuron connects to the neurotransmitter-containing postsynaptic area of a target neuron. Astrocytes possess a variety of receptors for neurotransmitters and, consequently, the presynaptic and postsynaptic neurons communicate mutually with these glial cells at the so-called 'tripartite synapse' (Allen and Barres, 2009; Perea et al., 2009; Halassa and Haydon, 2010) **(Fig. 1-5)**. For example, astrocytic Ca_i rises can feedback on neuronal activity via (exocytotic) release of a gliotransmitter, e.g. adenosine triphosphate (ATP), glutamate or D-serine (Innocenti et al., 2000; Wang et al., 2000; Newman, 2001).

Since the milestone studies on developing multicolor fluorescent protein sensors (FPS) (Palmer and Tsien, 2006; Tsien, 2009), these genetically-engineered tools are increasingly used for live-cell imaging of various cellular signaling factors, e.g. Ca_i, membrane potential (V_m) or neurotransmitters such as glutamate. As examples, in collaboration with the Campbell laboratory at the University of Alberta, our group has studied with these FPS neural network properties in cultured (organotypic slices of) neonatal cortex, hippocampus or hypothalamus neurons and astrocytes (Wu et al., 2014; Zhao et al, 2014; Abdelfattah et al, 2016a,b; Shen et al, 2018). As a major advantage of FPS imaging, Ca_i signaling can now be (simultaneously) imaged with specific 'multicolor' sensors in the three major intracellular compartments, i.e. the cytosol, ER and mitochondria (Lin and Schnitzer, 2016; Suzuki et al., 2016) or Ca_i can be imaged simultaneously with glutamate (Wu et al., 2014)

Despite the increasing use of FPS, still a large number of studies uses 'classical' chemical fluorescent indicator molecules for cellular signaling, in the case of Ca_i imaging agents like Fura-2, Oregon green BAPTA or Fluo-4. As examples for such Ca_i imaging in isolated neonatal rodent brain tissues, including work from our laboratory **(Fig. 1-4)**, this approach was instrumental in studying mechanisms of respiration (Ruangkittisakul et al., 2006; 2009; 2012; Ballanyi and Ruangkittisakul, 2009; Bobocea et al., 2010), locomotion (O'Donovan et al., 2008) or CA_3 hippocampal 'early network oscillations' (Ballanyi, 2012; Kantor et al., 2012; Ruangkittisakul et al., 2015). In the (neonatal) LC, it is possible to visualize in individual neurons Ca_i rises associated with single Na^+ spikes at rates of ~1 Hz using a fast 'line-scanning' imaging approach (Sanchez-Padilla et al., 2014). Neuron-glia interactions might be important to study (with Ca_i imaging) in the LC as indicated by the findings that astrocytes are coupled to neighboring neurons via gap junctions (Ishimatsu and Williams, 1996) **(Fig. 1-4)** and that release of lactate from these glial cells excites neighboring neurons via a novel receptor (Tang et al., 2014) **(Fig. 1-5)**.

1.6. Mechanism of spontaneous LC neuron spiking

Intracellular LC neuron activity was recorded firstly in adult rat brain slices using current- and voltage-clamp recording techniques (Andrade and Aghajanian, 1984; Williams et al., 1984). This established that these neurons fire spontaneous APs at a rate of 0.5-3 Hz with a single spike duration of about 1.3-1.9 ms, depending on the age of the animals (Williams et al., 1984; Williams and Marshall, 1987; Alvarez et al., 2002) These APs have a tetrodotoxin (TTX) -sensitive and a TTX-insensitive component, the latter comprising a persistent inward Ca^{2+} current that is inhibited by Co^{2+}. Consequently, combined TTX and Co^{2+} application blocks the spontaneous APs completely (Williams et al., 1984). Each spike is followed by a slow AHP lasting 100-300 ms. Application of

the unselective voltage-gated Ca^{2+} channel blocker Cd^{2+} shortens the AHP and consequently accelerates spontaneous spiking as indication of the presence of Ca^{2+}dependent K^+ channels (Andrade and Aghajanian, 1984). Further slice studies on rats and mice showed that the slow AHP of LC neuron APs is mediated by the apamin-sensitive 'small conductance' Ca^{2+} activated K^+ (SK) channel subtype (Osmanovic et al., 1990; Osmanovic and Shefner, 1993; Matschke et al., 2014, 2015). In summary, the following intrinsic ion channels have been identified in LC neurons: the I_A, I_K, I_{KATP} and I_{Kir} subtypes of K^+ channels (Forsythe et al., 1992; Osmanović and Shefner, 1993; Nieber et al., 1995; Murai and Akaike, 2005; Zhang et al., 2010), voltage-gated Na^+ channels (Chieng and Bekkers, 1999) and L-, T-, N- and P/Q/R-type voltage-gated Ca^{2+} channels (Chieng and Bekkers, 1999; Connor et al., 1999; Sanchez-Padilla et al., 2014; Matschke et al., 2015). The interplay between these intrinsic ion channels is believed to play a pivotal role in spontaneous spiking (Williams et al., 1984, 1985; Osmanovic and Shefner, 1993; Matschke et al., 2015) as outlined in the following.

In vitro brain slices studies showed that LC neurons from neonatal and adult rats exhibit different properties **(Fig. 1-6)** (Williams & Marshall, 1987). Unlike in adult rat slices, Ca^{2+} dependent and TTX resistant subthreshold V_m oscillations are consistently observed in LC neurons of neonatal rat slices (Williams et al., 1984; Williams and Marshall 1987; Christie et al., 1989). The initial component of these subthreshold oscillations is due to progressive inactivation of SK channels whereas the subsequent progressive depolarization involves some of the above mentioned voltage-gated Ca^{2+} channels. Because the transition between both these processes is continuous, LC neurons do not have a 'resting' V_m. Importantly, the subthreshold V_m oscillations and the associated spontaneous spiking at their 'threshold' peak are independent on synaptic or other neurochemical inputs that are present in vivo or in slices because these activities persist in LC neurons isolated by

acute dissociation (Marshall et al., 1979). During postnatal maturation, the amplitude of the subthreshold V_m oscillations progressively diminishes and in adult LC neurons in situ, spontaneous spiking at higher rates is due to different, yet unknown mechanisms (Williams et al., 1985; Williams and Marshall, 1987; Travagli et al., 1995; Alvarez et al., 2002).

In parallel with this postnatal change in the extent of V_m fluctuations, the expression and functional relevance of gap junction-coupling of LC neurons diminishes during the first 24 days after birth (Christie et al., 1989; Christie, 1999; Maubecin and Williams, 1999; Alvarez et al., 2002; Ballantyne et al., 2004). While most of the latter work and other reports (Wang and Aghajanian, 1990; Shen and North, 1992a, b; 1993; Alreja and Aghajanian, 1993, 1994; Alvarez et al., 2000) state that gap junction-coupling synchronizes neuron spiking, one study noted that the subthreshold V_m oscillations are synchronous, but spiking not necessarily (Christie et al., 1989). The anatomical substrate of gap junctions are connexins and two studies on subtypes of these 'hemichannel' proteins in the LC provided different results. According to a report by Alvarez-Maubecin et al. (2002), LC neurons are coupled by connexion-26 and connexin-32 in their dendro-dendritic region whereas another study states that LC neurons are connected exclusively by connexion-36 hemichannels in both neonatal and adult rats (Rash et al., 2007). The importance of gap junction-coupling in (neonatal) LC network activity is indicated by the finding that the gap junction blocker carbenoxolone abolishes synchronous spiking **(Fig. 1-7)** (Travagli et al., 1995; Ishimatsu and Williams, 1996; Oyamada et al., 1998).

1.7. Modulation of LC neuronal activity by iGluR

iGluR activation is pivotal for rhythm generation in various spontaneously active (acutely isolated) neonatal neural circuits like locomotor (Hägglund et al., 2010) or respiratory (Ballanyi and Ruangkittisakul, 2009) networks, entorhinal cortex (Garaschuk et al., 2000) or hippocampus (Sipilä and Kaila, 2008). This might not be the case for LC activity as spontaneous spiking persists in LC neurons after their dissociation and in slices after pharmacological iGluR blockade (Olpe et al., 1989; Alvarez-Maubecin et al., 2000; Alvarez et al., 2002). Nevertheless, iGluR are functional in LC neurons in vitro as focal electrical stimulation of slice areas around the LC causes synaptic potentials that are (partly) blocked by iGluR antagonists (Egan et al., 1983; Cherubini et al, 1988; William et al., 1991). Moreover, extracellular single spike recording from LC neurons in coronal adult rat slices showed that bath-application of glutamate, KA, QUI or NMDA accelerates their spiking (Olpe et al., 1989). This study also revealed that these iGluR agonists have a concentration-dependent potency of action in the following order: KA ~ QUI > NMDA > glutamate, indicating the distinct sensitivity of LC neurons to different agonists. As one further important finding, it was shown in that report that all four agents accelerate the discharge of single APs without inducing spike bursts. This contrasts with in vivo findings showing that LC neurons can transform their activity pattern from single APs to burst discharge (Aston-Jones and Bloom 1981). As explanation for this discrepancy, the authors of the in vitro study argued that in vivo bursting may involve firing of afferent fibers that are silent in slices (Olpe et al., 1989). However, NMDA is capable to induce AP bursts of several seconds duration in slices of various brain circuits (Neuman et al., 1989; Zhu et al., 2004; Sharifullina et al., 2008; Mrejeru et al., 2011). This shows that mechanisms that cause discharge pattern transformation in neural networks can be preserved in slices.

Activation of iGluR also seems to be necessary to transform opioid-evoked LC spiking. This is indicated by the in vivo finding in adult rats that single AP discharge in LC neurons transforms into AP bursts during systemic application of the μ-opioid receptor agonist morphine and this effect is blocked by injection of the the unselective iGluR antagonist kynurenic acid into the LC (Zhu and Zhou, 2005) **(Fig. 1-8A)**. Preliminary findings from our group indicate that such activity pattern transformation also occurs in the LC of neonatal rat slices in response to low nanomolar doses of the synthetic μ-opioid receptor agonist [D-Ala$_2$,N-Me-Phe$_4$,Gly$_5$-ol]-Enkephalin (DAMGO) **(Fig. 1-8B)** (Panaitesu, 2012). While the latter finding indicates that the mechanism of the opioid-evoked LC discharge pattern change in the LC network is preserved in slices, it would be important to investigate which iGluR subtype is involved.

Another striking feature of iGluR agonist LC effects in vivo is 'post-agonist inhibition' or 'post-agonist depression' (PAD), the term that will be used here from hereon. In rat slices, extracellular single-unit recording revealed that bath-application of 1 mM glutamate for 30 s caused a 10-15-fold increase in LC neuron firing rate followed by a 30-45 s period of spike silencing in the early washout phase (Zamalloa et al., 2009) **(Fig. 1-9)**. In that study, these glutamate-induced responses were blocked by CNQX, but remained unaltered upon preincubation with the NMDAR antagonist 2-APV indicating the involvement of an AMPAR receptor-mediated mechanism. Also AMPA and QUI, but not NMDA and KA, acted like glutamate and AMPA was 30-100-fold more potent than glutamate in inducing the PAD (Zamalloa et al., 2009). Correspondingly, in vivo PAD occurred after sensory stimulation-evoked AP bursts (Cedarbaum and Aghajanian, 1976; Foote et al., 1980). As one possible mechanism of PAD, SK channels might be activated during the ongoing neuronal depolarization that likely causes a mainly voltage-activated Ca^{2+} channel-mediated Ca_i rise (Metzger et al., 2000; Kulik et al., 2002). In line with this view, in adult rats in vivo (Aghajanian

et al., 1983) and slices (Andrade and Aghajanian, 1984), the number of current-evoked spikes correlates with the duration of a pronounced hyperpolarization that is attenuated by increased cellular Ca^{2+} buffering. However, in a study on LC neurons in adult rat slices rather an AMPAR-triggered Na^{+}-dependent K^{+} current was proposed to cause the PAD as the SK channel blocker apamin did not counter its occurrence during glutamate washout (Zamalloa et al., 2009).

1.7.1. Transmembrane AMPAR regulatory proteins

AMPAR-mediated ion currents are blocked in most neurons by the competitive quinoxalinedione-type antagonists 6-cyano-7-nitroquinoxaline-2,3-dione (CNQX) or 6,7-dinitroquinoxaline-2,3(1H,4H)-dione (DNQX) (Traynelis et al., 2010). However, CNQX and DNQX can act as partial agonists at the AMPAR and consequently depolarize and enhance the firing rate, e.g. in principal neurons and (inhibitory) interneurons in the hippocampus (McBain et al., 1992; Maccaferri and Dingledine, 2002; Hashimoto, et al., 2004), thalamus (Lee et al., 2010), cerebellum (Brickley et al., 2001; Menuz et al., 2007) or spinal cord (Sullivan et al., 2017). In these and various other neurons, the AMPAR is coupled to a member of the family of auxiliary 'transmembrane AMPAR regulatory proteins' (TARP) and the quinoxalinediones bind to that TARP-AMPAR complex (Jackson and Nicoll, 2011; Greger et al., 2017; Maher et al., 2017). As exemplified in **Fig. 1-10**, the γ-2 subunit of TARP co-expressed with the iGluR channel isoform 'GluR1' in 'HEK' cells reduces glutamate-evoked desensitization and induces an inward current in response to CNQX (Turestky et al., 2005; Menuz et al., 2007). Structural analysis of CNQX and DNQX binding to the TARP-AMPAR complex was instrumental in understanding the possible mechanism of their partial agonistic effect. For example, several studies showed that CNQX induces a partial cleft

closure in the AMPAR ligand-binding domain in presence of TARP and that process may cause channel opening (Menuz et al., 2007; Milstein and Nicoll, 2008; Jackson and Nicoll, 2011; McLean and Bowie, 2011) **(Fig. 1-10)**. In addition to using expression systems like HEK cells, TARP-AMPAR complex-related ion currents can be analyzed in slices from control mice compared to animals with a 'knock-out' of TARP-coding genes like in a report pointing out the requirement of 'Type-I TARP γ-2' for inflammation-associated spinal AMPAR plasticity (Sullivan et al., 2017). Moreover, 'stargazer' mice that lack γ-2, and were therefore instrumental in TARP discovery, show neurological deficits like ataxia, dyskinesia and seizures (Jackson and Nicoll, 2011; Maher et al., 2017).

While TARP effects at the cellular level are established, their role in active neural networks is currently unknown. This is due to the fact that most rhythmically active brain circuits operate via iGluR and quinoxalinediones thus block their activity, like in locomotor (Hägglund et al., 2010) or respiratory (Ballanyi and Ruangkittisakul, 2009) networks, entorhinal cortex (Garaschuk et al., 2000) or hippocampus (Sipilä and Kaila, 2008). The LC might be an important new model for studying TARP-AMPAR complex roles as it innervates most brain structures and thus modulates many behaviors as outlined above **(1.2.1.)**. Moreover, presumably synchronous spiking in the gap junction-coupled (neonatal) rat LC neurons does not depend on iGluR activity as it is not blocked by quinoxalinediones (Oyamada et al., 1998; Alvarez-Maubecin et al., 2000) similar to persistence of tonic spiking in adult rat slices (Alvarez et al., 2002). Nevertheless, at both developmental stages LC neurons have functional AMPAR as specific agonists accelerate their spontaneous spiking (Kogan and Aghajanian, 1995; Olpe et al., 1989; Zamalloa et al., 2009).

1.8. Aims and Hypotheses

Preliminary studies from our group showed with suction electrode recording in the LC of newborn rat slices that the LC neural network generates at ~1 Hz a rhythmic LFP with ~0.2 s-lasting individual bursts (Kantor, 2012; Kantor et al., 2012; Panaitescu, 2012). The first major aim of this thesis was to investigate whether this rhythmic LFP bursting represents summated, not fully synchronized, neuronal spiking and if increasing the excitability of this network with raised superfusate K^+ or decreasing it with μ-opiod receptor activation causes a change in its pattern. If this was the case, involvement of different iGluR subtypes in such LFP pattern transformation and possible involvement of TARP was intended to be studied in further aims using LFP recording in combination with either whole-cell V_m recording from single LC neurons or Ca_i imaging from populations of LC neurons and astrocytes.

1.8.1. Project 1: Suction electrode recording in LC of newborn rat brain slices reveals network bursting comprising summated non-synchronous spiking

The LC is an established model to study mechanisms of synchronized neural network spiking. In newborn rat slices, gap junction-coupled LC neurons show synchronous Ca^{2+}-dependent V_m oscillations with a single spike at their peak (Williams and Marshall, 1987; Christie et al. 1989; Ishimatsu and Williams, 1996; Alvarez et al., 2002). If all LC neurons discharge in synchrony, this should result in a LFP. In fact, single-unit and MUA/LFP activities have been monitored in vivo under resting conditions or in response to sensory or electrical stimuli in both perinatal (Kimura and Nakamura, 1985; Sakaguchi and Nakamura, 1987; Nakamura et al., 1987) and adult rats (Cedarbaum and Aghajanian, 1976; Aston-Jones and Bloom, 1981; Aghajanian and VanderMaelen, 1982). This contrasts with the lack of evidence for a microelectrode-recorded LFP

in the LC of brain slices studied in superfusate with an ion content similar to that of the interstitial brain fluid. Several reports have revealed a modular organization of neurons in different LC areas regarding their neurotransmitter receptors, innervation and electrophysiological properties (Schwarz and Luo, 2015; Jin et al., 2016; Li et al., 2016). Based on these findings, spiking in these LC neuron subclasses may not be completely synchronized to cause the 0.2 s-lasting LFP. It was the first aim of this project to unravel with simultaneous single unit and LFP recording the organization of neonatal LC population spiking and detect novel network features.

Hypothesis for project 1: Population bursting in the neonatal LC comprises phase-locked and jittered spike discharge that can transform its pattern during changes in network excitability.

1.8.2. Project 2: TARP mediation of accelerated and more regular LC network bursting in neonatal rat brain slices

In neurons of various brain areas including the hippocampus, thalamus or cerebellum, the 'classical' AMPAR antagonists CNQX and DNQX have a partially agonistic, thus excitatory effect (McBain et al., 1992; Brickley et al., 2001; Maccaferri, 2002; Hashimoto, 2004; Menus et al., 2007; Lee et al., 2010). In these and related studies, it was either hypothesized or proven that the excitatory effect of these quinoxalinedione inhibitors is mediated by their action on a TARP-AMPAR complex leading to the hypothesis TARP play an important modulatory role in glutamate-mediated synaptic neurotransmission (Greger et al., 2017; Jackson and Nicoll, 2011; Maher et al., 2017). This and related work has provided important information about the molecular organization of the TARP-AMPAR complex and its action on single neurons.

However, how TARP affects spontaneous neural network activity is yet unknown because most of these circuits function via ongoing AMPAR activity and the quinoxalinediones block their rhythmic bursting (Garaschuk et al., 2000; Sipilä and Kaila, 2008; Ballanyi and Ruangkittisakul, 2009; Hägglund et al., 2010). Because rhythmic, presumably synchronized LC neuron spiking persists during CNQX application (Oyamada et al., 1998; Alvarez-Maubecin et al., 2000), the next aim of this thesis was to investigate whether CNQX has a stimulatory action on spiking in the LC network of newborn rat slices as indication of a functional TARP-AMPAR complex. If this was the case based on LFP recording, it was planned to study by combining such extracellular population recording with either V_m recording from single LC neurons or Ca_i imaging from populations of LC neurons and astrocytes to find out whether the entire neural network expresses the TARP-AMPAR complex or rather only some local modules and how astrocytes are affected. The eventual effect on LC network connectivity and thus synchronicity was assessed by analyzing with a 'cross-correlation' approach the timing between neuronal spiking and the LFP whose discharge regularity was also calculated.

Hypothesis for project 2: CNQX stimulates neonatal rat LC network bursting via an action on a functional TARP-AMPAR complex.

1.8.3. Project 3: LC network bursting in newborn rat brain slices is accelerated at increased regularity by AMPA and KA whereas QUI makes rhythm irregular

LC network activity is controlled by afferent glutamatergic inputs and the resulting output activity patterns have a plethora of behavioral effects that are influenced by iGluR modulators (Chandley and Ordway, 2012; Chandley et al., 2014). Electrophysiological studies on brain slices have

established by studying effects of the specific agonists AMPA, KA and QUI that the AMPAR is functional in neonatal and adult rat LC neurons (Olpe et al., 1989; Kogan and Aghajanian, 1995; Zamalloa et al., 2009). The latter studies only revealed an increase in the rate of spontaneous spiking in LC neurons during the action of the AMPAR agonists. However, LFP recording might be needed to find out whether the agents affect the connectivity of LC neurons to eventually reveal a transformation of the population activity pattern as shown for other neural networks (Ballanyi and Ruangkittisakul, 2009; Buzsáki et al., 2012; Einevoll et al., 2013). Such pattern transformation might be pivotal for modulating the behavior in brain structures innervated by the LC. Firstly, dose-response relationships were determined for AMPA, KA and QUI. Then, their effect on LC network connectivity and thus synchronicity was assessed by analyzing with a cross-correlation approach the timing between neuronal spiking and LFP rhythm whose regularity was also calculated.

Hypothesis for project 3: AMPAR activation transforms the LFP population discharge pattern in the neonatal rat LC by affecting network synchronicity and regularity.

1.8.4. Project 4: NMDA enhances and glutamate attenuates synchronization of spontaneous phase-locked LC network bursting in newborn rat brain slices

Project 3 deals with studying effects of AMPAR agonists on neonatal rat LC network bursting. But, also the NMDR comprising the remaining type of iGluR has substantial behavioral effects (Chandley and Ordway, 2012; Chandley et al., 2014). For example, disruption of NMDAR dependent glutamatergic input to the LC caused attenuation of morphine-induced sensitization and withdrawal (Rodriguez Parkitna et al., 2012). As another example, clinical studies have demonstrated that the NMDAR antagonist ketamine exerts antidepressant actions (Price et al.,

2009; DiazGranados et al., 2010). Moreover, research on neurons of various brain circuits in rodent slices has established that NMDA evokes several seconds-lasting rhythmic bursts (Neuman et al., 1989; Zhu et al., 2004; Sharifullina et al., 2008; Mrejeru et al., 2011). In contrast, NMDA application to LC neurons in slices only increased the rate of spontaneous spiking (Zamalloa et al., 2009). However, as outlined in the rationale for projects 1-3, only subclasses of LC neurons might show this activity pattern transformation, and this might be detected with LFP recording during a dose response determination. If the LFP pattern transforms under the influence of a particular NMDA dose, the eventual effect on LC network connectivity, and thus synchronicity, will be assessed with cross-correlation analysis. The effects of NMDA will then be compared with those of glutamate to investigate if activation of AMPAR and NMDAR plus diverse types of metabotropic glutamate receptors transforms the pattern of neonatal rat LC population bursting in different fashion.

Hypothesis for project 4: NMDAR (and AMPAR) activation as well as glutamate induce different types of population burst pattern transformation in the neonatal rat LC as indication that behaviors generated by target brain circuits can be fine-tuned by distinct types of rhythmic LC output.

1.9. Figures and Legends

Fig. 1-1

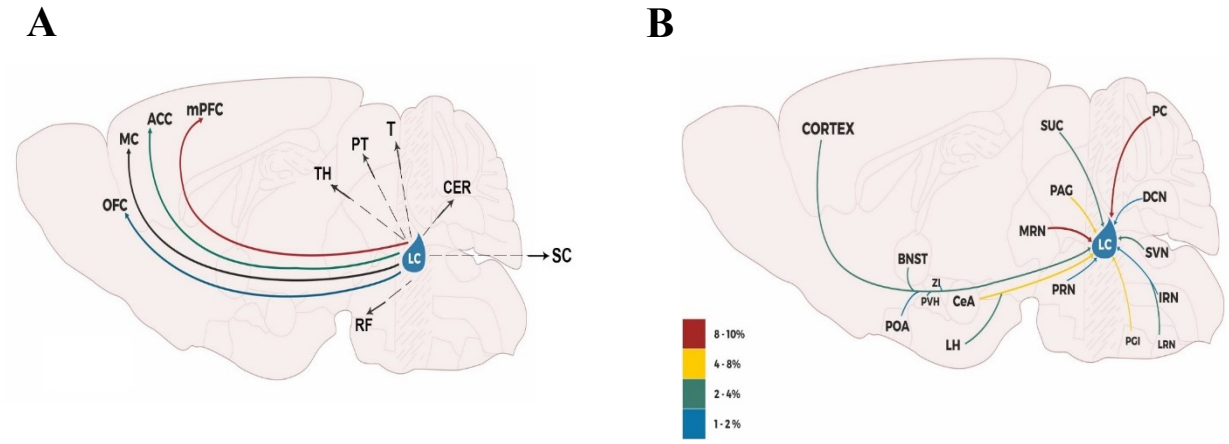

Fig. 1-1: Efferent and afferent LC projections. A, schema of the adult rat brain showing projection-specificity of LC neurons releasing noradrenaline (NA) in diverse target areas of the brain. Colored arrowed lines represent axon efferents originating from heterogenous LC neuron subpopulations. Dashed arrowed lines represent LC projections to other target areas whose projection-specific LC neuron subpopulations are not identified yet. (Abbreviations: ACC, anterior cingulate cortex; MC, motor cortex; mPFC, medial prefrontal cortex; OFC; orbitofrontal cortex; PT, pretectal area; RF, reticular formation; SC, spinal cord; T, tectum; TH, thalamus). **B**, schema of adult rat brain fferent input to the LC. Colored traces correspond to the scale shown in the bottom left representing the fraction of neurons sending input to LC. Neurons from PC and MRN send the largest fractions of afferents to LC. (BNST, bed nucleus of the stria terminalis; CeA, central amygdala; DCN, deep cerebellar nuclei; IRN, intermediate reticular nucleus; LH, lateral hypothalamus; LRN, lateral reticular nucleus; MRN, midbrain reticular nucleus; PVH, paraventricular hypothalamic nucleus; PGRN/GRN, paragiganto-cellular/gigantocelluar nucleus; PAG, periaqueductal gray; PRN, pontine reticular nucleus; POA, preoptic area; PC, Purkinje cells; SVN, spinal vestibular nucleus; SuC, superior colliculus; ZI, zona incerta). Modified with permission from Uematsu et al. (2015) **(A)** plus Sara (2009) and Schwarz et al. (2015) **(B)**.

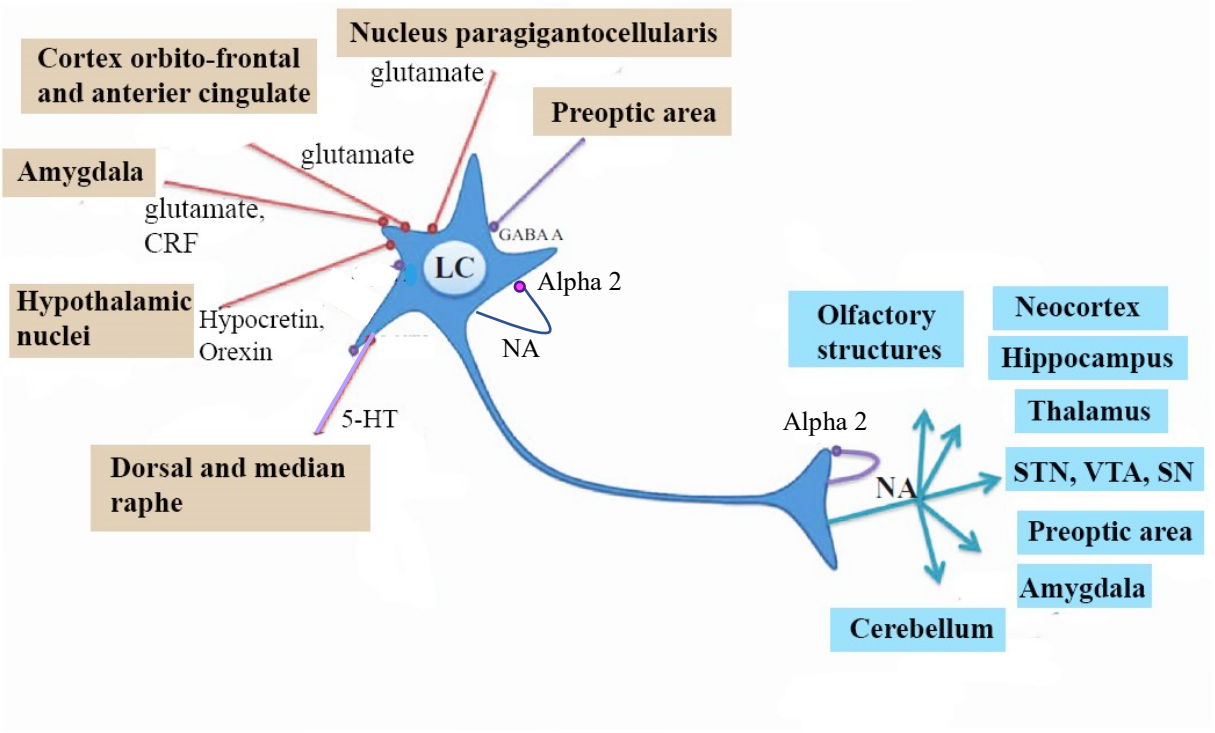

Fig. 1-2. Neurotransmitter-specific afferent projection to LC and release of NA to distinct target brain regions. Schema shows major afferents to (in brown) and efferents from (in blue) the LC. LC neuronal firing and NA release is under continuous control predominantly by excitatory neurotransmitters such as glutamate, corticotrophin releasing factor (CRF), Orexin, Hypocretin, serotonin and γ-aminobutyric acid (GABA) acting on A-type ($GABA_A$) receptors. LC neurons also express α_2 adrenoceptors on their soma and axon terminals and in turn inhibit the release of NA by negative feed-back regulation. (STN, subthalamic nucleus, VTA, ventral tagmental area, SN, substantia nigra). Modified with permission from Delaville et al. (2011).

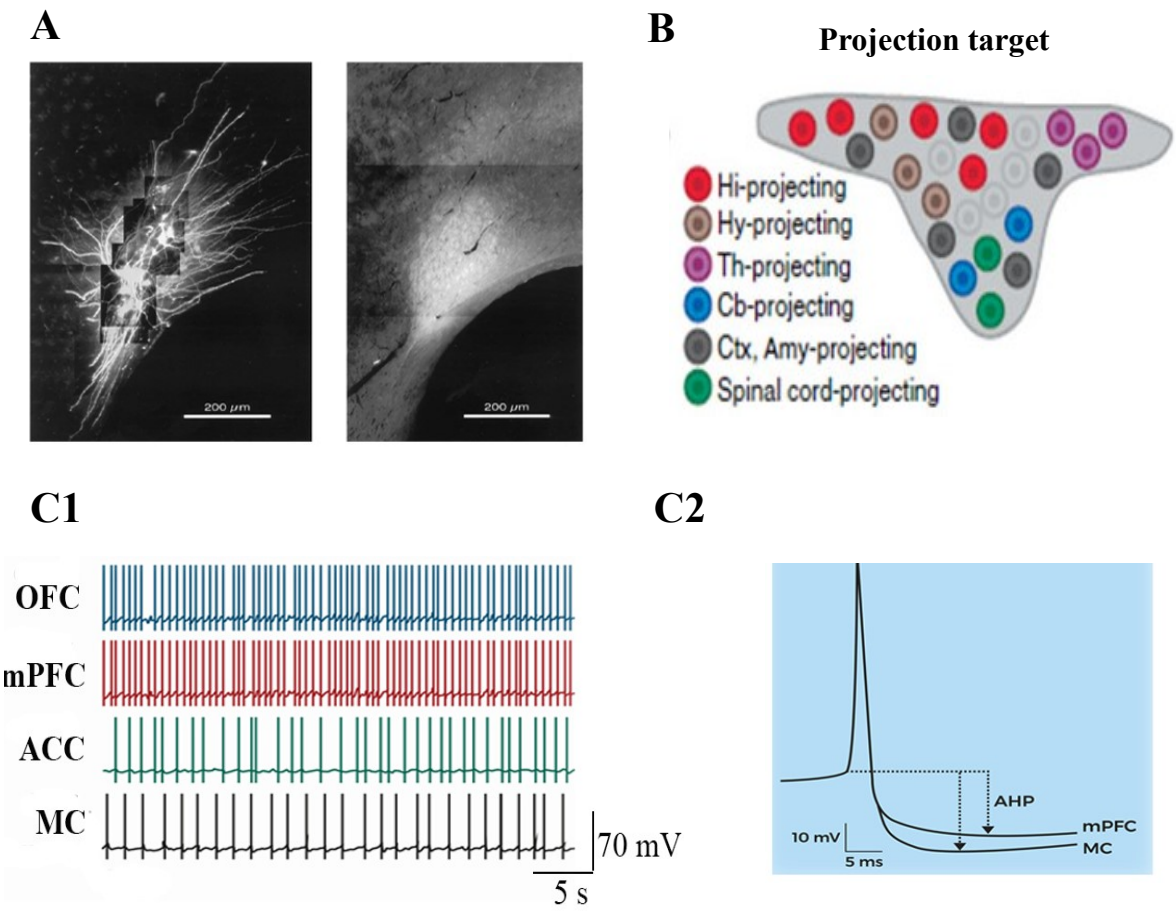

Fig. 1-3: Modular LC organization and differential firing properties. A, left photo shows dendritic projections in Cy5-filled LC neurons of horizontal adult rat brain slice. Right photo shows catecholamine fluorescence image of LC in the same slice. The 4th ventricle is visible on the lower right. **B**, schema showing distinct organization of LC neuron subpopulations based on projection target specificity. **C1**, spontaneous action potential (AP) recording reveals that OFC and mPFC-projecting LC neurons fire at higher frequency (>1 Hz) than those projecting to the ACC and MC regions of the brain (<1 Hz). **C2**, APs recorded from LC neurons projecting to mPFC and MC revealed shorter after hyperpolarization amplitude in mPFC-projecting cells than in MC projecting ones. Modified with permission from Ishimatsu and Williams (1996) **(A)**, Schwarz and Luo (2015) **(B)** and Chandler et al. (2014) **(C)**.

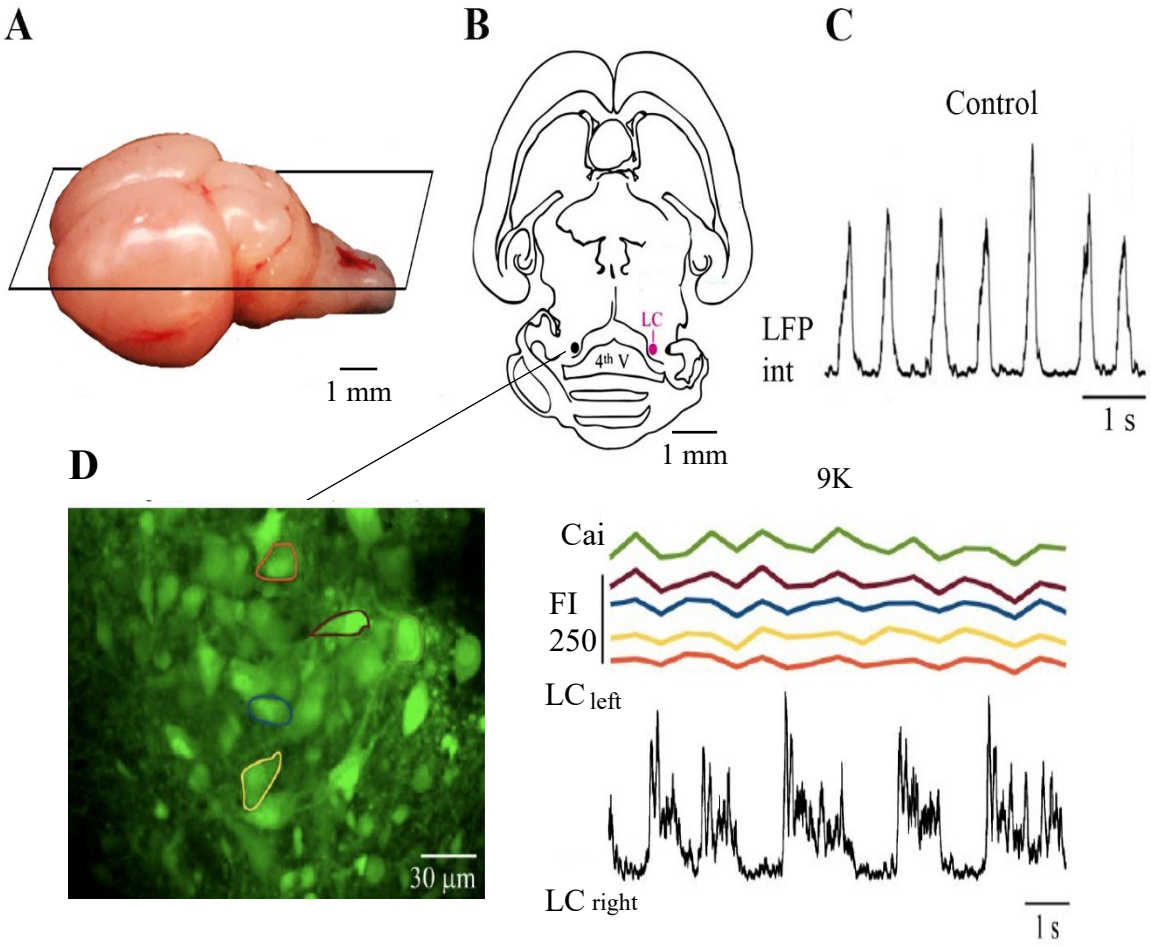

Fig. 1-4: Simultaneous extracellular local field potential (LFP) recording and imaging of the free cytosolic Ca^{2+} concentration (Ca_i) in the LC of newborn rat brain slices. A, photo of a postnatal day (P) 1 rat brain. Black frame indicates the horizontal brain sectioning plane. **B**, schema of a horizontal brain slice showing the bilaterally-organized LC at the base of the 4th ventricle (V) in the brainstem. **C**, LFP recording from 400 µm thick horizontal brain slice from P2 rat in a control superfusate with 3 mM K^+. **D**, imaging from cells in the Fluo-4-AM-stained LC shows burst-related Ca_i rises at increased K^+ (9 mM). LC bursting in 3 mM K^+ occurs at rates of >1 Hz, which is beyond the binding/unbinding kinetics of this commonly used Ca^{2+}-sensitive dye. **B-D** reproduced with permission from Kantor et al. (2012).

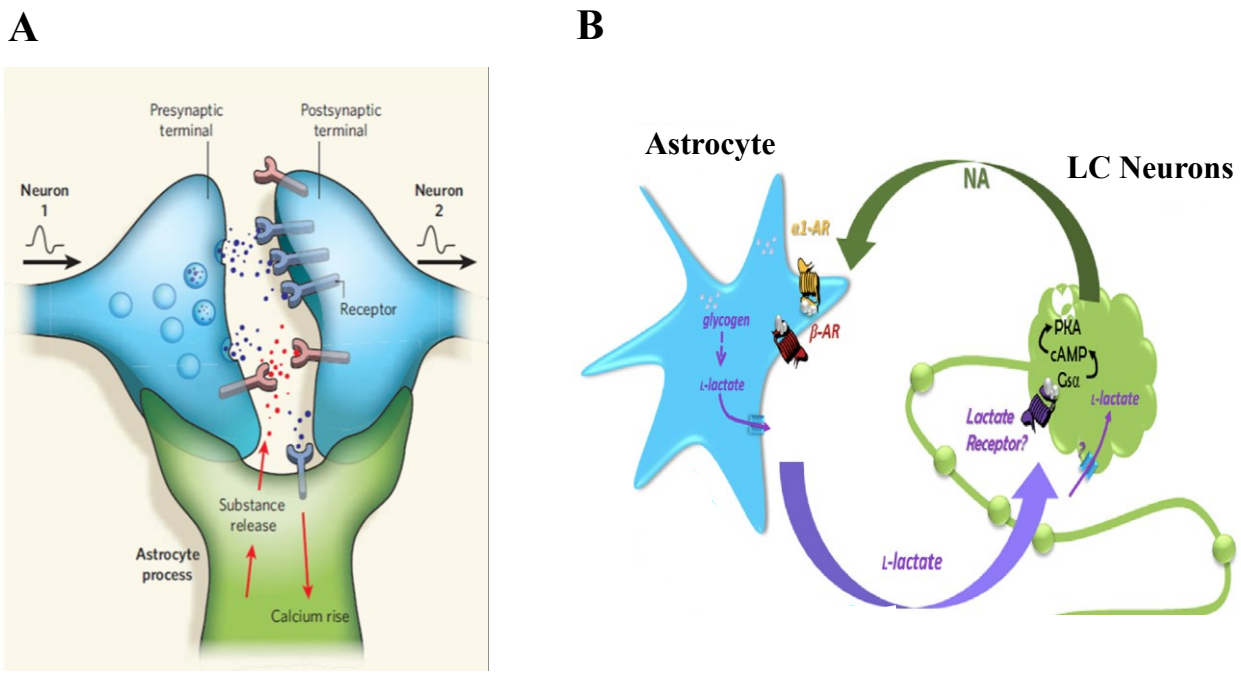

Fig. 1-5: Neuron-glia interactions. A, astrocytes modulate the electrical discharges of neighboring neurons. The array of a pre- and post-synaptic neuron with an astrocyte is called 'tripartite synapse'. In such 'neural networks' astrocytes integrate synaptic information and in turn modulate neurotransmission. **B**, schema exemplifying LC neuron-glia communication. Presumably, astrocytes in the vicinity to LC neurons release L-lactate as a gliotransmitter upon activation by NA via α_1 or β adrenoceptors. L-lactate has subsequently an excitatory effect on LC neurons mediated via yet unidentified L-lactate receptor. NA and L-lactate stimulate release of each other through positive feedback regulation. Reproduced with permission from Allen and Barres (2009) **(A)** and Teschemacher and Kasparov (2017) **(B)**.

Fig. 1-6

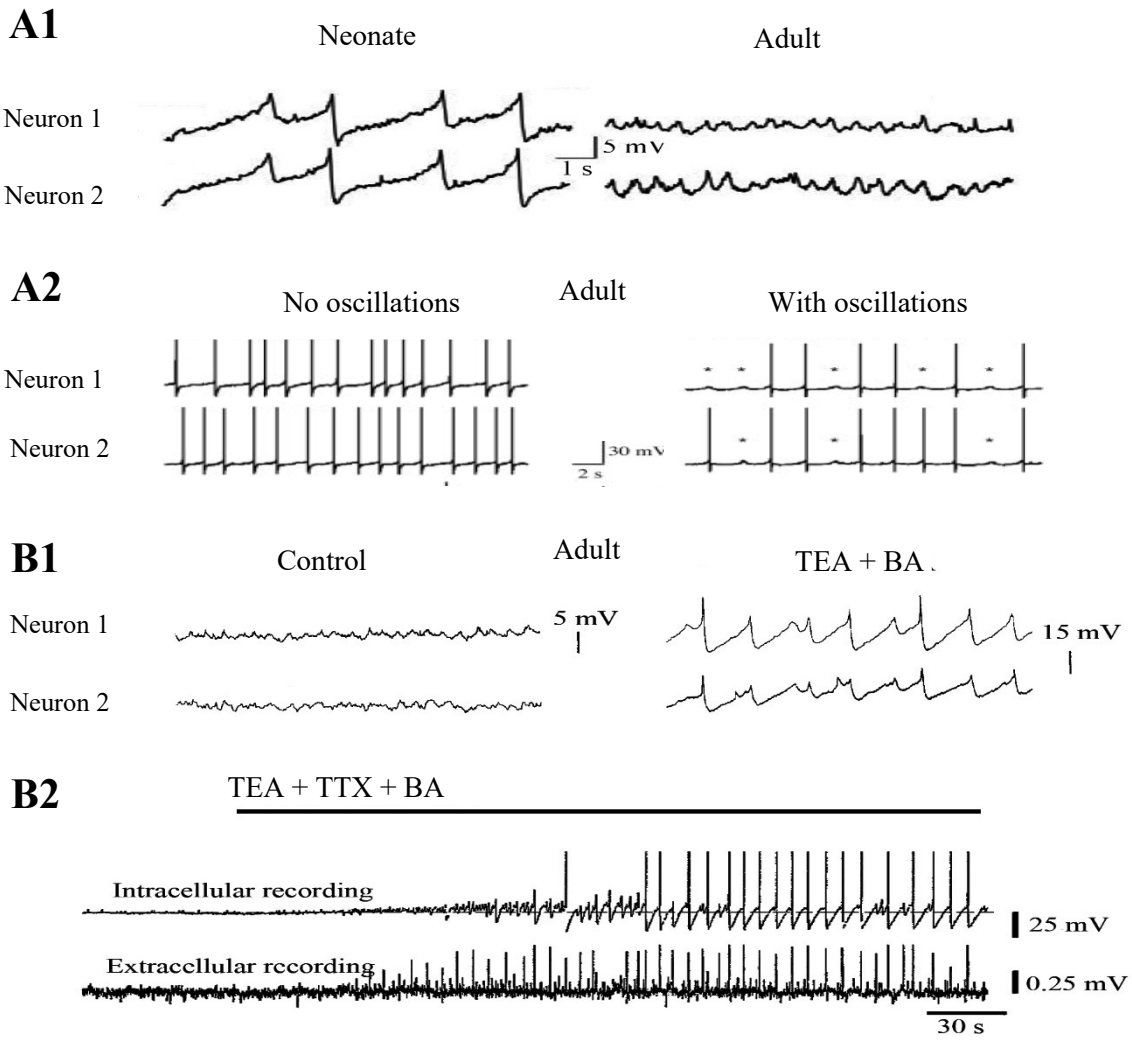

Fig. 1-6: Electrophysiological recording in neonatal vs. adult LC neurons. A1, simultaneous dual recording shows spontaneous synchronized 'subthreshold' membrane potential (V_m) oscillations in LC neurons from neonatal rat brain slice and these events are greatly diminished in adult rat LC neurons. **A2**, paired recording from neurons from adult slices without (left panel) and with (right panel) subthreshold V_m oscillations - marked by *. Action potentials were synchronized in neurons having subthreshold oscillations (right panel). **B1**, simultaneous recording from two adult LC neurons shows that partially synchronized V_m oscillations develop in the presence of tetraethylammonium (TEA) and $BaCl_2$. **B2**, intracellular and extracellular recordings from LC neurons in adult rat brain slice show rhythmic APs and an LFP bursts evoked by TEA, tetrodotoxin (TTX) and $BaCl_2$. Modified with permission from Alvarez et al. (2002) **(A1**, **A2)**, Christie et al. (1989) **(B1)** and Ishimatsu and Williams (1996) **(B2)**.

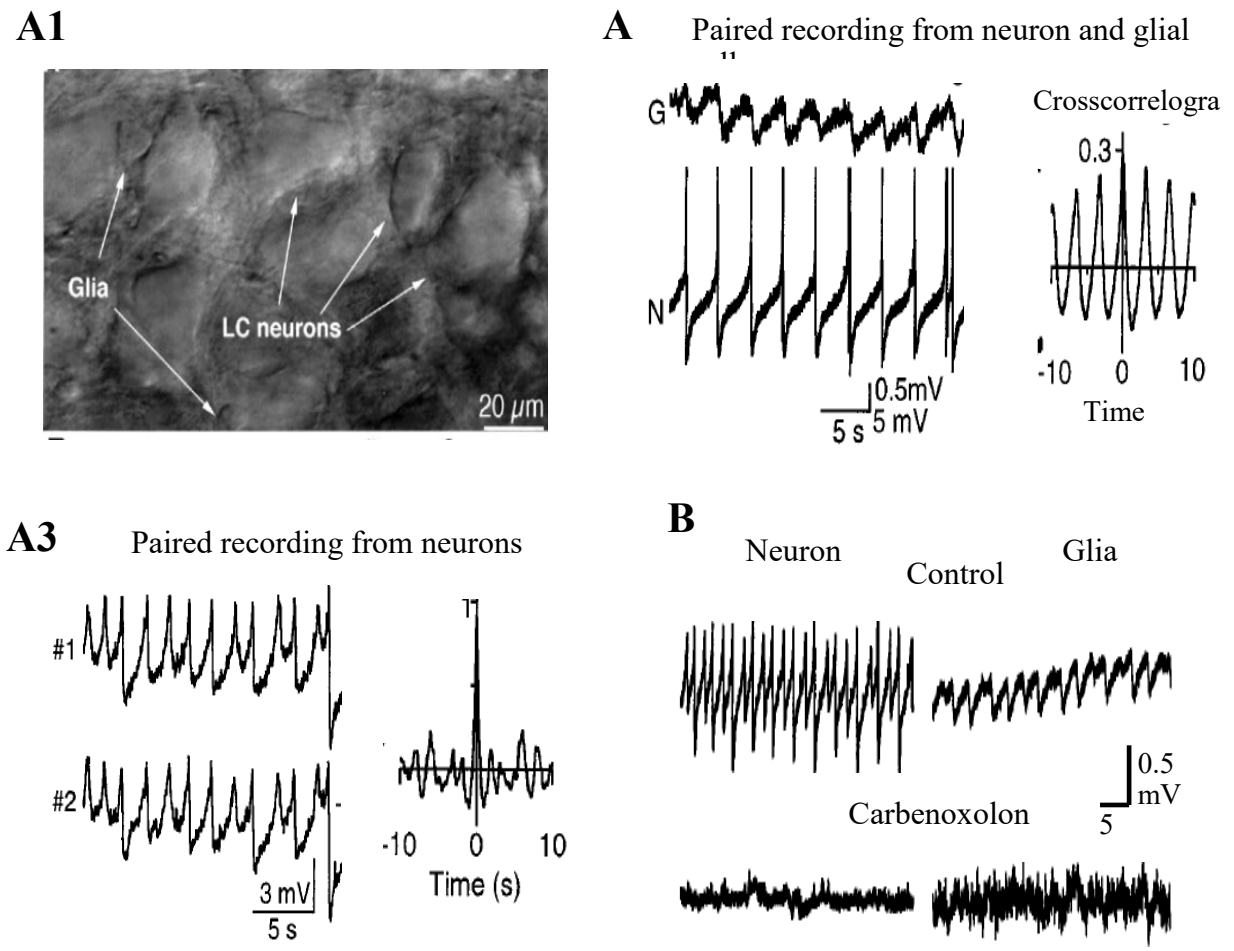

Fig. 1-7. SynchronousV_m oscillations in neonatal LC neurons and glia as indication of connectivity. A1, image under infrared illumination of the LC in a brain slice from 1-week-old rat. Neurons and glial cells are identified based on differences in size and morphology. **A2**, paired 'whole-cell' patch-clamp recording from a neuron and an astrocyte reveals synchronous V_m oscillations with a peak of 0.20 and a phase shift of 10 ms in the cross-correlogram **A3**, paired whole-cell recording from two LC neurons showing synchronized activity with a peak of 0.94, a phase shift of 10 ms in cross-correlogram. **B**, whole cell recording showing blockade of neuronal and glial V_m oscillations in presence of carbenoxolone (100 μM) indicating gap junction-coupling in the neonatal LC network. Modified with permission from Alvarez-Maubecin et al. (2000).

Fig. 1-8

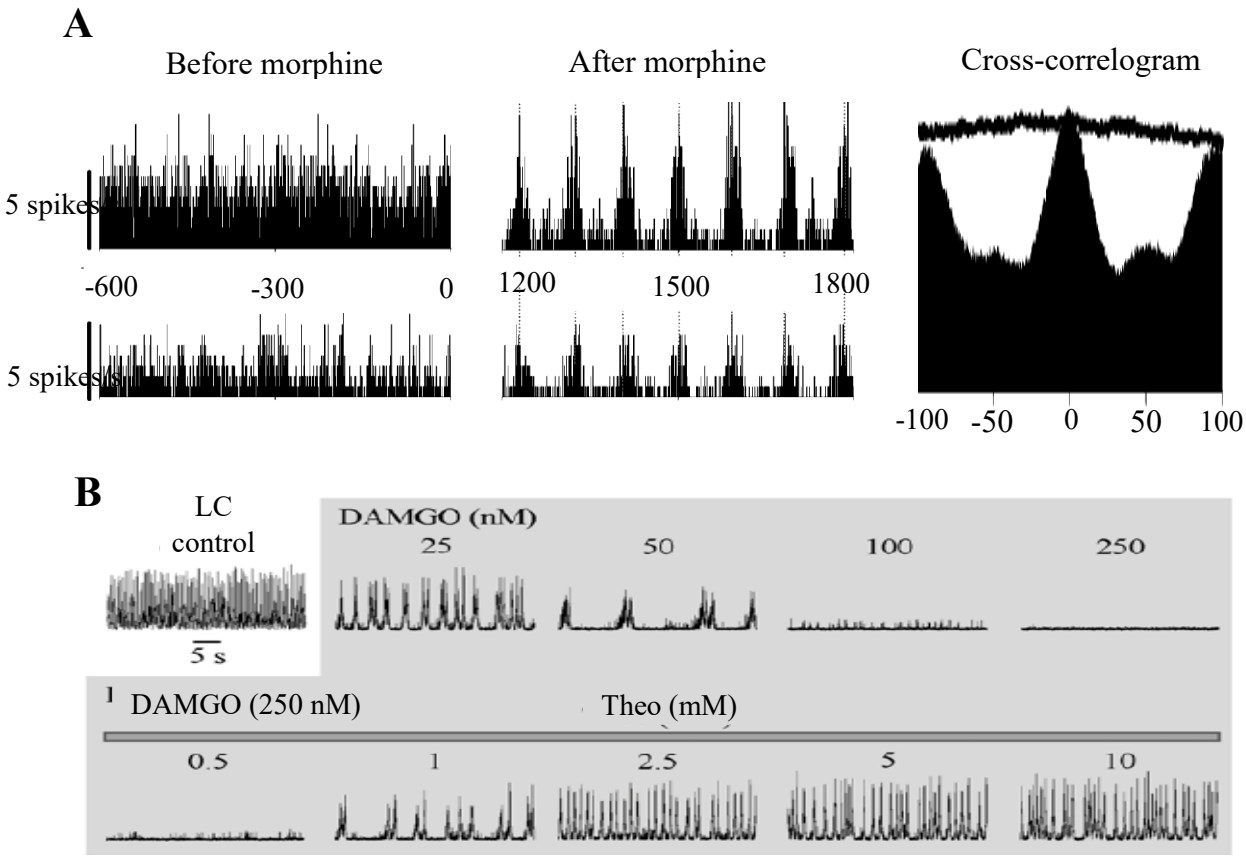

Fig. 1-8: Opioid-induced pattern transformation of LC activity. A, simultaneous single-unit recording of spiking in two LC neurons before and after systemic administration of the μ-opioid receptor agonist morphine to an adult rat shows a pattern transformation from fast tonic spiking to slower bursting. Cross-correlation analysis indicates the synchronicity of both neuronal activities. **B**, LFP recording from the LC in a neonatal rat brain slice shows transformation of regular rhythm to multipeak bursts evoked by 25 and 50 nM the synthetic μ-opioid receptor agonist [D-Ala$_2$,N-Me-Phe$_4$,Gly$_5$-ol]-Enkephalin (DAMGO) whereas rhythm was abolished at 250 nM. Theophylline (Theo) reactivated periodic bursts at 1 mM while 2.5-10 mM Theo restored normal bursting. Modified with permission from Zhu and Zhou (2001) **(A)** and Panaitescu (2012) **(B)**.

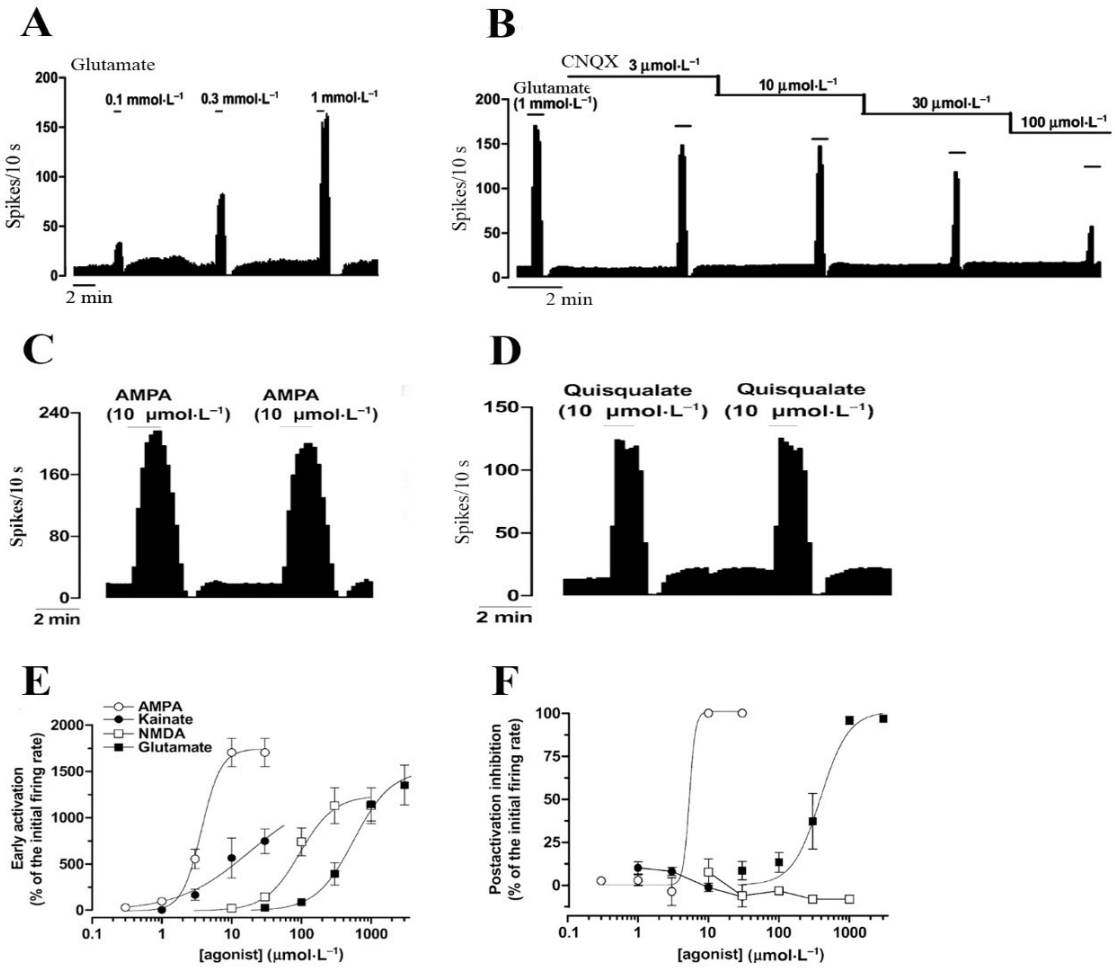

Fig. 1-9: Effects of ionotropic glutamate receptor (iGluR) activation on spontaneous spiking in LC neurons of adult rat brain slices. A, extracellular spiking due to bath-applied glutamate is initially accelerated and then blocked due to post-agonist depression (PAD) early during washout. Note that PAD duration increased with increasing glutamate dose. **B**, PAD induced by glutamate was blocked by the competitive α-amino-3-hydroxy-5-methyl-4-isoxazolepropionic acid (AMPA) receptor (AMPAR) antagonist 6-cyano-7-nitroquinoxaline-2,3-dione (CNQX) indicating a non-N-methyl-D-aspartate receptor (NMDAR) -mediated mechanism. **C**, **D**, recording of LC neurons showing bi-phasic response similar to glutamate mediated by the iGluR agonists AMPA and quisqualate, respectively. **E**, **F**, dose-dependent effect of glutamate agonists on early excitation and PAD. As indicated in **F**, NMDA and kainate failed to induce PAD at any concentrations tested. Modified with permission from Zamalloa et al. (2009).

Fig. 1-10

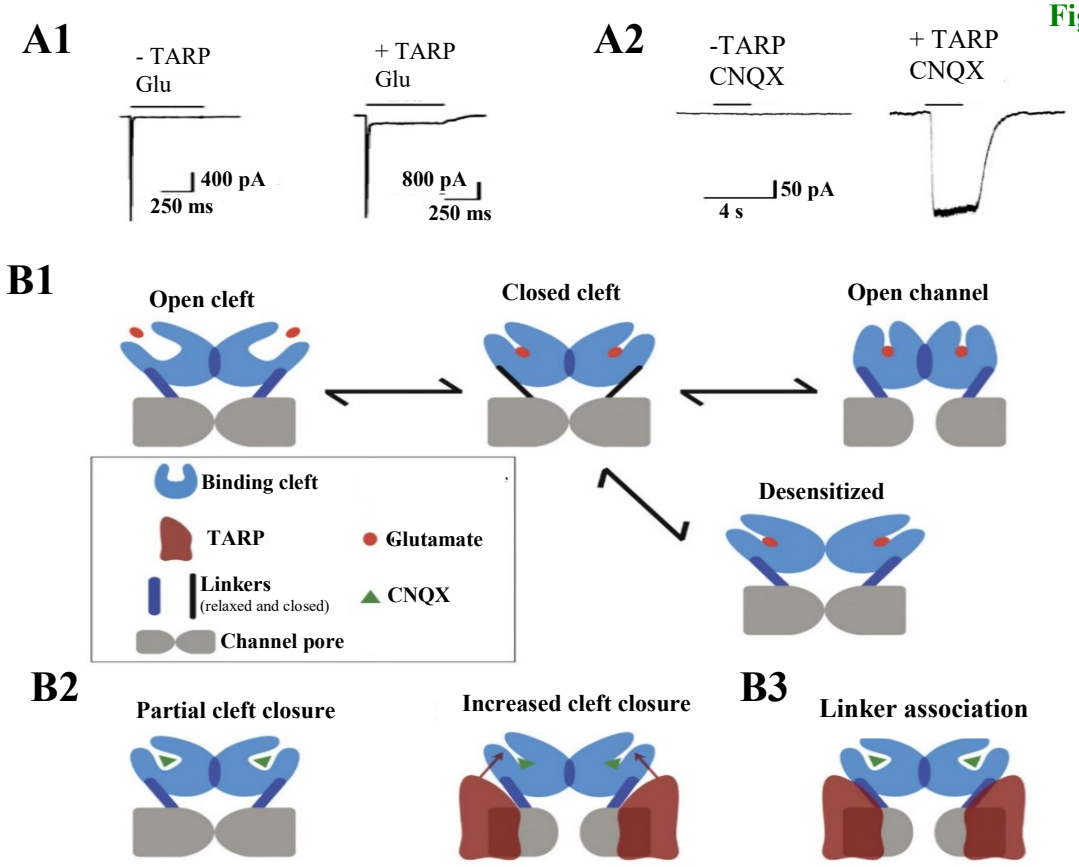

Fig. 1-10: TARP regulation of AMPAR activity. A1, whole-cell recording from HEK cells expressing AMPAR shows reduced desensitization of glutamate-induced inward current in presence of TARP. Reduction of glutamate-evoked desensitization results from an allosteric interaction between TARP and ligand-binding domain which destabilizes the desensitized state of the AMPA as shown in **B1** and **B2. A2**, whole-cell recording showing a CNQX-induced inward current in HEK cells expressing the TARP-AMPAR complex indicating CNQX acts as a partial AMPAR agonist. **B1**, schema of TARP regulation of AMPAR gating. Glutamate binding to two ligand binding domains in AMPAR induces closer of the binding cleft, converting linker domains from a relaxed to a tensed state. The linker domain reverses back to relaxed state either by receptor desensitization or open channel confirmation. **B2**, according to the 'increased cleft closer' model, TARP changes the binding domain in CNQX bound state explaining the partial agonist effect of CNQX. **B3**, the 'linker association' model proposes a direct interaction between TARP and linker domain resulting in channel opening in the CNQX-bound state. Modified with permission from Turetsky et al. (2005) **(A1)**, Menuz et al. (2007) **(A2)** and Milstein and Nicoll (2008) **(B)**.

CHAPTER 2

General Methods

2.1. Preparation and solutions

The experiments were performed on horizontal brain slices from 0-5 days-old CD-001 (SD) rats of unknown sex (Charles River Laboratory Inc., Wilmington, MA, USA). All procedures were approved by the University of Alberta Animal Care and Use Committee and in compliance with the guidelines of the Canadian Council for Animal Care and in accordance with the Society for Neuroscience's 'Policies on the Use of Animals and Humans in Neuroscience Research'.

Procedures for generating LC-containing brain slices are described elsewhere in detail (Kantor et al., 2012). In brief, rats were anesthetized with 2-3 % isoflurane to a level that caused disappearance of the paw withdrawal reflex. They were then decerebrated and the neuraxis was isolated at 18-20 °C in superfusate containing (in mM): 120 NaCl, 3 KCl, 1.2 $CaCl_2$, 2 $MgSO_4$, 26 $NaHCO_3$, 1.25 NaH_2PO_4, and 10 D-glucose (pH adjusted to 7.4 by gassing with carbogen, i.e. a mixture of 95 % O_2 plus 5 % CO_2). The brain was glued on its ventral surface to a metal cutting plate which was then inserted into the vise of a vibratome (Leica VT1000S; Leica Microsystems, Richmond Hill, ON, Canada). In carbogenated superfusate, horizontal brain slices were cut at room temperature, initially at 400-600 µm steps, until the 4th ventricle appeared. Slice thickness was then reduced to 100 µm. Once the LC started to appear as a dark oval area close to the lateral border of the 4th ventricle, a single 400 µm thick slice was cut. This slice typically contained >50 % of the dorsoventral aspect of the spindle-shaped LC which extends in newborn rodents by 300-400 µm in the horizontal plane (Ishimatsu and Williams, 1996).

As the LC is bilaterally-organized, one hemisected slice was immediately used while the contralateral half could be stored without apparent changes in LC properties at 30 ^{o}C for up to 5 h

in a glass beaker filled with continuously carbogenated superfusate. For recording, a slice was mechanically fixed with a platinum 'harp' in an acrylic chamber (volume ~1 ml) with glass bottom (Warner Instruments, Hamden, CT, USA). The LC and individual cells were visualized with a 20x objective (XLUMPlanF1, numerical aperture 1.0) of an MPE microscope (Olympus, Markham, ON, Canada) or an IR-DIC video camera (OLY-150, Olympus). A peristaltic pump (Sci-Q 403U/VM, Watson-Marlow, Wilmington, MA, USA) was used to apply at a rate of 5 ml/min carbogenated superfusate which was removed from the chamber with vacuum applied to a hypodermic needle. Superfusate temperature in the chamber was kept at 28 °C via a heat control system (Thermo-Haake DC10-V15/B, Sigma-Aldrich, Canada).

2.2. Pharmacological agents

All salts and the following agents were from Sigma Aldrich unless specified otherwise: CNQX (10, 25 and 50 μM; stock 25 mM in H_2O), kynurenic acid (0.25-2.5 mM; stock 100 mM in DMSO), GYKI 53655 (25 μM; stock 25 mM in H_2O; Tocris, Canada), nifedipine (100 μM; stock 100 mM in DMSO), TTX (50 nM or 1 μM; stock 1 mM in 1 N NaOH; Alamone, Jerusalem, Israel), AMPA (0.05, 0.1, 0.25, 0.5 and 1 μM; stock 1 M in H_2O), KA (0.05, 0.1, 0.25, 0.5, 1, 2.5, 5 and 10 μM; stock 1 mM in H_2O), QUI (0.05, 0.1, 0.25, 0.5 and 1 μM; stock 5 mM in H_2O), NMDA (5, 10, 25, 50 and 100 μM; stock 25 mM in H_2O), glutamate (5, 10, 25, 50, 100, 250 and 500 μM; stock 1 M in H_2O), DAMGO (1 μM; stock 1 mM in H_2O), mefloquine hydrochloride (100 μM; stock 100 mM in DMSO).

2.3. Electrophysiological recording

Patch pipettes were pulled from borosilicate glass capillaries (GC-150TF-10; 1.5 mm outer Ø, 1.17 mm inner Ø, Harvard Apparatus) to an outer tip Ø of ~2 µm using a vertical puller (PC-10, Narishige International Inc., Amityville, NY, USA). They were used to record either (*i*) the LFP (after breaking the tip to obtain a suction electrode), (*ii*) extracellular spiking from a LC neuron pair or (*iii*) V_m in a single LC neuron. Electrophysiological signals were sampled at 4-20 kHz into a digital recorder (Powerlab 8/35 + LabChart 7 software, ADI instruments, Colorado Springs, CO, USA) connected to a personal computer.

2.3.1. Suction electrode recording

The major aim of this study was to analyze if glutamate and iGluR agonists transform the LFP pattern. Recently, we reported that LFP recording in the LC is difficult with fine-tipped microelectrodes contrary to using suction electrodes (Rancic et al., 2018). This type of electrodes is often applied to monitor nerve activities or neuronal population bursting within the isolated breathing center of newborn rodent brainstem slices (Lieske et al., 2000; Ballanyi and Ruangkittisakul, 2009). For suction electrode LFP recording, patch pipettes were broken and subsequently beveled manually with sand paper (Ultra Fine 600 Grit, Norton-Saint Gobain, Worcester, Wa, USA) at an angle of 45º to an oval-shaped tip with an inner opening of 40-60 µm. After filling with superfusate, the dc resistance of the suction electrodes was ~200 kΩ (Rancic et al., 2018). Following insertion into a patch electrode holder system (ESP-M15P and MHH-25, Warner Instruments), 15-30 mmHg suction was applied to the electrode with a syringe (BD Diagnostics, Franklin Lakes, NJ, USA) and controlled via a differential pressure sensor

(Honeywell, SCX05DN, Fort Worth, TX, USA). A MP-285 micromanipulator (Sutter Instrument Company, Novato, CA, USA) was used to position the suction electrode opening at a flat angle of ~30º on the slice surface followed by application of <5 mmHg negative pressure. The 'raw' suction electrode signal was amplified (x10k) and band-pass-filtered (0.3-3 kHz) using a Model-1700 differential amplifier (AM-Systems, Sequim, WA, USA). In parallel, the signal was processed for another recording channel by integration with a time constant of 50 ms using a MA-821/RSP unit (CWE, www.cwe-inc.com). This is a convenient way to represent neuronal bursting as routinely used, e.g., for respiratory (Ballanyi and Ruangkittisakul, 2009; Panaitescu et al., 2013) and locomotor (Pearlstein et al., 2005; Taccola et al., 2012) network analyses.

2.3.2. Paired neuron spike recording

For extracellular single-cell spike recording, superfusate-filled unbroken patch electrodes with a dc resistance of 4-5 MΩ (Rancic et al., 2018) were inserted into the above mentioned holder and 2 MP-285 micromanipulators (Sutter) were used to position them at an angle of ~30º on the slice surface close to a target cell. Repetitive single Na^+ spike discharge was recorded in >90 % of neurons when the electrode was pushed slightly against their soma and ~20 mmHg negative pressure was applied. Recordings were mostly stable for >5 min, in ~50 % of cases for >30 min. Spiking was recorded in current-clamp mode at 10x amplification using a patch-clamp amplifier (EPC-10 HEKA Lambrecht, Germany).

2.3.3. Whole-cell recording

For neuronal V_m recording using an EPC-10 amplifier, patch pipettes were filled with (in mM): 140 K-gluconate, 1 NaCl, 0.5 $CaCl_2$, 1 $MgCl_2$, 1 Na_2-ATP, 1 mM BAPTA and 10 Hepes (pH was adjusted to 7.4 with KOH; dc resistance in superfusate was 5-8 MΩ). When dimpling of the soma area occurred while visually targeting a neuron using the same manipulator as for extracellular recording, 20 mmHg positive pressure was released, and negative pressure was applied for giga seal formation (>1 GΩ). Whole-cell recording was established by abrupt suction (~100 mmHg). Only cells were analyzed in which spike amplitude was >70 mV while V_m was stable for a 5 min control period during which series resistance (10-42 MΩ, n= 4) was compensated and input resistance was measured (200-250 MΩ, n= 4). Due to ongoing 'subthreshold' V_m oscillations **(Figs. 1-6, 1-7)** (Christie et al., 1989), LC neurons do not have a 'resting' V_m which was thus defined as the voltage value at 50 % of the interval between spikes occurring at the oscillation peak.

2.4. Multiphoton population Ca_i imaging

Population Ca_i imaging enables visualization of brain activity (Yang and Yuste, 2017). We have used this approach in neonatal rat brain slices to visualize synchronous neuronal depolarizations in the inspiratory center (Ballanyi and Ruangkittisakul, 2009; Ruangkittisakul et al., 2009) and hippocampal CA3 area (Ruangkittisakul et al., 2015). Also in the LC, it is principally possible to visualize in single neurons Ca_i rises associated with single Na^+ spikes at rates of ~1 Hz using fast 'line-scanning' or a small region of interest (ROI) (Sanchez-Padilla et al., 2014). However, we aimed here at analyzing the activity of multiple LC cells in the same confocal plane. As this required xy-scanning at a rate of 1.1 frames/s, fast rhythmic Ca_i rises could not be resolved.

For population Ca_i imaging, a broken patch pipette (outer diameter, 5-10 µm) was filled with the membrane-permeant green fluorescent Ca^{2+} dye Fluo-4-AM (5 mM in 20 % DMSO + pluronic acid, further diluted to 0.5 mM in superfusate, Invitrogen, Carlsbad, CA, USA) and then pressure-injected (30-50 mmHg) for 10 min at 40-50 µm depth into the LC. Within 10 min, an area of 150-300 µm in diameter was stained. Fluorescence signals were typically measured 50-60 µm below the slice surface using the above specified Olympus 20x objective and MPE system emitting Ti:Sa laser light at 810 nm. Ca_i baseline changes were visualized in the somata of 15-25 cells in a single xy-image plane at 2x digital zoom with a sampling rate of 1.1 frames/s.

2.5. Immunohistochemistry

By far most LC cells are neurons whereas the rest comprises astrocytes and some oligodendrocytes (Alvarez-Maubecin et al., 2000). Here, we showed with double-staining using the neuronal marker TH and the astrocyte marker S100β that ~90 % of LC cells are neurons with a soma diameter >20 µm vs. ~10 % of notably smaller astrocytes. For their identification, 3 brains from 0 days-old pups were isolated and then chemically fixed in a solution comprising 4 % paraformaldehyde in phosphate buffer (i.e. a 1:2 mixture of 0.1 M NaH_2PO_4 + 0.1 M Na_2HPO_4 in H_2O, pH 7.2). After at least 24 h, 60 µm thick horizontal sections containing the LC were sliced and incubated overnight at 4 ºC in monoclonal rabbit anti-TH (1:1000, Life Technologies, Camarillo, CA, USA) and mouse anti-S100β (1:1000, Sigma Aldrich) antibodies in TBS (i.e. 0.9 % w/v NaCl plus 0.6 % w/v tris base, sigma, pH 7.4) also containing 0.3 % Triton X-100. Subsequently, the sections were incubated at room temperature in secondary goat anti-rabbit Alexa 594 (1:500, life technologies) and goat anti-mouse Alexa 488 (Jackson Immunoresearch Laboratories Inc, West Grove, PA,

USA) for 90 min. From each brain, cells in the section with the largest LC extension were analyzed using the MPE system.

2.6. Data Analysis

Burst rates and amplitudes were quantified during 1 min recording time periods in control or at steady-state of drug effects. LFP burst duration was defined with Clampfit software (Molecular Devices Corporation, Chicago, Il, USA) as the time interval from when the averaged signal increased above and decreased below a threshold set at 10 % of peak amplitude, respectively. The extent of LC network synchronicity was determined with Clampfit software by comparing over a time period of 10 s the cross-correlation between whole-cell-recorded single neuron spiking and the integrated LFP burst. The peaks in cross-correlograms refer to the cross-correlation function estimate (CFE) values for the accuracy of synchronicity. The lag time quantifies the shift in the peak between these events and thus gives a measure of spike jitter. This approach is applied to correlate single neuron with (nerve) population bursting, e.g. in respiratory (Fietkiewitcz et al., 2011) and locomotor networks (Pearlstein et al., 2005).

The regularity of LC network bursting was determined by quantifying the irregularity score which is an established parameter to analyze rhythmic neural network bursting, e.g. of the inspiratory center (Garcia et al., 2017). The formula for its determination is: Irregularity score = 100 * [$\Sigma(P_n - P_{n-1})/P_{n-1}$]/N, where N is the number of bursts, P_n is the period of n^{th} burst and P_{n-1} is the period of the preceeding burst. Note that the score has no unit. The lower the value, the more regular is the network rhythm.

For analysis of spike jitter, 10-20 cycles of LFP bursts and neuronal spiking were temporally aligned to the LFP peak using Clampfit software. Aligned traces were then overlapped and analyzed using a numerical matrix technique (Origin 6, Microcal Software). A summated LFP was obtained by averaging the 15-20 cycles. The average time point of neuronal spiking and its SD was used as a measure of the jitter.

Ca_i imaging analysis was done using Olympus Fluoview software (FV10-ASW, version 03.01.01.09). Relative changes in Ca_i baseline were referred to a percentage change in fluorescence intensity. Quantified was the ratio of the difference of the final value (average of the peak response) and the initial value (average baseline values) over the initial value multiplied by 100. Ca_i imaging revealed in ~30 % of recordings a modest linear drift of baseline fluorescence intensity which was compensated during offline analysis.

Values are given as means ± SD and n-values correspond to measurements in 1 slice per animal. Significance values, i.e., non-significant (ns): $P > 0.05$, $*P < 0.05$, $** P < 0.01$, $***P < 0.001$) were assessed by paired two-tailed t test or one-way ANOVA with Dunnett's post-test using Prism software (GraphPad Software Inc., La Jolla, CA, USA).

CHAPTER 3

Suction electrode recording in locus coeruleus of newborn rat brain slices reveals network bursting comprising summated non-synchronous spiking

Vladimir Rancic, Bijal Rawal, Bogdan Panaitescu, Araya Ruangkittisakul & Klaus Ballanyi

Department of Physiology, Faculty of Medicine & Dentistry, 750 MSB, University of Alberta, Edmonton, T6G2H7, Canada

Author contributions: VR and KB contributed to the conception and design as well as acquisition, analysis or interpretation of data for the work plus drafting the final work or revising it critically for important intellectual content. BR, BP and AR contributed to the data acquisition and analysis.

Publication: Rancic V, Rawal B, Panaitescu B, Ruangkittisakul A, Ballanyi K (2018) Suction electrode recording in locus coeruleus of newborn rat brain slices reveals network bursting comprising summated non-synchronous spiking. Neurosci Lett 671:103-107

3.1. Abstract

The brainstem locus coeruleus (LC) controlling behaviors like arousal, sleep, breathing, pain or opioid withdrawal is an established model for spontaneous action potential synchronization. Such synchronous 'spiking' might produce an extracellular field potential (FP) which is a crucial tool for neural network analyses. We found using ≥10 µm tip diameter suction electrodes in newborn rat brainstem slices that the LC generates at ~1 Hz a robust rhythmic FP (rFP). During distinct rFP phases, LC neurons discharge with a jitter of ±33 ms single spikes that summate to a ~200 ms-lasting population burst. The rFP is abolished by blocking voltage-gated Na^+ channels with tetrodotoxin (TTX, 50 nM) or gap junctions with mefloquine (100 µM) and activating µ-opioid receptors with [D-Ala2,N-Me-Phe4,Gly5-ol]-Enkephalin (DAMGO, 1 µM). Raising superfusate K^+ from 3 to 7 mM either increases rFP rate or transforms its pattern to slower and longer multipeak bursts similar to those during early recovery from DAMGO. The results show that electrical coupling of neonatal LC neurons does not synchronize their spiking as previously proposed. They also indicate that both increased excitability (by elevated K^+) and recovery from inhibition (by opioids) can enhance spike desynchronization to transform the population burst pattern. Both observations show that this gap junction-coupled neural network has a more complex connectivity than currently assumed. These new findings along with the inhibitory drug effects that are in line with previous reports based on single neuron recording point out that field potential analysis is pivotal to further the understanding of this brain circuit.

3.2. Introduction

The locus coeruleus (LC) provides noradrenergic innervation to various brain structures and controls multiple behaviors including the sleep-wake cycle, arousal, memory, breathing, pain modulation and opioid withdrawal (Foote et al., 1983; Berridge and Waterhouse, 2003; Schwarz and Luo, 2015; Llorca-Torralba et al., 2016; Ahmadi-Soleimani et al., 2017). In vitro studies mostly using newborn rodent brain slices established the LC as a model for analyzing action potential ('spike') discharge patterning in neural networks. Such research presented evidence that gap junction-coupled neonatal LC neurons show synchronous subthreshold membrane potential oscillations that cause discharge of a spike at their peak (Williams and Marshall, 1987; Christie et al., 1989; Christie, 1997; Alvarez et al., 2002). If such rhythmic single spike discharge occurs synchronously, this might generate an extracellular field potential (FP) which is a pivotal measure to analyze neural network properties in other brain regions (Buzsáki et al., 2012; Einevoll et al., 2013). Yet, no study reported a rhythmic FP (rFP) reflecting normal repetitive neonatal LC activity. In newborn rodent brainstem slices, a rFP in the spontaneously active breathing center is not seen with sharp or patch microelectrodes often used for FP recording whereas a robust signal is revealed with suction electrodes originally designed for nerve recording (Lieske et al., 2000; Ballanyi and Ruangkittisakul, 2009). Accordingly, it was the aim of our study to identify in horizontal newborn rat brain slices with suction electrode rFP recording novel features of the LC neural network.

3.3. Materials and methods

(see **Chapter 2)**

3.4. Results

3.4.1. rFP characteristics

A rFP comprising overlapping single spike discharge was seen when a suction electrode was positioned on the superficial LC neuron soma layer **(Fig. 3-1A)**. The crescendo-decrescendo-type shape of the integrated signal, its amplitude, duration and rate were stable for several hours particularly when < 5 mmHg suction was applied. In 20 slices, burst rate ranged from 0.85 to 1.78 Hz (mean 1.13 ± 0.2 Hz or 68.15 ± 13.47 bursts/min) and single burst duration ranged from 0.08 to 0.32 s (mean 0.19 ± 0.06 s). As tested in 10 different slices, both LC aspects showed similar, but non-synchronous rFP bursting **(Fig. 3-1A)**. rFP amplitude was maximal when recorded with 200 µm tip electrodes while typically used 40–60 µm electrodes detected ~80% of the signal (i.e. 937 ± 267 µV, n= 4) that was still robust using 10 µm tip electrodes **(Fig. 3-1B)**. Unbroken patch electrodes did not detect a rFP when positioned without pressure application between LC neurons **(Fig. 3-1B)**. Contrary, a small amplitude signal was seen in 7 of 12 experiments when modest positive pressure was applied during electrode positioning and slight suction was then applied in the recording spot **(Fig. 3-2)**. Single-cell spiking was seen when the electrode was removed from the extracellular position between LC neurons and then slightly pushed against the soma membrane of one cell **(Fig. 3-2)**. Simultaneous rFP and cell pair recording showed that LC neurons spike during a distinct phase within the rFP and the exact time point varies between activity cycles, on average by 33.18 ± 13.9 ms (n= 27 neurons from 3 slices) **(Fig. 3-3)**. There was no correlation between the time phase of this 'jittered' phase-locked spiking and LC neuron location. Accordingly, in 4 slices mapped with 40–60 µm tip electrodes, rFP shape, amplitude and burst duration were very similar in different spots within the LC whereas rFP amplitude was smaller in the pericoerulear dendritic region (Ishimatsu and Williams, 1996).

3.4.2. Pharmacological rFP modulation

Similar to previous reports using single LC neuron recording, the rFP was abolished in 5 slices each by inhibiting voltage-gated Na^+ channels with TTX (Williams and Marshall, 1987) **(Fig. 3-4A)** or gap junctions, here with mefloquine **(Fig. 3-4B)** (Alvarez-Maubecin et al., 2000; Connors, 2012) and by the μ-opioid receptor agonist DAMGO (Williams and Marshall, 1987) **(Fig. 3-4C)**. The mefloquine effect was irreversible whereas the rFP recovered from TTX and DAMGO in ~30 and ~15 min, respectively. During the first 5-7 min of DAMGO recovery, the rFP pattern transformed into slower rate (from 73.20 ± 19.62 to 16.4 ± 6.84 bursts/min, $P< 0.05$), longer duration (from 0.27 ± 0.04 to 2.64 ± 1.89 s, $P< 0.05$) multipeak events **(Fig. 3-4C)**. Increasing LC excitability in 6 slices by raising superfusate K^+ from 3 mM to 7 mM increased rFP rate from 64 ± 11 to 93 ± 13 bursts/min ($P< 0.05$), but transformed rFP pattern in 3 other slices into slower rate (from 90 ± 6 to 11.5 ± 3.2 bursts/min, $P< 0.05$), longer duration (from 0.21 ± 0.03 s to 2.83 ± 0.77 s, $P< 0.05$) multipeak events similar to those during early DAMGO recovery **(Fig. 3-4D)**.

3.5. Discussion

3.5.1. Conditions for rFP recording

Recording with ≥10 μm tip size suction electrodes revealed a robust and stable rFP whereas it was barely detectable using unbroken patch electrodes which though picked up single LC neuron spiking. Similarly, single-cell or multi-unit discharge, but no rFPs, were seen with microelectrodes in the fetal and neonatal rat LC in vivo (Nakamura et al., 1987; Sakaguchi and Nakamura, 1987). In the only slice study aiming at FP recording in the adult rat LC, a rFP was seen with 'broken glass electrodes' solely when excitability was raised with Ba^{2+} and/or tetraethylammonium (Ishimatsu and Williams, 1996). Thus, it appears that larger tip glass microelectrodes are needed

to reliably record a spontaneous rFP in the neonatal LC as in the breathing center of newborn rodent brainstem slices (Lieske et al., 2000; Ballanyi and Ruangkittisakul, 2009). Moreover, we found that rFPs are very robust and stable for >10 h in the hippocampus of newborn rat brain slices (Ruangkittisakul et al., 2015). This suggests that suction electrode recording is well suited for long-term (pharmacological) analysis of neuronal activity also in other isolated (neonatal) brain areas and possibly also in vivo.

3.5.2. rFP mechanism

FP analysis is a pivotal tool for neural network analysis (Buzsáki et al., 2012; Einevoll et al., 2013). Here, rFP recording unraveled two novel features of the LC network that have not been reported previously using extracellular or intracellular single neuron (pair) recording (Nakamura et al., 1987; Sakaguchi and Nakamura, 1987; Williams and Marshall, 1987; Christie et al., 1989; Christie, 1997; Ishimatsu and Williams, 1996; Alvarez-Maubecin et al., 2000; Zhu and Zhou, 2001; Alvarez et al., 2002; Ahmadi-Soleimani et al., 2017). Namely, LC neurons do not spike synchronously, but rather in a phase-locked jittered fashion while the population burst pattern can transform during changes of network excitability. Regarding the first point, it was unexpected that a rFP burst lasts on average 190 ms given that presumably synchronized single spike discharge (Williams and Marshall, 1987; Christie et al., 1989; Christie, 1997; Alvarez et al., 2002) should have caused a summated signal of substantially shorter duration. We found that rFP duration is sustained because LC neuron subclasses are preferentially active either during the early phase, peak or late phase of the rFP and thus do not discharge synchronously. Moreover, spiking in each LC neuron shows a cycle-to-cycle jitter of ±33 ms. As one possible explanation for both phenomena, the slope and/or amplitude of Ca^{2+}-dependent subthreshold membrane potential oscillations eliciting a Na^{+} spike at

their peak (Williams and Marshall, 1987; Christie et al., 1989; Christie, 1997; Alvarez et al., 2002) may be modulated by random and/or tonic excitatory or inhibitory synaptic inputs (Schwarz and Luo, 2015). Consequently, Na^+ spike threshold may be reached earlier or later, respectively. In line with our results, paired LC neuron recording in adult rat brain slices showed that spontaneous spiking is not fully synchronous contrary to synchronous subthreshold membrane potential oscillations (Christie et al., 1989). The authors did not analyse this finding further but noted electrical coupling of newborn LC neurons might not be sufficient for synchronous spontaneous spiking (Christie et al., 1989). Nevertheless, gap junctions seem to be pivotal for synchronizing subthreshold depolarizations and rFP generation as indicated by the blocking effects on both signals, respectively, of carbenoxolone (Alvarez et al., 2002; Alvarez-Maubecin et al., 2000) and mefloquine (present study) (Connors, 2012). The finding that the rFP was abolished by TTX indicates that this signal is not caused by subthreshold oscillations, but rather due to Na^+ spiking that is also the source for Ba^{2+}- and tetraethylammonium-evoked rFPs in the LC of adult rat slices (Ishimatsu and Williams, 1996).

3.5.3. rFP pattern transformation

The rFP pattern changed from ~1 Hz bursting to a notably slower rhythm with longer multipeak bursts during early recovery from DAMGO. Similarly, extracellular (paired) LC neuron recording in adult rats in vivo showed that morphine transforms repetitive single spiking into oscillatory burst discharges (Zhu and Zhou, 2001). Correspondingly, a transition from fast subthreshold membrane potential oscillations with discharge of a single spike to slower and longer-lasting oscillations with multiple spike discharge was detected with intracellular recording in LC neurons in slices from young rats in response to cocaine (Williams and Marshall, 1987). The actions of opioids and

cocaine involve different signaling pathways. It is thus possible that the rFP pattern transformation induced in a subpopulation of slices by 7 mM K^+ is caused by release of an endogenous agent that acts on one of these signaling pathways. Future pharmacological rFP analysis will likely further the understanding of this scenario. Regarding the functional role of the rFP, we agree with the view of the authors by the latter studies (Williams and Marshall, 1987; Zhu and Zhou, 2001) that robust sustained rhythmic oscillations of LC neurons may facilitate release of noradrenaline in the diverse LC-innervated brain regions. Here, we showed for the first time that the neonatal LC forms a coupled neural network that does not generate synchronized single spikes under control conditions, but rather shows rhythmic activity with a sustained oscillatory population burst pattern that can transform under the influence of various neuromodulators.

3.6. Figures and Legends

Fig. 3-1

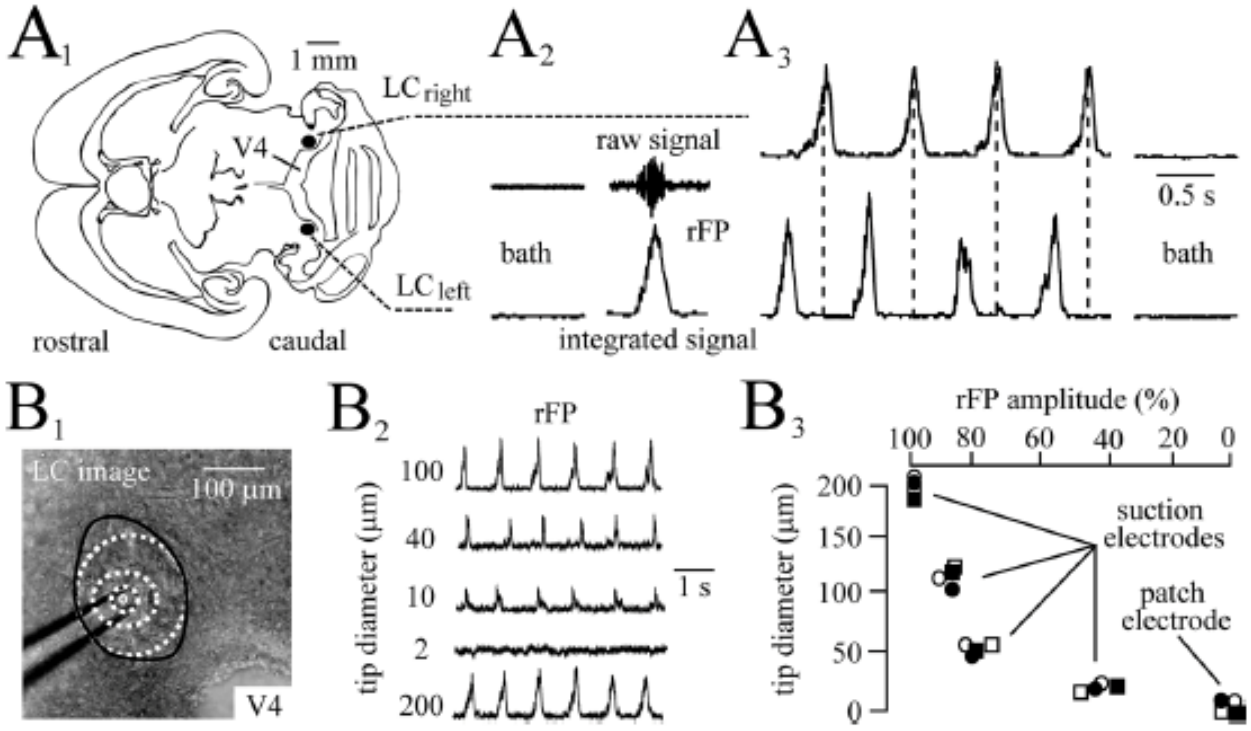

Fig. 3-1. Spontaneous rhythmic field potential (rFP) in locus coeruleus (LC) of newborn rat brain slices. **A_1**, schema represents the horizontal slice with the bilateral LC aspects. **A_2**, shows both the raw and integrated signal 24 min after a superfusate-filled suction electrode was repositioned from the superfusate in the recording chamber ('bath') to the surface of the left LC. After positioning a further suction electrode on the right LC, a non-synchronous rFP of similar amplitude and rate was seen **(A_3)**. **B_1**, rFP recording in a different slice with (suction) electrodes of different diameter indicated by dashed lines. **B_2**, **B_3** show that rFP amplitude was maximal using a 200 µm tip electrode and decreased with smaller tip sizes whereas no rFP was seen with a 2 µm tip superfusate-filled patch electrode (but compare **Fig. 3-2**). V4 in **A_1** and **B_1** stands for 4th ventricle and different symbols in **B_3** for individual experiments in 4 slices. Reproduced with permission from Rancic et al. (2018).

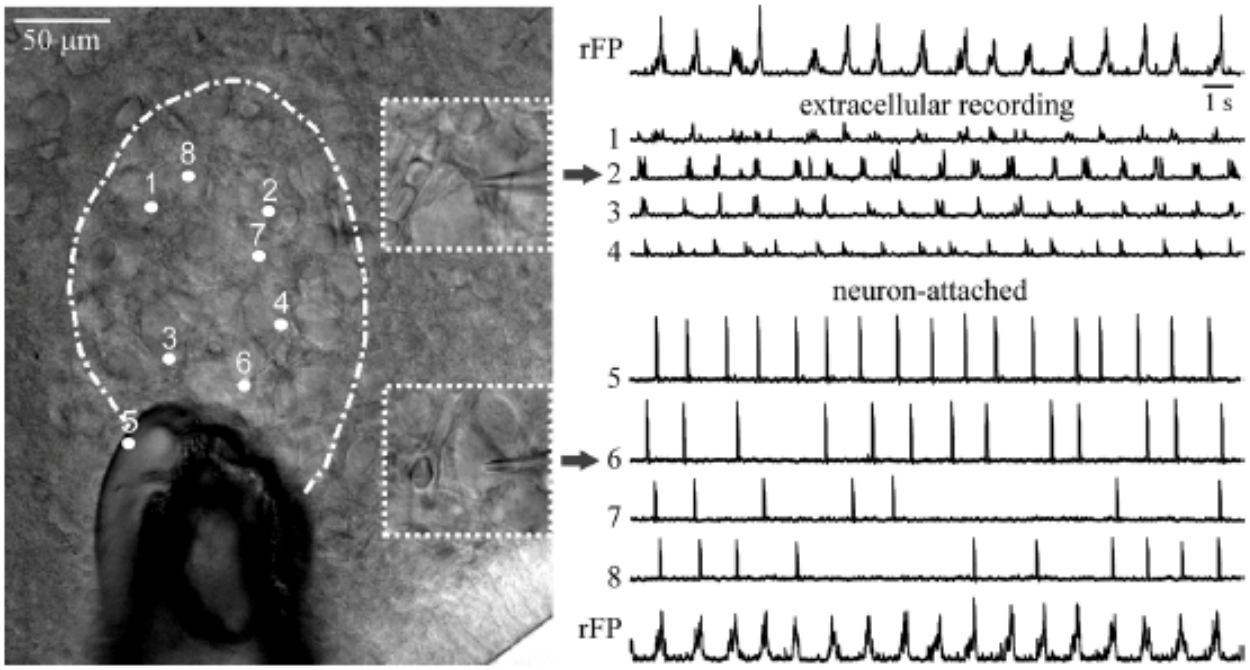

Fig. 3-2. Simultaneous rFP and single neuron action potential ('spike') recording. Image shows a suction electrode positioned close to caudal rim of LC whose neuronal somata area is outlined by dashed line. White circles and numbers indicate positions of a superfusate-filled patch electrode that was placed extracellularly firstly between cells (positions 1-4) and was then slightly pushed against 4 neuron somata (positions 5-8). In positions 1-4, a small amplitude rFP was only seen with 20 mmHg positive pressure applied to the electrode during positioning while afterwards 20-30 mmHg negative pressure was applied at the recording spot. In positions 5-8, single neuron spiking was seen independent on whether pressure was applied or not. Uppermost and lowermost traces show rFP recorded simultaneously with single neuron activity shown next to trace. Reproduced with permission from Rancic et al. (2018).

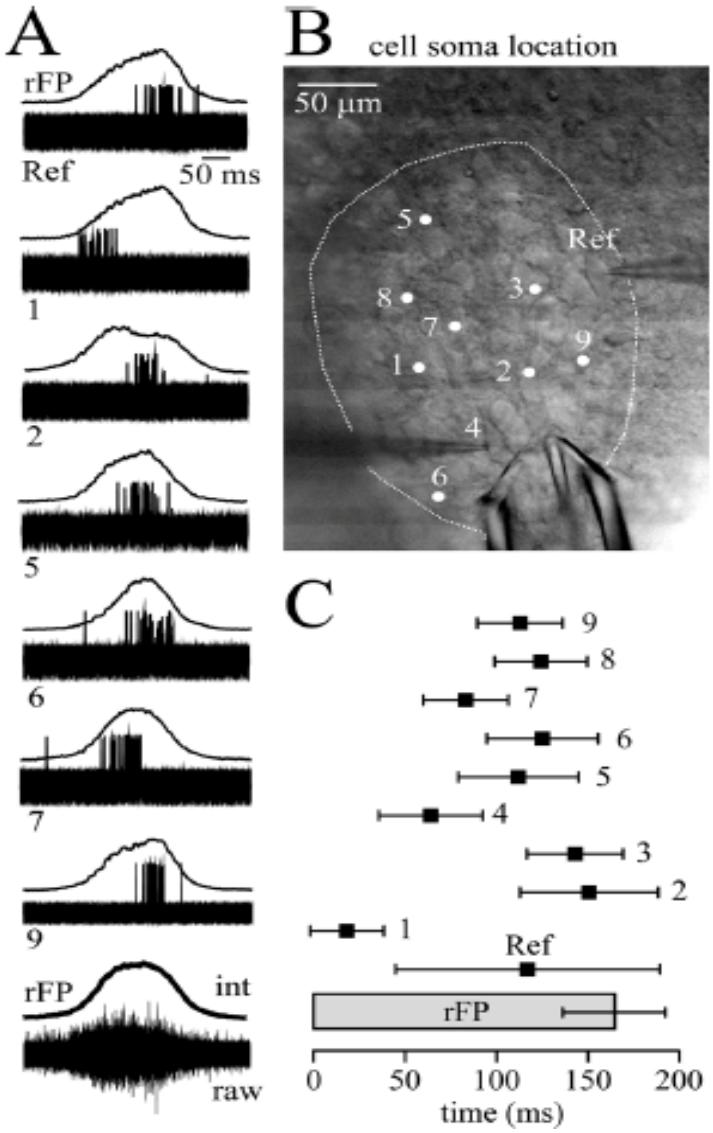

Fig. 3-3. Jittered and phase-locked LC neuron discharge comprising the rFP. A, overlay of 20 cycles of extracellular spiking shown with corresponding averaged integrated rFP trace of a reference neuron (Ref) and 6 of the 9 other cells recorded consecutively along with the Ref neuron at the LC spots indicated in **B**. Bottom traces show the averaged integrated rFP and overlayed raw rFP signals from all cycles. **C**, shows means ± SD of rFP burst duration (grey bar) and the average time point of spiking of all 10 LC neurons and its SD demonstrating a 'jitter' of their discharge as also evident from the original recordings in **A**. Reproduced with permission from Rancic et al. (2018).

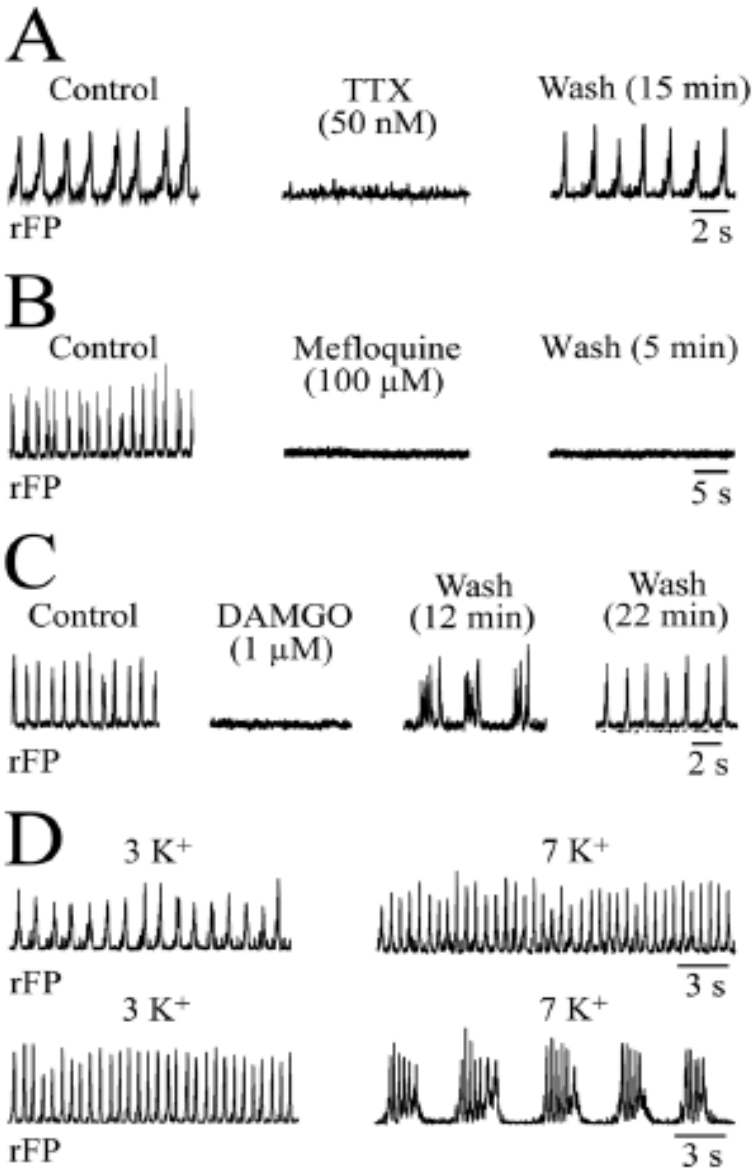

Fig. 3-4. Effects on rFP of bath-applied modulators of neural network activity. A, the rFP was reversibly blocked by tetrodotoxin (TTX, 50 nM). **B**, the gap junction blocker mefloquine (100 µM) abolished the rFP irreversibly. **C**, the µ-opioid receptor agonist [DAla2, N-Me Phe4,Gly5-ol]-Enkephalin (DAMGO, 1 µM) reversibly blocked the rFP. Note that rFP burst pattern was transformed to slower and longer duration multipeak events in the early phase of DAMGO recovery. **D**, in 6 of 9 slices rFP rate increased by raising superfusate K^+ concentration from 3 to 7 mM whereas in other 3 slices this transformed the burst pattern similar to that seen during early recovery from DAMGO. Reproduced with permission from Rancic et al. (2018)

CHAPTER 4

TARP mediation of accelerated and more regular locus coeruleus network bursting in neonatal rat brain slices

Bijal Rawal, Vladimir Rancic & Klaus Ballanyi

Department of Physiology, Faculty of Medicine & Dentistry, 7-50 MSB, University of Alberta, Edmonton, T6G2H7, Alberta, Canada

Author contributions: BR and KB contributed to the conception, design and writing. BR contributed to >85% of data acquisition, analysis or interpretation of data. VR contributed to <15% of data acquisition.

Publication: Rawal B, Rancic V, Ballanyi K (2019) TARP mediation of accelerated and more regular locus coeruleus network bursting in neonatal rat brain slices. Neuropharmacology 148: 169-177.

4.1. Abstract

Transmembrane AMPA receptor (AMPAR) regulatory proteins (TARP) increase neuronal excitability. However, it is unknown how TARP affect rhythmic neural network activity. Here we studied TARP effects on local field potential (LFP) bursting, membrane potential and cytosolic Ca^{2+} (Ca_i) in locus coeruleus neurons of newborn rat brain slices. LFP bursting was not affected by the unselective competitive ionotropic glutamate receptor antagonist kynurenic acid (2.5 mM). TARP-AMPAR complex activation with 25 μM CNQX accelerated LFP rhythm 2.2-fold and decreased its irregularity score from 63 to 9. Neuronal spiking was correspondingly 2.3-fold accelerated in association with a 2-5 mV depolarization and a modest Ca_i rise, whereas Ca_i was unchanged in neighboring astrocytes. After blocking rhythmic activities with tetrodotoxin (1 μM), CNQX caused a 5-8mV depolarization and also the Ca_i rise persisted. In tetrodotoxin, both responses were abolished by the non-competitive AMPAR antagonist GYKI 53655 (25 μM) which also reversed stimulatory CNQX effects in control solution. The CNQX-evoked Ca_i rise was blocked by the L-type voltage-activated Ca^{2+} channel inhibitor nifedipine (100 μM). The findings show that ionotropic glutamate receptor-independent neonatal locus coeruleus network bursting is accelerated and becomes more regular by activating a TARP-AMPAR complex. The associated depolarization-evoked L-type Ca^{2+} channel-mediated neuronal Ca_i rise may be pivotal to regulate locus coeruleus activity in cooperation with SK-type K^+ channels. In summary, this is the first demonstration of TARP-mediated stimulation of neural network bursting. We hypothesize that TARP-AMPAR stimulation of rhythmic locus coeruleus output serves to fine-tune its control of multiple brain functions thus comprising a target for drug discovery.

4.2. Introduction

In mammalian neurons, fast excitatory neurotransmission is mostly mediated by an α-amino-3-hydroxy-5-methyl-4-isoxazole propionic acid receptor (AMPAR) comprising one type of ionotropic glutamate receptors (iGluR) (Traynelis et al., 2010). Molecularly diverse AMPAR subtypes are coupled to a member of the family of auxiliary transmembrane AMPAR regulatory proteins (TARP) (Jackson and Nicoll, 2011; Greger et al., 2017; Maher et al., 2017). As reviewed in the latter reports, TARP activation can modulate the excitability of certain neuron types and competitive AMPAR antagonists, like the quinoxalinediones 6-cyano-7-nitroquinoxaline-2,3-dione (CNQX) and 6,7- dinitroquinoxaline-2,3(1H,4H)-dione (DNQX), are pivotal tools for studying this. Specifically, they act as partial agonists at the TARP-AMPAR complex and consequently depolarize and enhance firing, e.g. in principal neurons and (inhibitory) interneurons in the hippocampus (McBain et al., 1992; Maccaferri and Dingledine, 2002; Hashimoto et al., 2004), thalamus (Lee et al., 2010), cerebellum (Brickley et al., 2001; Menuz et al., 2007) or spinal cord (Sullivan et al., 2017). Regarding functional TARP roles, most of the above studies on acute brain slices showed that quinoxalinedione-evoked firing augments spontaneous (inhibitory) postsynaptic currents. Such currents can be analyzed in control mice compared to animals with a 'knock-out' of TARP-coding genes like in a report pointing out the requirement of 'Type-I TARP γ-2' for inflammation-associated spinal AMPAR plasticity (Sullivan et al., 2017). Moreover, 'stargazer' mice that lack γ-2, and were therefore instrumental in TARP discovery, show neurological deficits like ataxia, dyskinesia and seizures (Jackson and Nicoll, 2011; Maher et al., 2017). While TARP effects at the cellular level are established, their role in active neural networks is currently unknown. This is due to the fact that most rhythmically active brain circuits operate via iGluR and quinoxalinediones thus block their activity like in locomotor (Hägglund et al., 2010) or respiratory (Ballanyi and Ruangkittisakul, 2009) networks, entorhinal cortex (Garaschuk et al.,

2000) or hippocampus (Sipilä and Kaila, 2008). The locus coeruleus (LC) in the brainstem might be an important model for studying TARP-AMPAR complex roles for two reasons. Firstly, it innervates most brain structures and thus modulates many behaviors including arousal, sleep-wake cycle, memory, anxiety or opioid (withdrawal) effects (Foote et al., 1983; Berridge and Waterhouse, 2003). Secondly, in newborn rats gap junction-coupled LC neurons generate presumably synchronous Na^+ action potentials via a mechanism that may not depend on iGluR as such 'spiking' is not blocked by quinoxalinediones (Alvarez-Maubecin et al., 2000) similar to persistence of tonic spiking in adult rats (Alvarez et al., 2002). Nevertheless, at both developmental stages LC neurons have functional NMDA- and AMPA/Kainate-type iGluR as specific agonists increase their spike rate (Olpe et al., 1989; Kogan and Aghajanian, 1995; Zamalloa et al., 2009). Local field potential (LFP) recording is a potent tool to analyze neural network functions (Ballanyi and Ruangkittisakul, 2009; Buzsáki et al., 2012; Einevoll et al., 2013; Totah et al., 2018). We recently reported that spiking of LC neurons at ~1 Hz in newborn rat slices generates a rhythmic ~0.2 s-lasting crescendo-decrescendo-shaped LFP (Rancic et al., 2018). It was the aim of the present study to investigate by combining LFP monitoring with either 'whole-cell' membrane potential (V_m) recording or imaging of the free cytosolic Ca^{2+} concentration (Ca_i) in LC neurons and neighboring astrocytes whether CNQX has a TARP-mediated modulatory action on rhythmic population activity in this spontaneously active neonatal neural network.

4.3. Materials and methods

(see **Chapter 2)**

4.4. Results

Initial analysis of iGluR blocker effects on LFP recording-based network bursting was followed by neuronal V_m analysis and Ca_i imaging in groups of Fluo-4-AM loaded neurons and astrocytes.

4.4.1. Stimulatory CNQX effect on iGluR-independent network bursting

As a precondition for testing TARP roles in LC network function, it was studied if LFP rhythm persists during iGluR blockade (see section **4.2.**). This was indeed the case as the non-selective competitive iGluR antagonist kynurenic acid had no effect on the LFP in 4 slices **(Fig. 4-1)**. As exemplified in **Fig. 4-2A** for 1 of 12 slices, 5 min bath-application of 25 µM CNQX caused within 1-2 min a stable effect on the LFP that washed out within 5-15 min. While CNQX did not change LFP amplitude (101.6 ± 2.6% of control, P= 0.07) **(Fig. 4-2B)**, it increased its rate 2.24 ± 0.5 -fold (from 53.4 ± 10.6 to 116 ± 19.1 bursts/min) **(Fig. 4-2C)** and decreased its single burst duration from 268 ± 56.1 to 205 ± 29.4 ms **(Fig. 4-2D)**. In 3 of the 12 slices, the accelerated rhythm had an almost sinusoidal oscillatory pattern lacking an inactivity phase between bursts and could include burst amplitude fluctuations by <15 % **(Fig. 4-2A**, see also **Figs. 4-3A**, **4-4A** and **4-6A)**. As exemplified in **Fig. 4-3A**, recording of neuronal V_m in 7 of the 12 slices revealed a very similar 2.29 ± 0.43 -fold acceleration of spike rate (from 50.4 ± 9.0 to 113 ± 9.2 spikes/min) **(Fig. 4-2E, F)** and a concomitant depolarization by 2-5 mV (3.1 ± 0.9 mV) from a resting V_m of −45.8 ± 3.2 mV **(Tab. 4-1)**. These results show that neonatal LC network bursting does not depend on iGluR and indicate that a TARP-AMPAR complex is functional. LFP and V_m were next simultaneously recorded after abolishing rhythmic activities with TTX to (i) better quantify the CNQX depolarization, (ii) minimize a potentially short-circuiting V_m effect of SK-type K^+ channel activation due to spike-related Ca^{2+} influx (Kulik et al., 2002) and (iii) exclude that enhanced

spiking causes endogenous neurotransmitter/modulator release (Singewald and Phillipu, 1998; Schwarz and Luo, 2015). As tested in 5 of the above 7 neurons, TTX blocked in 0.5-3 min the LFP, Na^+ spikes and subthreshold oscillations with no effect on resting V_m (which stabilized at −46.6 ± 3.9 mV) **(Fig. 4-3B) (Tab. 4-1)**. Subsequent CNQX application depolarized V_m by 5-8 mV (6.6 ± 1.3 mV) with no change in input resistance (238 ± 82 MΩ in control vs. 234 ± 75 MΩ in CNQX, *P*= 0.42) **(Fig. 4-3C) (Tab. 4-1)**.

4.4.2. Reversal of stimulatory CNQX effect by non-competitive iGluR antagonist

In cerebellar neurons, the CNQX-evoked TARP-mediated depolarization was blocked by the non-competitive AMPAR antagonist GYKI (Menuz et al., 2007). Also here, CNQX failed, after preincubating slices in GYKI + TTX, to change V_m in 6 neurons (-44.8 ± 5.1 mV vs. -44.7 ± 5.2 mV) **(Fig. 4-4A) (Tab. 4-1)**. In 3 different neurons, CNQX was continuously applied in control solution. When the accelerating effect on spiking and LFP rate was stable after 1-2 min, addition of GYKI to the CNQX-containing solution reversed the CNQX effects within ∼1 min **(Fig. 4-4B)**.

4.4.3. Uniform L-type Ca^{2+} channel-mediated CNQX-evoked Ca_i rise in LC neurons

The finding that CNQX depolarized all neurons to a similar (modest) extent indicates that the entire nucleus may show a uniform response. To test this, population Ca_i imaging was done to determine (i) whether the depolarization and the associated accelerated spiking raises Ca_i, (ii) how many LC neurons in the same optical plan show such a response and (iii) whether CNQX also affects Ca_i in neighboring astrocytes that show in control solution depolarizations which are synchronous with subthreshold neuronal V_m oscillations (Alvarez-Maubecin et al., 2000).

Fig. 4-5A illustrates that TH-immunostained LC neurons with a soma diameter >20 µm comprise ~90 % of LC cells and notably smaller S100β-immunostained astrocytes the remaining ~10 %. **Fig. 4-5B** shows Fluo-4-AM loaded neurons and astrocytes in one image plane during the steady-state effect of CNQX. **Fig. 4-5C** exemplifies for 4 of these neurons that CNQX caused a very similar modest Ca_i increase whereas 4 astrocytes did not respond. Corresponding findings were obtained in a total of 174 neurons and 44 astrocytes of 8 slices **(Fig. 4-5D)**. Two of the 4 astrocytes in **Fig. 4-5C**, and 23 % in total, showed spontaneous Ca_i 'spikes' unrelated to CNQX application. Similar modest Ca_i rises were seen during CNQX in control solution (30.14 ± 0.08 %) and in TTX (27.83 ± 0.07 %) which itself lowered Ca_i baseline by 28.13 ± 0.03 % **(Fig. 4-5C, D)**. After recovery from CNQX in TTX and preincubation of 4 of the above 8 slices in TTX plus either the L-type voltage-activated Ca^{2+} channel blocker nifedipine or GYKI, CNQX did not change neuronal Ca_i **(Fig. 4-5D)**.

4.4.4. CNQX effect on network synchronicity and regularity of bursting

The above finding that CNQX shortened the LFP burst suggests that CNQX enhances LC network synchronization. This was studied by correlating cellular spiking with LFP events at steady-state, typically 90 s after start of application as exemplified in **Fig. 4-6A** for the neuron shown in **Fig. 4-3**. The correlograms in **Fig. 4-6B** did not reveal a CNQX-induced change of the CFE value for this neuron whereas the lag time was shortened. For all 7 neurons in which CNQX effects have been analyzed above, the scatter plots did not indicate a change in the CFE value (0.33 ± 0.04 in control vs. 0.33 ± 0.04 in CNQX) while there was a trend for a decrease in lag time (87.8 ± 26.1 ms in control vs. 59.3 ± 23.5 ms in CNQX) **(Fig. 4-6C)**. But, as analyzed in the 12 slices analyzed above,

CNQX made the LFP rhythm more regular as evident from a decrease of the irregularity score from 63.1 ± 19.7 to 8.8 ± 4.2 **(Fig. 4-6D)**.

4.5. Discussion

This study reports for the first time TARP effects on spontaneous neural network activity, specifically in the LC of newborn rat brain slices. This network was chosen because it comprises a small nucleus in which coordinated discharge of a single spike in each neuron causes a robust rhythmic LFP that can be analyzed pharmacologically (Rancic et al., 2018). LFP recording in combination with either whole-cell V_m recording or Ca_i imaging unraveled, in summary, (i) non-synchronous, yet phase-locked, spiking does not rely on iGluR, (ii) CNQX causes in all neurons a modest depolarization and Ca_i rise, (iii) CNQX-evoked depolarization more than doubles cellular and network discharge rates with a concomitant decrease in jitter and increased regularity of network bursting. Underlying mechanisms and the potential physiological relevance are discussed.

4.5.1. LFP analysis of CNQX stimulation of iGluR-independent network bursting

Spontaneous neonatal LC neuron spiking is presumably synchronous (Christie, 1997). But, one of the reports establishing this view stated that subthreshold V_m oscillations are synchronous whereas Na^+ spikes at their peak not necessarily (Christie et al., 1989). In our recent study (Rancic et al., 2018), we showed that spiking is not synchronous, but rather jittered, yet phase-locked, to the LFP burst. We also found in that report that increasing LC excitability with raised extracellular K^+ transforms the LFP pattern from ~0.2 s-lasting crescendo-decrescendo-shaped bursts to ~3 s-lasting multipeak events. Here, we show firstly that LFP properties are not changed by the broad

spectrum competitive iGluR antagonist kynurenic acid (Traynelis et al., 2010). It was already reported that single LC neuron spiking in newborn and adult rat brain slices persists in presence of diverse iGluR antagonists (Olpe et al., 1989; Alvarez- Maubecin et al., 2000; Alvarez et al., 2002). The lack a blocking effect by these antagonists is not due to absence of functional iGluR in LC neurons. In fact, both NMDA-type and AMPA/Kainate-type iGluR agonists evoke inward currents that depolarize these neurons to accelerate their spontaneous spiking (Olpe et al., 1989; Williams et al., 1991; Kogan and Aghajanian, 1995; Zamalloa et al., 2009). Our results point out, in addition, that blocking all iGluR subtypes with kynurenic acid does not abolish LC network bursting. This contrasts with findings in other spontaneously active (neonatal) rodent neural networks showing that iGluR antagonists block rhythm generation. Specifically, these networks are the locomotor central pattern generator (Hägglund et al., 2010), the breathing center (Ballanyi and Ruangkittisakul, 2009), the inferior olive (Placantonakis and Welsh, 2001; Devor and Yarom, 2002), the entorrhinal cortex (Garaschuk et al., 2000) and the hippocampal CA3 area (Sipilä and Kaila, 2008). A study on LC neurons in newborn rat brainstem-spinal cords anecdotally mentioned that CNQX caused a small depolarization and accelerated their tonic spiking (Oyamada et al., 1998). Also here, CNQX accelerated neuronal spiking (and LFP rate as well). Already these findings prove that pharmacological LFP analysis is a powerful tool to analyze this neural network.

4.5.2. TARP mediation of a uniform excitatory CNQX effect

Like in LC neurons of newborn rat brainstem-spinal cords (Oyamada et al., 1998), CNQX caused here a modest (~5 mV) depolarization that nevertheless more than doubled LFP and spike rates. The lack of a CNQX-evoked decrease in input resistance indicates that (synaptic) ion channels causing the depolarization might be located primarily on the pericoerulear dendrites and space-

clamp might thus not be sufficient to reveal their activation with somatic injection of current pulses (Ishimatsu and Williams, 1996). Accordingly, the depolarization and concomitant Ca_i rise might be more pronounced in distal dendrites. The inhibitory TTX effects on both Na^+ spikes and subthreshold V_m oscillations were similar to those in the latter report (Oyamada et al., 1998). Contrary, others noted that V_m oscillations are TTX-resistant in (most) LC neurons of slices from juvenile rats (Christie et al., 1989) or mice (Sanchez-Padilla et al., 2014). The fact that TTX did not attenuate the CNQX depolarization indicates that accelerated spiking in CNQX does not cause neurotransmitter/modulator release which might potentially contribute to this response (Singewald and Phillipu, 1998; Schwarz and Luo, 2015). The observation that CNQX raised Ca_i in all neurons within the same optical plane indicates that the agent causes a depolarization of similar amplitude in the entire network. However, this does not mean that all LC neurons respond directly to the drug as they are coupled by gap junctions which act as a 'low-pass filter' (Christie et al., 1989; Ishimatsu and Williams, 1996; Christie, 1997). LC neurons do not comprise a homogeneous class of brain cells. For example, ventrally-located adult rat LC neurons with shorter spikes and smaller afterhyperpolarizations than LC core neurons act as a 'pontospinal- projecting module' (Li et al., 2016). Moreover, dorsomedially located small and densely packed GABAergic neurons in juvenile mice show faster spiking with enhanced adaptation (Jin et al., 2016). Finally, topographically distinct LC modules exist also regarding both afferent synaptic inputs and efferent projections (Schwarz and Luo, 2015) and their in vivo activity (Totah et al., 2018). Consequently, future studies may determine whether a TARP-AMPAR complex is functional in all (neonatal) LC neurons or rather only in a cluster that transmits TARP enhanced activity via the gap junction-coupling to neighboring cells. In any case, a sustained activity burst from afferent glutamatergic neurons, particularly in the nucleus paragigantocellularis, the lateral habenula or prefrontal cortex (Herkenham and Nauta, 1979; Aston-Jones et al., 1986; Jodo and Aston-Jones, 1997; Singewald

and Phillipu, 1998) may depolarize these neurons more effectively than those lacking that TARP-AMPAR complex. But, the outcome may be similar as the additional excitation plus the resulting Ca_i rise can potentially spread via the gap junctions throughout the nucleus. Contrary to the uniform CNQX-evoked neuronal Ca_i rises, there was no effect on neighboring astrocytes. This is somehow surprising as LC neurons and astrocytes are gap junction-coupled as evidenced by their synchronous spontaneous V_m oscillations and dye diffusion between them (Alvarez-Maubecin et al., 2000).

Our finding of an excitatory neuronal CNQX action is in line with results from previous slice studies. Early reports showed that both excitatory and inhibitory neurons are depolarized by CNQX and (mostly) DNQX, but not NBQX (McBain et al., 1992; Brickley et al., 2001; Maccaferri and Dingledine, 2002; Hashimoto et al., 2004). The authors noted that the effect indicates a novel type of excitatory action of these quinoxalinedione-type iGluR antagonists. In more recent work on neurons in slices or after dissociation, it was hypothesized (Lee et al., 2010) or proven (Menuz et al., 2007; Rigby et al., 2015; Sullivan et al., 2017) that CNQX activates a TARP-AMPAR complex. Since their discovery a decade ago, TARP-AMPAR complex structures and functions have been analyzed thoroughly, often in expression systems or genetically-engineered (e.g. 'stargazer') mice as reviewed comprehensively (Jackson and Nicoll, 2011; Greger et al., 2017; Maher et al., 2017). This work also established that TARP-AMPAR complex activation by the 'partial agonist' CNQX is prevented by non-competitive antagonists (including 'GYKI'-type agents) which, by themselves, exert no partial agonist action on this structure (Brickley et al., 2001; Menuz et al., 2007). Accordingly, we found that preincubation with GYKI in TTX blocked both the CNQX-evoked depolarization plus Ca_i rise and reversed its stimulatory action in control solution. Based on the

above arguments, our results strongly suggest that the excitatory CNQX action on the LC network is due to activation of a TARP-AMPAR complex.

4.5.3. Functional TARP role

Regarding possible functions of the AMPAR-TARP complex, augmentation of a glutamate-mediated Ca_i rise might regulate the excitability of LC neurons which seem to be very sensitive to this pivotal second-messenger and vice versa. This assumption is based on our finding that nifedipine (in TTX) abolished the likely modest somatic CNQX-evoked Ca_i rise indicating that L-type voltage-activated Ca^{2+} channels are activated by the ~5 mV depolarization from a resting V_m of about −50 mV. Likely, these channels are also responsible for the TTX-sensitive spike-related tonic increase in Ca_i baseline also seen, for example, in dorsal vagal neurons that spike spontaneously at a similar rate (Kulik et al., 2002). As one explanation for the latter findings, these, and possibly also other voltage-activated Ca^{2+} channel subtypes, may interact closely with SK-type Ca^{2+}-activated K^+ channels in the neonatal rat LC. In fact, in adult rats in vivo (Aghajanian et al., 1983) and slices (Andrade and Aghajanian, 1984), the number of current-evoked spikes correlates with the duration of a pronounced hyperpolarization that is attenuated by increased cellular Ca^{2+} buffering. Moreover, the rate of spontaneous spiking in LC neurons of adult mouse slices is regulated by cooperation of L- and T-type Ca^{2+} channels with SK2 channels (Matschke et al., 2015, 2018). If this is the case also in the neonatal rat LC, even the modest TARP-dependent depolarization, that might though be more pronounced in the dendrites (see above), may serve to fine-tune network activity while an excessive increase in such activity may be a crucial factor in neurodegenerative diseases. In that regard, findings from combined whole-cell-recording and Ca_i imaging in LC neurons of juvenile mouse slices indicate that activity-related L-type channel-

mediated Ca^{2+} entry and resulting mitochondrial stress may contribute to the etiology of Parkinson's or Alzheimer's disease (Sanchez-Padilla et al., 2014).

Regarding physiological TARP roles, the neural network in the inferior olive shares properties with that in the LC, including subthreshold V_m oscillations that are synchronized by gap junction-coupling (Placantonakis and Welsh, 2001; Devor and Yarom, 2002). A more recent modeling study on the inferior olive network concluded that 'subthreshold oscillations of the individual neurons and the electrical gap junctions make this system a powerful encoder and generator of spatiotemporal patterns with different, but coordinated oscillatory rhythms' (Latorre et al., 2013). Similarly, recent findings from our lab (Rancic et al., 2018) and other groups, both in vivo and in vitro, indicate that the LC transforms its activity pattern under the influence of (glutamatergic) inputs or neuromodulators like noradrenaline, cocaine or opioids (Zhu and Zhou, 2005; Chandley and Ordway, 2012; Safaai et al., 2015; Totah et al., 2018). In addition to our previous observation that opioids and high K^+ transform the LFP pattern (Rancic et al., 2018), we found here that TARP makes the rhythm more regular while, at the same time, more than doubling its output population burst rate. These dynamic properties may serve to fine-tune the LC control of multiple brain circuits and thus of behaviors including arousal, sleep-wake cycle, breathing, memory, pain sensation, anxiety and opioid (withdrawal) effects (Foote et al., 1983; Berridge and Waterhouse, 2003). Consequently, regarding various diseases in these systems, TARP within the LC might be a potent target to improve drug efficacy while mitigating adverse effects (Jackson and Nicoll, 2011; Maher et al., 2017).

Tab. 4-1

Effect of bath-application of CNQX (25 µM) on membrane potential (V_m) in locus coeruleus (LC) neurons of newborn rat brain slices. CNQX was either applied in drug-free superfusate (control) or after preincubation in TTX (1 µM) and/or GYKI (25 µM). Reproduced with permission from Rawal et al. (2019).

V_m (mV)			
Control	-45.8 ± 3.2 (n= 7)	-46.4 ± 3.5 (n= 5)	-44.5 ± 4.6 (n= 6)
TTX		-46.6 ± 3.9 (*P*= 0.37, n= 5)	
CNQX	-42.4 ± 3.7 (*P*< 0.001, n= 7) ΔV_m = 3.1 ± 0.9		
TTX + CNQX		-40.0 ± 4.5 (*P*< 0.001, n= 5) ΔV_m = 6.6 ± 1.3	
TTX + GYKI			-44.8 ± 5.1 (*P*= 0.17, n= 6)
TTX + GYKI + CNQX			-44.6 ± 5.1 (*P*= 0.36, n= 6)

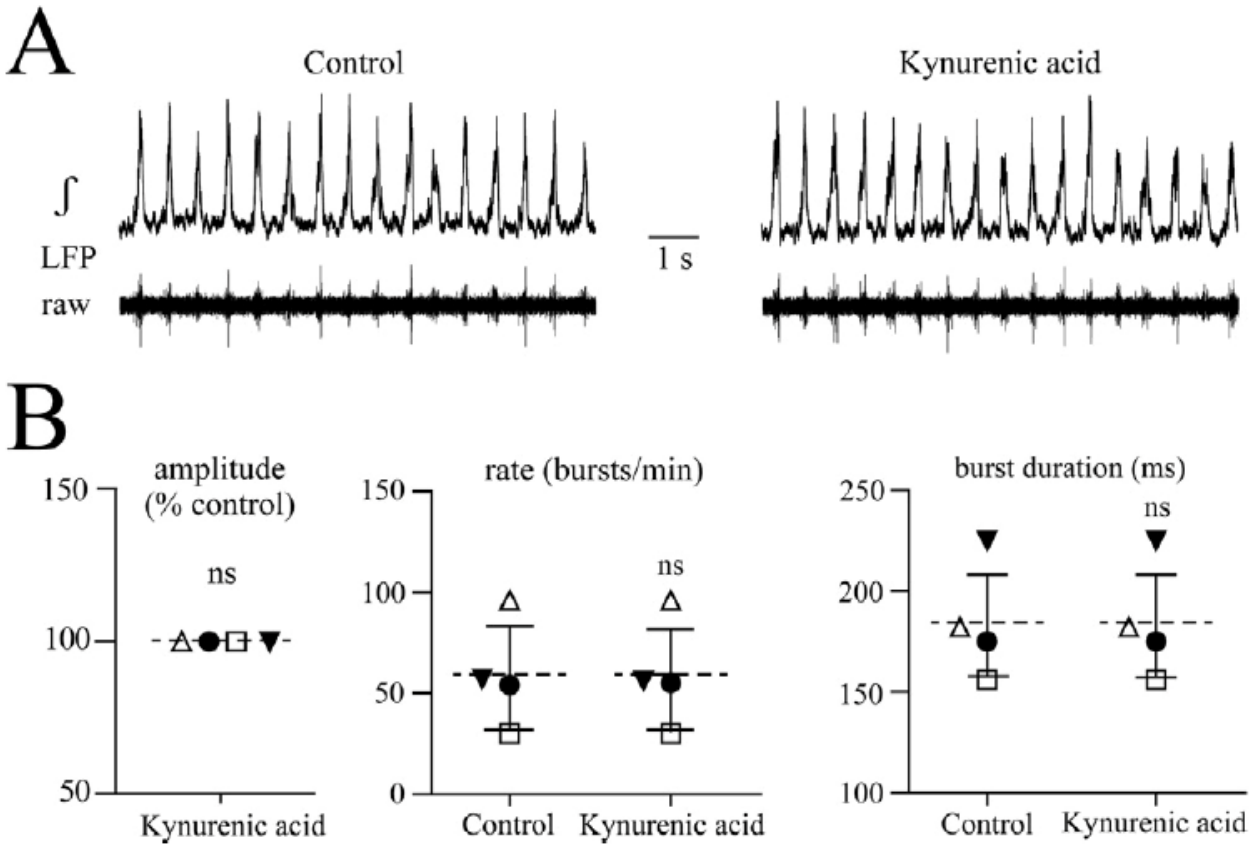

Fig. 4-1. Lack of ionotropic glutamate receptor (iGluR) involvement in neonatal locus coeruleus (LC) neural network bursting. A, **B**, extracellular local field potential (LFP) recording was done from the surface of a newborn rat brain slice in the LC neuron soma area, **A**, rhythmic crescendo-decrescendo-shaped LC neuron population bursting occurred at ~1 Hz as particularly evident in the integrated '∫' trace vs. the differentially amplified and band-pass filtered 'raw' signal. Bath-application of 2.5 mM of the broad-spectrum competitive iGluR blocker kynurenic acid for 5 min did neither affect LFP rate, single burst duration nor amplitude as quantified for 4 slices in **B**. Lines indicate means (broken) ± SD (solid), significance was determined with paired two tailed t-test (ns, non-significant, $P > 0.05$). Reproduced with permission from Rawal et al. (2019).

Fig. 4-2

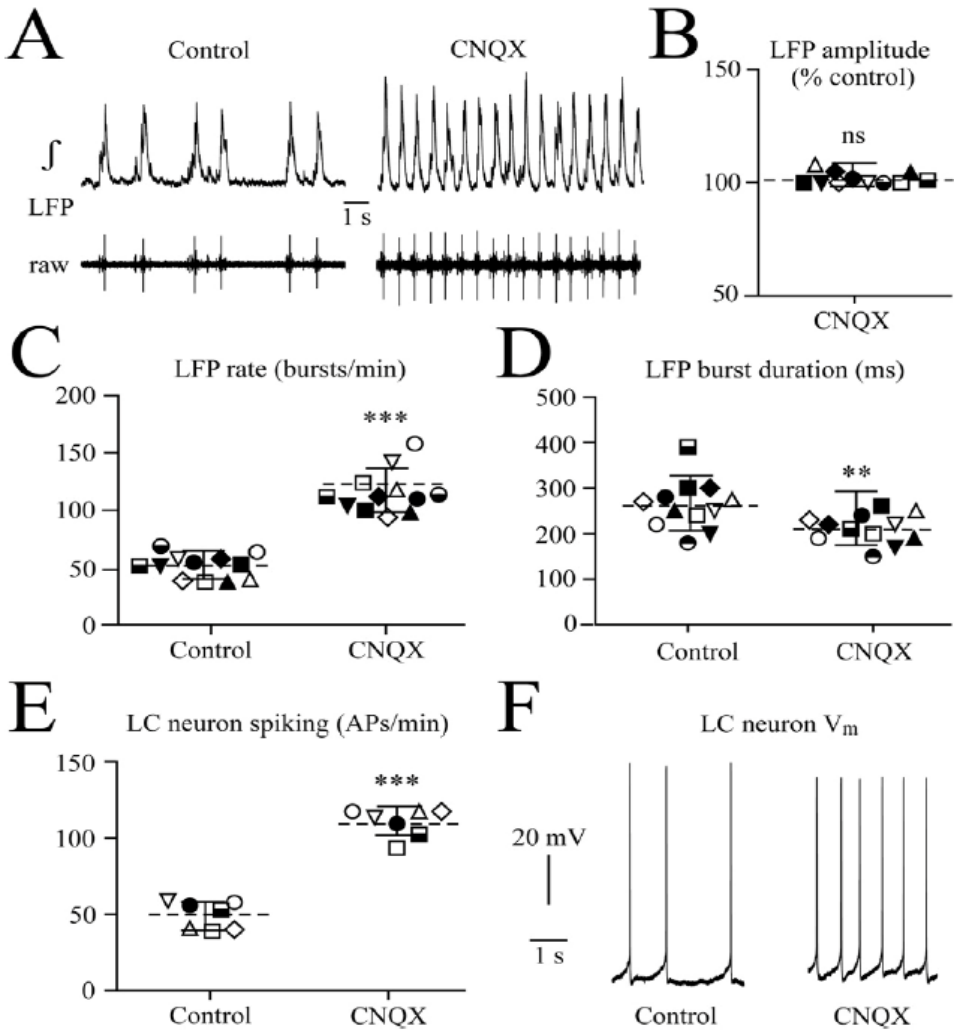

Fig. 4-2. Accelerating effect of the 'classical' competitive 'non-NMDA'-type iGluR antagonist 6-cyano-7-nitroquinoxaline-2, 3-dione (CNQX) on LFP and neuronal discharge. A, LFP rate more than doubled during 5 min bath-application of 25 µM CNQX, a blocker of the α-amino-3-hydroxy-5-methyl-4- isoxazole propionic acid (AMPA)/Kainate iGluR subtype. **B-D,** in 12 slices CNQX did not change single burst amplitude **(B)**, but accelerated LFP bursting (2.24 ± 0.47 -fold) **(C)** and decreased burst duration **(D)**. **E**, recording membrane potential (V_m) in 7 LC neurons simultaneously with LFP in 7 of the above slices (indicated by identical symbols) revealed a 2.29 ± 0.43 -fold acceleration of the rate of LFP-associated single Na^+ action potentials ('spikes') as exemplified in the traces on the right **(F)**. Significance was determined with paired two-tailed t-test (ns, non-significant, *P< 0.05, **P< 0.01, ***P< 0.001). Reproduced with permission from Rawal et al. (2019).

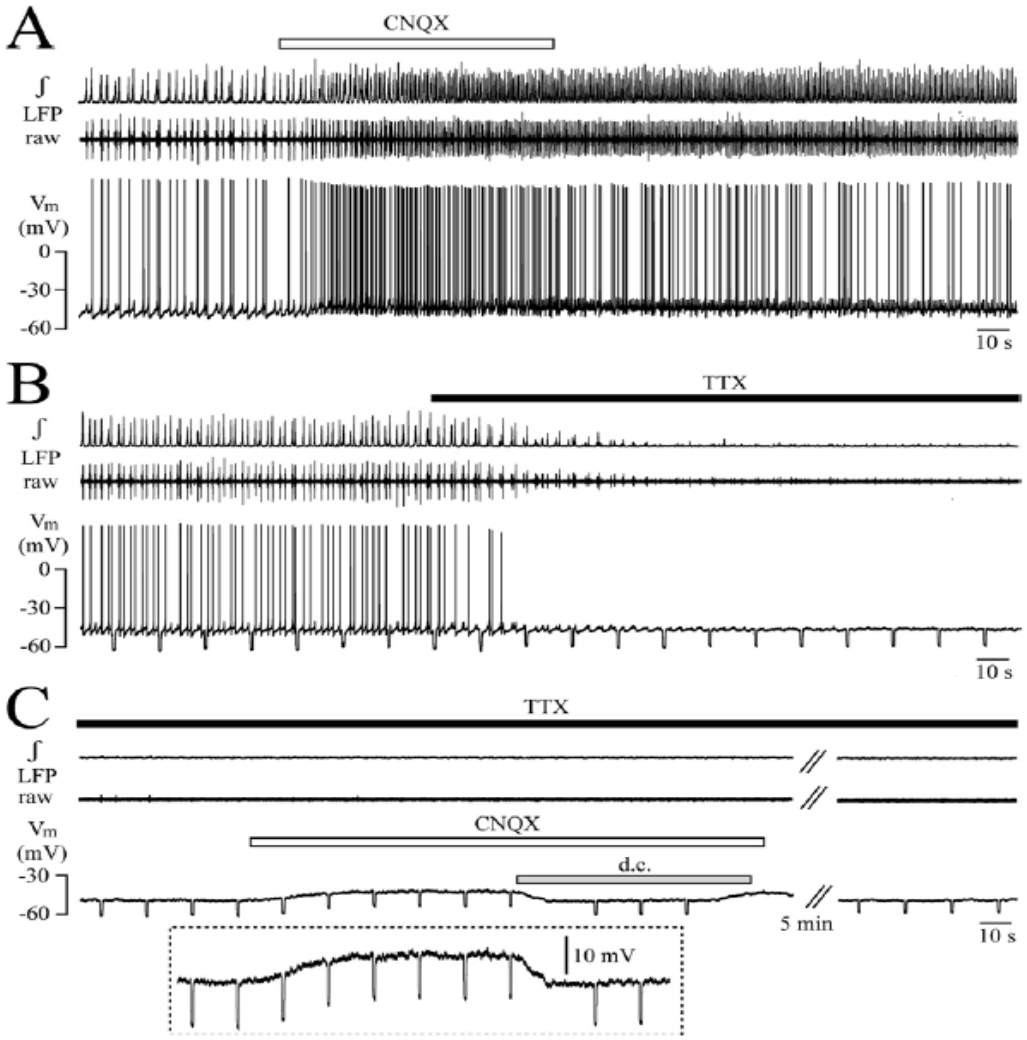

Fig. 4-3. Association of stimulatory CNQX effect with tetrodotoxin (TTX) -resistant depolarization. A, the continuous recording shows that acceleration of both LFP and cellular spiking by CNQX is accompanied by a modest depolarization. **B**, shows in the same neuron, after 20 min of CNQX washout, that 1 µM of the voltage-activated Na^+ channel blocker TTX abolishes the LFP and spiking plus subthreshold V_m oscillations within <1 min with no change in resting V_m or input resistance measured by injection of hyperpolarizing d.c. current pulses (-60 pA, 500 ms duration) at a regular interval. **C**, the continuation of the recording in **B** shows that CNQX in TTX depolarizes V_m by 8 mV (see magnified inset in dotted box) with no change in resistance (also when V_m was brought back to its resting value by d.c. current injection). The interruption in the traces indicates a 5 min time period during which V_m recovered from CNQX in TTX. Reproduced with permission from Rawal et al. (2019).

Fig. 4-4

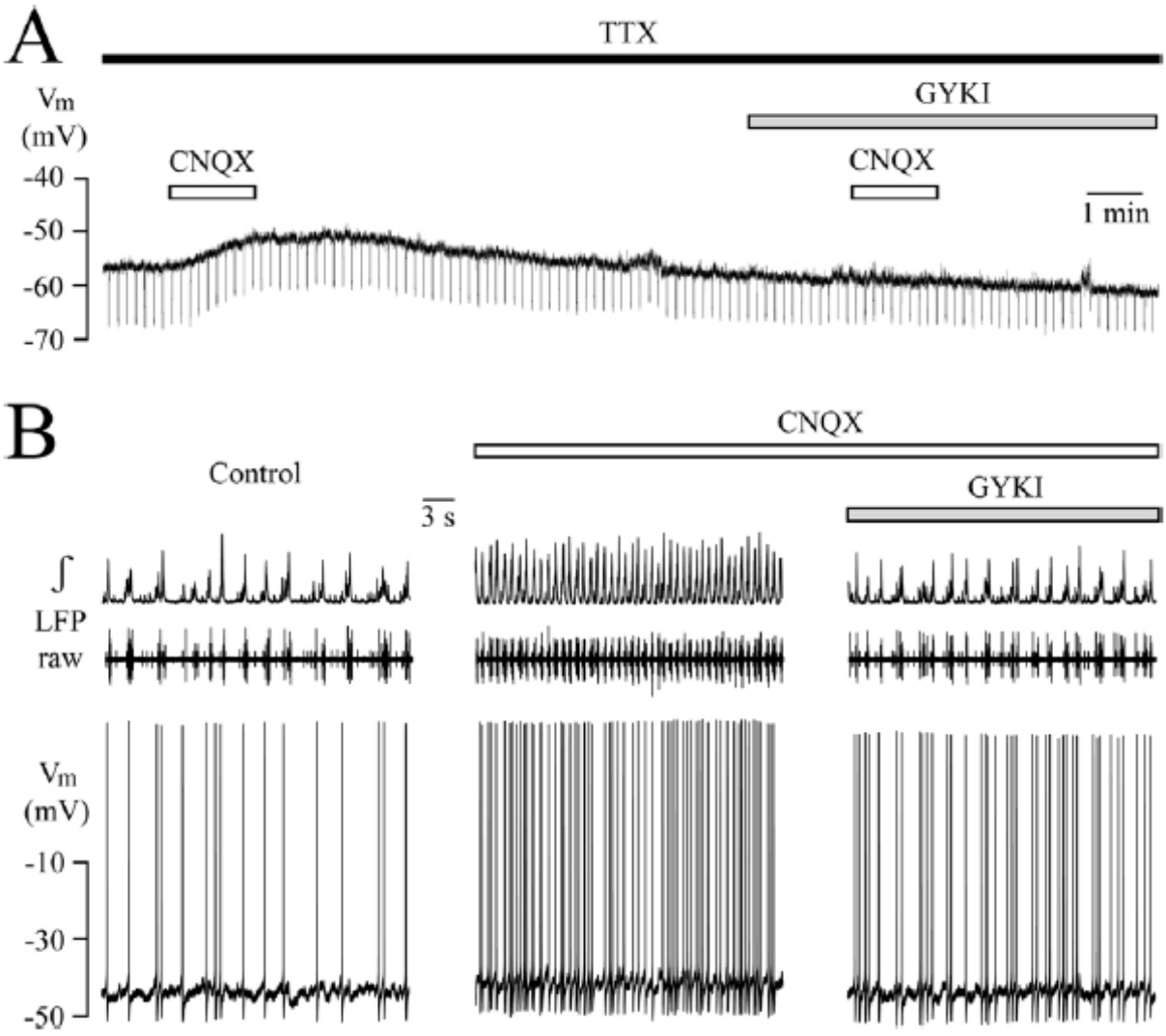

Fig. 4-4. Blockade of CNQX depolarization and related stimulatory effects by the non-competitive AMPA/Kainate-type iGluR antagonist GYKI. A, in presence of TTX, CNQX depolarized V_m with unchanged input resistance. Bath-application of 25 μM GYKI blocked the CNQX-evoked depolarization. **B**, in a different neuron all stimulatory CNQX effects were reversed within 2 min after addition of 25 μM GYKI to the CNQX-containing solution. Reproduced with permission from Rawal et al. (2019).

Fig. 4-5

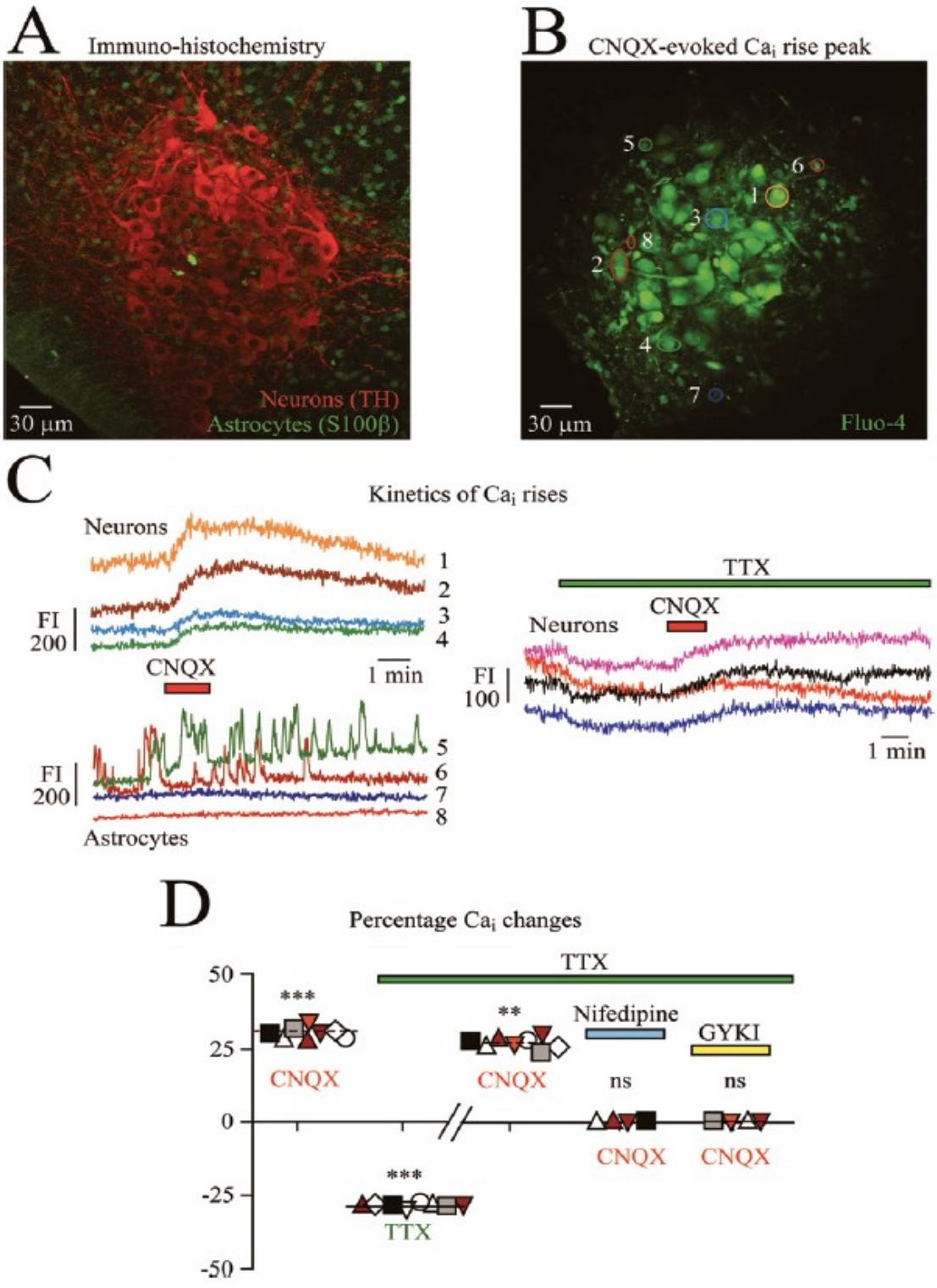
A
Immuno-histochemistry
Neurons (TH)
Astrocytes (S100β)
30 μm
B
CNQX-evoked Ca$_i$ rise peak
1
2
3
4
5
6
7
8
30 μm
Fluo-4
C
Kinetics of Ca$_i$ rises
Neurons
FI
200
CNQX
1 min
Astrocytes
TTX
CNQX
Neurons
FI
100
1 min
D
Percentage Ca$_i$ changes
TTX
50
25
0
-25
-50
***
**
Nifedipine
GYKI
CNQX
CNQX
ns
ns
CNQX
CNQX
***
TTX

Fig. 4-5. CNQX-evoked increase of the free cytosolic Ca^{2+} concentration (Ca_i) in LC neurons, but not astrocytes. A, exemplifies in a chemically fixed slice with double immuno-histochemical staining that the LC comprises ~90 % of densely packed tyrosine hydroxylase (TH) -positive neurons with a >20 µm soma size while the remaining smaller cells are glial cells, mostly S100β-positive astrocytes. **B**, is a fluorescence image (at the peak of the CNQX response) of LC cells in a living slice bulk-loaded via focal pressure-injection with the membrane-permeant green fluorescent Ca^{2+} dye Fluo-4-AM. The numbered colored shapes are regions of interest (ROIs) drawn offline via Fluoview software around 4 neurons (# 1–4) and 4 presumptive astrocytes (# 5–8). **C**, shows in the left panels that CNQX-evoked Ca_i rises, indicated by an increase in Fluo-4 fluorescence intensity (FI), are similar in all 4 ROI-identified neurons in **B** whereas the 4 astrocytes labeled in **B** didn't respond, but 2 cells showed spontaneous Ca_i rises. The traces in the right panels show for 4 neurons of a different slice that the CNQX-evoked Ca_i rise persists after preincubation in TTX which decreases Ca_i baseline. **D**, shows for 174 neurons in 8 slices (including the ones in **B** and **C**) the percentage change in FI in response to CNQX (left group of symbols), TTX in control solution (2nd group from left), CNQX in TTX with baseline value in TTX set to 0 (middle group) and for 4 of the 8 slices each during CNQX in TTX plus either nifedipine (88 neurons, 2nd group from right) or GYKI (86 neurons, right group). Each symbol/color in **D** represents the same slice. Significance was determined with one-way ANOVA with Dunnett's test ($F(1, 5) = 13.91$) (ns, non-significant, $^{**}P < 0.01$, $^{***}P < 0.001$). Reproduced with permission from Rawal et al. (2019).

Fig. 4-6

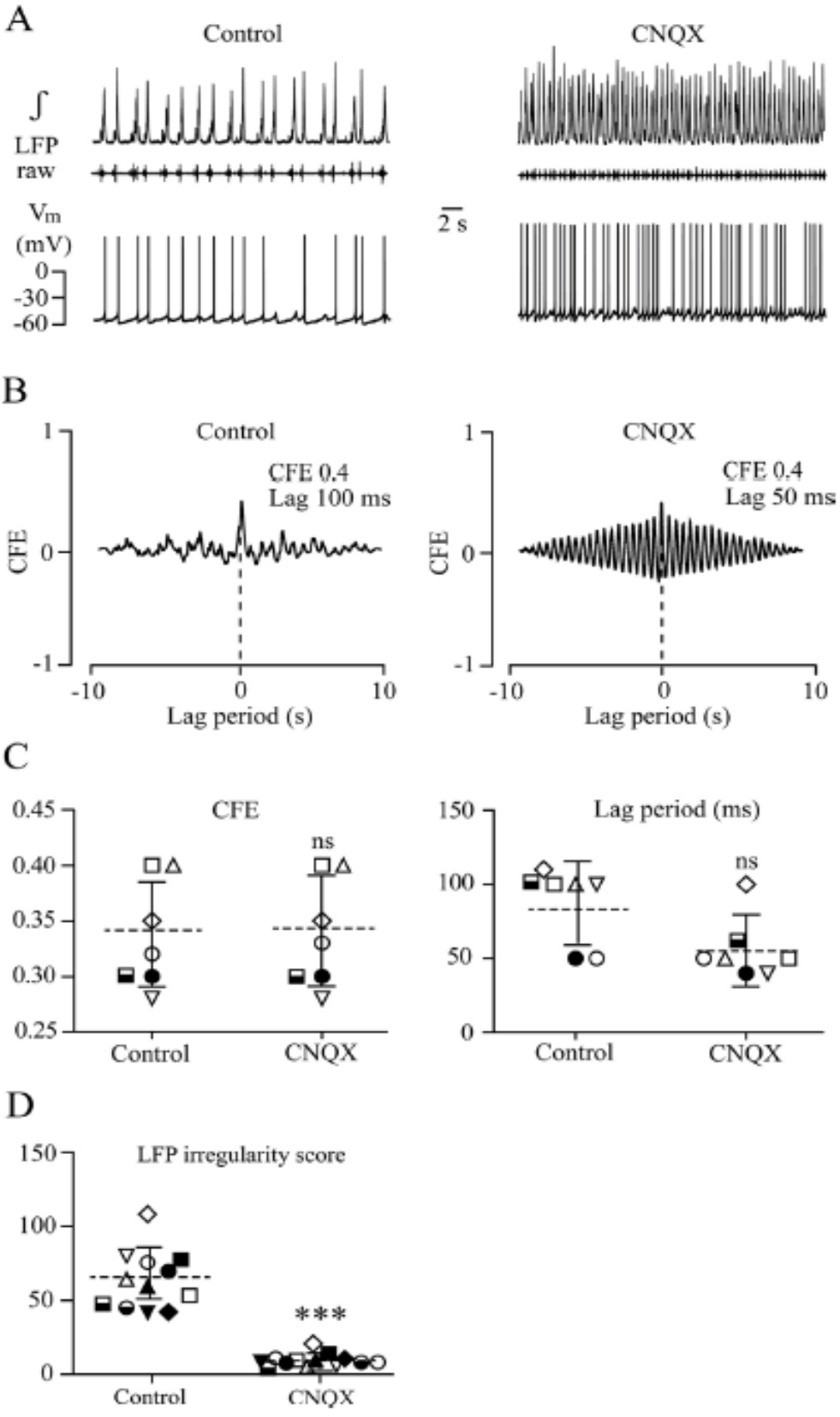
A
Control
CNQX
∫
LFP
raw
Vm
(mV)
0
-30
-60
2 s
B
Control
CFE 0.4
Lag 100 ms
CNQX
CFE 0.4
Lag 50 ms
CFE
1
0
-1
-10
0
10
Lag period (s)
C
CFE
ns
0.45
0.40
0.35
0.30
0.25
Control
CNQX
Lag period (ms)
150
100
50
0
D
LFP irregularity score
***

Fig. 4-6. CNQX does not increase LC network synchronicity, but makes LFP rhythm more regular. A, excerpt at higher time resolution from the recording in **Fig. 4-3A** showing in the right panel at steady-state in CNQX acceleration of LFP rhythm and cellular spiking accompanied by V_m depolarization. **B**, cross-correlogram between neuronal spikes and LFP during control (left panel) and CNQX (right panel) shows no change in the correlation function estimate (CFE) value, indicating a lack of increased synchronicity, but a decrease of the time lag. **C**, scatter plots from the neurons shown in **Fig. 4-2E**, **F** indicate no CNQX effect on synchronicity (CFE value with no unit; Lag period in ms). **D**, scatter plot for the LFP indicates a decrease in the irregularity score (no unit) after CNQX application in the 12 slices used for the above analyses **(Fig. 4-2A–D)**. Significance was determined with paired two-tailed t-test (ns, non-significant, ***$P<$ 0.001). Reproduced with permission from Rawal et al. (2019)

CHAPTER 5

Locus coeruleus network bursting in newborn rat brain slices is accelerated at increased regularity by AMPA and kainate whereas quisqualate makes rhythm irregular

Bijal Rawal and Klaus Ballanyi

Department of Physiology, Faculty of Medicine & Dentistry, 750 MSB, University of Alberta, Edmonton, T6G2H7 Canada

Author Contributions: BR and KB contributed to the conception, design, interpretation and writing of the study. BR did all data acquisition and analysis.

5.1. Abstract

Locus coeruleus (LC) neurons are controled by glutamatergic inputs. Here, we studied in neonatal rat brain slices effects of the ionotropic glutamate receptor (iGluR) agonists AMPA, kainate and quisqualate on phase-locked non-synchronous LC neuron spiking at ~1Hz summating to ~0.2s-lasting bursts. At 0.25/0.5µM, AMPA merged bursts into 4.5/5-fold faster and 32/45% shorter oscillatory events. Several minutes into 0.5µM and earlier into 1µM, oscillation amplitude declined and tonic activity appeared before rhythm stopped. Kainate had similar effects starting at 0.25µM whereas 0.5/2.5µM caused 2.7/5.8-fold faster and 26/40% shorter oscillations. At 5/10µM, initial oscillations progressively declined during tonic activity before rhythm stopped. During stable oscillations, that were more regular than control LFP, 0.25/2.5µM AMPA/kainate depolarized neurons by 4.0/4.2mV, accelerated their spiking 3.0/5.3-fold and shortened spike jitter to 64/42% of control, respectively. Quisqualate, at 0.1-0.25µM, made bursts more irregular with 1.6-fold increased duration and decreased their amplitude with eventual occurrence of tonic discharge while neurons depolarized by 3.4mV with 1.8-fold accelerated spiking. At 0.5/2.5µM quisqualate, the latter effects on LFP were initially more pronounced before rhythm stopped. LFP pattern transformations by all agonists were reversed by the unspecific iGluR antagonist kynurenic acid (0.5-2.5mM). Our findings show that AMPA/kainate-evoked neuronal spike acceleration with enhanced phase-lock causes faster and more regular LC network bursting whereas less accelerated spiking accompanies more irregular network bursting during quisqualate. This is the first demonstration that iGluR activation by AMPA and kainate vs. quisqualate has different effects on neural network activity. The potential functional impact for LC function is discussed.

5.2. Introduction

Multiple brain functions including arousal, sleep-wake cycle, memory, anxiety and opioid (withdrawal) effects are under afferent noradrenergic control by the locus coeruleus (LC) in the dorsal pons (Berridge and Waterhouse, 2003; Aston-Jones and Cohen, 2005). In vivo, LC neurons show spontaneous pacemaker-like ('tonic') single action potential 'spiking' or they discharge phasically during synaptic inputs involving various neurotransmitters including glutamate (Jodo and Aston-Jones, 1997; Singewald and Phillipu, 1998; Berridge and Waterhouse, 2003; Schwarz and Luo, 2015). The important functional role of afferent glutamatergic control of the LC is indicated by notable behavioral effects of systemic or focal LC application of ionotropic glutamate receptor (iGluR) modulators (Chandley and Ordway, 2012; Chandley et al., 2014). For example, iGluR activation is involved in transformation of tonic LC neuron spiking into oscillatory ('burst') discharge during systemic morphine application in adult rats (Zhu and Zhou, 2005). As stated in the latter report, dose-response studies are needed to elucidate the contribution of iGluR subtypes to this transformation. Regarding iGluR subtypes, fast excitatory neurotransmission is typically mediated by α-amino-3-hydroxy-5-methyl-4-isoxazole propionic acid (AMPA) binding to a receptor (AMPAR) that is also activated by kainate (KA) or quisqualate (QUI) (Traynelis et al., 2010). The other iGluR subtype is activated by NMDA and this NMDR plays important roles in modulating AMPAR-mediated synaptic responses, e.g. in memory processing (Traynelis et al., 2010). Electrophysiological studies on brain slices have established that both iGluR subtypes are functional in LC neurons as the above agonists accelerate their spontaneous spiking (Olpe et al., 1989; Kogan and Aghajanian, 1995; Zamalloa et al., 2009).

The ability of opioids to transform LC network spiking into bursting is preserved in brain slices that are devoid of intact glutamatergic innervation, e.g. from the nucleus paragigantocellularis, the

lateral habenula and the prefrontal cortex (Herkenham and Nauta, 1979; Aston-Jones et al., 1986; Jodo and Aston-Jones, 1997; Singewald and Phillipu, 1998). This view is based on findings in our previous study on newborn rat slices establishing that non-synchronous, yet phase-locked LC neuron spiking at ~1 Hz summates to ~0.2 s-lasting bursts representing a rhythmic local field potential (LFP) (Rancic et al., 2018). Regarding LC discharge pattern transformation, this report revealed that the crescendo-decrescendo-shaped ('bell-shaped') LFP pattern changes to rhythmic, several seconds-lasting multipeak bursts during recovery from opioid inhibition and also during enhanced network excitation caused by raising extracellular K^+. We hypothesized in that study for the latter effect that high K^+ may cause glutamate release into the LC which then acts on iGluR to transform the LFP pattern. In fact, our recent study on the LC in neonatal rat slices indicated that activation of auxiliary transmembrane AMPAR regulatory proteins (TARP) by the partial agonist 6-cyano-7-nitroquinoxaline-2,3-dione (CNQX) can transform the LFP pattern, though in this case into fast oscillations (Rawal et al., 2019). Here, we firstly analyzed with dose-response relationships how exactly iGluR activation by AMPA, KA or QUI may transform the LFP pattern and at which high dose coordinated network bursting collapses, likely due to inactivation blockade of single neuron spiking. We then combined LFP assessment with whole-cell membrane potential (V_m) recording at intermediate agonist doses to analyze a potential change in the phase-lock of cellular spiking as indication of a change in the extent of network synchronization.

5.3. Materials and methods

(see **Chapter 2)**

5.4. Results

Initial analysis of LFP properties and dose-dependent LFP pattern changes during NMDA or glutamate application was followed by cellular analyses with combined LFP and V_m recording.

5.4.1. AMPA-evoked LFP oscillations

Firstly, effects of 5 min bath-applied AMPA were studied on the suction electrode-recorded LFP. AMPA effects on a single slice are exemplified in **Fig. 5-1** while statistical analysis in 5 slices is presented in **Fig. 5-2**. As particularly evident from the integrated traces, AMPA had no effect at 0.05 µM whereas 0.1 µM accelerated LFP rate about 1.5-fold **(Fig. 5-1A)**. LFP acceleration was notably more pronounced at 0.25 µM and bell-shaped single bursts merged into sinusoidally-shaped events showing with a period time of 2-3 s rhythmic amplitude fluctuations by 10-40 % **(Fig. 5-1B)**. Similar effects were seen at 0.5 µM AMPA, but burst amplitude decreased progressively, even into the early phase of washout **(Fig. 5-1C$_1$)**. The LFP amplitude fluctuations during AMPA-evoked oscillations were due to the occurrence of spontaneous non-phase-locked 'tonic' discharge that was evident in the raw traces and could increase the baseline of the integrated LFP trace **(Fig. 5-1C$_2$,D)**. At 1 µM, AMPA evoked the same oscillations and amplitude fluctuations, but rhythm was blocked at the end of application **(Fig. 5-1D)**.

The summarized findings from 6 slices in **Fig. 5-2** show that AMPA accelerated LFP rate from 53.6 ± 20.9 bursts/min (i.e. 0.89 ± 0.34 Hz) in control to 225 ± 54.2 bursts/min (i.e. 4.5 ± 1.6 -fold) at 0.25 µM and to 305 ± 80.7 bursts/min (i.e. 5.1 ± 0.8 -fold) at 0.5 µM **(Fig. 5-2A$_1$)**. Correspondingly, single event duration was shortened from 157 ± 16.0 ms in control to 106 ± 22.8 ms (i.e. 68.2 ± 17.6 % of control) at 0.25 µM and to 81.8 ± 18.0 ms (i.e. 54.6 ± 16.6 % of control)

at 0.5 µM **(Fig. 5-2A$_2$)**. Single event amplitude decreased to 73.0 ± 4.0 % of control at 0.25 µM and to 58.0 ± 13.0 % of control at 0.25 µM **(Fig. 5-2A$_3$)**. The inset in **Fig. 5-2A$_3$** shows that the bell-shape of the LFP burst was retained during AMPA application. Effects of 1 µM AMPA were not quantified as rhythm was depressed too quickly. Within 11.0 ± 4.0 min after start of washout, the LFP recovered after depression or blockade which occurred in 4 slices at 1.0 µM. At intermediate concentrations not causing a major depression or blockade of rhythm during application, no 'post-agonist depression' occurred as seen in rat slices with extracellular spike analysis (Kogan and Aghajanian, 1995; Zamalloa et al., 2009).

The original recordings indicated that 0.25 and 0.5 µM AMPA made LFP rhythm more regular. As quantified in the above 6 slices for 0.25 µM, the irregularity score value decreased from 60.1 ± 9.7 in control to 9.2 ± 5.2 in AMPA **(Fig. 5-2A$_3$)** confirming that LFP bursting became more regular.

5.4.2. KA-evoked LFP oscillations

Next, effects of 5 min bath-applied KA were studied. Findings on a single slice are exemplified in **Fig. 5-3** while statistical analysis in 5 slices is shown in **Fig. 5-4**. KA effects were very similar to those of AMPA, except for a shift to slightly higher doses. Specifically, 0.05 and 0.1 µM KA had no effect while 0.25 µM accelerated the still separate LFP bursts which merged at 0.5 µM **(Fig. 5-3A,B)**. At 1 µM KA, effects were similar to 0.5 µM with appearance of amplitude fluctuations indicating rhythmically occurring tonic discharge. At 2.5 µM similar effects were seen plus the integrated signal trace baseline increased slightly indicating tonic discharge **(Fig. 5-3C)**. At 5 µM, KA caused initially prominent LFP oscillations with amplitude fluctuations and an integrated

signal baseline increase. Subsequently, oscillations were then progressively depressed until rhythm was blocked at 4.5 min of application and bursting recovered after 15 min of washout **(Fig. 5-3D)**.

The summarized findings from 5 slices in **Fig. 5-4** show that KA accelerated LFP rate from 50.7 ± 12.7 bursts/min (i.e. 0.84 ± 0.21 Hz) in control to 134 ± 32.4 bursts/min (i.e. 2.7 ± 0.6 -fold) at 0.5 µM, to 181 ± 36.3 bursts/min (i.e. 3.6 ± 0.6 -fold) at 1 µM and to 282 ± 88.8 bursts/min (i.e. 5.8 ± 2.5 -fold) at 2.5 µM **(Fig. 5-4A$_1$)**. Correspondingly, single event duration was shortened from 186 ± 48.8 ms in control to 133 ± 18.9 ms (i.e. 74.2 ± 16.3 % of control) at 0.5 µM, to 127 ± 15.4 ms (i.e. 70.9 ± 13.5 % of control) at 1.0 µM and 107 ± 24.8 ms (i.e. 60.2 ± 17.6 % of control) at 2.5 µM **(Fig. 5-4A$_2$)**. Single event amplitude decreased only at 1.0 µM (77.9 ± 11.8 % of control) and 2.5 µM (66.3 ± 14.2 % of control) **(Fig. 5-4A$_3$)**. The inset in **Fig. 5-4A$_1$** shows that the bell-shape of the LFP burst was retained during KA. Effects of 5 µM AMPA were not quantified as rhythm was depressed and then blocked too quickly in all 5 slices. Within 4.5 ± 0.9 min after start of washout, the LFP recovered after such blockade. At intermediate concentrations not causing a major depression or blockade of rhythm during application, no post-agonist depression occurred. As analyzed in all 5 slices at 2.5µM, KA decreased the irregularity score value from 56.4 ± 25.6 in control to 7.8 ± 3.6 thus making LFP bursting more regular **(Fig. 5-4B)**.

5.4.3. QUI-evoked LFP irregularity

The above results showed that both AMPA and KA, the most commonly used AMPAR agonists cause very similar fast oscillations and increase the regularity of LC network bursting. While QUI is a further agonist for this iGluR subtype, it can potentially also activate metabotropic glutamate receptors (Traynelis et al., 2010).

Indeed, QUI effects on LFP differed notably from those induced by AMPA and KA as exemplifed for 1 slice in **Fig. 5-5** and analyzed for 7 slices in **Fig. 5-6**. Specifically, 0.05 µM had no effect whereas 0.1 µM decreased burst amplitude and increased their duration slightly **(Fig. 5-5A)** with occasional appearance of (ramp-shaped) multipeak discharges **(Fig. 5-7)**. At 0.25 µM, LFP bursts decreased further in amplitude and became more frequent, but individual events could not be discriminated anymore **(Fig. 5-5B)**. At 0.5 µM, bursts became initially faster at similarly reduced amplitude before rhythm was blocked close to the end of application and rhythm recovered after 15 min **(Fig. 5-5C)**.

As quantified in 4 of 7 slices, 0.05 µM QUI had no effect on burst rate, duration or amplitude **(Fig. 5-6A$_{1-3}$)**. As analyzed in all 7 slices, 0.1 µM QUI did not change LFP rate (48.8 ± 17.5 bursts/min (i.e. 0.81 ± 0.29 Hz) in control vs. 56.3 ± 20.3 bursts/min in QUI) **(Fig. 5-6A$_1$)**, but increased burst duration from 241 ± 61.6 ms in control to 404 ± 138 ms (i.e. 1.6 ± 0.2 -fold **(Fig. 5-6A$_2$)** while its amplitude decreased to 75.0 ± 7.9 % of control **(Fig. 5-6A$_3$)**. The inset in **Fig. 5-6A$_3$** shows that the bell-shape of the LFP burst was changed during QUI. The fact that the irregularity score value was not changed in the 7 slices (43.7 ± 7.5 vs. 40.5 ± 6.9) **(Fig. 5-6C)** indicates that burst rate did not become more irregular at that dose. Effects of 0.25 µM QUI could not be quantified as rhythm became too irregular while 0.5-1 µM blocked the rhythm too quickly. Within 13.7 ± 10.9 min after start of washout, the LFP recovered after such blockade. At intermediate concentrations not causing a major depression or blockade of rhythm during application, no post-agonist depression occurred.

5.4.4. Receptor-specificity of agonist effects

As shown above, AMPA and KA evoked regular fast oscillations with shortened event duration whereas QUI made rhythm irregular. The latter effect might be due to a QUI action on metabotropic receptors. To test this, the unselective iGluR antagonist kynurenic acid was applied during QUI-evoked LFP transformation **(Fig. 5-5D)**. As studied in 3 slices, the effect was significant as kynurenic acid reversed both the QUI-evoked prolongation of the LFP burst **(Fig. 5-6A$_2$)** and the decrease of its amplitude **(Fig. 5-6A$_3$)**. Corresponding results were obtained with combined LFP and neuronal V_m recording. The example in **Fig. 5-7** shows that 0.1 µM QUI prolonged LFP bursts and reduced their amplitude while it slightly depolarized the neuron to increase its AP rate and the effects were reversed by kynurenic acid. In 3 neurons, 0.1 µM QUI depolarized V_m from -46.6 ± 1.5 mV by 3.3 ± 1.1 mV ($P< 0.05$) and showed a trend to increase AP rate from 53.6 ± 15.3 to 85.3 ± 29.4 spikes/min **(Fig. 5-6A$_4$)** whereas addition of kynurenic acid to the QUI-containing solution restored both V_m and AP rate to control values, i.e. -48.1 ± 1.0 mV ($P= 0.27$) and 42.6 ± 11.0 spikes/min ($P= 0.37$).

Correspondingly, kynurenic acid countered AMPA and KA effects. In 7 neurons, 0.25 µM AMPA depolarized V_m from -44.0 ± 2.3 mV by 4.0 ± 1.0 mV ($P< 0.01$) and increased AP rate from 56.1 ± 12.5 to 175.1 ± 68.0 spikes/min ($P< 0.01$). Kynurenic acid restored V_m from -41.2 ± 1.1 mV to -45.2 ± 1.2 mV and AP rate from 192.5 ± 82.2 to 50.2 ± 19.5 spikes/min as tested in 4 of these neurons **(Fig. 5-8)**. Similarly, 2.5 µM KA depolarized V_m of 7 neurons from -47.14 ± 2.1 by 4.5 ± 1.5 mV ($P< 0.01$) and increased AP rate from 63.57 ± 22.6 to 272.5 ± 78.8 spikes/min ($P< 0.01$) **(Fig. 5-9)**. Kynurenic acid restored V_m in 4 of these neurons from -42.25 ± 2.5 to -46.75 ± 2.6 mV and AP rate from 290 ± 87 to 85 ± 28 spikes/min (not shown). The correspondingly antagonizing kynurenic effect on LFP tested in 5 slices is exemplified in **Fig. 5-3D**.

5.4.5. Combined LFP and V_m analysis of AMPAR agonist effects on network synchronicity

Our recent study showed that the ~0.2 s-lasting LFP bursts comprise overlapping single spikes from individual LC neurons that are not synchronous, but rather locked to a particular phase of the population signal and show each a ±33 ms jitter (Rancic et al., 2018). The finding of a shortened burst duration by AMPA and KA indicates that the agents reduce single spike jitter and might thus increase network synchronicity while the opposite QUI effects suggest it decreases synchronicity further. To test this, firstly the effect of the agonists on AP jitter was determined. In 5 neurons during LFP pattern transformation by 0.25 µM AMPA, the jitter was reduced from ±89.3 ± 24.2 to ±61.4 ± 26.3 ms (i.e. 66.5 ± 12.0 % of control) **(Fig. 5-10A)**. Corresponding values for 2.5 µM KA were ±71.5 ± 34.5 vs. ±24.2 ± 11.1 ms (i.e. 37.9 ± 19.1 % of control) **(Fig. 5-10B)** whereas QUI increased jitter in 2 neurons from ±75.7 ± 18.0 to ±228 ± 45.2 ms (i.e. 302 ± 12.0 % of control, or 3.0 ± 0.1-fold) **(Fig. 5-10C)**. These results indicate that AMPA and KA increase phase-lock of LC network bursting whereas QUI has the opposite effect.

Finally, cross-correlation analysis was done by comparing the integrated LFP signal with intracellularly recorded spiking. In the above 7 neurons in which AMPA was tested, mean control values for CFE and lag time were, respectively, 0.31 ± 0.08 and 112.8 ± 28.1 ms **(Fig. 5-11A,D)**. Corresponding control values for the 7 neurons recorded during KA were, respectively, 0.36 ± 0.05 and 109.3 ± 21.6 ms **(Fig. 5-11B,D)**. For 2 neurons tested during QUI, control values were, respectively, 0.31 ± 0.09 and 105 ± 21.02 ms **(Fig. 5-11,D)**. It was not possible to determine for any of these neurons the CFE or lag time values during the agonist effect **(Fig. 5-11)**.

5.5. Discussion

It was found here that LFP rhythm in the neonatal rat LC transforms its burst pattern during AMPAR activation. Specifically, AMPA and KA cause bell-shaped bursts to merge into faster, more regular and shorter oscillations, the latter reflected by decreased cellular spike jitter. Contrary, QUI makes rhythm more irregular and, if still recognizable, smaller amplitude bursts have an increased duration due to enhanced spike jitter. All LFP pattern transformations were reversed by the non-selective iGluR blocker kynurenic acid. In summary, this is the first demonstration that the AMPAR agonist QUI has a different action on neural network bursting than the more commonly used AMPA and KA. Possible mechanisms and consequences for LC functions are discussed.

5.5.1. AMPAR-mediated effects on LFP

We showed previously that spontaneous LC neuron spiking is jittered, yet phase-locked to generate rhythmic ~0.2-lasting LFP bursts (Rancic et al., 2018). Here, we found that LFP bursts are bell-shaped in control and also during AMPAR stimulation indicating that spike jitter in the neurons generating this signal distributes equally around the LFP peak. In our above report, the LFP pattern changed to ~3 s-lasting multipeak plateaus upon increasing LC excitability with raised extracellular K^+ or during recovery from opioid inhibition (Rancic et al., 2018). Here, neither agonist transformed the LFP pattern to such prolonged bursting. Specifically, AMPA and KA merged separate LFP bursts into faster and shorter oscillatory events showing amplitude fluctuations that reflect increased tonic activity during the smaller amplitude phase. Contrary, low QUI doses caused smaller and prolonged LFP bursts. All changes were caused by AMPAR activation as they were countered by the unselective iGluR antagonist kynurenic acid. It is not clear why AMPA- and KA-evoked pattern transformation was opposite to that induced by QUI. Properties of AMPA-, KA- or

QUI-evoked currents differ mainly in their AMPAR affinity, amplitude or activation vs. desensitization characteristics (Traynelis et al., 2010; Reiner and Levitz, 2018). However, a recent study revealed different binding sites in the TARP-AMPAR complex for QUI vs. KA (Chen et al., 2017). It remains to be elucidated whether this might result in a basically different electrophysiological response to these agents in situ.

At high AMPA and KA doses, tonic LC network spiking was more pronounced as indicated by an increased integrated LFP trace baseline. A similar effect was seen during (enhanced seizure-like) rhythmic LFP discharge in the neonatal rat inspiratory center (Panaitescu et al., 2009, 2013) and the lumbar spinal locomotor network (Taccola et al., 2012). Spiking in single LC neurons of juvenile and adult rat slices persisted at increased rate at 10 µM AMPA, KA or QUI (Kogan and Aghajanian, 1995; Zamalloa et al., 2009) whereas here the LFP was abolished by 1 µM AMPA, 5 µM KA and 0.5 µM QUI. V_m recording at these doses is needed to determine if LC neurons under the present experimental conditions (or at that earlier developmental stage) are more sensitive to spike inactivation by the agents or network connectivity collapses already at lower doses. However, if the latter would be the case, tonic LFP discharge should have been observed here whereas all activities were blocked. As a further discrepancy with previous studies, no iGluR desensitization-related post-agonist depression occurred early during washout of the agents as detected previously with single spike recording (Kogan and Aghajanian, 1995; Zamalloa et al., 2009).

In summary, suction electrode-based LFP recording revealed here novel features of neonatal LC network organization as in our recent studies (Rancic et al., 2018; Rawal et al., 2019).

5.5.2. LC synchronicity analysis with combined LFP and neuronal V_m recording

AMPA- or KA-evoked LFP oscillations were faster and shorter than control bursts whereas QUI increased the duration of separate bursts if still present. However, the hypothesis that AMPA and KA enhance neonatal LC synchronicity, whereas QUI weakens it, was not substantiated by cross-correlation analysis of neuronal spiking and LFP although both agonists reduced intracellular spike jitter **(Fig. 5-11)**. As possible explanation, neonatal LC neurons are coupled via gap junctions. Specifically, in neonatal rat slices V_m recording in LC neuron pairs and use of the blocker carbenoxolone established that gap junctions synchronize intrinsic rhythmic Ca^{2+}-dependent V_m oscillations with a spike at their peak (Williams and Marshall, 1987; Christie et al., 1989; Ishimatsu and Williams, 1996; Christie, 1997). Moreover, the LFP persists during iGluR blockade with kynurenic acid, shown recently (Rawal et al., 2019) and here, and also during combined blockade of $GABA_A$ and glycine receptors (Kantor et al., 2012). Correspondingly, single LC neuron spiking in slices persisted in the presence of these inhibitors of the most common excitatory and inhibitory synaptic transmission (Alvarez et al., 2002; Olpe et al., 1988, 1989; Zamalloa et al., 2009). If gap junctions are mainly important for neonatal LC network connectivity, then AMPA and KA might increase and QUI decrease such coupling like in the inferior olive neural network (Turecek et al. 2014). Contrary, in the adult rat LC neuromodulators do presumably not directly counteract the postnatal decrease of gap junction coupling and instead neuromodulator-evoked spike slowing itself reverses this decrease (Alvarez et al., 2002). While that study did not reveal a correlation in neonatal rats between spike rate and gap junction-coupling, we found that faster spiking increases (for AMPA and KA) or decreases (for QUI) the regularity of rhythm. We hypothesized recently that incomplete neonatal LC synchronicity reflects neuronal differences regarding spontaneous neuromodulator release which changes V_m close to the oscillation peaks thus altering spike threshold (Rancic et al., 2018). Therefore, a QUI-evoked decrease in the regularity of LFP rhythm

may also occur if LC neuron subclasses express different types and/or numbers of AMPAR and are thus depolarized to different extent and reach spike threshold at diverging times. This is discussed in detail below.

5.5.3. Mechanism of AMPA- and KA-evoked LFP amplitude fluctuations

The observation that during both AMPA and KA larger amplitude faster oscillatory bursts alternated rhythmically with periods of smaller amplitude bursts might be explained as follows. The increased spike rate during AMPA and KA here and in previous slice studies (Olpe et al., 1989; Alvarez et al., 2002; Zamalloa et al., 2009) likely causes an enhanced Ca^{2+} influx (Metzger et al., 2000; Kulik et al., 2002). This might activate SK-type Ca^{2+}-activated K^+ channels that presumably cooperate with L-type and T-type Ca^{2+} channels to regulate pacemaker-like spike discharge in LC neurons of mouse slices (Matschke et al., 2015, 2018). The number of these channel types, their distribution between soma and the 'pericoerulear' dendrites (Ishimatsu and Williams, 1996) or the distance between them might differ between LC neuron subtypes. Accordingly, similarly accelerated spiking might cause SK channel-mediated after-hyperpolarizations of different amplitude to delay by a different extent the next spike discharge to result in decreased phase-lock. The number of neurons recorded here was too small to analyze a correlation between the tonic activity periods and irregularities between cellular spiking. This analysis can be done in future studies with either multi-electrode array recording (Ferrea et al., 2012) or (fluorescent protein) voltage sensor imaging (Abdelfattah et al., 2016; Quicke et al., 2017).

5.5.4. LFP transformation due to modular LC organization

Our findings that an already complex LC population burst can transform into different patterns during AMPA, KA vs. QUI (here), CNQX-evoked TARP activation (Rawal et al., 2019) and, in different fashion during high K^+ or opioids (Rancic et al., 2018), indicates that neuron-astrocyte modules cooperate within the LC. There seems to be a causal link between LC discharge pattern transformation, opioids and iGluR. Specifically, transformation of tonic spiking into oscillatory ('burst') discharge during systemic μ-opioid receptor activation in adult rats was reversed by injecting NMDAR or AMPAR blockers into the LC (Zhu and Zhou, 2015). The authors hypothesized in this study that iGluR-dependent LC bursting is important for opioid tolerance and dependence. In fact, modulation of iGluR activity in LC neurons has a plethora of behavioral effects (Price et al., 2009; DiazGranados et al., 2010; Chandley and Ordway, 2012; Chandley et al., 2014) that might critically depend on burst patterns. Similarly, pulse trains (but not single pulses) applied to the adult rat LC in vivo elicit changes in medial prefrontal cortex activity resembling those in LC noradrenaline input-dependent memory tasks (Marzo et al., 2014). A related study from that group proposed that the temporal structure of [LC-mediated] noradrenergic modulation may dynamically enhance or attenuate cortical responses to stimuli (Safaai et al., 2015). Their recent multi-unit recording in adult rats LC in vivo revealed only synchronicity in few neuron assemblies while they discovered a novel infra-slow (0.01-1 Hz) fluctuations of LC unit spiking (Totah et al., 2018). They concluded that 'the [adult] LC is a complex and differentiated neuromodulatory system'. Our in vitro findings extend this view to the neonatal rat LC and future studies will likely unravel novel neuropharmacological interactions in the neuron-astrocyte modules.

5.6. Figures and Legends

Fig. 5-1

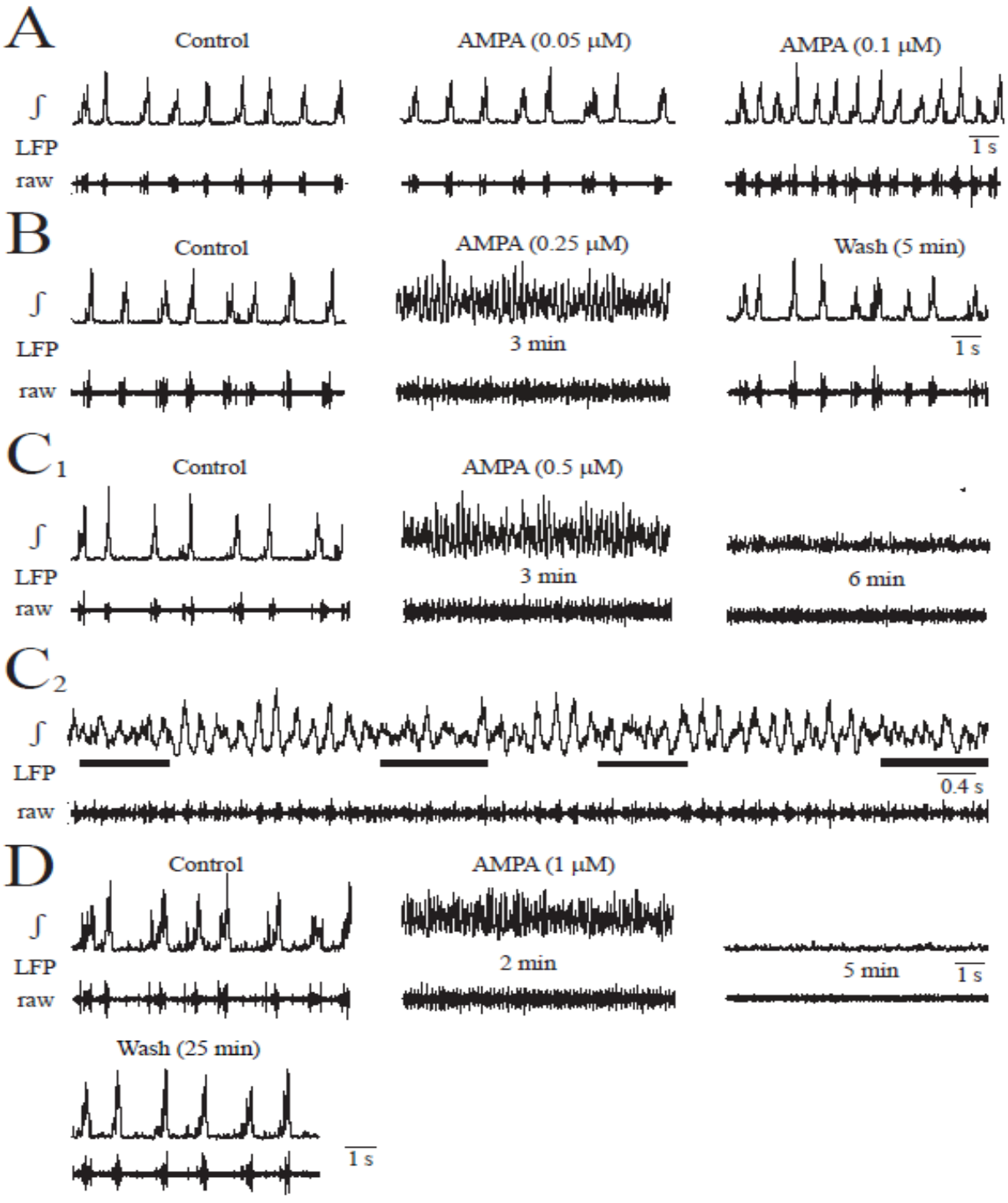

Fig. 5-1: Pattern transformation of local field potential (LFP) in one newborn rat locus coeruleus (LC) slice by α-amino-3-hydroxy-5-methyl-4-isoxazole propionic acid (AMPA). The LFP was recorded with a 40-60 µm tip size superfusate-filled suction electrode positioned on the slice surface in LC neuron soma area. The differentially-amplified (10 k) and bandpass-filtered (0.3-3 kHz) 'raw' signal was also recorded after integration (∫, time-constant 50 ms). 5 min bath-application of the ionotropic glutamate receptor (iGluR) agonist AMPA slightly accelerated LFP rate at 0.1 µM **(A)** whereas 0.25 µM merged separate bursts into faster sinusoidally-shaped oscillations showing every 2-3 s periodic amplitude fluctuations by 10-40 % **(B). C1, C2** Within the first 3 min into 0.5 µM AMPA, similar oscillations occurred which then showed a progressive decrease in amplitude that continued into the early phase of washout. **D,** After initially similar effects, 1 µM AMPA abolished rhythm which recovered within 25 min after start of washout.

Fig. 5-2

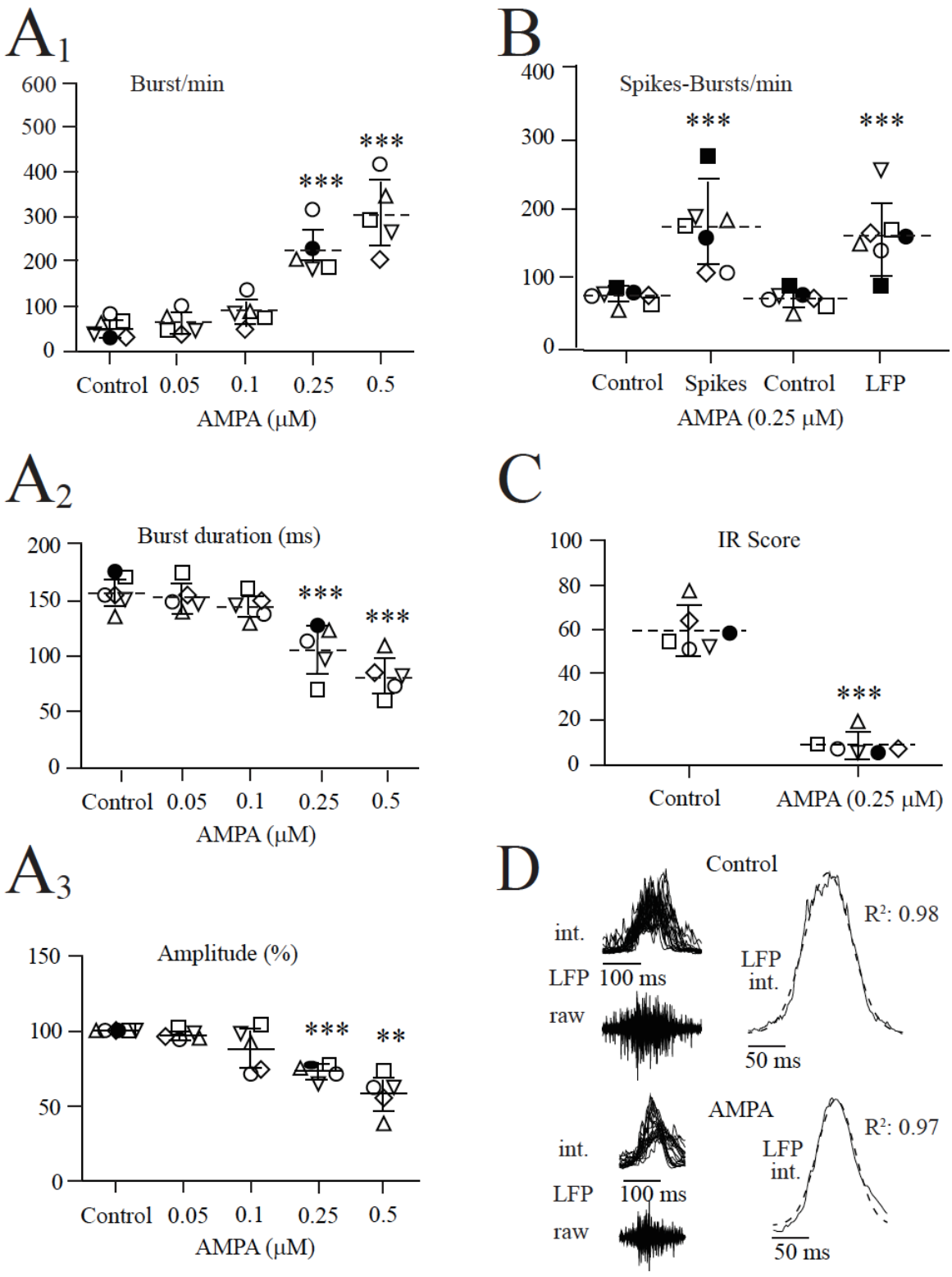
A1
Burst/min
600
500
400
300
200
100
0
***
***
Control 0.05 0.1 0.25 0.5
AMPA (µM)
A2
Burst duration (ms)
200
150
100
50
0
***
***
Control 0.05 0.1 0.25 0.5
AMPA (µM)
A3
Amplitude (%)
150
100
50
0
***
**
Control 0.05 0.1 0.25 0.5
AMPA (µM)
B
Spikes-Bursts/min
400
300
200
100
0
***
***
Control Spikes Control LFP
AMPA (0.25 µM)
C
IR Score
100
80
60
40
20
0
***
Control
AMPA (0.25 µM)
D
Control
int.
LFP
raw
100 ms
LFP
int.
R²: 0.98
50 ms
AMPA
int.
LFP
raw
100 ms
LFP
int.
R²: 0.97
50 ms

Fig. 5-2. Quantification of AMPA effects on LFP and single neuron spiking. A, analysis in 5 slices indicated by each symbol revealed that LFP burst rate **(A_1)** increased and single event duration **(A_2)** and amplitude **(A_3)** decreased at 0.25 and 0.5 µM **(A_3)**. **B**, in 6 different slices simultaneous LFP monitoring and whole-cell membrane potential (V_m) recording in a single neuron unraveled a similar increase in LFP burst rate and cellular spiking at 0.25 µM AMPA. **C**, in 6 different slices determination of the irregularity score showed that 0.25 µM AMPA made LFP rhythm more regular. **D**, overlay and subsequent averaging of 5 subsequent bursts from 4 slices revealed a bell-shaped LFP envelope during both control and AMPA 0.25 µM AMPA with a Gaussian fit of R^2= 0.98 and R^2= 0.97, respectively. Lines indicate mean values (dotted line) ± SD (solid line), significance was determined with one-way ANOVA with Dunnett's post test in **A_1** ($F(1, 5) = 29.64$, $P< 0.0001$), **A_2** ($F(1, 5) = 20.42$, $P< 0.0001$) and **A_3** ($F(1, 5) = 20.58$, $P< 0.0001$) and two-tailed paired t test in **B** and **C** $^{**}P< 0.01$, $^{***}P< 0.001$).

Fig. 5-3

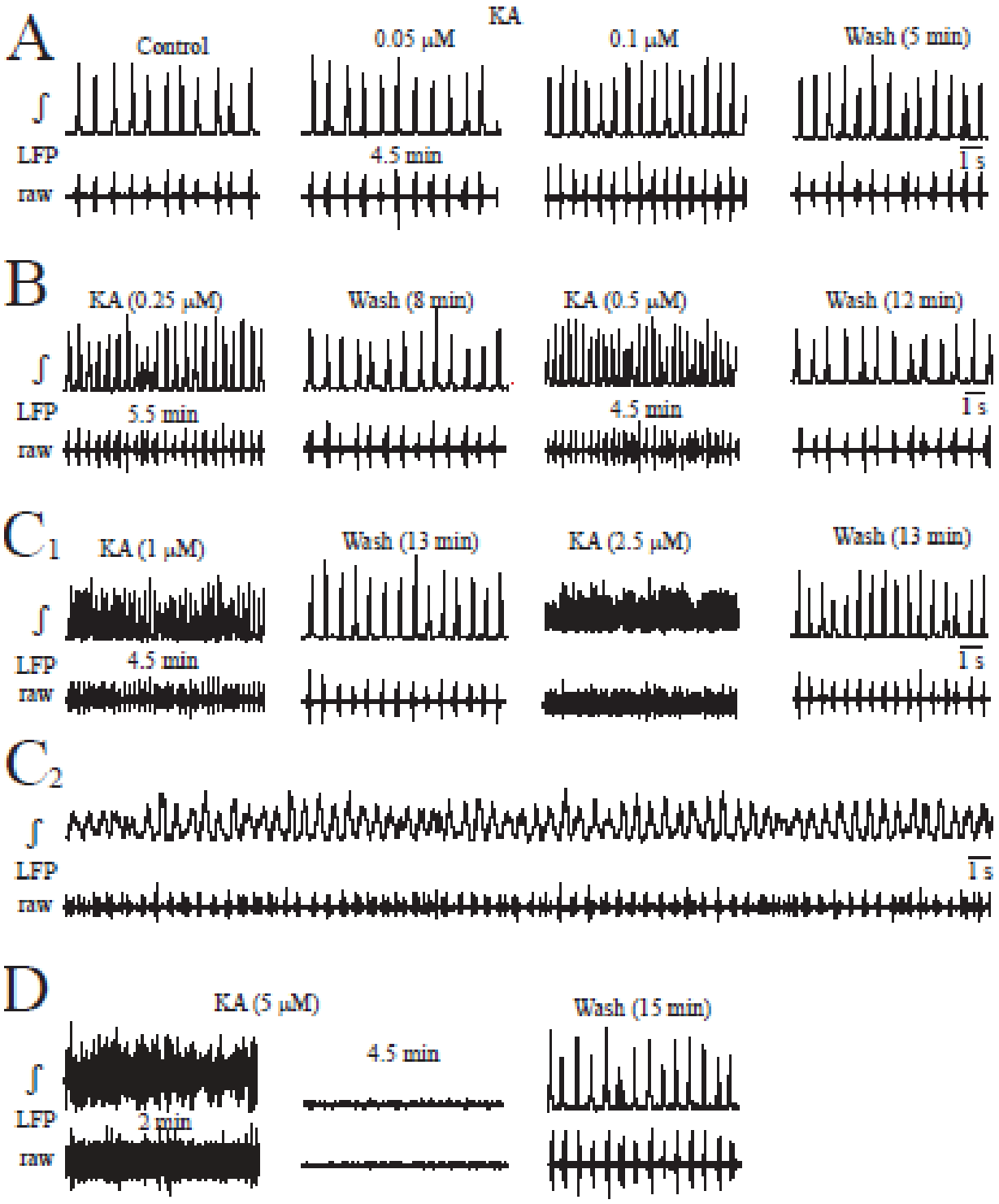
A
KA
Control
0.05 μM
0.1 μM
Wash (5 min)
∫
LFP
raw
4.5 min
1 s
B
KA (0.25 μM)
Wash (8 min)
KA (0.5 μM)
Wash (12 min)
∫
LFP
raw
5.5 min
4.5 min
1 s
C1
KA (1 μM)
Wash (13 min)
KA (2.5 μM)
Wash (13 min)
∫
LFP
raw
4.5 min
1 s
C2
∫
LFP
raw
1 s
D
KA (5 μM)
Wash (15 min)
∫
LFP
raw
2 min
4.5 min

Fig. 5-3: Effects on LFP of 5 min bath-application of the iGluR agonist kainate (KA). A, **B**, 0.1 and 0.25 µM KA accelerated LFP bursts which merged at 0.5 µM into faster sinusoidally-shaped events with 10-40 % amplitude fluctuations every 2-3 s. **C**, at 1 µM KA, oscillation rate increased further and amplitude fluctuations were more pronounced like at 1 µM which also increased the baseline of the integrated signal trace as indication of tonic discharge **(C_1)**. The traces in **C_2** from the dotted line box in **C_1** show at higher time resolution that smaller amplitude oscillatory events on the integrated trace at 2.5 µM KA are due to appearance of tonic discharge in the raw trace. **D**, at 5 µM KA initially oscillatory events with amplitude fluctuations turned within 4.5 min after start of application into blockade of rhythm which recovered after 15 min of washout.

Fig. 5-4

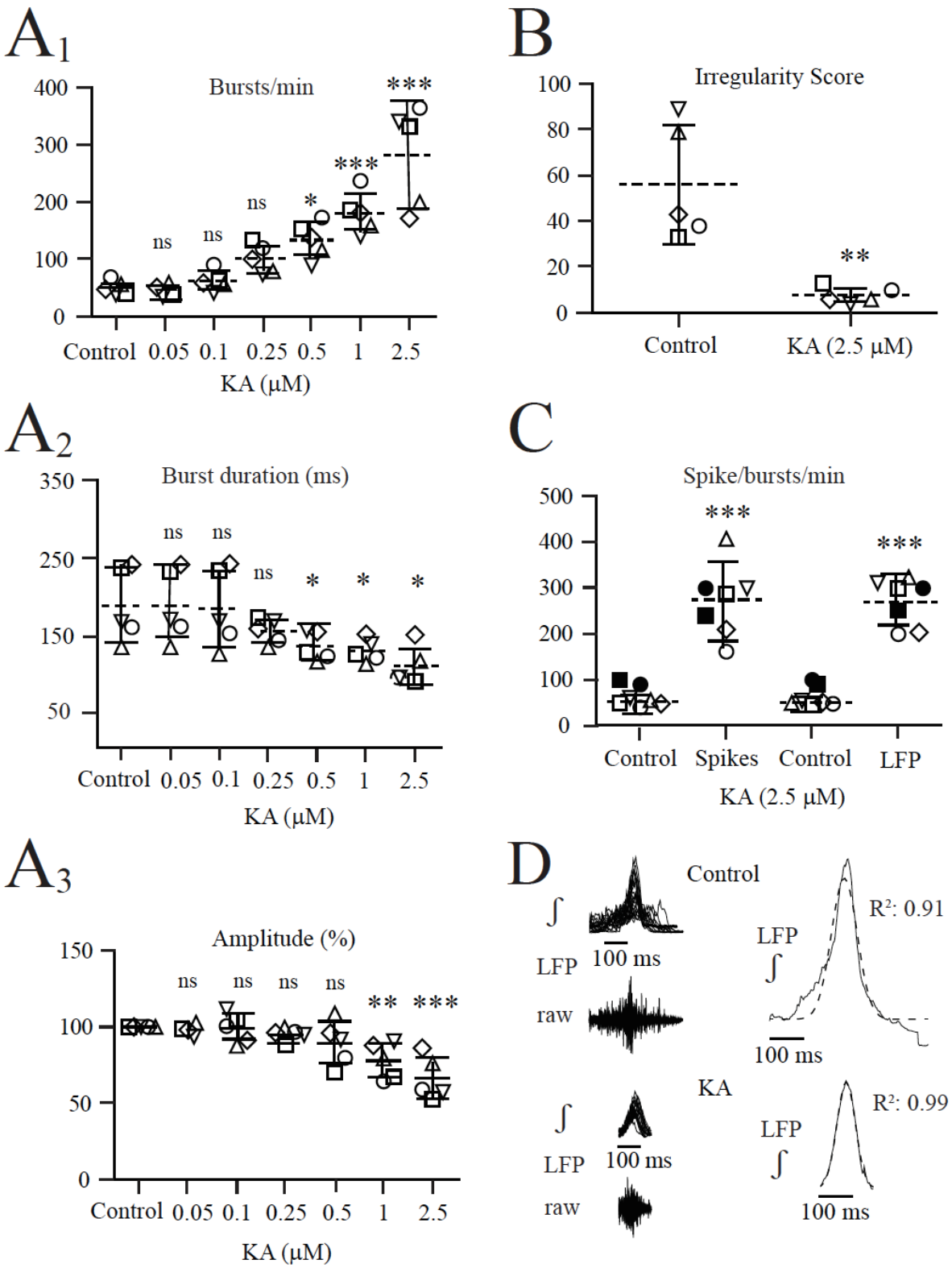
A1
Bursts/min
400
300
200
100
0
ns
ns
ns
*
***
***
Control 0.05 0.1 0.25 0.5 1 2.5
KA (µM)
A2
Burst duration (ms)
350
250
150
50
ns ns ns * * *
Control 0.05 0.1 0.25 0.5 1 2.5
KA (µM)
A3
Amplitude (%)
150
100
50
0
ns ns ns ns ** ***
Control 0.05 0.1 0.25 0.5 1 2.5
KA (µM)
B
Irregularity Score
100
80
60
40
20
0
**
Control
KA (2.5 µM)
C
Spike/bursts/min
500
400
300
200
100
0
*** ***
Control Spikes Control LFP
KA (2.5 µM)
D
Control
∫
LFP
100 ms
raw
LFP
∫
R²: 0.91
100 ms
KA
∫
LFP
100 ms
raw
LFP
∫
R²: 0.99
100 ms

Fig. 5-4: Quantification of KA effects on LFP and single neuron spiking. A, analysis in 5 slices revealed that LFP burst rate **(A_1)** increased and single event duration **(A_2)** decreased at 0.5 1.0 and 2.5 µM KA whereas its amplitude decreased only at 1.0 and 2.5 µM **(A_3)**. **B**, in 5 different slices simultaneous recording of LFP and V_m in a single neuron revealed a similar increase in LFP burst rate and cellular spiking at 2.5 µM KA. **C**, in 5 different slices the irregularity score shows that 2.5 µM KA made LFP rhythm more regular. **D**, overlay and subsequent averaging of 5 subsequent bursts from 4 slices revealed a bell-shaped LFP envelope during both control and 2.5 µM KA with a Gaussian fit of R^2= 0.91 and R^2= 0.99, respectively. Lines indicate mean values (dotted line) ± SD (solid line), significance was determined with one-way ANOVA with Dunnett's post test in **A_1** ($F(1, 7) = 20.98$, $P< 0.0001$), **A_2** ($F(1, 7) = 4.55$, $P< 0.05$) and **A_3** ($F(1, 7) = 7.90$, $P< 0.01$) and two-tailed paired t test in **B** and **C** $^{**}P< 0.01$, $^{***}P< 0.001$).

Fig. 5-5

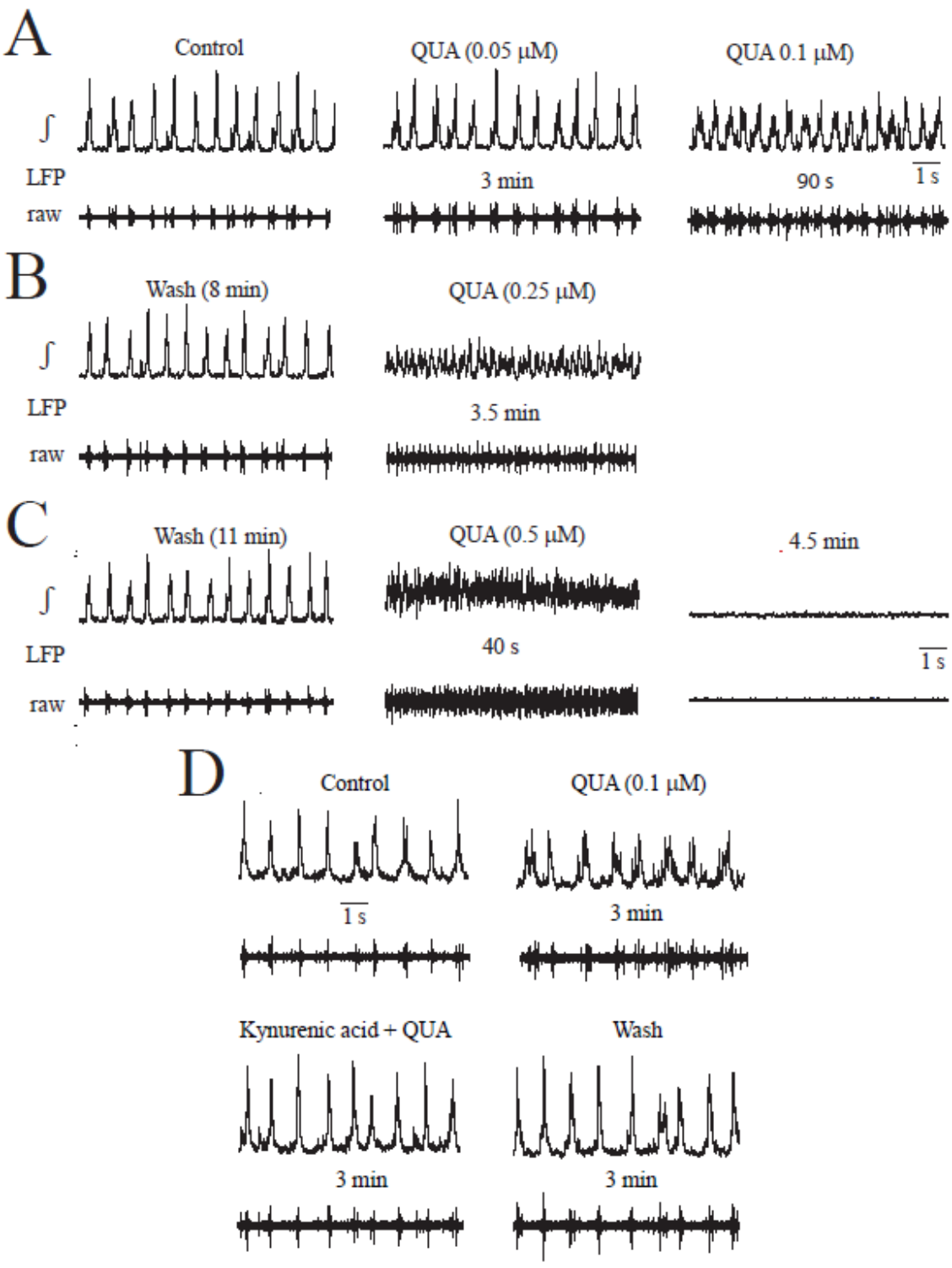
A
Control
QUA (0.05 μM)
QUA 0.1 μM)
∫
LFP
raw
3 min
90 s
1 s
B
Wash (8 min)
QUA (0.25 μM)
∫
LFP
raw
3.5 min
C
Wash (11 min)
QUA (0.5 μM)
4.5 min
∫
LFP
raw
40 s
1 s
D
Control
QUA (0.1 μM)
1 s
3 min
Kynurenic acid + QUA
Wash
3 min
3 min

Fig. 5-5: Effects on LFP of 5 min bath-application of the AMPAR-type iGluR agonist quisqualate (QUI). A, 0.05 µM QUI had no effect whereas 0.1 µM decreased burst amplitude and increased its duration. **B**, following recovery of LFP within 8 min of wash 0.25 µM QUI turned rhythm into small amplitude irregular events. **C**, at 0.5 µM QUI rhythm became initially irregular with tonic discharge causing an increase of integrated signal baseline before it was blocked 0.5 min before the end of application. **D**, in a different slice LFP pattern transformation by 0.1 µM QUI was reversed in the continuous presence of QUI after 2 min preincubation of the unselective iGluR antagonist kynurenic acid (2.5 mM).

Fig. 5-6

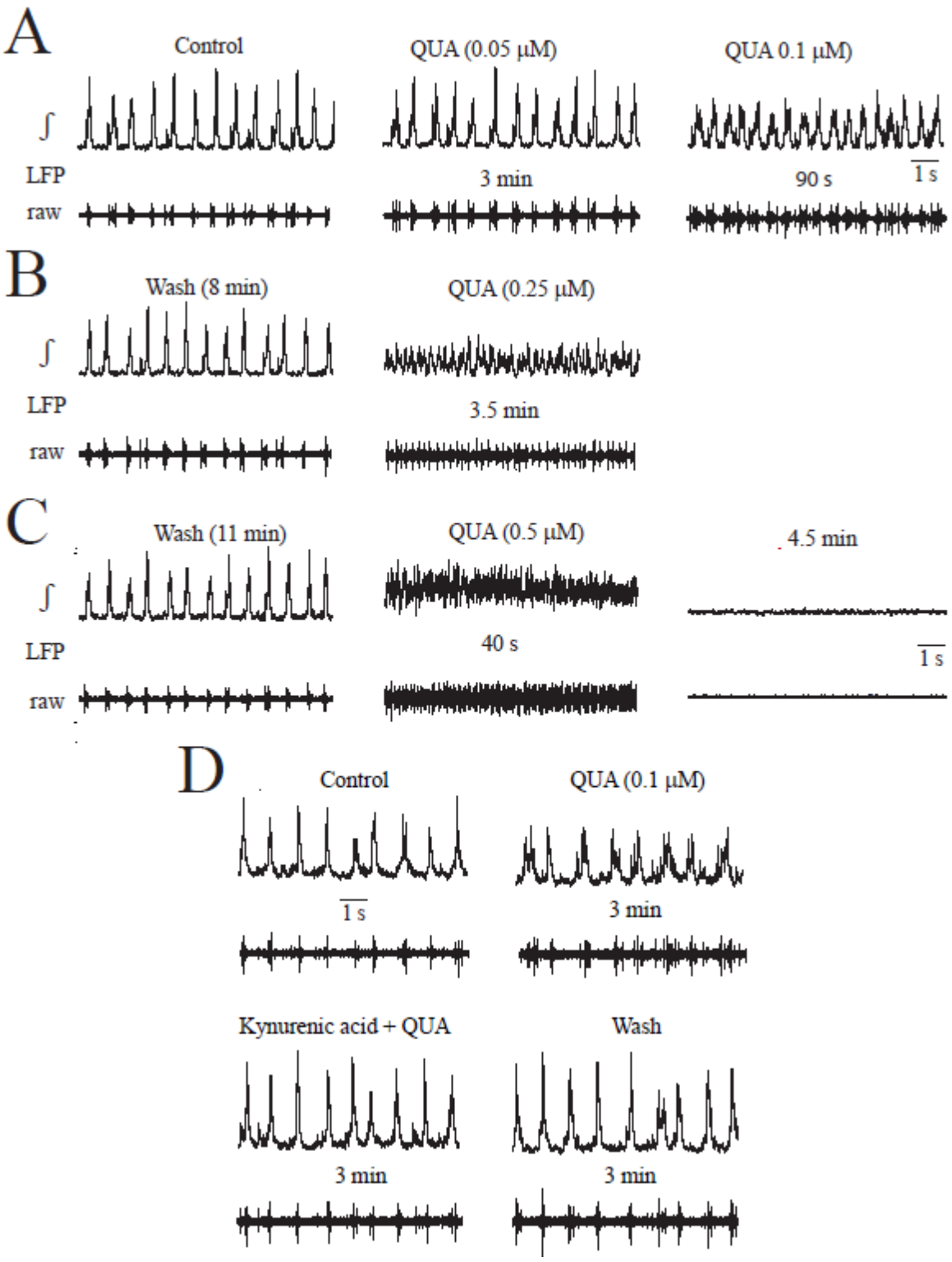
A
Control
QUA (0.05 μM)
QUA 0.1 μM)
∫
LFP
raw
3 min
90 s
1 s
B
Wash (8 min)
QUA (0.25 μM)
∫
LFP
raw
3.5 min
C
Wash (11 min)
QUA (0.5 μM)
4.5 min
∫
LFP
raw
40 s
1 s
D
Control
QUA (0.1 μM)
1 s
3 min
Kynurenic acid + QUA
Wash
3 min
3 min

Fig. 5-6: Quantification of QUI effects on LFP and single neuron spiking. A, analysis in 6 slices showing still separate bursts during LFP pattern transformation in QUI revealed that burst rate **(A_1)** changed neither during 0.05 or 0.1 µM QUI nor 0.1 µM QUI in 2.5 mM kynurenic acid. Contrary, 0.1 µM QUI increased burst duration **(A_2)** plus decreased its amplitude **(A_3)** and both effects were reversed in 3 of these slices tested by kynurenic acid **(A_2, A_3)**. **B**, in 5 different slices simultaneous recording of LFP and V_m in a single neuron showed no change in LFP or cellular spike rate at either 0.1 or 0.15 µM QUI. **C,** in 7 different slices the irregularity score value was not changed indicating no effect on regularity of LFP rhythm. **D**, overlay and subsequent averaging of 5 subsequent bursts from 4 slices revealed a bell-shaped LFP envelope during both control and 100 µM QUI with a Gaussian fit of R^2= 0.96 and R^2= 0.94, respectively. Lines indicate mean values (dotted line) ± SD (solid line), significance was determined with one-way ANOVA with Dunnett's post test in **A_1** ($F(1, 5) = 0.24$, $P= 0.93$), **A_2** ($F(1, 7) = 4.03$, $P< 0.05$) and **A_3** ($F(1, 7) = 24.90$, $P< 0.0001$) and two-tailed paired t test in **B** and **C** $^{**}P< 0.01$, $^{***}P< 0.001$.

Fig. 5-7

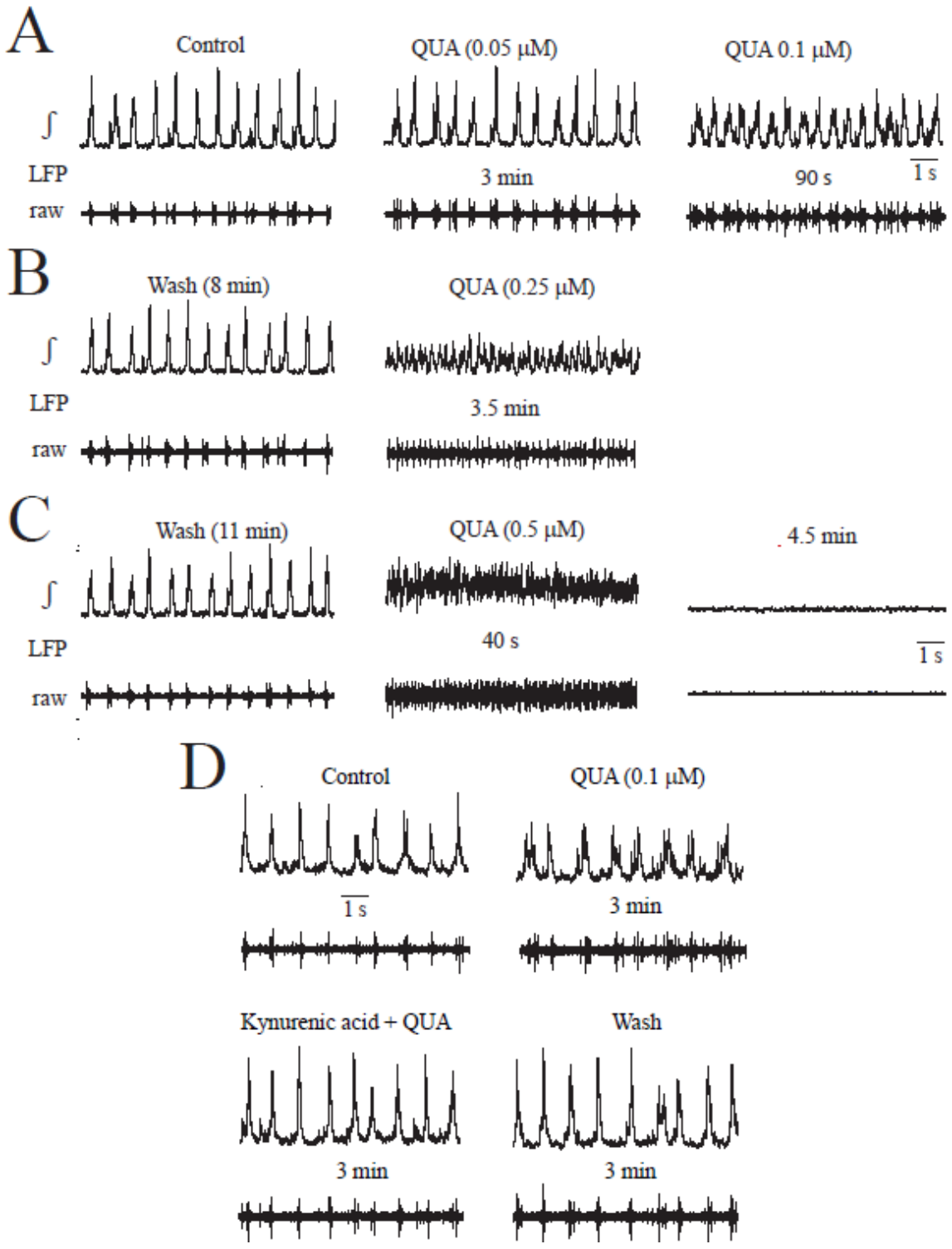
A
Control
QUA (0.05 μM)
QUA 0.1 μM)
∫
LFP
raw
3 min
90 s
1 s
B
Wash (8 min)
QUA (0.25 μM)
∫
LFP
raw
3.5 min
C
Wash (11 min)
QUA (0.5 μM)
4.5 min
∫
LFP
raw
40 s
1 s
D
Control
QUA (0.1 μM)
1 s
3 min
Kynurenic acid + QUA
Wash
3 min
3 min

Fig. 5-7: Effects of QUI and kynurenic acid on LFP and neuronal V_m. A, the continous traces show that QUI transformed the LFP pattern with a concomitant increase of neuronal spike rate and that kynurenic acid reversed these effects. **B**, the traces on an expanded time scale taken at the time period indicated by the grey boxes show that LFP burst shape was transformed by QUI into prolonged ramp-shaped events while neuronal spiking was accelerated although resting V_m only depolarized by 2.5 mV **(B_1)** and that kynurenic acid restored a control LFP burst shape and decreased spike rate in association with 2 mV repolarization of V_m **(B_2)**.

Fig. 5-8

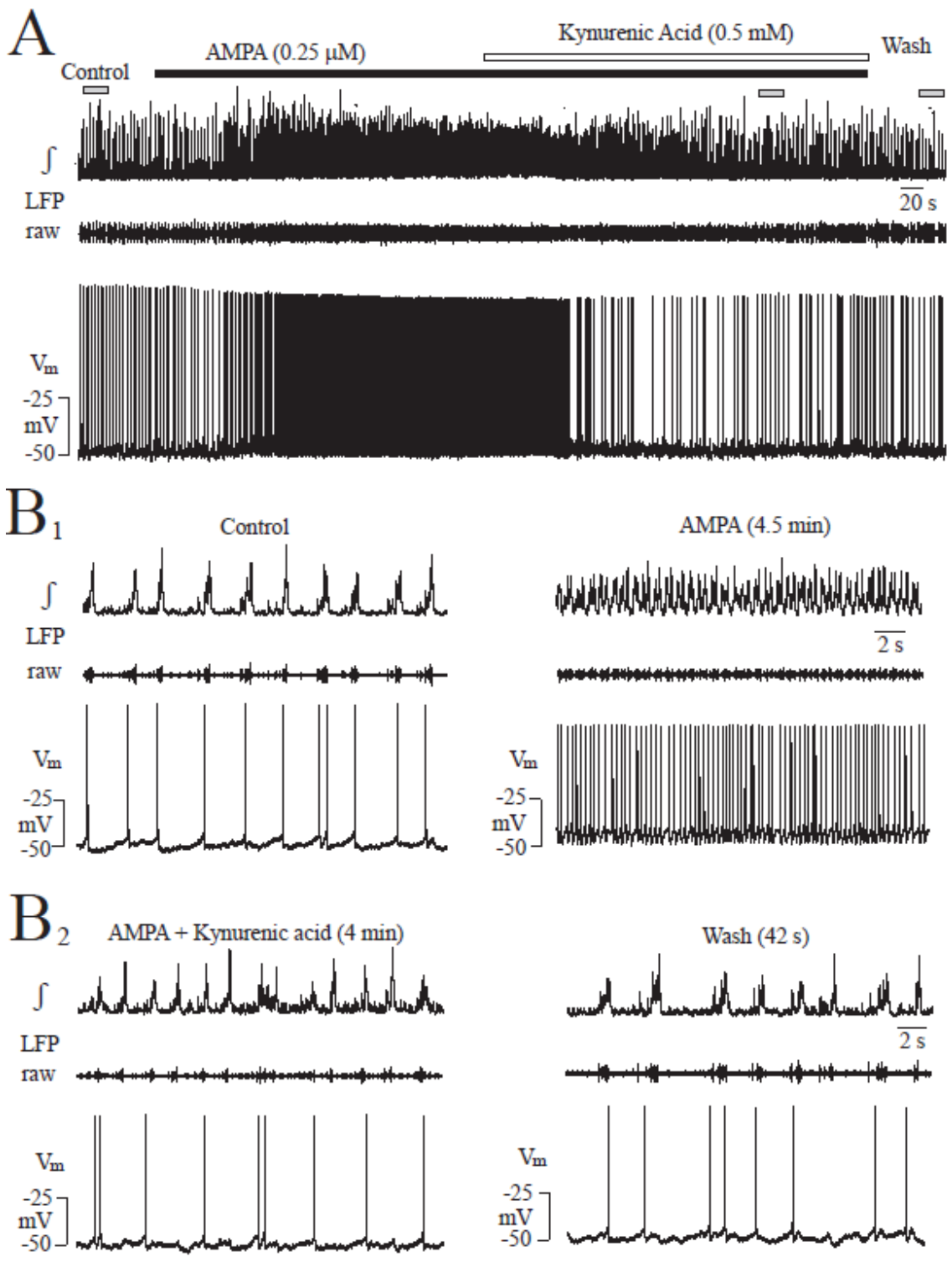
A
Control
AMPA (0.25 µM)
Kynurenic Acid (0.5 mM)
Wash
∫
LFP
raw
20 s
Vm
-25
mV
-50
B1
Control
AMPA (4.5 min)
2 s
B2
AMPA + Kynurenic acid (4 min)
Wash (42 s)

Fig. 5-8: AMPA and kynurenic acid effects on LFP and neuronal V_m. A, the continous traces show that AMPA transformed the LFP pattern into fast oscillations with concomitant acceleration of neuronal spiking and that kynurenic acid reversed these effects. **B**, the traces on an expanded time scale taken at the time indicated by the grey boxes shows AMPA-evoked fast LFP oscillations associated with accelerated neuronal spiking due to V_m depolarization by 5 mV **(B_1)** while kynurenic acid restored a control LFP pattern and decreased spike rate in association with a 5 mV repolarization of V_m **(B_2)**.

Fig. 5-9

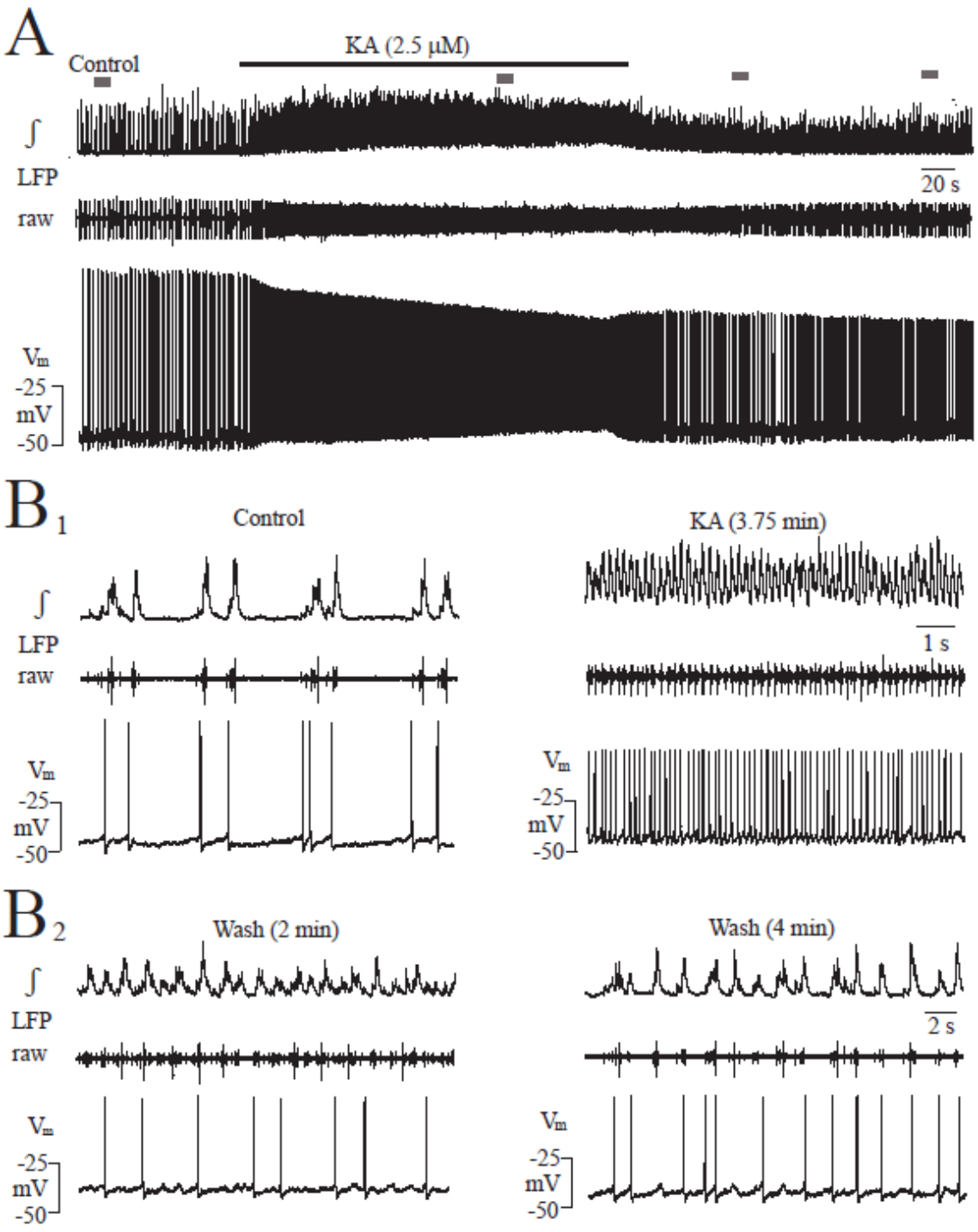
A
Control
KA (2.5 μM)
∫
LFP
raw
20 s
Vm
-25
mV
-50
B1
Control
KA (3.75 min)
∫
LFP
raw
1 s
Vm
-25
mV
-50
B2
Wash (2 min)
Wash (4 min)
∫
LFP
raw
2 s
Vm
-25
mV
-50

Fig. 5-9: Effects of KA on LFP and neuronal V_m and reversal of LFP pattern transformation by kynurenic acid. A, the continous traces show that KA transformed the LFP pattern into fast oscillations with a concomitant increase of neuronal spike rate. **B**, the traces on an expanded time scale taken at the time indicated by the grey boxes show that LFP burst shape was transformed by AMPA into fast oscillations with accelerated neuronal spiking due to V_m depolarization by 5 mV. **B**, in a different slice kynurenic acid restored the KA-evoked LFP oscillations to a normal burst pattern.

Fig. 5-10

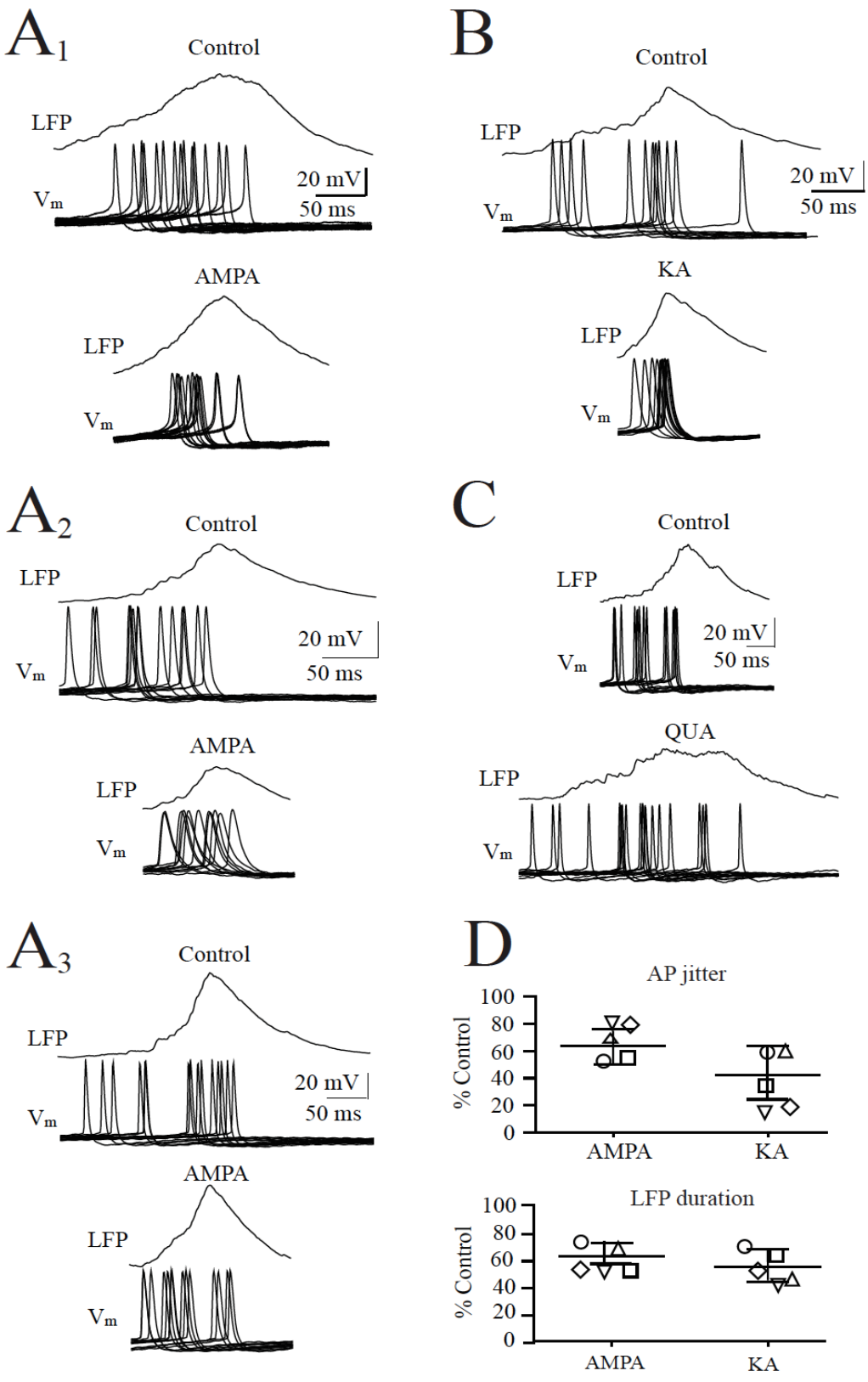
A1
Control
LFP
Vm
20 mV
50 ms
AMPA
LFP
Vm
A2
Control
LFP
Vm
20 mV
50 ms
AMPA
LFP
Vm
A3
Control
LFP
Vm
20 mV
50 ms
AMPA
LFP
Vm
B
Control
LFP
Vm
20 mV
50 ms
KA
LFP
Vm
C
Control
LFP
Vm
20 mV
50 ms
QUA
LFP
Vm
D
AP jitter
% Control
100
80
60
40
20
0
AMPA
KA
LFP duration
% Control
100
80
60
40
20
0
AMPA
KA

Fig. 5-10: AMPA- and KA-evoked reduction and QUI-evoked increase in neuronal spike jitter. A, simultaneous recording of LFP and V_m revealed in 3 different neurons **(A_1-A_3)** that 0.25 µM AMPA shortened LFP duration (average from 11-15 consecutive bursts) with a concomitant reduction of spike jitter (overlay of V_m traces for the corresponding LFP bursts). Note that the neurons differed regarding the phase-lock of spiking, e.g., the neuron in **A_1** discharged primarily between the first third and the peak of the LFP, whereas the neuron in **A_3** discharged either very early or around the LFP peak. **B**, **C**, example for a corresponding reduction in spike jitter in a neuron during 2.5 µM KA **(B)** and, in a different cell, an increase in jitter during 0.1 µM QUI **(C)**. **D**, averages for the percentage reduction in LFP duration (upper traces) and spike jitter (lower traces) in 4 neurons during 0.25 µM AMPA and 2.5 µM KA. Statistics could not be calculated for the QUI-evoked increase in spike jitter as only 2 neurons were tested (in which jitter increased 3.10 and 2.93 -fold compared to control. Lines indicate mean values (dotted line) ± SD (solid line), significance was determined with two-tailed paired t-test with $^{**}P < 0.01$, $^{***}P < 0.001$).

Fig. 5-11

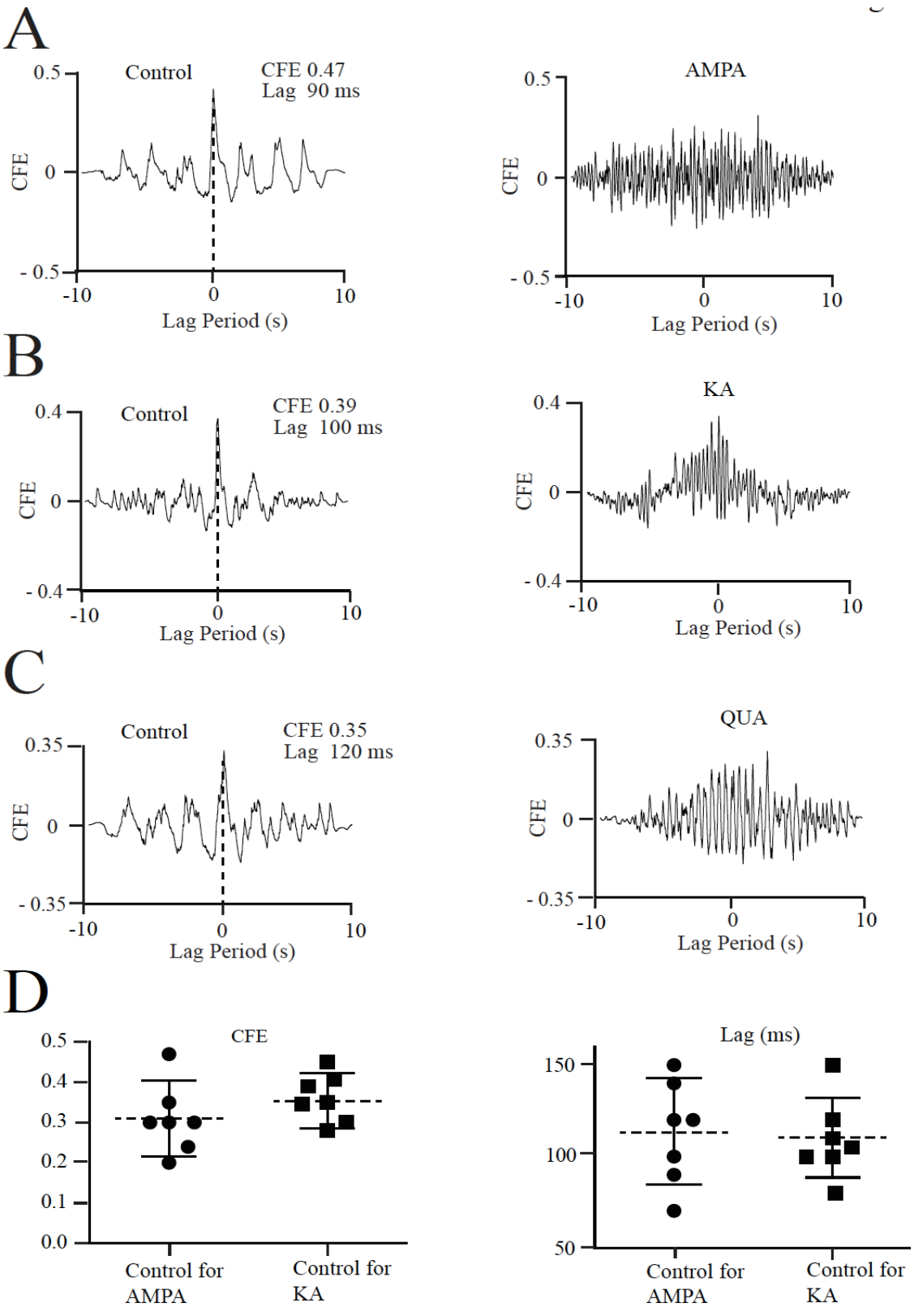
A
Control
CFE 0.47
Lag 90 ms
AMPA
CFE
Lag Period (s)
B
Control
CFE 0.39
Lag 100 ms
KA
C
Control
CFE 0.35
Lag 120 ms
QUA
D
CFE
Lag (ms)
Control for AMPA
Control for KA

Fig. 5-11: Cross-correlation analysis between neuronal spiking and LFP peak during AMPA, KA and QUI. A, left panel illustrates for the neuron shown in **Fig. 4-8A** that the cross-correlation function estimate (CFE) value and the lag time were 0.47 and 90 ms, respectively, indicating a certain extent of synchronicity. In contrast, no values could be determined during AMPA. **B**, **C**, corresponding results were obtained for a neuron in 2.5 µM KA **(B)** and 100 µM QUI **(C)**. **D**, shows statistical data for CFE and lag time values in control for 6 neurons tested subsequently for AMPA and 5 different cells analyzed for KA. Lines indicate mean values (dotted line) ± SD (solid line), significance was determined with two-tailed paired t-test with non-significan (ns) $P > 0.06$.

.

CHAPTER 6

NMDA enhances and glutamate attenuates synchronization of spontaneous phase-locked locus coeruleus network bursting in newborn rat brain slices

Bijal Rawal, Vladimir Rancic & Klaus Ballanyi

Department of Physiology, Faculty of Medicine & Dentistry, 750 MSB, University of Alberta, Edmonton, T6G2H7 Canada

Contributions: BR and KB contributed to the conception, design and writing of the paper. BR contributed to >90 % of data acquisition and analysis of data. VR contributed <10 % of data acquisition and analysis.

6.1. Abstract

Locus coeruleus (LC) neurons are controled by glutamatergic inputs. Here, we studied in brain slices of neonatal rats NMDA and glutamate effects on phase-locked LC neuron spiking at ~1Hz summating to ~0.2s-lasting bell-shaped bursts. NMDA: 10μM accelerated this local field potential (LFP) 1.7-fold whereas 25 and 50μM, respectively, increased LFP rate 3.2- and 4.6-fold while merging bursts into 43 and 56% shorter oscillations. After 4-6 min, LFP oscillations stopped every 6s for 1s resulting in 'oscillation trains' progressively decreasing in amplitude and duration. 100μM abolished rhythm. 32μM depolarized neurons by 8.4mV to cause 7.2-fold accelerated spiking at reduced jitter (±14ms vs. ±104ms in control) and enhanced synchronization with the LFP as evident from cross-correlation. Glutamate: 25-50μM made rhythm more irregular and LFP pattern transformed in 60% of cases into 2.7-fold longer-lasting multipeak bursts. 100μM initially enhanced these effects before LFP amplitude and duration declined. 250-500μM blocked rhythm. 25-50μM depolarized neurons by 5mV to cause 3.7-fold acceleration of spiking that was less synchronized with LFP as evident from cross-correlation. Both agents: evoked 'post-agonist depression' of LFP that correlated with the amplitude and kinetics of V_m hyperpolarization. A similar depression was seen initially during countering glutamate effects with kynurenic acid (0.25-2.5mM). The findings show that accelerated spiking during both NMDA and glutamate is associated, respectively, with enhanced or attenuated LC synchronization causing distinct LFP pattern transformations. Consequently, ionotropic glutamate receptors differentially shape LC population burst dynamics to potentially enable this 'modular' network to fine-tune its influence on multiple brain functions.

6.2. Introduction

The locus coeruleus (LC) in the dorsal pons is the source for noradrenergic innervation of most brain structures and consequently controls multiple behaviors including arousal, sleep-wake cycle, breathing, memory, pain sensation, anxiety and opioid (withdrawal) effects (Foote et al., 1983; Berridge and Waterhouse, 2003; Aston-Jones and Cohen, 2005). LC neurons show In vivo spontaneous pacemaker-like ('tonic') single action potential firing or they discharge phasically during afferent synaptic inputs involving various neurotransmitters including glutamate (Jodo and Aston-Jones, 1997; Singewald and Phillipu, 1998; Berridge and Waterhouse, 2003; Aston-Jones and Cohen, 2005; Schwarz and Luo, 2015). The important role of glutamate for LC functions is evident from the fact that application of modulators of ionotropic glutamate receptors (iGluR) notably affects brain activities (Chandley and Ordway, 2012; Chandley et al., 2014). For example, the NMDA-type iGluR antagonist ketamine has an acute antidepressant action that can reduce suicide ideation (Price et al., 2009; DiazGranados et al., 2010). Moreover, iGluR activation is involved in transformation of tonic LC neuron spiking into oscillatory ('burst') discharge during systemic morphine application in adult rats (Zhu and Zhou, 2005). According to that study, dose-response analyses are needed to determine whether both NMDA-type receptors (NMDAR) and non-NMDA-type (i.e. AMPAR-type) iGluR are involved in this opioid-evoked discharge pattern transformation. The authors also noted it is unknown whether systemic morphine primarily affects brain areas outside the LC. In that regard, particularly the nucleus paragigantocellularis, the lateral habenula and the prefrontal cortex send glutamatergic axons to the LC (Herkenham and Nauta, 1979; Aston-Jones et al., 1986; Jodo and Aston-Jones, 1997; Singewald and Phillipu, 1998). Electrophysiological recording in brain slices that are devoid of these and other afferent glutamatergic structures has established though that activation of either type of iGluR accelerates tonic LC neuron spiking (Olpe et al., 1989; Kogan and Aghajanian, 1995; Zamalloa et al., 2009).

The lack of occurrence of NMDAR- and AMPAR-dependent LC bursting in vitro might be due to the fact that responses of single neurons were monitored in the latter studies. Instead, local field potential (LFP) recording might have revealed a more complex LC network response as seen in various brain structures, both in vivo and in vitro (Ballanyi and Ruangkittisakul, 2009; Buzsáki et al., 2012; Einevoll et al., 2013; Totah et al., 2018). In that regard, we found with suction electrode recording that the LC in newborn rat brain slices generates a spontaneous ~0.2 s-lasting LFP at a rate of ~1 Hz (Rancic et al., 2018). As one major new finding, we reported in that study that this LFP pattern can transform to rhythmic several seconds-lasting multipeak bursts during either increased LC network excitability evoked by raised extracellular K^+ or recovery from opioid inhibition. Such transformed bursting resembles NMDA-evoked rhythmic neuronal activities in slices of various brain circuits (Neuman et al., 1989; Zhu et al., 2004; Sharifullina et al., 2008; Mrejeru et al., 2011).

Here, we firstly analyzed with dose-response relationships whether iGluR activation by NMDA or glutamate mimics the K^+- or opioid-evoked LFP pattern transformation. Secondly, we combined LFP assessment with membrane potential (V_m) recording to analyze whether NMDA and glutamate effects on network bursting are more complex than the above mentioned dose-dependent acceleration of single neuron spiking and at which dose activity pattern transformation might occur.

6.3. Materials and methods

(see **Chapter 2)**

6.4. Results

Initial analysis of LFP properties and dose-dependent LFP pattern changes during NMDA or glutamate application was followed by cellular analyses using combined LFP and V_m recording.

6.4.1. LFP shape and signal analysis

Recently, we reported that the neonatal rat LC generates in a brain slice at 1 Hz rhythmic ~0.2 s-lasting LFP bursts comprising non-synchronous, yet phase-locked single spikes from individual LC neurons (Rancic et al., 2018). Here, we studied these bursts in more detail to enable a comparison with potential LFP pattern transformations during NMDA or glutamate. The LFP was immediately seen when the suction electrode touched the slice surface in the LC neuron somata area. Its amplitude increased progressively until steady-state was reached after 0.5-1 h. The signal was stable, often for >5 h, particularly when up to 5 mmHg negative pressure was applied to the electrode (and sometimes needed to be re-applied when signal amplitude decreased spontaneously). Using the same 40-60 µm tip diameter electrode in a given slice, LFP amplitude and shape did not vary at different positions within the LC. In >70 % of 29 slices in total, LFP burst rate, duration and amplitude was regular **(Fig. 6-1A1-A3)**. In the other cases, the rhythm was more irregular and LFP bursts could show several peaks evident in the integrated signal **(Fig. 6-1A4)**.

In 5 slices with regular rhythm and typical burst shape, LFP rate ranged from 0.80 to 1.40 Hz (mean 1.09 ± 0.22 Hz, i.e. 65 ± 14 bursts/min). Burst duration ranged from 0.13 to 0.2 s (mean 0.16 ± 0.02 s) and integrated LFP amplitude was 0.65 to 0.97 mV (mean 0.82 ± 0.13 mV). **Fig. 6-1B** shows overlayed traces of 5 consecutive LFP bursts from each of these 5 slices. The mean of the integrated trace was fitted well with a bell-shaped Gauss function (R^2 value: 0.98) **(Fig. 6-1B)**.

The typically sparse irregularity of LFP bursts between slices and also between cycles in the same slice **(Fig. 6-1)** is due to the fact that not every neuron spikes during each cycle and phase-lock of their spiking, related to that of other neurons and the LFP, shows a jitter (Rancic et al., 2018). This was also seen here in LFP plus extracellular spike recording from 5 neuron pairs **(Fig. 6-2)**. The suction electrode was positioned at the rim of the LC close to the 4th ventricle while the spike-detecting patch electrodes were positioned in randomly chosen spots within the LC **(Fig. 6-2A)**. There was no correlation between spike pattern and the patch electrode position. Due to the variability of spiking that overlaps to form the LFP, it was not possible to determine exact numbers of contributing neurons. However, typically each LC neuron discharges only 1 AP per cycle or shows a spike failure **(Fig. 6-2B)**. Thus, based on an estimate of the number of partially overlapping spikes in the raw signal, the LFP typically represents summated discharge in 5-15 cells. In some cases, the LFP contained large amplitude spikes from 1-3 neurons whose somata were likely located closer to the electrode than those from cells with smaller amplitude signals **(Fig. 6-1A).**

6.4.2. NMDA and glutamate-evoked LFP pattern transformation

The above findings indicate that the LFP burst is bell-shaped due to a normal distribution of the occurrence of single spikes that jitter similarly around the LFP peak. Next, dose-response relationships were studied for effects of bath-applied NMDA and glutamate to determine the thresholds for putative LFP pattern transformation and elucidate whether high concentrations perturb network bursting as previously reported for single neuron spiking (Olpe et al., 1989).

NMDA effects on LFP: Examples for NMDA effects are given in **Fig. 6-3** while statistical analysis from very similar findings in 4 slices is summarized in **Fig. 6-4**. At 10 µM, 5 min NMDA

application slightly increased the rate of LFP bursts and shortened their duration **(Fig. 6-3A)**. 25-50 µM NMDA enhanced these effects in the early phase when separate bursts merged to sinusoidal, still bell-shaped, oscillations with <15 % amplitude fluctuations. As discussed before (Rawal et al., 2019), the low amplitude LFP occurs during a time when the network shows decreased phase-lock resulting in more random 'tonic' activity **(Fig. 6-3B$_1$, B$_2$, C$_1$, C$_2$)**. In the later phase of 25-50 µM NMDA, LFP oscillations were rhythmically depressed for ~1 s **(Fig. 6-3B$_1$, B$_2$, C$_1$)**. During resulting LFP 'oscillation trains', the rate of individual oscillations increased slightly further, but single event duration did not decrease more. After 2-5 stable cycles, oscillation trains became shorter with a decline of both oscillation amplitude and regularity toward their end **(Fig. 6-3B$_2$, C$_1$, C$_3$)**. The onset of oscillation trains and also their progressive amplitude decrease was less delayed at 50 and 100 µM NMDA than at 25 µM, transforming rhythm later during the application into 'spikes' before the LFP was blocked (in 3 of 4 cases at 100 µM and in the other case at the end of at 50 µM) **(Fig. 6-3C3)**. The modest stimulatory NMDA effects at 10 µM, and initially at 25 µM, were consistent for the 4 slices. Contrary, transition of accelerated LFPs into LFP trains occurred at 25 µM in 2 of these slices and at increasing the dose from 25 to 50 µM in the other 2 cases.

In the 4 slices, LFP duration (in ms) decreased from 183 ± 38 to 133 ± 18 at 10 µM, 105 ± 19 early at 25 µM, 78 ± 23 late (i.e. during oscillation trains) at 25 µM and 81 ± 5 early at 50 µM **(Fig. 6-4A, B)**. Conversely, the rate of the still bell-shaped LFP (see inset in **Fig. 6-4)** increased (in bursts/min) from 77 ± 25 in control to 126 ± 19 (1.7-fold) at 10 µM, 250 ± 30 (3.2-fold) 'early' at 25 µM, 356 ± 46 (4.6-fold) 'late' at 25 and 347 ± 48 (4.5-fold) 'early' at 50 µM **(Fig. 6-4A, C)**. LFP amplitude did not change at any NMDA dose **(Fig. 6-4A, D)**. While for the determination of mean amplitudes, their fluctuations were averaged out, the extent of the periodic amplitude change of early LFP oscillations tended to increase from <15 % at 25 µM to 40-50 % at 50 µM. When LFP

oscillation trains at 50 µM (n= 4) were stable in their early phase for 3 cycles, their duration was 6.06 ± 2.64 s and rhythmic LFP blockade lasted 0.94 ± 0.34 s.

Glutamate-effects on LFP: An example for glutamate effects is given in **Fig. 6-5** for 1 of 6 slices tested. In 4 slices at 25 µM, and the other 2 upon changing from 25 to 50 µM, glutamate made the rhythm more irregular with appearance of variable amplitude and duration events that included in 4 of these cases ramp-shaped multipeak bursts **(Fig. 6-5A, B)**. Applying glutamate to these slices at one dose above the pattern-transforming one (i.e. at 50 or 100 µM) firstly had the same effect. After 1-2 min though, tonic discharge developed and activity decreased 1-2 min later **(Fig. 6-5C)**. 100, 250 and 500 µM glutamate caused initially similar tonic discharge which then progressively declined until rhythm stopped at 250 µM in 4 of the 6 slices and in 1 case each at 100 or 500 µM **(Fig. 6-5D)**. In 2 of the 4 slices, irregular small amplitude ~0.05 s-lasting LFP spikes persisted during blockade of rhythm at 250 µM (not shown).

As glutamate made rhythm irregular, effects could only be quantified in the 4 slices (2 at 25 and 2 at 50 µM) showing separate ramp-shaped multipeak bursts. In these cases, burst duration increased from 232 ± 27.7 ms in control to 624 ± 150 ms (P= 0.002) (i.e. 2.7-fold) while LFP rate showed a trend to rise from 42.3 ± 7.2 /min to 57.3 ± 15.6 bursts/min (P= 0.13).

6.4.3. NMDA and glutamate effects on network synchrony and irregularity

The above findings showed firstly that (during the later phase of) 50-100 µM NMDA and 100-500 µM glutamate the LFP was blocked. Whereas these values are similar to those causing inactivation of single LC neuron spiking in adult rat brain slices in 1 study (Olpe et al., 1989), spiking persisted

at substantially increased rate in 2 similar reports (Kogan and Aghajanian, 1995; Zamalloa et al., 2009). While 10-50 µM NMDA notably accelerated the LFP, glutamate did not increase burst rate, but transformed regular LFP bursting into an irregular rhythm. Contrary, 25-50 µM NMDA changed the LFP pattern to higher frequency, shorter duration oscillations initially, until the oscillations became rhythmically interrupted later during the application. The NMDA-evoked shortening of burst duration indicates an increase in network synchronization whereas the observed increased burst duration and irregularity of rhythm indicates the opposite for glutamate. To substantiate this assumption, cross-correlation analysis was done between LFP peaks and the associated intracellular spikes.

Glutamate-evoked attenuated synchronization: Cross-correlation analysis of glutamate effects was done in 6 slices. In 3 of these cases, 25 µM glutamate transformed the LFP pattern within 2-3 min. In the other 3 cases, the glutamate dose was increased after 5 min from 25 µM to 50 µM which transformed the pattern within further 2-3 min. An example for the latter approach is shown in **Fig. 6-6A**. In this neuron, LFP pattern transformation by 50 µM glutamate was accompanied by a 7 mV depolarization of V_m from its 'resting' value of -45 mV. Concomitant with this depolarization, cellular discharge was accelerated from 48 to 228 spikes/min. The cross-correlogram in **Fig. 6-6A** for the recording from this neuron showed a shallower peak in glutamate vs. control indicating decreased synchronization and, correspondingly, the CFE value decreased from 0.5 to 0.35 while time lag increased from 90 to 150 ms **(Fig. 6-6B)**. The scatter plots for 5 neurons show that the effects were significant **(Fig. 6-6C)**. Spiking in 1 apparently similarly responding neuron did not cross-correlate with the LFP could thus not be analyzed. For the 6 neurons, mean values were -47.3 ± 2.9 mV for resting V_m, 5.0 ± 1.1 mV ($P< 0.001$) for the glutamate-evoked depolarization

and 52.1 ± 4.6 vs. 194 ± 61.0 spikes/min ($P< 0.001$) (i.e. a 3.7-fold acceleration) for control vs. glutamate.

NMDA-evoked enhanced network synchronization: Based on the above results from the dose-response relationships, 32 µM NMDA was applied to 7 neurons for cross-correlation analysis as this dose should rapidly transform the LFP pattern while not evoking oscillation trains too quickly. In the neuron of **Fig. 6-7A**, 32 µM NMDA caused from -50 mV a 10 mV depolarization early during pattern transformation and its discharge rate increased at the same time from 39 to 336 spikes/min. The cross-correlogram for this recording revealed enhanced synchronization in NMDA as the CFE value increased from 0.32 to 0.73 with a concomitant decrease of time lag from 110 to 3 ms **(Fig. 6-7B)**. The scatter plots for 5 neurons show that the effects were significant **(Fig. 6-7C)**. Spiking in the other 2 apparently similarly responding neurons did not cross-correlate with LFP and could thus not be analyzed. For the 7 neurons, mean values were -48.6 ± 2.4 mV for resting V_m, 8.4 ± 2.3 mV ($P< 0.001$) for the NMDA-evoked depolarization and 49.4 ± 6.1 vs. 355 ± 35.6 spikes/min ($P< 0.001$) (i.e. a 7.2-fold acceleration) for control vs. NMDA. In line with the assumption based on these findings that network synchronization was enhanced, the jitter of the time point of spiking in these neurons related to the LFP decreased from ±103.8 ± 34.4 ms in control to ±13.9 ± 2.25 ms in NMDA (i.e. to 15.2 ± 7.2 % of control) **(Fig. 6-7D)**.

6.4.4. V_m changes during NMDA-evoked oscillation trains

Next, it was studied how NMDA-evoked LFP oscillation trains correlate with the changes of neuronal V_m. 32 µM NMDA was used again as oscillation trains in 25 µM tended to start only after several minutes whereas 50 µM depressed them too quickly. **Fig. 6-8** exemplifies this for the

neuron shown in **Fig. 5-6A**, **B**, **D**. During rhythmic LFP inhibition starting 4 min into NMDA, V_m repolarized for ~0.5 s close to its resting value of -48 mV with concomitant spiking arrest. Then, a ramp-like depolarization developed that caused after ~0.5 s spike onset when also LFP oscillations recurred **(Fig. 6-8A)**. Between the onset and the end of a ramp depolarization by 18 mV, spiking accelerated from a value slightly lower than at steady-state before start of the trains to a value slighty higher with a corresponding amplitude decline. Over the next 30 s, LFP oscillation trains and ramp depolarizations shortened, the latter with a steeper slope and more depolarized peak (to a V_m value between -28 and -30 mV), a similar change in spike rate, but more pronounced amplitude decrease **(Fig. 6-8B)**. To test if bursting is network-dependent, this neuron was hyperpolarized 30 s later to -68 mV by injection of -100 pA dc current **(Fig. 6-8B)**. Bursting persisted (as also in other 5 cells tested), but at shorter duration with overlaying repetitive spiking, along with LFP transformation into small amplitude descrescendo-shaped bursts. At 6 min into NMDA, LFP was blocked while some random spiking persisted, and the neuron was depolarized further, now showing steep offset rhythmic hyperpolarizations with an initial 'rebound' spike. All effects reversed within 12 min after start of washout.

For 6 neurons, several parameters were analyzed for the most stable and longest oscillation train early during their appearance. Specifically, the train lasted for 7.1 ± 0.9 s, NMDA caused at the end of the train a 20.0 ± 6.3 mV depolarization from -48.3 ± 2.5 mV (P= 0.0006) and spike rate during the last second was 462 ± 45.7 spikes/min compared to 49.3 ± 6.7 spikes/min in control (P< 0.001) (thus 9.3-fold faster). V_m repolarized after the end of the train to -46.8 ± 2.9 mV (P= 0.06) and the pause until the next train started was 1.0 ± 0.1 s.

6.4.5. Post-agonist depression of LFP

Apart from their opposite action on LC synchronicity, both agents exerted a similar inhibitory effect. Specifically, 0.5-2 min after start of washout of NMDA **(Fig. 6-9A)** or glutamate **(Fig. 6-9B)**, V_m hyperpolarized and at the same time cellular spiking and LFP were blocked.

In 4 neurons, NMDA depolarized V_m at the start of such 'post-agonist depression' (PAD) from a resting value -48.7 ± 2.5 mV by 22.5 ± 6.4 mV (P= 0.006). Subsequently, V_m hyperpolarized during the inhibition maximally to -65.7 ± 5.0 mV (P= 0.005) and the effect reversed after 9.0 ± 1.4 min. In 4 different neurons, glutamate had depolarized V_m before the start of PAD from -48.5 ± 3 mV by 5.2 ± 3.2 mV (P= 0.04). During glutamate washout, the maximal hyperpolarization was to -52.0 ± 1.6 mV (P= 0.03) and the effect reversed after 1.5 ± 0.4 min.

6.4.6. Receptor-specificity of glutamate effects

Whereas NMDA binds selectively to NMDA-type iGluR, glutamate can act on NMDAR,AMPAR plus metabotropic glutamate receptors. To study if metabotropic receptors contribute to the observed glutamate effects, the unselective ionotropic glutamate receptor antagonist kynurenic acid was used.

In the neuron of **Fig. 6-10A**, kynurenic acid (500 µM) was applied during LFP pattern transformation due to 50 µM glutamate. After 20 s into kynurenic acid, LFP was blocked along with a 15 mV hyperpolarization and spike arrest. Several seconds later, V_m started to repolarize. Spikes and LFP bursts recurred after 80 s and control-like LFPs and spike rates were seen in the

presence of glutamate and kynurenic acid after 3 min **(Fig. 6-10A)**. Subsequent washout of the blocker in glutamate re-established the initial glutamate effects within 3-5 min (not shown). Specifically, in 4 neurons glutamate had depolarized V_m at the start of the kynurenic acid-evoked hyperpolarization from a resting V_m of -44.7 ± 0.5 mV by 3.5 ± 0.5 mV (P= 0.001). Early during kynurenic acid application in glutamate, the maximal hyperpolarization was to -52.5 ± 2.8 mV (P= 0.009) and the effect reversed after 2.3 ± 0.4 min. The late countering kynurenic acid effect shows that glutamate effects are mediated by iGluR. Kynurenic acid does not exert a novel inhibitory effect as our recent study (Rawal et al., 2019) showed that bath-application of 2.5 mM of the agent has no effect on the LFP and this was confirmed by 4 additional experiments of that type here **(Fig. 6-10B)**.

6.4.7. Persistence of single neuron spiking during network inhibition

NMDA- and glutamate-evoked blockade of intracellular spiking correlated well with inactivation of most of the 5-15 neurons typically comprising the LFP. However, early during kynurenic acid application in glutamate small amplitude random LFP spiking was seen when normal LFP bursts and neuronal spikes were blocked **(Fig. 6-10A)**. Similarly, mostly small amplitude LFP activity generated by few neurons persisted during either inhibition between NMDA-evoked oscillation trains, blockade of rhythm by the agents at high dose or the PAD **(Figs. 6-3C$_1$, 6-8, 6-9A, B)**. This indicates that some neurons are resistant to inhibitory NMDA and glutamate effects.

6.5. Discussion

We found that LFP bursting generated by non-synchronous phase-locked and jittered spiking of LC neurons changes during NMDA to fast oscillations due to enhanced synchronization whereas glutamate makes rhythm irregular by weakening synchronization. This is the first demonstration of opposing neural network burst pattern transformations by iGluR. We also found that NMDA and glutamate evoke PAD. Mechanisms and consequences for LC organization are discussed.

6.5.1. LFP recording of LC burst transformation

In our recent study, we have unraveled with suction electrode recording that LC neurons show jittered spiking that is yet phase-locked to generate rhythmic ~0.2-lasting LFP bursts (Rancic et al., 2018). Here, we found LFP bursts have a bell-shaped integrated signal envelope during both control and NMDA stimulation. This indicates that the jitter of spiking in estimated 5-15 neurons comprising this signal distributes equally around a center of activity comprising the LFP peak in both conditions. In the latter report, we also found that the LFP pattern changes to ~3 s-lasting multipeak plateaus by either increasing LC excitability with raised extracellular K^+ or during recovery from opioid inhibition (Rancic et al., 2018). Here, glutamate and NMDA elicited different LFP pattern transformations indicating that these changes in LC excitability do not eventually cause release of glutamate (Singewald and Philippu, 1998; Pal, 2018) which might then act on burst-generating NMDA receptors (for details, see below). Glutamate elicited pattern transformation at 25-50 µM. This can be functionally relevant as extracellular glutamate rises in vivo from a 1-10 µM baseline to >20 µM, e.g. during treatment with µ-opioid (ant) agonists (Feng et al., 1995; Singewald and Philippu, 1998; Pal, 2018).

The finding that kynurenic acid reversed the glutamate-evoked LFP pattern transformation shows a lack of involvement of metabotropic glutamate receptors in this effect. Contrary to our observation of distinct LFP transformations, single neuron recording here and previously (Olpe et al., 1989; Williams et al., 1991; Kogan and Aghajanian, 1995; Zamalloa et al., 2009) showed that glutamate and iGluR agonists only accelerate tonic spiking. As evident from this and the following discussion, LFP recording is a powerful tool to study the obviously complex organization of the neonatal LC.

6.5.2. LC synchronicity analysis with combined LFP and single neuron recording

NMDA-evoked LFP oscillations were more regular, faster and shorter than control bursts whereas glutamate made the rhythm irregular and more than doubled the duration of separate bursts, if still present. The conclusion that NMDA enhances and glutamate weakens neonatal LC synchronicity was proven by cross-correlating neuronal spikes with LFP peaks **(Figs. 6-6, 6-7)**. Besides, NMDA notably reduced intracellular spike jitter. Regarding mechanisms for these transformations, rhythm generation does not involve glutamatergic, GABAergic or glycinergic neurotransmission instead of coupling via gap junctions (Williams and Marshall, 1987; Christie et al., 1989; Christie, 1997; Ishimatsu and Williams, 1996). Consequently, NMDA and glutamate may enhance and weaken electrical coupling, respectively. In that regard, NMDA stabilizes synchronized LFP oscillations in gap junction-coupled inferior olive neurons of rat slices involving Ca^{2+}/calmodulin-dependent protein-kinase-I activation which enhances weak coupling of non-neighboring neurons (Turecek et al. 2014). Contrary, in the adult rat LC neuromodulators do presumably not directly counteract the postnatal decrease of gap junction coupling and instead neuromodulator-evoked spike slowing itself reverses this decrease (Alvarez et al., 2002). While that study did not reveal a correlation in

neonatal rats between spike rate and gap junction-coupling, we found here that faster spiking either increases (NMDA) or decreases (glutamate) synchronicity. We hypothesized recently that incomplete neonatal LC synchronicity reflects neuronal differences regarding spontaneous neuromodulator release which changes the V_m value shortly before the oscillation peaks, thus altering spike threshold (Rancic et al., 2018). Therefore, glutamate-evoked LC network desynchronization may also occur if neuron subclasses express different types and/or numbers of AMPAR and are consequently depolarized to different extent thus reaching spike threshold at diverging times. This is discussed in detail below.

6.5.3. PAD and periodic NMDA-evoked inhibition

While both types of LFP pattern transformation were associated with increased spiking, NMDA and glutamate also acted inhibitory. Specifically, during washout of both agents neuronal hyperpolarization was associated with a PAD-type spike and concomitant LFP depression whereas periodic inhibition of oscillations developed later during NMDA application. In vivo, PAD occurs after sensory stimulation-evoked bursting (Cedarbaum and Aghajanian, 1976; Foote et al., 1980). Regarding the mechanism, it was shown in adult rat slices that a AMPAR-triggered Na^+-dependent K^+ current causes PAD after glutamate, but not NMDA (Zamalloa et al., 2009). As both agents were effective here, we rather hypothesize that SK-type Ca^{2+}-activated K^+ channels are involved as ongoing neuronal depolarization likely causes a cytosolic Ca^{2+} rise mainly mediated by voltage-activated Ca^{2+} channels (Metzger et al., 2000). In fact, in adult rats in vivo (Aghajanian et al., 1983) and slices (Andrade and Aghajanian, 1984), numbers of current-evoked spikes correlate with the duration of a pronounced hyperpolarization that is attenuated by increased cytosolic Ca^{2+} buffering. Moreover, the pacemaker rate in LC neurons of mouse slices is regulated by cooperation of L- and

T-type Ca^{2+} channels with SK2 channels (Matschke et al., 2015, 2018). Enhanced cooperation of these channels may also contribute to the NMDA-related periodic interruption of LFP oscillations. As explanation, the cellular correlate of oscillation trains is rhythmic ramp-like LC neuron depolarization and concomitant spiking followed by spike-depressing hyperpolarization, possibly when Ca^{2+} rises reach the threshold for SK channel activation. Our finding that NMDA-evoked neuronal bursting persists during current-evoked hyperpolarization indicates that these events are voltage-clamped by gap junction-coupled neighboring neurons like in juvenile rat CA3 hippocampus (Neuman et al., 1989). Pharmacological analysis beyond the scope of this study is required to analyze underlying cellular mechanisms that can differ notably between neuron types showing similar NMDA-evoked bursting (Neuman et al., 1989; Zhu et al., 2004; Sharifullina et al., 2008; Mrejeru et al., 2011).

6.5.4. Burst transformation potentially due to modular LC organization

We hypothesized above and recently (Rawal et al., 2019) that iGluR effects on LC population burst patterns may be caused by 'modular' differences in neuronal properties. Specifically, ventrally-located adult rat LC neurons with shorter spikes and smaller afterhyperpolarizations than LC core neurons act as a 'pontospinal-projecting module' (Li et al., 2016) whereas dorsomedially-located small and densely packed GABAergic neurons in juvenile mice show faster spiking with enhanced adaptation (Jin et al., 2016). Topographically distinct LC modules exist also regarding afferent synaptic inputs and efferent projections (Schwarz and Luo, 2015). Two findings here support the concept of functional LC modules. Firstly, 3 of 10 neurons were uncoupled from network bursting as revealed with cross-correlation analysis and, secondly, spiking of some LC neurons persisted during oscillation train inhibition, NMDA- orglutamate-evoked blockade of rhythm at high doses,

PAD or kynurenic acid depression **(Figs. 6-3C$_1$, 6-8, 6-9, 6-10A)**. If some LC neurons are more sensitive to iGluR activation than others, these cells may release noradrenaline within their module to change the activities of neighboring neurons and astrocytes. E.g., if astrocytes are then activated via their α_1 receptor, they may release lactate to excite LC neurons in positive feedback via a novel receptor (Tang et al., 2014). While our bath-application approach for NMDA and glutamate was adequate for the aim of this study, in future work the agents should also be applied focally (or glutamatergic synapses activated optogenetically) to study whether LC modules differ in their sensitivity to iGluR agonists.

There seems to be a causal link between pattern transformations, opioids and iGluR. Specifically, transformation of tonic spiking into oscillatory ('burst') discharge during systemic μ-opioid receptor activation in adult rats was reversed by injecting NMDAR or AMPAR blockers into the LC (Zhu and Zhou, 2015). The authors hypothesized in this study that iGluR-dependent LC bursting is important for opioid tolerance and dependence. Reports from our laboratory showed that a similar LFP pattern transformation also occurs in the LC of neonatal rat slices during application of low doses (Panaitescu, 2012) and recovery from high doses (Rancic et al., 2018) of the μ-opioid receptor agonist DAMGO. Next, it could be studied, whether this in vitro LC burst pattern transformation (and also the similarly transformed pattern in raised extracellular K^+) can be antagonized by iGluR receptor antagonists.

6.6. Figures and Legends

Fig. 6-1

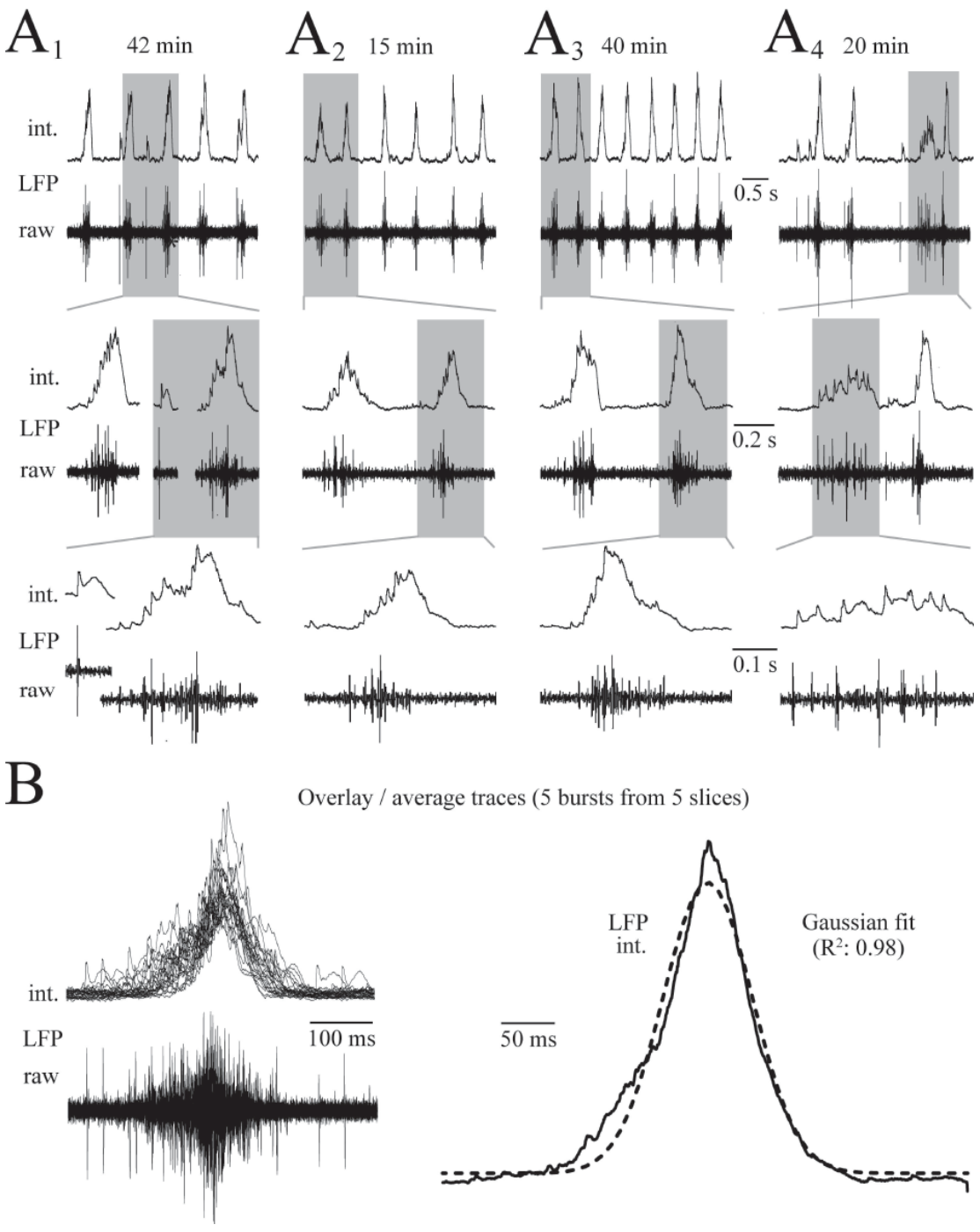

Fig. 6-1: Spontaneous local field potential (LFP) in newborn rat locus coeruleus (LC) slices. **A**, LFP was recorded with 40-60 µm tip size superfusate-filled suction electrodes positioned on slice surface in the LC neuron soma area. The differentially-amplified (10 k) and bandpass-filtered (0.3-3 kHz) 'raw' signal was also recorded after integration (∫, time-constant 50 ms). LFP examples in **A_1-A_3** from 3 different slices show that the integrated signal has a similar shape and occurs at quite regular rate and amplitude. However, displaying individual bursts at higher time resolution indicates in raw traces that active neuron numbers, their distance from the electrode (indicated by spike amplitude) and time points of their discharge differ notably. In ~30 % of slices, the LFP pattern is less regular and smaller amplitude bursts typically show a more dispersed pattern **(A_4)**. **B**, traces on the left are overlaid from 5 consecutive bursts of the 3 slices shown in **A_1-A_3** plus 2 further slices with similarly regular LFP pattern. Traces on the right represent the average of integrated traces in the left plus Gaussian fit for its kinetics revealing a bell-shaped LFP envelope.

Fig. 6-2

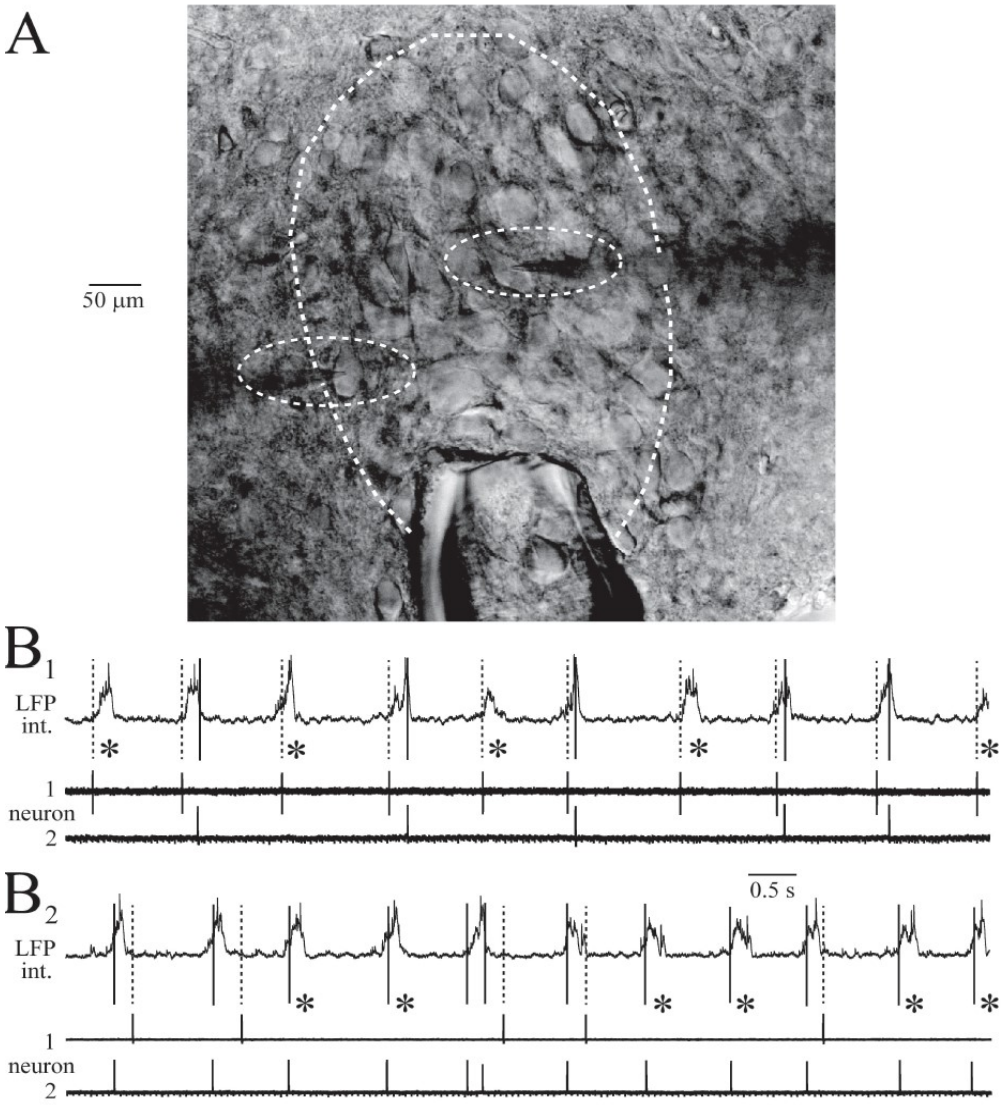

Fig. 6-2: LC neuron spike jitter and failure. A, shows a photograph of the LC with the suction electrode positioned close to the rim of the LC neuron somata area next to the 4th ventricle (not shown) while two patch electrodes were positioned onto the soma of LC neurons for recording their spiking. **B**, shows such recording in 2 slices **(B_1, B_2)**. In both examples, with **B_1** corresponding to the photo in **A**, 1 neuron fires a single spike during each LFP burst whereas the other cell shows spike failures (see asterisks). The LFP comprises likely mostly discharge from 5-15 neurons (see Results). Thus, random spike failures cause differences in LFP amplitude while jitter regarding the time point of discharge during the LFP (see distance between solid and dotted lines and compare **Fig. 6-7D**) explains LFP duration and shape variability.

Fig. 6-3

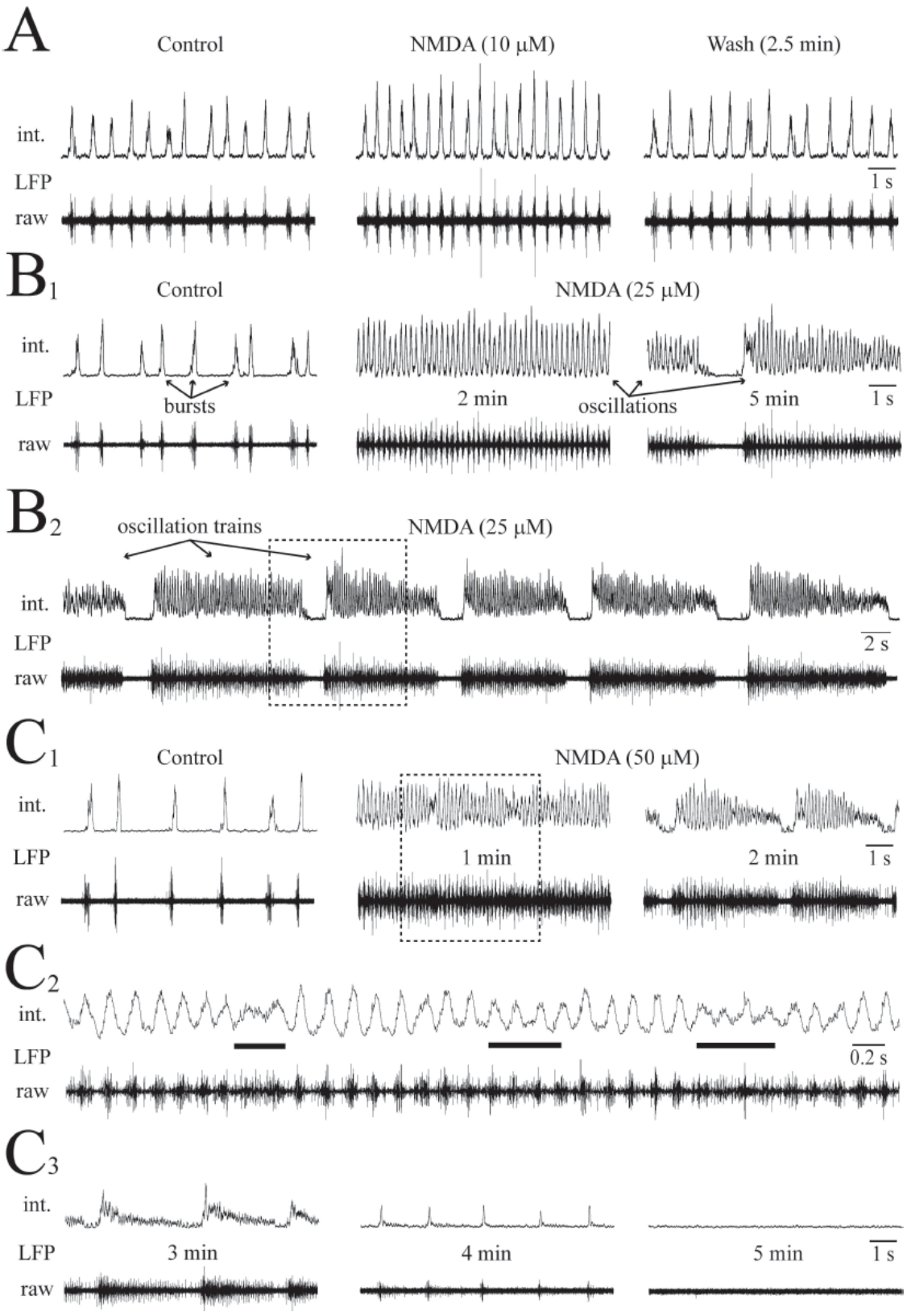
A
Control
NMDA (10 μM)
Wash (2.5 min)
int.
LFP
raw
1 s
B1
Control
NMDA (25 μM)
int.
LFP
raw
bursts
2 min
oscillations
5 min
1 s
B2
oscillation trains
NMDA (25 μM)
int.
LFP
raw
2 s
C1
Control
NMDA (50 μM)
int.
LFP
raw
1 min
2 min
1 s
C2
int.
LFP
raw
0.2 s
C3
int.
LFP
raw
3 min
4 min
5 min
1 s

Fig. 6-3: NMDA effects on LFP. A, 10 μM NMDA increased LFP rate and shortened burst duration. **B_1**, at 2 min 25 μM NMDA evoked fast 'oscillations' lacking an interevent inactivity phase like in control LFP rhythm (compare left and middle panels). At 5 min, LFP oscillations were transiently depressed (right pannels). **B_2**, shows several cycles of resulting 'oscillation trains' at lower time resolution (train in **B_1** indicated by dashed-line box). Initially, early oscillation and oscillation train rates and durations were similar. However, over several train cycles oscillation amplitude diminished and rhythm became irregular toward the end of each event. **C_1**, at 1 min 50 μM NMDA caused oscillations similar to those in 25 μM, though this time amplitude fluctuation occurred (middle panels). Dashed-line box indicates time period for which oscillations are displayed at higher time resolution in **C_2** showing on the raw trace that smaller amplitude integrated signals were due to tonic activity. Right panels in **C_1** show augmented decline of amplitude, duration and regularity of oscillation trains at 2 min compared to effects in 25 μM NMDA at ~5 min. **C_3**, at 3 min in NMDA oscillation trains were notably attenuated (left) whereas only a spike-shaped rhythm remained at 4 min and no activity was seen at 5 min.

Fig. 6-4

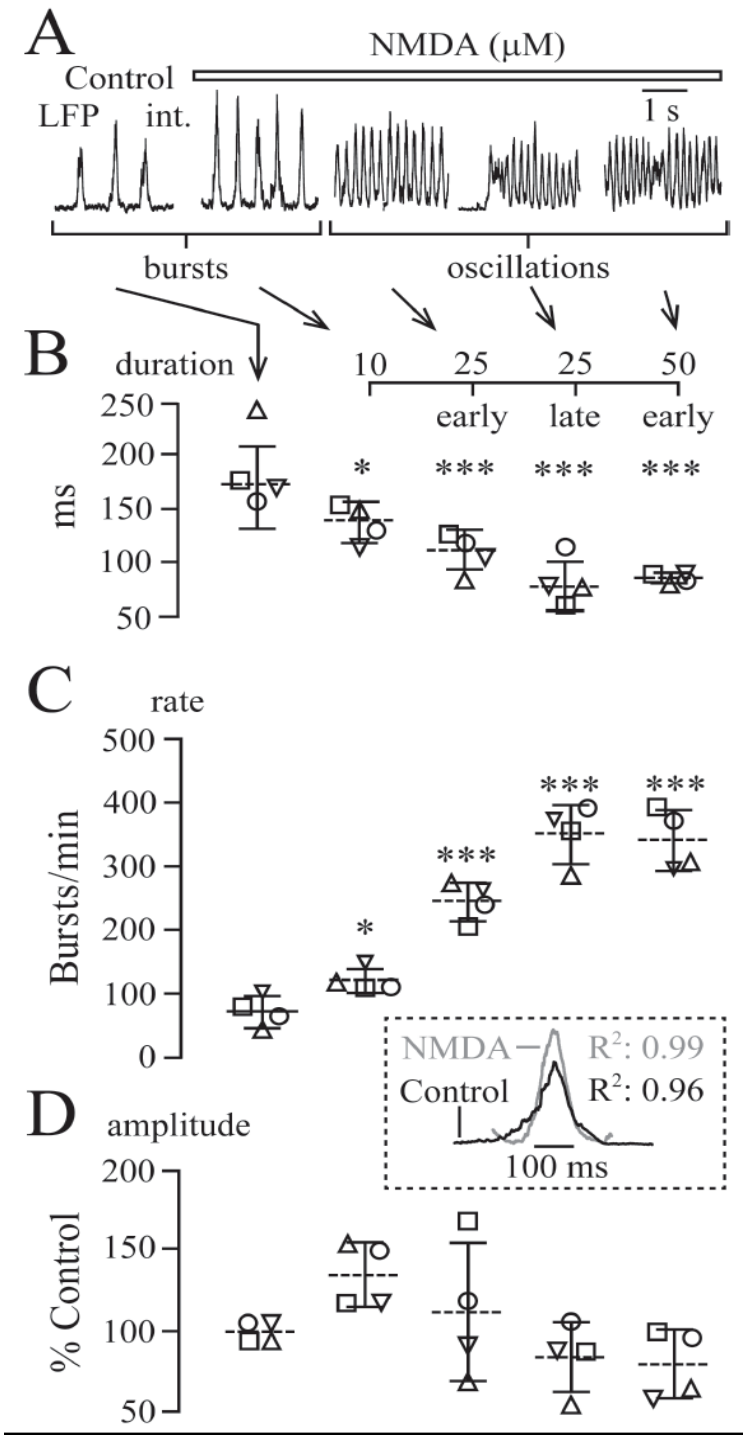
A
NMDA (μM)
Control
LFP
int.
1 s
bursts
oscillations
B
duration
10
25
25
50
early
late
early
ms
250
200
150
100
50
*
***
***
***
C
rate
Bursts/min
500
400
300
200
100
0
*
***
***
***
NMDA
Control
R²: 0.99
R²: 0.96
100 ms
D
amplitude
% Control
200
150
100
50

Fig. 6-4: Quantification of NMDA effects on LFP pattern. A, summary of LFP pattern transformation parameters exemplified in **Fig. 6-2**. 'Early' oscillations occurred during the first 1-3 min in 25 and 50 µM NMDA. In 'late' phase between 3-5 min (or at the start of wash), oscillation trains developed in 25 and 50 µM NMDA. **B-D**, analysis in 4 slices indicated by each symbol revealed that single event duration **(B)** and rate **(C)** decreased progressively at all doses whereas amplitude **(D)** did not change. The inset shows for averaged integrated traces from 5 consecutive bursts in 3 of the 4 slices that the LFP has a Gaussian shape in both control LFP and NMDA. Lines indicate mean values (dotted line) ± SD (solid line), significance was determined with one-way ANOVA with Dunnett's post test ($F(1, 5) = 13.91$, $P < 0.0001$, ANOVA). *$P < 0.05$, *** $P < 0.001$).

Fig. 6-5

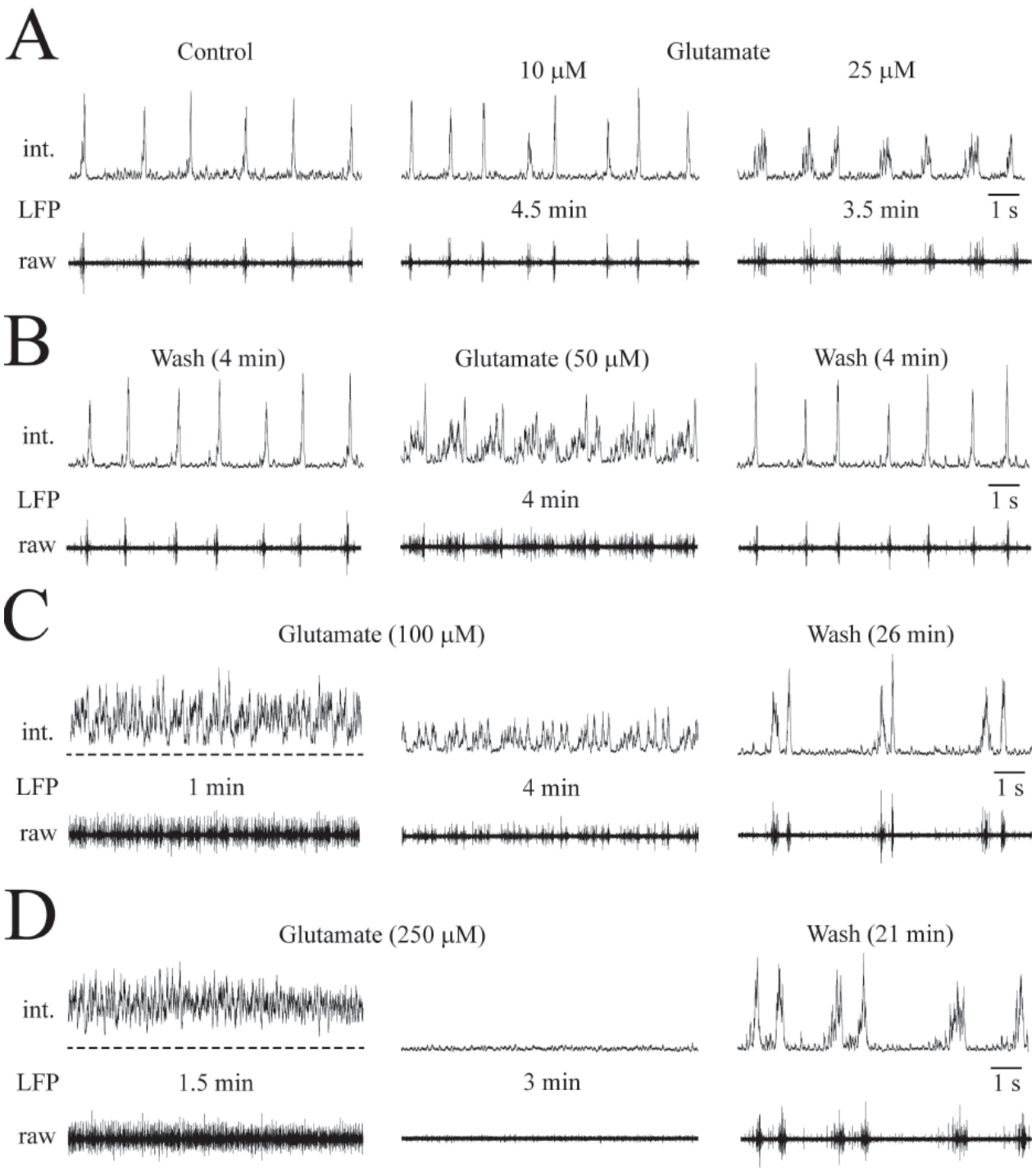
A
Control
Glutamate
10 μM
25 μM
int.
LFP
4.5 min
3.5 min
1 s
raw
B
Wash (4 min)
Glutamate (50 μM)
Wash (4 min)
int.
LFP
4 min
1 s
raw
C
Glutamate (100 μM)
Wash (26 min)
int.
LFP
1 min
4 min
1 s
raw
D
Glutamate (250 μM)
Wash (21 min)
int.
LFP
1.5 min
3 min
1 s
raw

Fig. 6-5: Glutamate effects on LFP pattern. Recording is from a single slice. **A**, 10 µM glutamate had no effect whereas 25 µM changed LFP pattern to longer-lasting, smaller amplitude bursts at similar rate as in control. **B**, after wash 50 µM evoked almost merged ramp-like multi-peak bursts. **C**, 100 µM glutamate at 1 min raised integrated trace baseline as indication of tonic activity evident on raw trace, but still showed groups of multipeak bursts before rhythm declined at 4 min. Recovery resulted in same number of bursts as in control, but they appeared as doublets. **D**, 250 µM glutamate caused initially massive tonic activity before rhythm ceased at 3 min. Recovery after 21 min re-established bursting at a rate similar to control. This time LFP doublets were intermingled with single bursts and all events had ramp-like shape similar to those in 25 and 50 µM glutamate.

Fig. 6-6

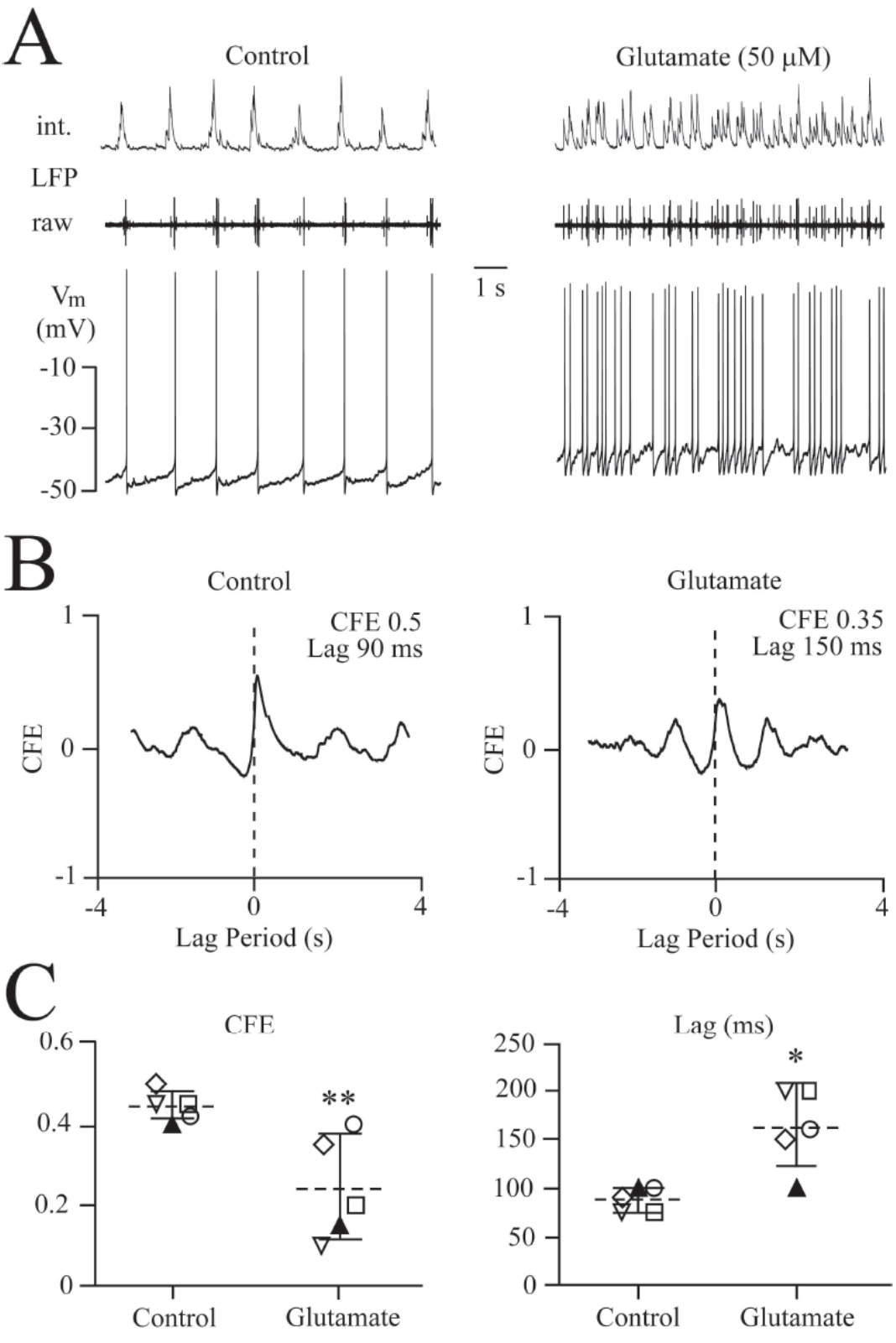
A
Control
Glutamate (50 µM)
int.
LFP
raw
Vm
(mV)
-10
-30
-50
1 s
B
Control
Glutamate
CFE 0.5
Lag 90 ms
CFE 0.35
Lag 150 ms
CFE
1
0
-1
-4
0
4
Lag Period (s)
C
CFE
Lag (ms)
0.6
0.4
0.2
0
250
200
150
100
50
**
*
Control
Glutamate

Fig. 6-6: Cross-correlation of desynchronizing glutamate effects. A, left panel shows that a whole-cell-recorded LC neuron 'spiked' at the peak of membrane potential (V_m) oscillations that were in phase with the simultaneously recorded LFP. Right panel shows that 50 μM glutamate, 2 min after start of application, transformed LFP pattern to irregular bursting accompanied by a neuronal depolarization of 7 mV and accelerated spiking with concomitant ~20 % amplitude decrease that was reversible as evident from the continuous recording from that neuron shown in **Fig. 6-10A**. **B**, cross-correlogram between neuronal spike and LFP during control (left panel) and glutamate (right panel) shows desynchronizing effect on LC network indicated by a decreased correlation function estimate (CFE) value and increased lag time. CFE is the measure of the peak value on Y axis and lag time indicates the shift of peak from 0 time on the X-axis. **C**, scatter plots from neuron in **A** (filled symbol) and 4 other neurons reveal a difference in CFE values (left) and lag times (right) for control vs. glutamate as determined with two-tailed paired t-test. **P*= 0.034, ***P*= 0.0072.

Fig. 6-7

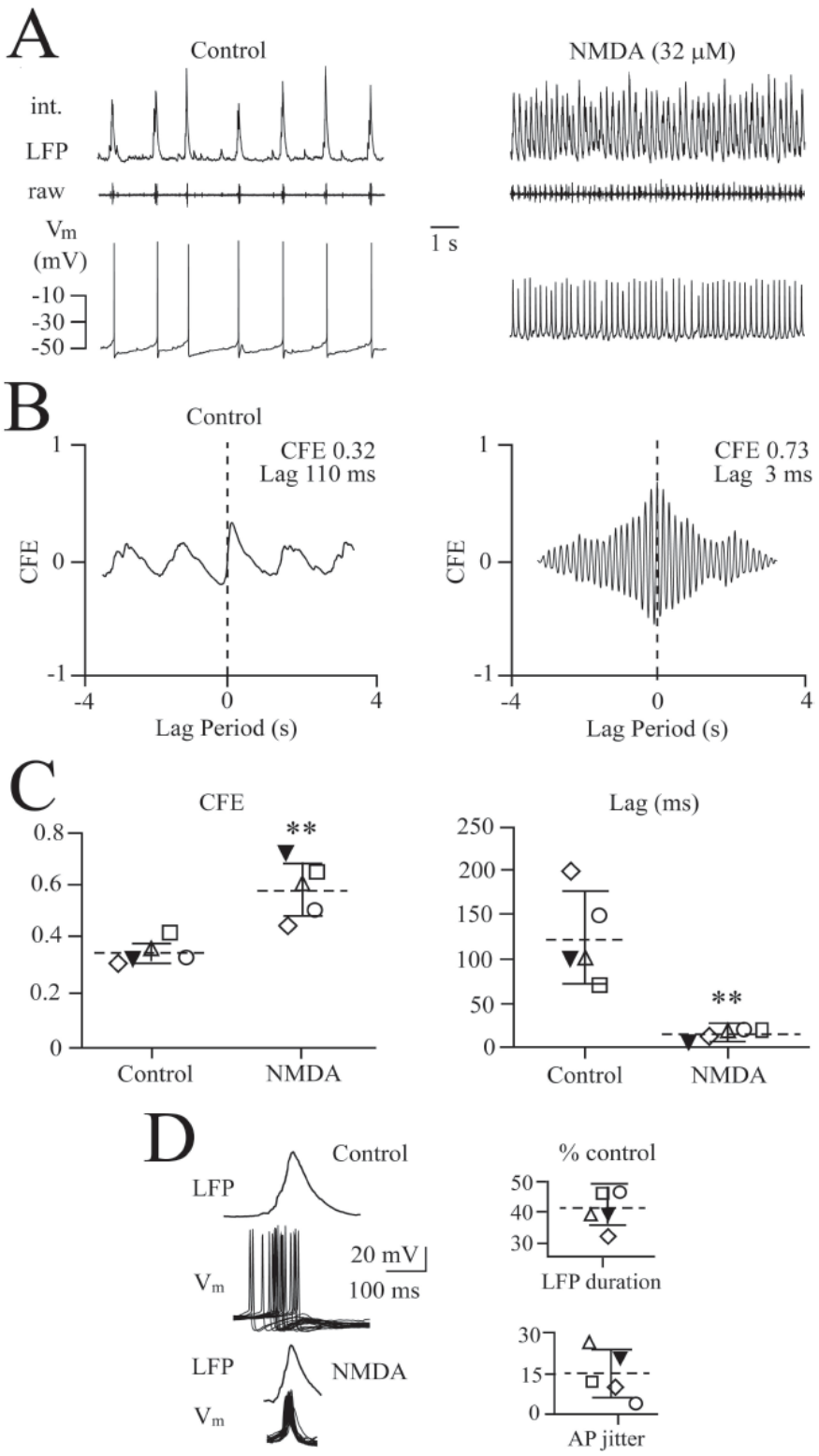
A
Control
NMDA (32 μM)
int.
LFP
raw
Vm
(mV)
-10
-30
-50
1 s
B
Control
CFE 0.32
Lag 110 ms
CFE 0.73
Lag 3 ms
CFE
Lag Period (s)
C
CFE
Lag (ms)
Control
NMDA
D
Control
LFP
20 mV
100 ms
Vm
NMDA
% control
LFP duration
AP jitter

Fig. 6-7: Cross-correlation of NMDA effects. A, shows the LFP pattern transformation to faster oscillations at steady-state in 32 µM NMDA accompanied by V_m depolarization of 10 mV and accelerated spiking with a concomitant ~20 % amplitude decrease that was reversible as evident from the continuous recording from that neuron shown in **Fig. 6-8A**. **B**, cross-correlogram between neuronal spike and LFP during control (left panel) and NMDA (right panel) shows synchronizing effect on LC network indicated by higher CFE value and lower lag time. **C**, scatter plots from neuron in **A** (filled symbol) and 4 other cells reveal significant difference in CFE values (left) and lag time (right) for control vs. NMDA as determined with two-tailed paired t-test $^{**}P = 0.0059$ and $^{**}P = 0.009$ respectively. **D**, overlaid traces (also averaged for LFP signal) from 20 consecutive events in control (upper traces) and NMDA (lower traces) in neuron of **A** reveals a notably reduced jitter of cellular spiking in NMDA, plotted as a percentage change from control in lower right scatter plot for this neuron (filled symbol) and the other 4 cells. Upper scatter plot represents the percentage change in integrated LFP duration for the same experiments. Significance for both plots was determined with two-tailed paired t-test ($^{**}P = 0.0059$ and $^{**}P = 0.009$, respectively).

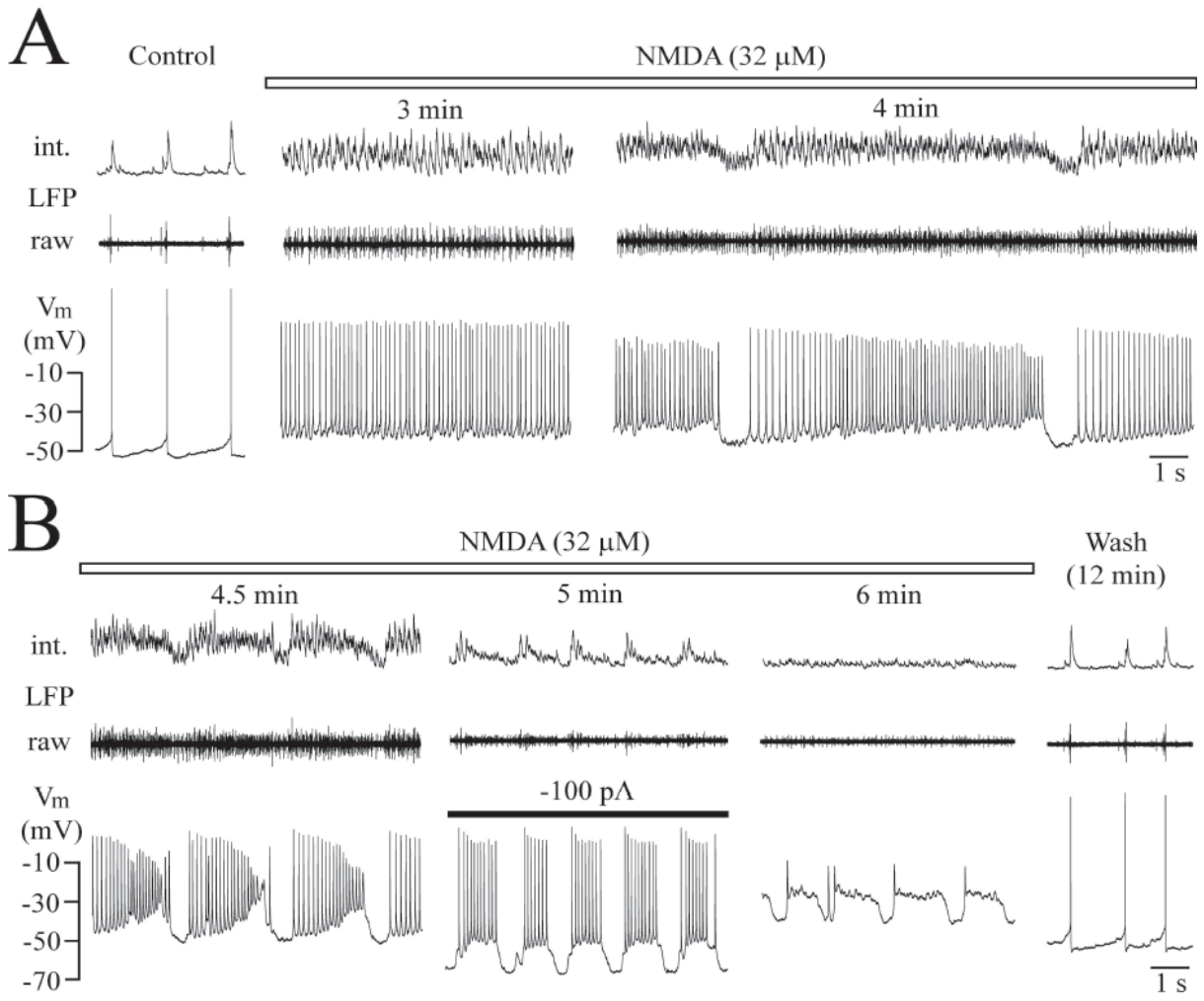

Fig. 6-8: Cellular NMDA effects. A, in continuation of the recording from the neuron shown in **Fig. 6-7A** (left and middle panels), NMDA-evoked V_m oscillations started to become interrupted by ~1 s-lasting rhythmic hyperpolarizations causing spike blockade. The resulting LFP oscillation trains started after the inactivity phase with concomitant progressive neuronal depolarization leading to accelerated spiking at decreased amplitude (right panels). **B**, at 4.5 min into NMDA LFP oscillation trains became shorter in synchrony with V_m burst time periods (left panels). 30 s later, rhythmic bursting persisted during hyperpolarization to -68 mV due to d.c. current injection via the patch electrode. 30 s after cessation of current injection LFP was blocked at 6 min NMDA, but tonic spiking from some neurons was still evident in raw signal. The neuron showed at a more depolarized level V_m hyperpolarizations with sharp offset evoking a small 'rebound' spike. Both V_m and LFP recovered 12 min after start of wash.

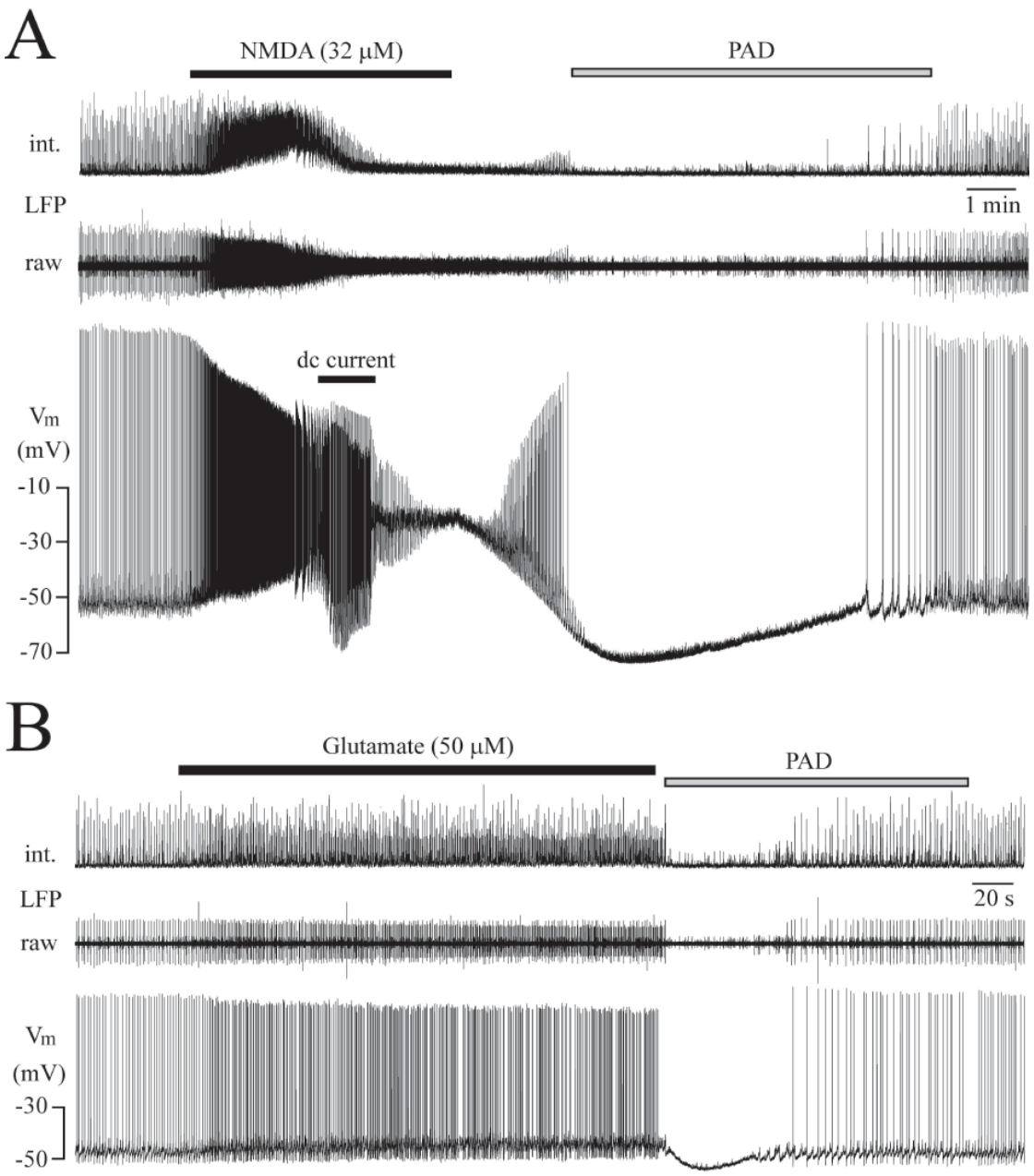

Fig. 6-9: Post-agonist depression (PAD). A, shows the continuous recording from the neuron of **Figs. 6-6** and **6-7** on a condensed time scale. The emphasis here is on showing that immediately upon start of NMDA washout, the neuron starts to hyperpolarize concomitantly with partial recovery of blocked LFP bursting. However, after 2 min, in synchrony with pronounced neuronal hyperpolarization, cellular spikes and also LFP were blocked again by PAD. Neuronal spiking and LFP bursting resumed again after about 5 min. **B**, shows an example for corresponding glutamate-evoked PAD in a different neuron.

Fig. 6-10

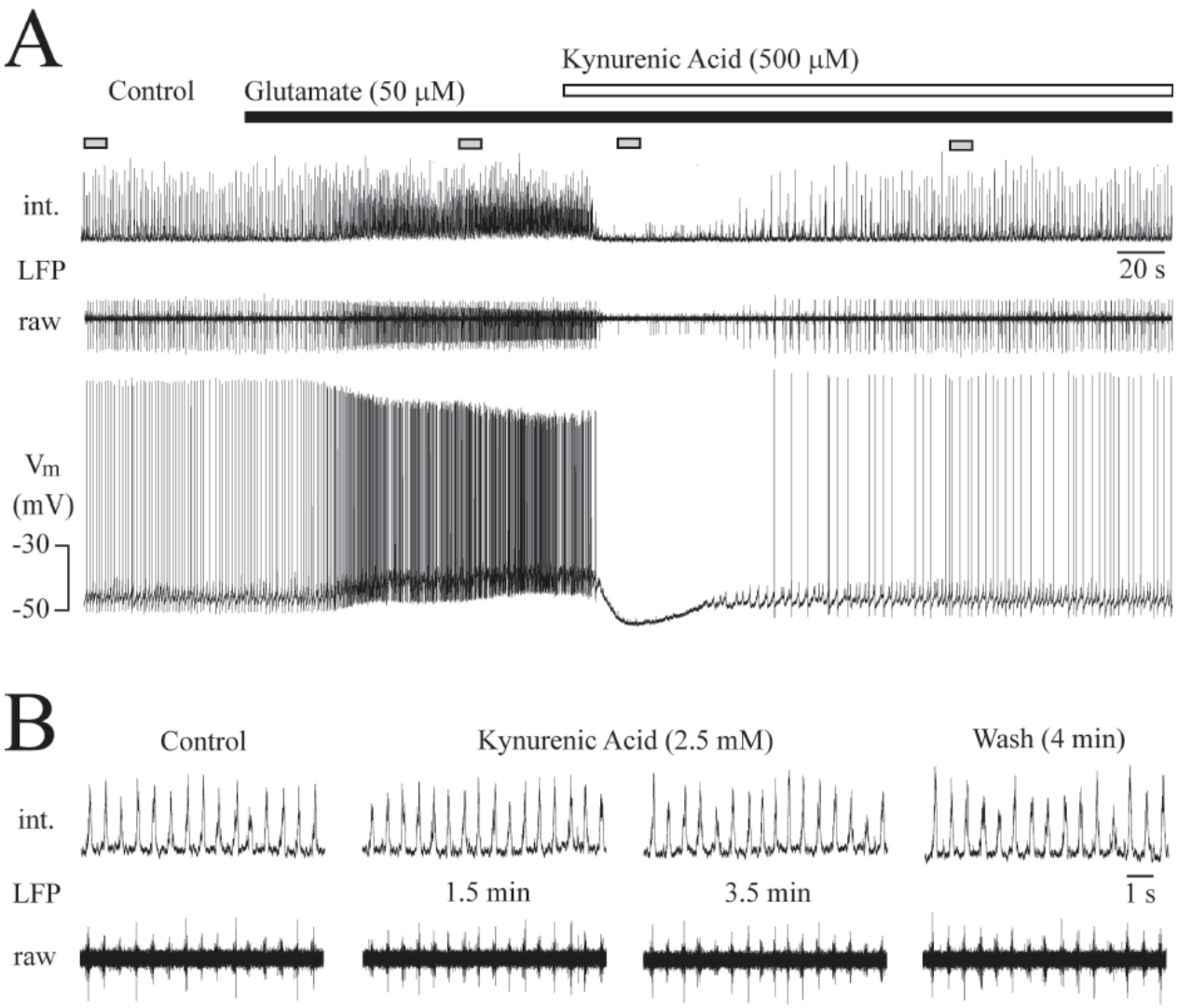

Fig. 6-10: Receptor-specificity of glutamate effects. A, shows for the same neuron illustrated in **Fig. 6-6** the pattern-transforming response to glutamate on a condensed time scale. In the initial phase of application of the non-selective competitive ionotropic glutamate receptor blocker kynurenic acid (500 µM), LFP and neuronal spiking were abolished along with a pronounced hyperpolarization. Subsequently, LFP, V_m and spiking recovered to control levels during continuous application of kynurenic acid in glutamate. **B**, the initial inhibitory kynurenic acid action on LFP and neuron bursting depended on the presence of glutamate as addition of the drug to control superfusate had no effect on LFP as measured in a different slice.

CHAPTER 7

General Discussion

The rationale for this thesis is based on preliminary findings from our laboratory showing that the neonatal rat LC network isolated in a brain slice generates rhythmic ~0.2 s-lasting LC population bursts as revealed with suction electrode recording (Kantor, 2012; Kantor et al., 2012; Panaitescu, 2012). These reports showed some properties of this rhythm, like its response to changes in superfusate Ca^{2+} (Kantor, 2012; Kantor et al., 2012) or to theophylline (Panaitescu, 2012). However, the mechanism of this LFP is not explored yet and it is also not clear whether this population bursting can change its activity pattern in quantitative fashion under the influence of an unspecific increase in LC excitability evoked by raised superfusate K^+ or, more specifically, by glutamate and agonists of its iGluR subtypes, namely the AMPAR and the NMDAR. The present findings revealed various novel features of the isolated neonatal LC network that are pivotal to understand its functional organization in more detail. Specifically, so far both the neonatal and adult LC are mostly considered to comprise a relatively simple neural circuit generating mostly synchronous spiking (Christie, 1997). However, since recently an increasing number of studies emerges showing that the adult LC is a 'complex neuromodulatory system'. This is expressed also in the title of a pivotal publication in 'Neuron' by the Logothetis/Eschenko/Totah group who are among the international leaders in analyzing in vivo brain activities (Totah et al., 2018). Correspondingly, the present findings show that already the neonatal LC has a multiplicity of features indicating a complex and modular organization.

7.1. Summary of novel findings on LC properties based on LFP recording

The neonatal rat LC comprises ~1000 neurons and ~100, mainly astrocytic, glial cells that form a spindle-shaped nucleus of ~300 µm diameter in rostrocaudal and ~700 µm in dorsoventral

extension (Ishimatsu and Williams, 1996; Ballantyne et al., 2004). As the gap junction-coupled LC neurons were assumed to discharge at the same time a single action potential at a rate of ~1 Hz, one could assume that this generates a rhythmic LFP of 1-5 ms duration as seen with extracellular recording in synchronously active neurons of various brain structures, both in vivo and in vitro (Ballanyi and Ruangkittisakul, 2009; Buzsáki et al., 2012; Einevoll et al., 2013; Totah et al., 2018). However, in the only slice study aiming at LFP/MUA recording in the adult rat LC, a signal was seen with 'broken glass electrodes' only when network excitability was raised with Ba^{2+} and/or tetraethylammonium (Ishimatsu and Williams, 1996). Also in the pre-BötC breathing center with similar dimensions as the LC in neonatal rats, extracellular recording with fine-tipped microelectrodes failed to unravel a rhythmic inspiratory-related LFP. Contrary, a robust LFP was seen by the group of Ramirez when they positioned a superfusate-filled suction electrode, typically used for monitoring respiratory-related rhythmic bursting of motor neurons in ventral nerve roots (Ballanyi and Ruangkittisakul, 2009), above the pre-BötC on the surface of the 'breathing' brainstem slices (Lieske et al., 2000). In the preliminary studies from our group (Kantor, 2012; Kantor et al., 2012; Panaitescu, 2012), the same suction electrode-based recording approach was successful to reveal a robust LFP in the LC of neonatal rat slices. Our recently published study representing project-1 in this thesis (Rancic et al., 2018), showed firstly that it is principally possible to record a small amplitude LFP in the extracellular space between visually identified neuron somata with a superfusate-filled unbroken patch electrode. But, this was mostly only the case when slight positive pressure was applied to avoid clogging of the electrode tip. By just slightly moving the position of the recording patch electrode closer to the membrane of a single LC neuron, larger amplitude rhythmic single action potential discharge could be recorded from that cell whereas the LFP disappeared. This indicates that the extracellular space within the LC has a complex geometry of submicrometer scale current sources and sinks (Buzsáki et al., 2012; Einevoll

et al., 2013). As a conclusion from these technical aspects of LFP recording, this study revealed that suction electrodes of 40-60 µm outer tip diameter are optimal for recording the LFP rhythm with a very good signal-to-noise ratio for several hours from the same spot within or at the edge of the LC (Rancic et al., 2018).

Apart from this technical aspect, that study established that the extensive gap junction-mediated electrical coupling of neonatal LC neurons is not sufficient to synchronize their spontaneous pacemaker-like single AP spiking as previously proposed in various reports (Williams & Marshall, 1987; Christie et al., 1989; Ishimatsu & Williams, 1996; Christie, 1997). Instead, it was demonstrated in this thesis with combined LFP recording and monitoring of either extracellular dual single-unit activity or intracellular spiking in one neuron (projects-1, -3 and -4) that the rhythmic ~0.2 s-lasting LC population bursts represent summated APs from 5-15 neurons. Each of these LC neurons discharges a single AP during a particular phase of the LFP and such spiking shows a jitter of several tens of milliseconds. The LFP has a bell-shaped, i.e. Gaussian, envelope that is particularly evident from the integrated signal trace **(Fig. 7-1)**. This indicates that the single neuron AP discharge distributes normally around the peak of LC network bursting.

This initial work of project-1 (Rancic et al., 2018) also showed that the neonatal rat LC is capable of transforming its bell-shaped LFP pattern after its isolation in a slice. Specifically, very similar, several seconds lasting multipeak bursts were seen either upon increasing network excitability by raising superfusate K^+ from the physiological value of 3 mM to 7 mM or early during recovery from blockade of rhythm by activating µ-opioid receptors with DAMGO **(Fig. 7-1)**. The common link between these similar pattern transformations of LC network bursting might be as follows. In vivo, a corresponding burst pattern transformation in LC neurons, seen during systemic application

of the μ-opioid receptor agonist morphine, is blocked by kynurenic acid (Zhu and Zhou, 2005) whereas raised superfusate K^+ may cause release of glutamate within the slice (Ballanyi, 1999; Pál, 2018). This might indicate that iGluR receptor activation is involved in both these scenarios. In fact, that was the rationale for project-4, i.e. to study effects of glutamate and NMDA on LFP pattern and LC neuron activities. NMDA was chosen as this iGluR agonist causes activity bursts lasting for several seconds in neurons of slices from diverse brain regions (Neuman et al., 1989; Zhu et al., 2004; Sharifullina et al., 2008; Mrejeru et al., 2011).

In fact, project-4 revealed that both glutamate and NMDA transform the LFP pattern. However, neither agent was able to mimic the effect of high K^+ or DAMGO washout. Instead, glutamate made the rhythm irregular and decreased network synchronicity whereas NMDA did the opposite by increasing the regularity and the synchronicity of LC bursting. While NMDA caused rhythmic oscillation trains lasting several seconds, that LFP pattern differed substantially from the one evoked by high K^+ and recovery from DAMGO **(Fig. 7-1)**. These results indicate that the latter pattern transformation is not simply due to an effect of an evoked increase of interstitial glutamate levels (in case of high K^+) or caused by tonic interstitial glutamate in conjunction with activation of a $G_{i/o}$ protein-mediated cellular signaling pathway activated by opioids (in case of DAMGO) (Williams and North, 1984; North and Williams et al., 1985). It was surprising that glutamate evoked the pattern transformation already at 50 μM, which is only slightly higher than its tonic interstitial concentration in vivo at rest and similar to levels seen in vivo, e.g. during treatment with μ-opioid (ant)agonists (Feng et al., 1995; Singewald and Philippu, 1998; Pal, 2018). This may mean that a uniform slight increase in interstitial glutamate within the LC might perturb the normally phase-locked rhythmic output activity of its neurons and this might change the efficacy of NA release at the target sites in diverse brain regions (Totah et al., 2018). However, it needs to

be considered that in all projects of this thesis, agents were administered by addition to the superfusate ('bath-application'). This means that local increases of glutamate evoked by afferent synaptic input to some neuron-astrocyte 'modules' within the LC might have a different effect on the output activity of this module in vivo. In any case, the bath-application approach revealed that different iGluR agonists change the LC rhythm in different ways as shown in projects-3 and 4. Specifically, both glutamate and QUI act very similarly by making LFP bursting irregular and prolonging the duration of single bursts that can show, if still present, a ramp-like pattern. Contrary, AMPA, KA and NMDA accelerate LFP rate to result in merged events of sinusoidal shape. These oscillations persist during 5 min bath-application of AMPA or KA and show rhythmic amplitude fluctuations that are particularly evident in the integrated signal trace and indicate the occurrence of intermittent tonic discharge. In the case of NMDA, the LFP oscillations stop for ~1 s after several minutes of application and then reoccur as 'oscillation trains' with rhythmic interruptions. All these LFP burst pattern transformations were caused by the specific effects of the agents on iGluR because they were reversed by the unselective competitive iGluR antagonist kynurenic acid. This indicates that also the effects of glutamate and QUI, that can both principally also activate metabotropic glutamate receptors (Traynelis et al., 2010), is restricted to activation of iGluR. It was not expected that QUI had different effects on the LFP than AMPA and KA. This is because in isolated neurons or expression systems all three agents activate the AMPAR and they differ mostly regarding their efficacy of binding as well as activation and/or inactivation kinetics of ion currents through the receptor-coupled cation ion channel (Traynelis et al., 2010). Thus, this is the first study showing that QUI effects on iGluR can evoke a basically different action on spontaneous neural network bursting than AMPA and KA who both act similarly on LC rhythm.

In projects-3 and 4, dose response relationships revealed on the one hand that the LFP is accelerated by similar doses of AMPA, KA and NMDA as single neuron spiking in previous slices studies on rats. Specifically, spiking in single LC neurons of juvenile and adult rat slices persisted at increased rate at 10 µM AMPA, KA or QUI (Kogan and Aghajanian, 1995; Zamalloa et al., 2009). Here, the LFP was blocked by 1 µM AMPA, 5 µM KA and 0.5 µM QUI. V_m recording at these concentrations is needed in follow-up studies to analyze if neonatal LC neurons under the present experimental conditions (or at the early postnatal developmental stage) are more sensitive to AP inhibition by the agents.

As a further new finding, no iGluR-related PAD occurred early during washout of AMPA, KA or QUI whereas both glutamate and NMDA evoked such inhibition. Specifically, during washout of both agents the amplitude of the post-agonist hyperpolarization in single inactivated LC neurons was correlated with the extent and time course of LFP depression whereas in the case of NMDA periodic inhibition of oscillations developed later during sustained application of the agent. Similarly, in vivo post-activity depression occurred after sensory stimulation-evoked bursting (Cedarbaum and Aghajanian, 1976; Foote et al., 1980). Regarding the mechanism of both types of LC neuron inhibition, an AMPAR-triggered Na^+-dependent K^+ current caused PAD after glutamate, but not NMDA (Zamalloa et al., 2009). As both agents evoked PAD here, SK channels might rather beinvolved as ongoing neuronal depolarization likely causes a Ca_i rise mediated mostly by voltage-activated Ca^{2+} channels (Metzger et al., 2000; Kulik et al., 2002). In adult rats in vivo (Aghajanian et al., 1983) and slices (Andrade and Aghajanian, 1984), the number of Aps evoked by d.c. current injection correlates with the duration of a major hyperpolarization that is attenuated by increased Ca_i buffering. Moreover, theAP rate in LC neurons of mouse slices is modulated by cooperation of L- and T-type Ca^{2+} channels with SK2 channels (Matschke et al.,

2015, 2018). Enhanced interaction of these channels may also be involved in NMDA-related periodic interruption of LFP oscillations. For an explanation, the V_m correlate of oscillation trains is ramp-like rhythmic depolarization and concomitant spiking followed by spike-depressing hyperpolarization, possibly when Ca_i rises reach the SK channel activation threshold The finding that NMDA-evoked neuronal bursting persists during current-induced sustained V_m hyperpolarization indicates these events are voltage-clamped by gap junction-coupled neighboring neurons as in the CA_3 area of the juvenile rat hippocampus in vitro (Neuman et al., 1989).

As a further new result, neither the unselective competitive iGluR blocker kynurenic acid nor the non-competitive AMPAR blocker GYKI disrupted LFP bursting. On the one hand, this substantiates conclusions from previous slice studies on single neurons showing that the mechanism of generation of presumably synchronous spiking in the LC network does not depend on iGluR (Alvarez et al., 2002; Olpe et al., 1989; Zamalloa et al., 2009). On the other hand, this property of the neonatal LC enabled the analysis of a potential TARP-mediated stimulatory effect of the competitive AMPAR blocker CNQX on LC network bursting. In fact, the results that were just published from the study representing project-2 (Rawal et al., 2019), demonstrate that neonatal rat LC neurons express a functional TARP-AMPAR complex. Specifically, CNQX caused a modest (~5 mV) depolarization that was associated with more than doubling of LFP burst rate. Likely, the bath-applied CNQX depolarized all LC neurons as all these cells in a single multiphoton imaging plane showed a similar rise of Ca_i. However, with the slow bath-application approach, the depolarization might have spread via the gap junction coupling from some directly responsive neurons in a specific LC module with a functional TARP-AMPAR complex to neighboring neurons lacking this property. In any case, the stimulatory CNQX effect spread throughout the neuronal LC network whereas neighboring astrocytes, that are also coupled via gap junctions to the adjacent

neurons, didn't show a CNQX-evoked Ca_i increase instead of spontaneous Ca_i rises (in a subpopulation of cells). Regarding the mechanism, the CNQX-evoked neuronal Ca_i rises are possibly mediated by L-type voltage-gated Ca^{2+} channels as indicated by the blocking effect of nifedipine.

In summary of all the above findings, novel LFP recording using suction electrodes revealed that the (isolated) neonatal rat LC is a complex neural network that can transform its output activity pattern in distinct ways under the influence of changes in network excitability evoked by either high K^+ and opioids as well as glutamate, AMPA, KA or QUI, all acting on iGluR.

7.2. Findings based on simultaneous LFP and neuronal V_m recording

The above discussion shows that LFP recording was already sufficient to unravel that the neonatal rat LC is a differentiated and complex neural circuit. However, combining this approach with whole-cell V_m recording from individual neurons provided further new information. Firstly, as noted above V_m recording showed that the PAD of the LFP at the start of washout of glutamate and NMDA correlates with a sustained hyperpolarization of single neurons that abolishes their spiking. Furthermore, it showed that both the increased regularity of LFP rhythm during NMDA, AMPA and KA as well as the decreased regularity during glutamate and QUI are accompanied by only a modest depolarization yet causing an notable increase in cellular spike rate. The faster spiking during glutamate and QUI was not obviously more irregular than during AMPA, KA or NMDA. This indicates that the different iGluR agonists rather affect network connectivity to cause the basically different transformations of LFP pattern and regularity of rhythm. NMDA and glutamate may enhance and weaken electrical LC neuron coupling, respectively. This view is based

on the observation that NMDA stabilized synchronous LFP oscillations in gap junction-coupled inferior olive neurons of rat slices via Ca^{2+}/calmodulin-dependent protein-kinase-I activation which enhances the normally weak neuronal coupling (Turecek et al. 2014). Contrary, in the adult rat LC neuromodulators do apparently not counteract the postnatal diminution of gap junction coupling and, instead, neuromodulator-evoked AP slowing itself reverses this decrease (Alvarez et al., 2002). While that report did not describe a correlation in neonatal rats between AP rate and gap junction-coupling, we found that similarly faster spiking increases (NMDA) or rather decreases (glutamate) LC network synchronicity. We noted recently that the incomplete neonatal LC synchronicity may be due to neuronal differences regarding spontaneous neuromodulator release which changes V_m close to subthreshold oscillation peaks thus altering the AP threshold (Rancic et al., 2018). Thus glutamate-evoked desynchronization may develop if LC neuron subtypes express different types and/or numbers of AMPAR and are therefore depolarized to different extent thus reaching AP threshold at diverging times.

The findings that NMDA may increase, but glutamate decrease network synchrony was firstly indicated by the finding that the former shortened and the latter prolonged single LFP burst duration. This view was then substantiated by the results from cross-correlation analysis of the LFP peak and cellular spiking. Contrary, while also AMPA and KA shortened LFP bursts and QUI prolonged them, cross-correlation analysis did not reveal an opposite change in network synchronicity corresponding to the effects of NMDA and glutamate. In fact, while CFE values and lag times in control for neurons tested for AMPA, KA and QUI were similar to those for cells tested for NMDA and glutamate, the corresponding values could not be determined during the action of the AMPAR agonists. This result was even more surprising considering that AMPA and KA also reduced the intracellular spike jitter while QUI appeared to increase it. On the one hand, this

discrepancy might indicate that the iGluR agonists affect network synchronicity in a different way than glutamate and NMDA acting on NMDAR resulting in a more regular, but not more synchronous rhythm. On the other hand, this might indicate that correlating the LFP peak with cellular spiking is not always a valid approach to test for effects of pharmacological manipulation on network synchronicity. If this is the case, other analytical approaches like spike-field coherence and phase preference determination (Fries et al., 2001; Wolansky et al., 2006) should be applied to re-analyze the present data.

7.3. Modular LC organization as potential cause for LFP transformations

This section unifies and summarizes the discussion in sections **5.5.4** and **6.5.4** regarding whether the observed LFP pattern transformations are related to a modular LC organization that is established for the adult LC. Specifically, it was shown that LC modules differ in their efferent projections and also in their afferent synaptic inputs (Schwarz and Luo, 2015). Moreover, in the LC core of adult rats, 'pontospinal-projecting module' neurons have longer duration spikes with a larger AHP than neurons in the ventral LC aspect (Li et al., 2016). Correspondingly, hypothetic LC neurons with a higher sensitivity to iGluR activation may change the activities of adjacent neurons and astrocytes in their module by releasing NA. This could then, e.g. stimulate the α_1 receptor of the astrocytes which would subsequently release lactate to depolarize the neighboring neurons via a new receptor (Tang et al., 2014). This could be studied in situ instead of using bath-application with focal pressure-injection of drugs or optogenetic activation of either LC neurons or astrocytes.That neuron-astrocyte modules cooperate within the LC is suggested by the observation

that LFP bursting transforms into different patterns not only during high K^+ and opioids, but also upon application of glutamate, NMDA, AMPA, KA, QUI and CNQX.

An in vivo study on adult rats suggests there is a relationship between opioids, iGluR and LC discharge patterns. Particularly, bursting develops in LC neurons from their normally tonic spiking after global administration of the μ-opioid receptor agonist morphine and that response was antagonized by kynurenic acid injection into the LC (Zhu and Zhou, 2015). This led the authors conclude in that report that iGluR are pivotal for LC bursting and that this type of activity is critically involved in opioid dependence and tolerance.

Besides, changes in the activity in the medial prefrontal cortex evoked by application of electrical pulse trains to the LC are similar to those in NA input-dependent memory tasks (Marzo et al., 2014). In their related study, the latter group hypothesized that LC-evoked NA modulation can either enhance or attenuate stimulus-indiced cortical responses (Safaai et al., 2015). Finally, they showed recently that spike synchronicity is seen only in few neuron assemblies in the LC of adult rats in vivo contrary to fluctuations of unit spiking at an 'infra-slow' rate of 0.01-1 Hz (Totah et al., 2018). This led to the assumption that 'the [adult] LC is a complex and differentiated neuromodulatory system'. The results of this thesis indicate that this is also true for the neonatal rat LC and follow-up studies will likely show novel complex neuron (-astrocyte) interactions in the discrete LC modules.

7.4. Conclusions and Perspective

In summary of the above, the in vitro findings in this thesis will notably change the view on the organization of the neonatal LC, similar to recent finding on the adult rat LC in vivo (Totah et al., 2018). As the common conclusion from both studies, it is evident now that the LC is not a simple spike-generating system, but can undergo drastic changes in network output burst pattern. This resembles the intrinsic capability of the (isolated) pre-BötC breathing center which can show either normal ('eupneic') bursting or enhanced discharges during (emotionally-evoked) sighs and anoxia-evoked gasps (Lieske et al., 2000; Ballanyi and Ruangkittisakul, 2009; Garcia et al., 2011; Del Negro et al., 2018). Regarding the potential function of LC population bursting, different spike discharge patterns will influence the efficacy of NA release in the multiple target brain regions. If distinct LC modules can generate different burst patterns under the influence of specific afferent inputs and/or autoregulatory influences of neuromodulators intrinsic to the LC, these distinct activities can potentially modulate the discharge pattern, and thus function, of the multiple innervated brain structures in an orchestrated fashion.

While the present study is a first step in understanding complex neonatal LC functions, many topics need to be studied in the future. In fact, in parallel to the completed projects contained in this thesis, I have conducted various other projects that yet need to be finalized as outlined in the following. (i) As noted above, the present data on simultaneous LFP and V_m recording during the effects of the different iGluR agonists need to be re-evaluated with other approaches, such as spike-field coherence or circular phase preference analysis. This analysis might provide more concise information regarding their partly opposing effects on network synchronicity. (ii) Findings from a previous PhD thesis from our laboratory (Panaitescu, 2012) indicated that low nanomolar opioid doses transform the bell-shaped LFP pattern into multipeak bursts similar to those seen during

recovery from high opioid doses (Rancic et al., 2018) (compare **Figs. 1-8B**, **3-4C**). However, like the similar LFP pattern transformation during high K^+ (Rancic et al., 2018), this change does not occur in all slices. Rather, in some slices high K^+ just increases the rate of normal bursting whereas low opioid doses slow the rhythm. This indicates that this LFP pattern transformation depends on additional factors that are active only in a subpopulation of slices. (iii) Similar to the inconsistent occurrence of multipeak LFP bursts in the latter cases, NA and the inhibitory α_2 NA receptor agonist clonidine cause the same LFP pattern transformation in ~50 % of slices. This indicates that the $G_{i/o}$ protein-mediated cellular signaling cascade is involved in this phenomenon as this pathway is common to both α_2 and μ receptor activation (Aghajanian and Wang, 1987). In this project, I also obtained preliminary information using α_1 and α_2 receptor antagonists that at a wide range of doses NA has either a stimulatory or inhibitory effect on the LFP due to an overlap of activation of these receptors. (iv) To identify functionally different LC modules, Ca_i imaging was performed during repetitive electrical stimulation of areas surrounding the LC as in previous studies on V_m recording from LC neurons (Egan et al., 1983; Cherubini et al., 1988). This showed that, independent on the position of the stimulation electrode, activation of afferent inputs at 75-100 Hz for 1 s causes a notable Ca_i rise that is partly blocked by CNQX and partly by the α_1 receptor blocker prazosin. Furthermore, in ~50 % of LC neurons the stimulus-evoked Ca_i rise is followed by an undershoot below baseline and this response is blocked by the α_2 receptor blocker yohimbine. This shows that both the α_1 receptor and AMPAR provide the major synaptic inputs to neonatal LC neurons and that in a subpopulation of these cells the released NA also acts, in slower fashion, on α_2 receptors as shown for single LC neurons with V_m recording (Egan et al., 1983).

Finally, I started to study neuron-astrocyte interactions in the neonatal rat LC. A recent study showed that lactate, likely released from astrocytes within the LC, excites neighboring neurons via a novel receptor (Tang et al., 2014). My preliminary findings indicate that activation of α_1 receptors in the astrocytes causes a Ca_i rise and possibly subsequent vesicular release of lactate that contributes to an increase in LFP rate by acting on a yet unidentified receptor on LC neurons. These findings indicate a novel functional interaction between neurons and this type of glial cells.

7.5. Figures and Legends

Fig. 7-1

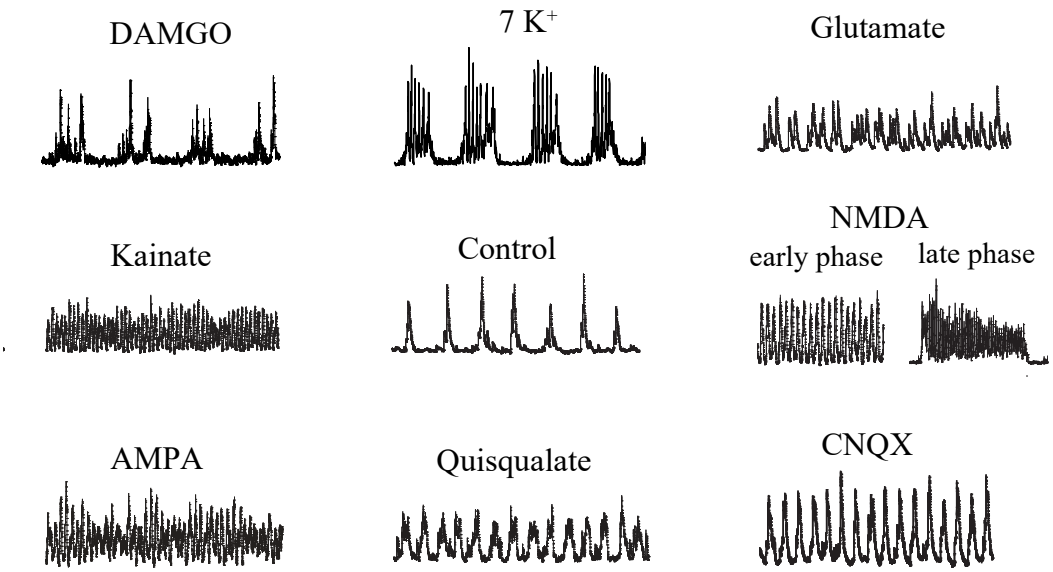

Fig. 7-1. The neonatal rat LC neural network exhibits distinct LFP pattern transformations. Suction electrode recording from the LC in neonatal rat brain slices reveals that it generates at ~1 Hz a spontaneous and robust LFP comprising rhythmic ~200 ms-lasting population bursts. The figure shows that LC neural network has the ability to transform this LFP to distinct patterns with varying burst duration, amplitude and frequency, partly as a result of changed network synchronicity. For example, NMDA transforms the control LFP to reduced duration faster events while enhancing network synchronicity. Contrary, glutamate results in increased burst duration events reflecting attenuated network synchronicity. Raised superfusate K^+ and early recovery from washout of the opioidDAMGO transforms the pattern to slower and longer-lasting bursts. CNQX makes network rhythm more regular with lower burst duration and increased rate events by activating a TARP-AMPAR complex. AMPA and KA induce sinusoidally-shaped LFP oscillations and increase network regularity. QUI decreases network regularity by transforming the LFP pattern into irregular and broadened LFP bursts.

General References

Abdelfattah AS, Farhi SL, Zhao Y, Brinks D, Zou P, Ruangkittisakul A, Platisa J, Pieribone VA, Ballanyi K, Cohen AE, Campbell RE (2016) A Bright and Fast Red Fluorescent Protein Voltage Indicator That Reports Neuronal Activity in Organotypic Brain Slices. J Neurosci 36: 2458-2472.

Abdelfattah AS, Rancic V, Rawal B, Ballanyi K, Campbell RE (2016) Ratiometric and photoconvertible fluorescent protein-based voltage indicator prototypes. Chem Comm 52: 14153-14156.

Abeles M (1991) Corticonics: neural circuits of the cerebral cortex. NewYork, Cambridge University Press.

Aghajanian GK, Cedarbaum JM, Wang RY (1977) Evidence for norepinephrine-mediated collateral inhibition of locus coeruleus neurons. Brain Res 136: 570–577.

Aghajanian GK, Kogan JH, Moghaddam B (1994) Opiate withdrawal increases glutamate and aspartate efflux in the locus coeruleus: an in vivo microdialysis study. Brain Res 636: 126.

Aghajanian GK, Vandermaelen CP (1982) alpha 2-adrenoceptor-mediated hyperpolarization of locus coeruleus neurons: intracellular studies in vivo. Science 215: 1394-1396.

Ahmadi Soleimani SM, Azizi H, Pachenari N, Mirnajafi-Zadeh J, Semnanian S (2017) Enhancement of μ-opioid receptor desensitization by orexin-A in rat locus coeruleus neurons. Neuropeptides 63: 28–36.

Ahmadi-Soleimani SM, Azizi H, Gompf HS, Semnanian S (2017) Role of orexin type-1 receptors in paragiganto-coerulear modulation of opioid withdrawal and tolerance: a site specific focus, Neuropharmacol 126: 25–37.

Akaoka H, Aston-Jones G (1991) Opiate withdrawal-induced hyperactivity of locus coeruleus neurons is substantially mediated by augmented excitatory amino acid input. J Neurosci 11: 3830–3839.

Allen NJ, Barres BA (2009) Neuroscience: Glia - more than just brain glue. Nature 457: 675-677.

Alreja M, Aghajanian GK (1993) Opiates suppress a resting sodium-dependent inward current and activate an outward potassium current in locus coeruleus neurons. J Neurosci 13: 3525–3532.

Alreja M, Aghajanian GK (1994) QX-314 blocks the potassium but not the sodium-dependent component of the opiate response in locus coeruleus neurons. Brain Res 639: 320–324.

Alvarez V, Chow C, Van Bockstaele E, Williams J (2002) Frequency-dependent synchrony in locus ceruleus: role of electrotonic coupling. Proc Natl Acad Sci 99: 4032-4036.

Alvarez-Maubecin V, Williams JT (1999) Developmental changes that regulate the activity of locus coeruleus neurons. Tokai J Exp Clin Med 24: 41-51.

Andrade R, Aghajanian G (1984) Locus coeruleus activity in vitro: Intrinsic regulation by a calcium- dependent potassium conductance but not alpha 2-adrenoceptors. J Neurosci 4: 161-170.

Armstrong-James M, Fox K (1983) Effects of ionophoresed noradrenaline on spontaneous activity of neurons in rat primary somatosensory cortex. J Physiol 335: 427–447.

Astier B, Van Bockstaele EJ, Aston-Jones G, Pieribone VA (1990) Anatomical evidence for multiple pathways leading from the rostral ventrolateral medulla (nucleus paragigantocellularis) to the locus coeruleus in rat. Neurosci Lett 118: 141–146.

Aston-Jones G, Bloom FE (1981) Activity of norepinephrine-containing locus coeruleus neurons in behaving rats anticipates fluctuations in the sleep-waking cycle. J Neurosci 8: 876-886.

Aston-Jones G, Ennis M, Pieribone VA, Nickell WT, Shipley MT (1986) The brain nucleus locus coeruleus: Restricted afferent control of a broad efferent network. Science 234: 734–737.

Aston-Jones G, Shipley MT, Chouvet G, Ennis M, van Bockstaele E, Pieribone V, Shiekhattar R, Akaoka H, Drolet G, Astier B, Charléty P, Valentino RJ, Williams JT (1991) Afferent regulation of locus coeruleus neurons: Anatomy, physiology and pharmacology. Prog Brain Res 88: 47–75.

Aston-Jones G, Shipley MT, Grzanna R (1995) The locus coeruleus, A5 and A7 noradrenergic cell groups. In: The rat nervous system, Ed 2 (Paxinos G, ed), pp 183-214. New York: Academic

Atweh S, Kuhar M (1977) Autoradiographic localization of opiate receptors in rat brain. ii. the brain stem. Brain Res 129: 1-12.

Baker M (2010) From promising to practical: tools to study networks of neurons. Nat Methods 7: 877–883.

Ballantyne D, Andrzejewski M, Mückenhoff K, Scheid P (2004) Rhythms, synchrony and electrical coupling in the Locus coeruleus. Respir Physiol Neurobiol 143: 199–214.

Ballanyi K, Ruangkittisakul A (2009) Structure-function analysis of rhythmogenic inspiratory pre-Botzinger complex networks in "calibrated" newborn rat brainstem slices. Respir Physiol Neurobiol 168: 158-178.

Ben-Ari Y, Cherubini E, Corradetti R, Gaiarsa JL (1989) Giant synaptic potentials in immature rat CA3 hippocampal neurones. J Physiol 416: 303–325.

Ben-Ari Y, Gaiarsa JL, Tyzio R, Khazipov R (2007) GABA: a pioneer transmitter that excites immature neurons and generates primitive oscillations. Physiol Rev 87: 1215–1284.

Berridge CW, Foote SL (1991) Effects of locus coeruleus activation on electroencephalographic activity in neocortex and hippocampus. J Neurosci 11: 3135-3145.

Berridge CW, Waterhouse BD (2003) The locus coeruleus-noradrenergic system: Modulation of behavioral state and state-dependent cognitive processes. Brain Res Rev 42: 33-84.

Biancardi V, Bicego KC, Almeida MC, Gargaglioni LH (2008) Locus coeruleus noradrenergic neurones and CO2 drive to breathing. Eur J Physiol. 455: 1119–1128.

Brette R, Destexhe A (2012) Handbook of Neural Activity Measurement, Cambridge University Press, Cambridge, UK.

Brickley SG, Revilla V, Cull-Candy SG, Wisden W, Farrant M (2001) Adaptive regulation of neuronal excitability by a voltage-independent potassium conductance. Nature 409: 88-92.

Buzsáki G, Anastassiou CA, Koch C (2012) The origin of extracellular fields and currents--EEG, ECoG, LFP and spikes. Nat Rev Neurosci 13: 407–420.

Cedarbaum J, Aghajanian G (1976) Noradrenergic neurons of the locus coeruleus: Inhibition by epinephrine and activation by the α antagonist piperoxane. Brain Res 112: 413-419.

Chandler DJ, Gao WJ, Waterhouse BD (2014) Heterogeneous organization of the locus coeruleus projections to prefrontal and motor cortices. Proc. Natl. Acad. Sci. U.S.A. 111: 6816–6821.

Chandley MJ, Ordway GA (2012) Noradrenergic Dysfunction in Depression and Suicide. In: Dwivedi Y, editor. The Neurobiological Basis of Suicide. Boca Raton (FL): CRC Press/Taylor & Francis. Chapter 3. PMID: 23035291.

Chandley MJ, Szebeni A, Szebeni K, Crawford JD, Stockmeier CA, Turecki G, Kostrzewa RM, Ordway GA (2014) Elevated gene expression of glutamate receptors in noradrenergic neurons from the locus coeruleus in major depression. Int J Neuropsychopharmacol 17: 1569-1578.

Chen S, Zhao Y, Wang Y, Shekhar M, Tajkhorshid E, Gouaux E (2017) Activation and Desensitization Mechanism of AMPA Receptor-TARP Complex by Cryo-EM. Cell 170: 1234-1246.

Cherubini E, North RA, Williams JT (1988) Synaptic potentials in locus coeruleus neurones. J Physiol 406: 431–442.

Chieng B, Bekkers JM (1999) GABA(B), opioid and alpha2 receptor inhibition of calcium channels in acutely-dissociated locus coeruleus neurones. Br J Pharmacol 127: 1533-1538.

Chiti Z, Teschemacher A (2007) Exocytosis of norepinephrine at axon varicosities and neuronal cell bodies in the rat brain. FASEB J 21: 2540-2550.

Christie MJ (1997) Generators of synchronous activity of the locus coeruleus during development. Semin Cell Dev Biol 8: 29–34.

Christie MJ, Williams JT, North RA (1989) Electrical coupling synchronizes subthreshold activity in locus coeruleus neurons in vitro from neonatal rats, J Neurosci 9: 3584–3589.

Clark FM, Proudfit HK (1991) The projection of locus coeruleus neurons to the spinal cord in the rat determined by anterograde tracing combined with immunocytochemistry. Brain Res 538: 231–245.

Clavier R (1979) Afferent projections to the self-stimulation regions of the dorsal pons, including the locus coeruleus, in the rat as demonstrated by the horseradish peroxidase technique. Brain Res Bull 4: 497-504.

Cokic B, Stein V (2008) Stargazin modulates AMPA receptor antagonism. Neuropharmacol 54: 1062–1070.

Connor M, Borgland SL, Christie MJ (1999) Continued morphine modulation of calcium channel currents in acutely isolated locus coeruleus neurons from morphine-dependent rats. Br J Pharmacol 128: 1561–1569.

Connors BW (2012) Tales of a dirty drug: carbenoxolone, gap junctions, and seizures. Epilepsy Curr 12: 66–68.

Dahlström A, Fuxe K (1964) Localization of monoamines in the lower brain stem. Experientia 20: 398-399.

Dawitz J, Kroon T, Hjorth JJJ, Meredith RM (2011) Functional Calcium Imaging in Developing Cortical Networks. J Vis Exp:1–8.

Del Negro CA, Funk GD, Feldman JL (2018) Breathing matters. Nat Rev Neurosci 19: 351-367.

Delaville C, Deurwaerdère PD, Benazzouz A (2011) Noradrenaline and Parkinson's disease. Front Syst Neurosci 5: 31.

Descarries L, Watkins KC, Lapieerre Y (1977) Noradrenergic axon terminals in the cerebral cortex of rat. III. Topometric ultrastructural analysis. Brain Res 133:197.

Deschenes M, Paradis M, Roy JP, Steriade M (1984) Electrophysiology of neurons of lateral thalamic nuclei in cat: resting properties and burst discharges. J Neurophysiol 51: 1196–1219.

Destexhe A (2011) Intracellular and computational evidence for a dominant role of internal network activity in cortical computations. Current Opinion Neurobiol 21: 717-725.

Devor A, Yarom Y (2002) Electrotonic coupling in the inferior olivary nucleus revealed by simultaneous double patch recordings. J Neurophysiol 87: 3048-3058.

DiazGranados N, Ibrahim LA, Brutsche NE, Ameli R, Henter ID, Luckenbaugh DA, Machado-Vieira R, Zarate CA Jr (2010) Rapid resolution of suicidal ideation after a single infusion of an N-methyl-D-aspartate antagonist in patients with treatment-resistant major depressive disorder. J Clin Psychiatry 71: 1605-1611.

Domyancic A V, Morilak DA (1997) Distribution of alpha1A adrenergic receptor mRNA in the rat Brain visualized by in situ hybridiation. J Comp Neurol 386: 358–378.

Douarin NML, Hallonet MER, Pourquié O (1994) Cell migrations and establishment of neuronal connections in the developing brain: A study using the quail-chick chimera system. Prog Brain Res 100: 3–18.

Egan TM, Henderson G, North RA, Williams LT (1983) Noradrenaline-mediated synaptic inhibition in rat locus coeruleus neurons. J. Physiol 345: 477-488.

Einevoll GT, Kayser C, Logothetis NK, Panzeri S (2013) Modelling and analysis of local field potentials for studying the function of cortical circuits. Nat Rev Neurosci 14: 770–785.

Einevoll GT, Pettersen KH, Devor A, Ulbert I, Halgren E, Dale AM (2007) Laminar Population Analysis: Estimating Firing Rates and Evoked Synaptic Activity From Multielectrode Recordings in Rat Barrel Cortex. J Neurophysiol 97: 2174–2190.

Ennis M, Aston-Jones G (1986) Evidence for self- and neighbor-mediated postactivation inhibition of locus coeruleus neurons. Brain Res 374: 299-305.

Ennis M, Aston-jones G (1988) Activation of locus coeruleus from nucleus paragigantocellularis: new excitatory amino acid pathway in brain. J Neurosci 8: 3644-3657.

Falck B, Hillarp N (1959) On the cellular localization of catechol amines in the brain. Cells Tissues Organs 38: 277-279.

Fallon JH, Loughlin SE (1982) Collateralization of monoamine neurons. Anat Rec 199: 79a.

Feldman JL, Del Negro CA (2006) Looking for inspiration: new perspectives on respiratory rhythm. Nat Rev Neurosci 7: 232-242.

Feng YZ, Zhang T, Rockhold RW, Ho IK (1995) Increased locus coeruleus glutamate levels are associated with naloxone-precipitated withdrawal from butorphanol in the rat. Neurochem Res 20: 745-751.

Ferrea E1, Maccione A, Medrihan L, Nieus T, Ghezzi D, Baldelli P, Benfenati F, Berdondini L (2012) Large-scale, high-resolution electrophysiological imaging of field potentials in brain slices with microelectronic multielectrode arrays. Front Neural Circuits 6: 80.

Field GD, Gauthier JL, Sher A, Greschner M, Machado TA, Jepson LH, Shlens J, Gunning DE, Mathieson K, Debrowski W, Paninski L, Litke AM, Chichilniski EJ (2010) Functional connectivity in the retina at the resolution of photoreceptors. Nature 467: 673–677.

Fietkiewicz C1, Loparo KA, Wilson CG (2011) Drive latencies in hypoglossal motoneurons indicate developmental change in the brainstem respiratory network. J Neural Eng 8: 065011

Florin-lechner SM, Druhan JP, Aston-jones G, Valentino RJ (1996) Enhanced norepinephrine release in prefrontal cortex with burst stimulation of the locus coeruleus. Brain Res 742: 89-97.

Foote SL, Aston-Jones G, Bloom FE (1980) Impulse activity of locus coeruleus neurons in awake rats and monkeys is a function of sensory stimulation and arousal. Proc Natl Acad Sci 77: 3033-3037.

Foote SL, Bloom FE, Aston-Jones G (1983) Nucleus locus ceruleus: new evidence of anatomical and physiological specificity. Physiol Rev 63: 844–914.

Forsythe ID, Linsdell P, Stanfield PR (1992) Unitary A-currents of rat locus coeruleus neurones grown in cell culture: rectification caused by internal Mg2+ and Na+. J Physiol 451: 553-583.

Fort P, Khateb A, Pegna A, Muhlethaler M, Jones BE, Physiologie D De, Universitaire CM, Servet RM, Geneva C-, Bernard C (1995) Noradrenergic modulation of cholinergic nucleus basalis neurons demonstrated by in vitro pharmacological and lmmunohistochemical evidence in the guinea-pig brain. Eur J Neurosci 7: 1502–1511.

Fries P, Reynolds JH, Rorie AE, Desimone R (2001) Modulation of oscillatory neuronal synchronization by selective visual attention. Science. 291: 1560-1563.

Fritschy JM, Grzanna R (1990) Demonstration of two separate descending pathways to the rat spinal cord: evidence for an intragriseal trajectory of locus coeruleus axons in the superficial layers of the dorsal horn. J Comp Neurol 291: 553–582.

Fuxe K, Dahlström AB, Jonsson G, Marcellino D, Guescini M, Dam M, Manger P, Agnati L (2010) The discovery of central monoamine neurons gave volume transmission to the wired brain. Prog Neurobiol 90: 82–100.

Garaschuk O, Linn J, Eilers J, Konnerth A (2000) Large-scale oscillatory calcium waves in the immature cortex. Nat Neurosci 3: 452–459.

Garcia AJ 3rd, Zanella S, Koch H, Doi A, Ramirez JM (2011) Chapter 3--networks within networks: the neuronal control of breathing. Prog Brain Res 188: 31-50.

Garcia, A.J. 3rd, Dashevskiy, T., Khuu, M.A., Ramirez, J.M., 2017. Chronic Intermittent Hypoxia Differentially Impacts Different States of Inspiratory Activity at the Level of the preBötzinger Complex. Front Physiol 8: 571.

Geffen LB, Livett BG (1971) Synaptic vesicles in sympathetic neurons. Physiol Rev 51- 98.

Gibb AJ, Edwards FA (1994) Patch clamp recording from cells in sliced tissues. In: Microelectrode Techniques (Ogden D, ed). 255–274. The Plymouth Workshop Handbook. Cambridge: The Company of Biologists Limited.

Goddard AW, Ball SG, Martinez J, Robinson MJ, Yang CR, Russell JM (2010) Current perspectives of the roles of the central norepinephrine system in anxiety and depression. Depress Anxiety 27: 339–350.

Goodman CS, Shatz CJ (1993) Developmental mechanisms that generate precise patterns of neuronal connectivity. Cell 72: 77–98.

Graham AW, Aghajanian GK (1971) Effects of amphetamine on single cell activity in a catecholamine nucleus, the locus coeruleus. Nature 234: 100-102.

Greger IH, Watson JF, Cull-Candy SG (2017) Structural and Functional Architecture of AMPA-Type Glutamate Receptors and Their Auxiliary Proteins. Neuron 94: 713-730.

Grzanna R, Fritschy JM (1991) Efferent projections of different subpopulations of central noradrenaline neurons. Prog Brain Res 88: 89-101.

Guyenet P, Young B (1987) Projections of nucleus paragigantocellularis lateralis to locus coeruleus and other structures in rat. Brain Research 406: 171-184.

Hagglund M, Borgius L, Dougherty KJ, Kiehn O (2010) Activation of groups of excitatory neurons in the mammalian spinal cord or hindbrain evokes locomotion. Nat Neurosci 13: 246:252.

Halassa MM, Haydon PG (2010) Integrated brain circuits: astrocytic networks modulate neuronal activity and behavior. Annu Rev Physiol 72: 335-355.

Hartman B (1973) Immunofluorescence of dopamine-β-hydroxylase application of improved methodology to the localization of the peripheral and central noradrenergic nervous system. J Histochem Cytochem 21: 312-332.

Hashimoto Y, Miyakawa H, Kudo Y, Inoue M (2004) 6-Cyano-7-nitroquinoxaline-2,3-dione (CNQX) increases GABAA receptor-mediated spontaneous postsynaptic currents in the dentate granule cells of rat hippocampal slices. Neurosci Lett 358: 33-36.

Henze DA, Borhegyi Z, Csicsvari J, Mamiya A, Harris KD, Buzsáki G (2000) Intracellular features predicted by extracellular recordings in the hippocampus in vivo. J Neurophysiol 84: 390–400.

Herkenham M, Nauta WJ (1979) Efferent connections of the habenular nuclei in the rat. J Comp Neurol 187: 19-47.

Hermann DM, Luppi PH, Peyron C, Hinckel P, Jouvet M (1997) Afferent projections to the rat nuclei raphe magnus, raphe pallidus and reticularis gigantocellularis pars α demonstrated by iontophoretic application of choleratoxin. J Chem Neuroanat 13: 1–21.

Hirata H, Aston-Jones, G (1994) A novel long-latency response of locus coeruleus neurons to noxious stimuli: Mediation by peripheral C-fibers. J Neurophysiol 71: 1752–1761.

Hoffer BJ, Siggins GR, Bloom FE (1971) Studies on norepinephrine-containing afferents to Purkinje cells of rat cerebellum. II. Sensitivity of Purkinje cells to norepinephrine and related substances administered by microiontophoresis. Brain Res 25: 523–534.

Hoffer BJ, Siggins GR, Oliver AP, Bloom FE (1973) Activation of the pathway from locus coeruleus to rat cerebellar Purkinje neurons: pharmacological evidence of noradrenergic central inhibition. J Pharmacol Exp Ther 184: 553–569.

Holstege JC, Kuypers HG (1987) Brainstem projections to spinal motoneurons: an Update. Neurosci 23: 809–821.

Innocenti B, Parpura V, Haydon PG (2000) Imaging extracellular waves of glutamate during calcium signaling in cultured astrocytes. J Neurosci 20: 1800–1808.

Ishimatsu M & Williams JT (1996) Synchronous activity in locus coeruleus results from dendritic interactions in pericoerulear regions. J Neurosci 16: 5196-5204.

Ivanov A (2013) Extranuclear dendrites of locus coeruleus neurons: activation by glutamate and modulation of activity by alpha adrenoceptors. J Neurophysiol 74: 2427-2436.

Jackson AC, Nicoll RA (2011) Stargazin (TARP γ-2) is required for compartment- specific AMPA receptor trafficking and synaptic plasticity in cerebellar stellate cells. J Neurosci 31: 3939-3952.

Jahnsen H (1986) Responses of neurons in isolated preparations of the mammalian central nervous system. Prog Neurobiol 2: 351-372.

Jin X, Li S, Bondy B, Zhong W, Oginsky MF, Wu Y, Johnson CM, Zhang S, Cui N, Jiang C (2016) Identification of a group of GABAergic neurons in the dorsomedial area of the locus coeruleus. PLoS One 11: 1-13.

Jodo E, Aston-Jones G (1997) Activation of locus coeruleus by prefrontal cortex is mediated by excitatory amino acid inputs. Brain Res 768: 327-332.

Kaila K (1994) Ionic basis of GABAA receptor channel function in the nervous system. Prog Neurobiol 42: 489–537.

Kandel ER, Schwartz JH, Jessell TM, Siegelbaum SA, Hudspeth AJ (2012) Principles of neural science. 5th edition, Columbus-McGrow Hill.

Kantor C, Panaitescu B, Kuribayashi J, Ruangkittisakul A, Jovanovic I, Leung V, Lee TF, MacTavish D, Jhamandas JH, Cheung PY, Ballanyi K (2012) Spontaneous neural network oscillations in hippocampus, cortex, and locus coeruleus of newborn rat and piglet brain slices. Neuromethods 73: 315-356.

Kiernan JA (2005) Barr's the Human Nervous System: An Anatomical Viewpoint. Maryland: Lippincott Williams and Wilkins.

Kim U, Bal T, McCormick DA (1995) Spindle waves are propagating synchronized oscillations in the ferret LGNd in vitro. J Neurophysiol 74: 1301–1323.

Kimura F, Nakamura S (1985) Locus coeruleus neurons in the neonatal rat: Electrical activity and responses to sensory stimulation. Dev Brain Res 23: 301-305.

Kogan JH, Aghajanian GK (1995) Long-term glutamate desensitization in locus coeruleus neurons and its role in opiate withdrawal. Brain Res 689: 111-121.

Kott S, Sager C, Tapken D, Werner M, Hollmann M (2009) Comparative analysis of the pharmacology of GluR1 in complex with transmembrane AMPA receptor regulatory proteins γ2, γ3, γ4, and γ8. Neuroscience 158: 78–88.

Krettek J, Price J (1978) Amygdaloid projections to subcortical structures within the basal forebrain and brainstem in the rat and cat. J Comp Neurol 178: 225-253.

Kulik A, Brockhaus J, Pedarzani P, Ballanyi K (2002) Chemical anoxia activates ATP-sensitive and blocks Ca2+-dependent K+ channels in rat dorsal vagal neurons in situ. Neuroscience 110: 541-554.

Latorre R, Aguirre C, Rabinovich MI, Varona P (2013) Transient dynamics and rhythm coordination of inferior olive spatio-temporal patterns. Front Neural Circuits 7: 138.

Lauder J, Bloom F (1974) Ontogeny of monoamine neurons in the locus coeruleus, raphe nuclei and substantia nigra of the rat. I. cell differentiation. J Comp Neurol 155: 469-481.

Lauder J, Bloom F (1975) Ontogeny of monoamine neurons in the locus coeruleus, raphe nuclei and substantia nigra of the rat. II. Synaptogenesis. J Comp Neurol 163: 251-264.

Lee SH, Govindaiah G, Cox CL (2010) Selective excitatory actions of DNQX and CNQX in rat thalamic neurons. J Neurophys. 103: 1728-1734.

Li CL, McIlwain H (1957) Maintenance of resting membrane potentials in slices of mammalian cerebral cortex and other tissues in vitro. J Physiol 139: 178-190.

Li Y, Hickey L, Perrins R, Werlen E, Patel AA, Hirschberg S, Jones MW, Salinas S, Kremer EJ, Pickering AE. (2016). Retrograde optogenetic characterization of the pontospinal module of the locus coeruleus with a canine adenoviral vector. Brain Res 1641: 274–290.

Lieske SP, Thoby-Brisson M, Telgkamp P, Ramirez JM (2000) Reconfiguration of the neural network controlling multiple breathing patterns: eupnea, sighs and gasps. Nat Neurosci 3: 600–607.

Lin MZ, Schnitzer MJ (2016) Genetically encoded indicators of neuronal activity. Nat Neurosci 19: 1142-1153.

Llinas R (1988) The intrinsic electrophysiological properties of mammalian neurons: insights into central nervous system function. Science 242: 1654-1664.

Llinas R, Sugimori M (1980) Electrophysiological properties of in vitro Purkinje cell dendrites in mammalian cerebellar slices. J Physiol 305: 197–213.

Llinas R, Yarom Y (1981) Electrophysiology of mammalian inferior olivary neurones in vitro. Different types of voltage-dependent ionic conductances. J Physiol 315: 549–567.

Llorca-Torralba M, Borges G, Neto F, Mico JA, Berrocoso E (2016) Noradrenergic Locus Coeruleus pathways in pain modulation. Neurosci 338: 93–113.

Logothetis NK (2003) The underpinnings of the BOLD functional magnetic resonance imaging signal. J Neurosci 23: 3963-3971.

Loizou L (1969) Projections of the nucleus locus coeruleus in the albino rat. Brain Res 15: 563-566.

Lotfi B, Zeng M, Sundén B, Wang Q (2014) 3D numerical investigation of flow and heat transfer characteristics in smooth wavy fin-and-elliptical tube heat exchangers using new type vortex generators. Energy 73: 233–257.

Loughlin SE, Foote SL and Bloom FE (1986a) Efferent projections of nucleus locus coeruleus: Topographic organization of cells of origin demonstrated by three-dimensional reconstructions. Neurosci 18: 291-306.

Loughlin SE, Foote SL, Grzanna R (1986b) Efferent projections of nucleus locus coeruleus: Morphologic subpopulations have different efferent targets. Neurosci 18: 307-319.

Luppi PH, Aston-Jones G, Akaoka H, Chouvet G, Jouvet M (1995) Afferent projections to the rat locus coeruleus demonstrated by retrograde and anterograde tracing with cholera-toxin B subunit and Phaseolus vulgaris leucoagglutinin. Neurosci 65: 119-160.

Maccaferri G, Dingledine R (2002) Complex effects of CNQX on CA1 interneurons of the developing rat hippocampus. Neuropharmacol 43: 523–529.

MacVicar BA, Tse FWY (1988) Norepinephrine and cyclic adenosine 3-5 cyclic monophosphate enhance a nifedipine sensitive calcium current in cultured rat astrocytes. Glia 1:359–365.

Maher MP, Matta JA, Gu S, Seierstad M, Bredt DS (2017) Getting a Handle on Neuropharmacology by Targeting Receptor-Associated Proteins. Neuron 96: 989-1001.

Marshall KC, Glmbarzevsky BP, Hendelman WJ (1979) Electrical activity of brain stem neurons in organized cultures of cerebellum. Can Physiol 10: 42.

Marshall KC, Christie MJ, Finlayson PG, Williams JT (1991) Developmental aspects of the locus coeruleus-noradrenaline system. Prog Brain Res 88: 173–185.

Marzo A, Totah NK, Neves RM, Logothetis NK, Eschenko O (2014) Unilateral electrical stimulation of rat locus coeruleus elicits bilateral response of norepinephrine neurons and sustained activation of medial prefrontal cortex. J Neurophysiol 111: 2570-2588.

Mason ST, Fibiger HC (1979) Regional topography within noradrenergic locus coeruleus as revealed by retrograde transport of horseradish peroxidase. J Comp Neurol 187: 703–724.

Matschke LA, Bertoune M, Roeper J, Snutch TP, Oertel WH, Rinné S, Decher N (2015) A concerted action of L- and T-type Ca2+ channels regulates locus coeruleus pacemaking. Mol Cell Neurosci 68: 293-302.

Matschke LA, Rinné S, Snutch TP, Oertel WH, Dolga AM, Decher N (2018) Calcium-activated SK potassium channels are key modulators of the pacemaker frequency in locus coeruleus neurons. Mol Cell Neurosci 88: 330-341.

McBain CJ, Eaton JV, Brown T, Dingledine R (1992) CNQX increases spontaneous inhibitory input to CA3 pyramidal neurones in neonatal rat hippocampal slices. Brain Res 592: 255-260.

McCarthy KD, Salm AK (1991) Pharmacologically-distinct subsets of astroglia can be identified by their calcium response to neuroligands. Neurosci 41: 325–333.

McIlwain H, Buchel L, Cheshire JD (1951) The inorganic phosphate and phosphocreatine of Brain especially during metabolism in vitro. Biochem J 48: 12-20.

Menuz K, Stroud RM, Nicoll RA, Hays FA (2007) TARP auxiliary subunits switch AMPA receptor antagonists into partial agonists. Science 318: 815–817.

Metzger F, Kulik A, Sendtner M, Ballanyi K (2000) Contribution of Ca2+-permeable AMPA/KA receptors to glutamate-induced Ca2+ rise in embryonic lumbar mtoneurons in situ. J Neurophysiol 83: 50-59.

Monaghan DT, Bridges RJ, Cotman CW (1989) The excitatory amino acid receptors: Their classes, pharmacology, and distinct properties in the function of the central nervous system. Annu Rev Pharmacol Toxicol 29: 365–402.

Moriceau S, Roth TL, Okotoghaide T, Sullivan RM (2004) Corticosterone controls the developmental emergence of fear and amygdala function to predator odors in infant rat pups. Int J Dev Neurosci 22: 415–422.

Moriceau S, Roth TL, Sullivan RM (2010) Rodent model of infant attachment learning and stress. Dev Psychobiol 52: 651–660.

Mrejeru A, Wei A, Ramirez JM (2011) Calcium-activated non-selective cation currents are involved in generation of tonic and bursting activity in dopamine neurons of the substantia nigra pars compacta. J Physiol 589: 2497-2514.

Murai Y, Akaike T (2005) Orexins cause depolarization via nonselective cationic and K+ channels in isolated locus coeruleus neurons. Neurosci Res 51: 55-65.

Nagai T, Satoh K, Imamoto K, Maeda T (1981) Divergent projections of catecholamine neurons of the locus coeruleus as revealed by fluorescent retrograde double labeling technique. Neurosci Lett 23: 117–123.

Nakamura S, Kimura F, Sakaguchi T (1987) Postnatal development of electrical activity in the locus coeruleus. J Neurophysiol 58: 510-524.

Nakamura S, Sakaguchi T, Kimura F, Aoki F (1988) The role of alpha 1-adrenoceptor-mediated collateral excitation in the regulation of the electrical activity of locus coeruleus neurons. Neurosci 27: 921-929.

Nestler EJ (1996) Under siege: The brain on opiates. Neuron 16: 897-900.

Neuman RS, Cherubini E, Ben-Ari Y (1989) Endogenous and network bursts induced by N-methyl-D-aspartate and magnesium free medium in the CA3 region of the hippocampal slice. Neurosci 28: 393-399.

Neves RM, Van Keulen S, Yang M, Logothetis NK, Eschenko O (2018) Locus coeruleus phasic discharge is essential for stimulus-induced gamma oscillations in the prefrontal cortex. J Neurophysiol 119: 904-920.

Newman EA (2001) Propagation of intercellular calcium waves in retinal astrocytes and Muller cells. J Neurosci 21: 2215–2223.

Nicolelis MA (2008) Methods for Neural Ensemble Recordings. Boca Raton (FL): CRC Press.

Nieber K, Sevcik J, Illes P (1995) Hypoxic changes in rat locus coeruleus neurons in vitro. J. Physiol 486: 33–46.

North RA, Williams JT (1985) On the potassium conductance increased by opioids in rat locus coeruleus neurones. J Physiol 364: 265-280.

O'Donovan MJ, Bonnot A, Mentis GZ, Arai Y, Chub N, Shneider NA, Wenner P (2008) Imaging the spatiotemporal organization of neural activity in the developing spinal cord. Dev Neurobiol 68: 788-803.

O'Brien CP, Testa T, O'Brien TJ, Brady JP, Wells B (1977) Conditioned narcotic withdrawal in humans. Science 195: 1000–1002.

Obien ME, Deligkaris K, Bullmann T, Bakkum DJ, Frey U (2014) Revealing neuronal function through microelectrode array recordings. Front Neurosci 8: 423.

Olpe HR, Steinmann M (1991) Responses of locus coeruleus neurons to neuropeptides. In: Barnes CD, Pompeiano O, editors. Progress in brain research. 88: 241–248.

Olpe HR, Steinmann M, Brugger F, Pozza M (1989) Excitatory amino acid receptors in rat locus coeruleus. Naunyn Schmiedebergs Arch Pharmacol 339: 312-314.

Olpe HR, Steinmann MW, Hall RG, Brugger F, Pozza MF (1988) GABAA and GABAB receptors in locus coeruleus: effects of blockers. Eur J Pharmacol 149: 183-185.

Olson L, Seiger A (1972) Early Ontogeny of central monoamine neurons in the rat: Fluorescence histochemical observations. Z Anat Entwickl-Gesch 137: 301-316.

Osborne P, Vidovic M, Chieng B, Hill C, Christie M (2002) Expression of mRNA and functional alpha1-adrenoceptors that suppress the GIRK conductance in adult rat locus coeruleus neurons. Br J Pharmacol 135: 226-232.

Osmanovic SS, Shefner SA (1993) Calcium-activated hyperpolarizations in rat locus coeruleus neurons in vitro. J Physiol 469: 89-109.

Osmanovic SS, Shefner SA, Brodie MS (1990) Functional significance of the apamin-sensitive conductance in rat locus coeruleus neurons. Brain Res 530: 283-289.

Oyamada Y, Ballantyne D, Muckenhoff K, Scheid P (1998) Respiration-modulated membrane potential and chemosensitivity of locus coeruleus neurones in the in vitro brainstem-spinal cord of the neonatal rat. J Physiol 513: 381-398.

Pál B (2018) Involvement of extrasynaptic glutamate in physiological and pathophysiological changes of neuronal excitability. Cell Mol Life Sci doi: 10.1007/s00018-018-2837-5.

Palmer AE, Tsien RY (2006) Measuring calcium signaling using genetically targetable fluorescent indicators. Nat Prot 1: 1057-65.

Panaitescu B (2012) Antagonistic modulation of spontaneous neural network activities in isolated newborn rat brainstem preparations by opioids and methylxanthines (Doctoral dissertation).

Panaitescu B, Kuribayashi J, Ruangkittisakul A, Leung V, Iizuka M, Ballanyi K (2013) Methylxanthines do not affect rhythmogenic preBötC inspiratory network activity but impair bursting of preBötC-driven motoneurons. Neuroscience 255: 158-176.

Panaitescu B, Ruangkittisakul A, Ballanyi K (2009) Silencing by raised extracellular Ca2+ of pre-Bötzinger complex neurons in newborn rat brainstem slices without change of membrane potential or input resistance. Neurosci Lett 456: 25-29.

Papay R, Gaivin R, Cune DANFMC, Rorabaugh BR, Macklin WB, Grath JCMC, Perez DM (2004) Mouse alpha1B -adrenergic receptor is expressed in neurons and NG2 oligodendrocytes. J Comp Neurol 478: 1–10.

Papay R, Gaivin R, Jha A, Mccune DANF, Mcgrath JC, Rodrigo MC, Simpson PC, Doze VANA (2006) Localization of the mouse alpha1A - adrenergic receptor (AR) in the brain : alpha1AAR is expressed in neurons , GABAergic interneurons , and NG2 oligodendrocyte Progenitors. J Comp Neurol 222: 209–222.

Pearlstein E, Ben Mabrouk F, Pflieger JF, Vinay L (2005) Serotonin refines the locomotor-related alternations in the in vitro neonatal rat spinal cord. Eur J Neurosci 21: 1338-1346.

Perea G, Araque A (2005) Properties of synaptically evoked astrocyte calcium signal reveal synaptic information processing by astrocytes. J Neurosci 25: 2192-2203.

Perea G, Navarrete M, Araque A (2009) Tripartite synapses: astrocytes process and control synaptic information. Trends Neurosci 32: 421–431.

Pickel VM, Joh TH, Reis DJ (1975) Ultrastructural localization of tyrosine hydroxylase in noradrenergic neurons of brain. Proc Natl Acad Sci 72: 659–663.

Pieribone A, Nicholas P, Dagerlind A (1994) Distribution of α1 adrenoceptors in rat brain revealed by in situ hybridization experiments utilizing subtype-specific probes J Neurosci 14: 4252-4268.

Placantonakis D, Welsh JP (2001) Two distinct oscillatory states determined by the NMDA receptor in rat inferior olive. J Physiol 534: 123-140.

Porter JT, McCarthy KD (1997) Astrocytic neurotransmitter receptors in situ and in vivo. Prog Neurobiol 51: 439–455.

Post S, J Mai (1980) Contribution to the amygdaloid projection field in the rat: a quantitative autoradiographic study. J fur Hirnforschung 21: 199-225.

Price J, Amaral D (1981) An autoradiographic study of the projections of the central nucleus of the monkey amygdala. J Neurosci 1: 1242-1259.

Price RB1, Nock MK, Charney DS, Mathew SJ (2009) Effects of intravenous ketamine on explicit and implicit measures of suicidality in treatment-resistant depression. Biol Psychiatry 66: 522-526.

Quicke P, Barnes SJ, Knöpfel T (2017) Imaging of Brain Slices with a Genetically Encoded Voltage Indicator. Methods Mol Biol 1563: 73-84.

Rancic V, Rawal B, Panaitescu B, Ruangkittisakul A, Ballanyi K (2018) Suction electrode recording in locus coeruleus of newborn rat brain slices reveals network bursting comprising summated non-synchronous spiking. Neurosci Lett 671: 103-107.

Rasmussen K (1995) The role of the locus coeruleus and n-methyl-d-aspartic acid (NMDA) and AMPA receptors in opiate withdrawal. Neuropsychopharmacol 13: 295-300.

Rasmussen K, Fuller RW, Stockton ME, Perry KW, Swinford RM, Ornstein PL (1991) NMDA receptor antagonists suppress behaviors but not norepinephrine turnover or locus coeruleus unit activity induced by opiate withdrawal. Eur J Pharmacol 197: 9-16.

Rasmussen K, Kendrick WT, Kogan JH, Aghajanian GK (1996) A selective AMPA antagonist, LY293558, suppresses morphine withdrawal-induced activation of locus coeruleus neurons and behavioral signs of morphine withdrawal. Neuropsychopharmacol 15: 497– 505.

Rasmussen K, Morilak DA, Jacobs BL (1986) Single unit activity of locus coeruleus neurons in the freely moving cat. I. During naturalistic behaviors and in response to simple and complex stimuli. Brain Res 371: 324-334.

Rawal B, Rancic V, Ballanyi K (2019) TARP mediation of accelerated and more regular locus coeruleus network bursting in neonatal rat brain slices. Neuropharmacol 148: 169-177.

Redmond DE, Huang YH, Snyder DR (1976) Behavioral effects of stimulation of the nucleus locus coeruleus in the stump tailed monkey. Brain Res 116: 502-510.

Reiner A, Levitz J (2018) Glutamatergic Signaling in the Central Nervous System: Ionotropic and Metabotropic Receptors in Concert. Neuron 98: 1080-1098.

Rigby M, Cull-Candy SG, Farrant M (2015) Transmembrane AMPAR regulatory protein gamma-2 is required for the modulation of GABA release by presynaptic AMPARs. J Neurosci 35: 4203-4214.

Room P, Postema F, Korf J (1981) Divergent axon collaterals of rat locus coeruleus neurons: demonstration by a fluorescent double labeling technique. Brain Res 221: 219–230.

Rotter a, Birdsall NJM, Field PM, Raisman G, Hill M, Iaa LNW (1979) Muscarinic receptors in the central nervous system of the rat. ii. distribution of binding of [3h] propylbenzilylcholine mustard in the midbrain and hindbrain. Brain Res. 180: 167-183.

Ruangkittisakul A, Okada Y, Oku Y, Koshiya N, Ballanyi K (2009) Fluorescence imaging of active respiratory networks, Respir Physiol Neurobiol 168: 26-38

Ruangkittisakul A, Schwarzacher SW, Secchia L, Poon BY, Ma Y, Funk GD, Ballanyi K (2006) High sensitivity to neuromodulator-activated signaling pathways at physiological [K^+] of confocally-imaged respiratory center neurons in online-calibrated newborn rat brainstem slices. J Neurosci 26: 11870-11880.

Ruangkittisakul A, Secchia-Ballanyi L, Panaitescu B, Bobocea N, Kuribayashi J, Iizuka M, Kantor C, Ballanyi K (2012) Anatomically 'calibrated' isolated respiratory networks from newborn rodents. In: Isolated Central Nervous System Circuits. Neuromethods Series. Springer New York: 61-124.

Ruangkittisakul A, Sharopov S, Kantor C, Kuribayashi J, Mildenberger E, Luhmann HJ, Kilb W, Ballanyi K (2015) Neuroscience 301: 106-120

Sakaguchi T, Nakamura S (1987) The mode of projections of single locus coeruleus neurons to the cerebral cortex in rats. Neuroscience 20: 221–230.

Samuels E, Szabadi E (2008) Functional neuroanatomy of the noradrenergic locus coeruleus: its roles in the regulation of arousal and autonomic function part i: principles of functional organisation. Curr Neuropharmacol 6: 235-253.

Sanchez-Padilla J, Guzman JN, Ilijic E, Kondapalli J, Galtieri DJ, Yang B, Schieber S, Oertel W, Wokosin D, Schumacker PT, Surmeier DJ (2014) Mitochondrial oxidant stress in locus coeruleus is regulated by activity and nitric oxide synthase. Nature Neurosci. 17: 832-840.

Sara S (2009) The locus coeruleus and noradrenergic modulation of cognition. Nat Rev Neurosci 10: 211-223.

Sara S, Bouret S (2012) Orienting and reorienting: the locus coeruleus mediates cognition through arousal. Neuron 76: 130-141.

Sawchenko PE, Swanson LW (1981) Central noradrenergic pathways for the integration of hypothalamic neuroendocrine and autonomic responses. Science 214: 685–687.

Sawchenko PE, Swanson LW (1982) Immunohistochemical identification of neurons in the paraventricular nucleus of the hypothalamus that project to the medulla or to the spinal cord in the rat. J Comp Neurol 205: 260-272.

Sawchenko PE, Swanson LW (1982) The organization of noradrenergic pathways from the brainstem to the paraventricular and supraoptic nuclei in the rat. Brain Res Rev 4: 275–325.

Scemes E, Giaume C (2006) Astrocyte calcium waves: what they are and what they do. Glia 54: 716–725.

Schuerger RJ, Balaban CD (1993) Immunohistochemical demonstration of regionally selective projections from locus coeruleus to the vestibular nuclei in rats . Exp Brain Res 92: 351-359.

Schwarz L, Luo L (2015) Organization of the Locus Coeruleus-Norepinephrine System. Curr Biol 25: R1051-R1056.

Schwarz L, Miyamichi K, Gao X, Beier K, Weissbourd B, DeLoach K, Ren J, Ibanes S, Malenka R, Kremer E, Luo L (2015) Viral-genetic tracing of the input–output organization of a central noradrenaline circuit. Nature 524: 88-92.

Segal M, Bloom FE (1974) The action of norepinephrine in the rat hippocampus. I. Iontophoretic studies Brain Res 72: 79–97.

Segal M, Bloom FE (1974) The action of norepinephrine in the rat hippocampus. II. Activation of the input pathway. Brain Res 72: 99–114.

Segal M, Landis S (1974a) Afferents to the hippocampus of the rat studied with the method of retrograde transport of horseradish peroxidase. Brain Research 78: 1-15.

Segal M, Landis S (1974b) Afferents to the septal area of the rat studied with the method of retrograde axonal transport of horseradish peroxidase. Brain Research 82: 263-268.

Senba E, Tohyama M, Shiosaka H, Takagi M, Sakanaka T, Matuzaki Y, Takahashi Y, Shimizu N (1981) Experimental and morphological studies of the noradrenaline innervations in the nucleus tractus spinal nervi trigemini of the rat with special reference to their fine structures. Brain Res 206: 39–50.

Sharifullina E, Ostroumov K, Grandolfo M, Nistri A (2008) N-methyl-D-aspartate triggers neonatal rat hypoglossal motoneurons in vitro to express rhythmic bursting with unusual Mg2+ sensitivity. Neuroscience 154: 804-820.

Shen KZ, North RA (1992a) Muscarine increases cation conductance and decreases potassium conductance in rat locus coeruleus neurones. J Physiol (Lond) 455: 471–485.

Shen KZ, North RA (1992b) Substance P opens cation channels and closes potassium channels in rat locus coeruleus neurons. Neurosci 50: 345–353.

Shen Y, Dana H, Abdelfattah AS, Patel R, Shea J, Molina RS, Rawal B, Rancic V, Chang YF, Wu L, Chen Y, Qian Y, Wiens MD, Hambleton N, Ballanyi K, Hughes TE, Drobizhev M, Kim DS, Koyama M, Schreiter ER, Campbell RE (2018) A genetically encoded Ca2+ indicator based on circularly permutated sea anemone red fluorescent protein eqFP578. BMC Biol 16:9.

Shiekhattar R, Aston-jones G (1992) Local application of bicuculline potentiates nmda-receptor-mediated sensory responses of brain noradrenergic neurons. 61: 54–61.

Simpson KL, Altman DW, Wang L, Kirifides ML, Lin RC, Waterhouse BD (1997) Lateralization and functional organization of the locus coeruleus projection to the trigeminal somatosensory pathway in rat. J Comp Neurol 385: 135–147.

Singewald N, Philippu A (1998) Release of neurotransmitters in the locus coeruleus. Prog Neurobiol 56: 237-267.

Sipilä ST, Kaila K (2008) GABAergic control of CA3-driven network events in the developing hippocampus. Results Probl Cell Differ 44: 99-121.

Sluka KA, Westlund KN (1992) Spinal projections of the locus coeruleus and the nucleus subcoeruleus in the Harlan and the Sasco Sprague-Dawley rat. Brain Res 579: 67–73.

Sly DJ, Colvill L, McKinley MJ, Oldfield BJ (1999) Identification of neural projections from the forebrain to the kidney, using the virus pseudorabies. J Auton Nerv Syst 77: 73–82.

Smetters D, Majewska A, Yuste R (1999) Detecting Action Potentials in Neuronal Populations with Calcium Imaging. Methods 18: 215-221.

Smiley JF, Subramanian M, Mesulam MM (1999) Monoaminergic cholinergic interacyions in the primate basal forebrain. Neurosci 93: 817–829.

Steindler DA (1981) Locus coeruleus neurons have axons that branch to the forebrain and cerebellum. Brain Res 223: 367–373.

Steriade M, Amzica F, Contreras D (1996) Synchronization of fast (30–40 Hz) spontaneous cortical rhythms during brain arousal J Neurosci 16: 392-417.

Steriade M, Deschenes M (1984) The thalamus as a neuronal oscillator. Brain Res Rev 8: 1–63.

Sterpenich V, D'Argembeau A, Desseilles M, Balteau E, Albouy G, Vandewalle G, Degueldre C, Luxen A, Collette F, Maquet P (2006) The locus ceruleus is involved in the successful retrieval of emotional memories in humans. J Neurosci 26: 7416-7423.

Stone TW (1973) Pharmacology of pyramidal tract cells in the cerebral cortex. Naunyn Schmiedebergs Arch Pharmacol 278: 333–346.

Stosiek C, Garaschuk O, Holthoff K, Konnerth A (2003) In vivo two-photon calcium imaging of neuronal networks. Proc Natl Acad Sci USA 100: 7319-7324.

Sullivan RM, Wilson DA, Lemon C, Gerhardt G (1994) Bilateral 6-OHDA lesions of the locus coeruleus impair associative olfactory learning in newborn rats. Brain Res 643: 306 –309.

Sullivan SJ, Farrant M, Cull-Candy SG (2017) TARP γ-2 Is Required for Inflammation-Associated AMPA Receptor Plasticity within Lamina II of the Spinal Cord Dorsal Horn. J Neurosci 37: 6007-6020.

Sutin, EL, Jacobowitz DM (1991) Neurochemicals in the dorsal pontine tegmentum. Prog Brain Res 88: 3–14.

Sutter ML, Schreiner CE, McLean M, O'connor KN, Loftus WC (1999) Organization of inhibitory frequency receptive fields in cat primary auditory cortex. J Neurophysiol 82: 2358–2371.

Suzuki J, Kanemaru K, Lino M (2016) Genetically Encoded Fluorescent Indicators for Organellar Calcium Imaging. Biophys J 111: 1119-1113.

Swanson LW (1976) The locus coeruleus: A cytoarchitectonic, Golgi and immunohistochemical study in the albino rat. Brain Res. 110: 39-56.

Swanson LW, Sawchenko PE (1983) Hypothalamic integration: organization of the paraventricular and supraoptic nuclei. Annu Rev Neurosci 6: 269–324.

Taccola G, Olivieri D, D'Angelo G, Blackburn P, Secchia L, Ballanyi K (2012) A1 adenosine receptor modulation of chemically and electrically evoked lumbar locomotor network activity in isolated newborn rat spinal cords. Neuroscience 222: 191-204.

Takahashi A, Camacho P, Lechleiter JD, Herman B (1999) Measurement of Intracellular Calcium. Physiol Rev 79: 1089–1125.

Taketani M, Baudry M (2006) Advances in Network Electrophysiology Using Multi-electrode Arrays. New York: Springer Press.

Tang F, Lane S, Korsak A, Paton JF, Gourine AV, Kasparov S, Teschemacher AG (2014) Lactate-mediated glia-neuronal signalling in the mammalian brain. Nat Commun 5: 3284.

Tomita S, Adesnik H, Sekiguchi M, Zhang W, Wada K, Howe JR, Nicoll RA, Bredit DS (2005) Stargazin modulates AMPA receptor gating and trafficking by distinct domains. Nature 435: 1052–1058.

Totah N, Neves R, Panzeri S, Logothetis N, Eschenko O (2018) The locus coeruleus is a complex and differentiated neuromodulatory system. Neuron 99: 1055-1068.

Travagli RA, Dunwiddie TV, Williams JT (1995) Opioid inhibition in locus coeruleus. J Neurophysiol 74: 519.

Traynelis SF, Wollmuth LP, McBain CJ, Menniti FS, Vance KM, Ogden KK, Hansen KB, Yuan H, Myers SJ, Dingledine R (2010) Glutamate receptor ion channels: structure, regulation, and function. Pharmacol Rev 62: 405-496.

Tsien RY (2009) Constructing and exploiting the fluorescent protein paintbox (Nobel Lecture). Angewandte Chemie 48: 5612-26.

Turecek J, Yuen GS, Han VZ, Zeng XH, Bayer KU, Welsh JP (2014) NMDA receptor activation strengthens weak electrical coupling in mammalian brain. Neuron 81: 1375-1388.

Ungerstedt U, Butcher LL, Butcher SG, Andén NE, Fuxe K (1969) Direct chemical stimulation of dopaminergic mechanisms in the neostriatum of the rat. Brain Res 14: 461.

Van Bockstaele EJ, Colago EE, Cheng P, Moriwaki A, Uhl GR, Pickel VM (1996). Ultrastructural evidence for prominent distribution of the mu-opioid receptor at extrasynaptic sites on noradrenergic dendrites in the rat nucleus locus coeruleus. J Neurosci. 16: 5037–5048.

Van Bockstaele EJ, Garcia-Hernandez F, Fox K, Alvarez VA, Williams JT (2004) Expression of connexins during development and following manipulation of afferent input in the rat locus coeruleus. Neurochem Internat 45: 421–428.

Van Bockstaele EJ, Peoples J, Valentino RJ (1999) Anatomic basis for differential regulation of the rostrolateral perilocus coeruleus region by limbic afferents. Biol Psychiatry 46: 1352-1363.

Viventi J, Kim DH, Vigeland L, Frechette ES, Blanco JA, Kim YS et al (2011) Flexible, foldable, actively multiplexed, high-density electrode array for mapping brain activity in vivo. Nat Neurosci 14: 1599–1605.

Wang G, Yu S, Zhang F, Li Y, Cao Y, Li Q, Song G, Zhang H (2004) Modulation of inspiratory inhibition of the Bötzinger complex by raphe pallidus and locus coeruleus in rabbits. Adv Exp Med Biol 551: 127–133.

Wang YY, Aghajanian GK (1990) Excitation of locus coeruleus neurons by vasoactive intestinal peptide: role of a cAMP and protein kinase A. J Neurosci 10: 3335–3343.

Wang Z, Haydon PG, Yeung ES (2000) Direct observation of calcium-independent intercellular ATP signaling in astrocytes. Analyt Chem. 72: 2001–2007.

Watabe K, Satoh T (1979) Mechanism underlying prolonged inhibition of rat locus coeruleus neurons following anti- and orthodromic activation. Brain Res 165: 343–347.

Westlund KN, Bowker, RM, Ziegler MG, Coulter JD (1983) Noradrenergic projections to the spinal cord of the rat. Brain Res 263: 15–31.

Williams JT, Bobker D, Harris G (1991) Synaptic potentials in locus coeruleus neurons in brain slices. Prog Brain Res 88:167-172.

Williams JT, Henderson G, North RA (1985) Characterization of α 2-adrenoceptors which increase potassium conductance in rat locus coeruleus neurones. Neurosci 14: 95–101.

Williams JT, Marshall KC (1987) Membrane properties and adrenergic responses in locus coeruleus neurons of young rats. J Neurosci 7: 3687-3694.

Williams JT, North RA (1984) Opiate-receptor interactions on single locus coeruleus neurones. Molec Pharmac 26: 489-497.

Williams JT, North RA, Shefner SA, Nishi S, Egan TM (1984) Membrane properties of rat locus coeruleus neurones. Neuroscience 13: 137–156.

Wolansky T, Clement EA, Peters SR, Palczak MA, Dickson CT (2006) Hippocampal Slow Oscillation: A Novel EEG State and Its Coordination with Ongoing Neocortical Activity. J Neurosci 26: 6213-6229.

Wu J, Abdelfattah AS, Miraucourt LS, Kutsarova E, Ruangkittisakul A, Zhou H, Ballanyi K, Wicks G, Drobizhev M, Rebane A, Ruthazer ES, Campbell RE (2014) A long Stokes shift red fluorescent protein Ca2+ indicator for 2-photon and ratiometric imaging. Nat Comm 5: 5262.

Yang W, Yuste R (2017) In vivo imaging of neural activity. Nat Methods 14: 349–359.

Young W, Kuhar M (1980) Radiohistochemical localization of benzodiazepine receptors in rat brain. J Pharmacol Exp Ther 212: 337-346.

Yuste R, Konnerth A, Masters B (2006). Imaging in Neuroscience and Development, A Laboratory Manual. J Biomed Opt 11, 19902.

Zaborszky L, Cullinan, WE (1996) Direct catecholaminergic-cholinergic interactions in the basal forebrain. I. dopamine-p-hydroxylase- and tyrosine hydroxylase input to cholinergic neurons. J Comp Neurol 554: 535–554.

Zamalloa T, Bailey CP, 709 Pineda J (2009) Glutamate-induced post-activation inhibition of locus coeruleus neurons is mediated by AMPA/kainate receptors and sodium-dependent potassium currents. Br J Pharmacol 156: 649-661.

Zhang X, Cui N, Wu Z, Su J, Tadepalli JS, Sekizar S, Jiang C (2010) Intrinsic membrane properties of locus coeruleus neurons in Mecp2-null mice. Am J Physiol Cell Physiol 298: C635–C646

Zhao Y, Abdelfattah AS, Zhao Y, Ruangkittisakul A, Ballanyi K, Campbell RE, Harrison DJ (2014) Microfluidic cell sorter-aided directed evolution of a protein-based calcium ion indicator with an inverted fluorescent response. Int Biol 6: 714-725.

Zhu H, Zhou W (2001) Morphine induces synchronous oscillatory discharges in the rat locus coeruleus. J Neurosci 21: RC179.

Zhu H, Zhou W (2005) Excitatory amino acid receptors are involved in morphine-induced synchronous oscillatory discharges in the locus coeruleus of rats. Eur J Pharmacol 528: 73-78.

Zhu Y, Aston-Jones G (1996) The medial prefrontal cortex prominently innervates a peri-locus coeruleus dendritic zone in rat. Soc Neurosci Abstr 22: 601.

Zhu ZT, Munhall A, Shen KZ, Johnson SW (2004) Calcium-dependent subthreshold oscillations determine bursting activity induced by N-methyl-D-aspartate in rat subthalamic neurons in vitro. Eur J Neurosci 19: 1296-1304.